AN ABSTRACT OF THE DISSERTATION OF

Logan E. Mitchell for the degree of Doctor of Philosophy in Geology presented on March 4, 2013.

Title: The Late Holocene Atmospheric Methane Budget Reconstructed from Ice Cores

Abstract approved: _____

Edward J. Brook

Ice cores are considered the gold standard for recording past climate and biogeochemical changes. However, gas records derived from ice core analysis have until now been largely limited to centennial and longer timescales because sufficient temporal resolution and analytical precision have been lacking, except during rare times when atmospheric concentrations changed rapidly. In this thesis I used a newly developed methane measurement line to make high-resolution, high-precision measurements of methane during the late Holocene (2800 years BP to present). This new measurement line is capable of an analytical precision of < 3 ppb using ~120 g samples whereas the previous highest resolution measurements attained a precision of ± 4.1 ppb using 500-1500g samples [MacFarling Meure et al., 2006]. The reduced sample size requirements as well as automation of a significant portion of the analysis process have enabled me to make >1500 discrete ice core methane measurements and construct the highest resolution records of methane available over the late Holocene. Ice core samples came from the recently completed West Antarctic Ice Sheet (WAIS) Divide ice core which has as one of its primary scientific objectives to produce the highest resolution records of greenhouse gases, and from the Greenland Ice Sheet Project (GISP2) ice core which is a proven paleoclimate archive. My thesis has the following three components.

I first used a shallow ice core from WAIS Divide (WDC05A) to produce a 1000 year long methane record with a ~9 year temporal resolution. This record confirmed the existence of multidecadal scale variations that were first observed in the Law Dome,

Antarctica ice core. I then explored a range of paleoclimate archives for possible mechanistic connections with methane concentrations on multidecadal timescales. In addition, I present a detailed description of the analytical methods used to obtain high-precision measurements of methane including the effects of solubility and a new chronology for the WDC05A ice core. I found that, in general, the correlations with paleoclimate proxies for temperature and precipitation were low over a range of geographic regions. Of these, the highest correlations were found from 1400-1600 C.E. during the onset of the Little Ice Age and with a drought index in the headwater region of the major East Asian rivers. Large population losses in Asia and the Americas are also coincident with methane concentration decreases indicating that anthropogenic activities may have been impacting multidecadal scale methane variability.

In the second component I extended the WAIS Divide record back to 2800 years B.P. and also measured methane from GISP2D over this time interval. These records allowed me to examine the methane Inter-Polar Difference (IPD) which is created by greater northern hemispheric sources. The IPD provides an important constraint on changes in the latitudinal distribution of sources. We used this constraint and an 8-box global methane chemical transport model to examine the Early Anthropogenic Hypothesis which posits that humans began influencing climate thousands of years ago by increasing greenhouse gas emissions and preventing the onset of the next ice age. I found that most of the increase in methane sources over this time came from tropical regions with a smaller contribution coming from the extratropical northern hemisphere. Based on previous modeling estimates of natural methane source changes, I found that the increase in the southern hemisphere tropical methane emissions was likely natural and that the northern hemispheric increase in methane emissions was likely due to anthropogenic activities. These results also provide new constraints on the total magnitude of pre-industrial anthropogenic methane emissions, which I found to be between the high and low estimates that have been previously published in the literature.

For the final component of my thesis I assembled a coalition of scientists to investigate the effects of layering on the process of air enclosure in ice at WAIS Divide.

Air bubbles are trapped in ice 60-100m below the surface of an ice sheet as snow compacts into solid ice in a region that is known as the Lock-In Zone (LIZ). The details of this process are not known and in the absence of direct measurements previous researchers have assumed it to be a smooth process. This project utilized high-resolution methane and air content measurements as well as density of ice, $\delta^{15}N$ of N_2, and bubble number density measurements to show that air entrapment is affected by high frequency (mm scale) layering in the density of ice within the LIZ. I show that previous parameterizations of the bubble closure process in firn models have not accounted for this variability and present a new parameterization which does. This has implications for interpreting rapid changes in trace gases measured in ice cores since variable bubble closure will impact the smoothing of those records. In particular it is essential to understand the details of this process as new high resolution ice core records from Antarctica and Greenland examine the relative timing between greenhouse gases and rapid climate changes.

The Late Holocene Atmospheric Methane Budget Reconstructed from Ice Cores

by
Logan E. Mitchell

A DISSERTATION

submitted to

Oregon State University

in partial fulfillment of
the requirements for the
degree of

Doctor of Philosophy

Presented March 4, 2013
Commencement June 2013

Doctor of Philosophy dissertation of Logan E. Mitchell presented March 4, 2013.

APPROVED:

Major Professor, representing Geology

Dean of the College of Earth, Ocean, and Atmospheric Sciences

---

Dean of the Graduate School

I understand that my dissertation will become part of the permanent collection of Oregon State University libraries. My signature below authorizes release of my dissertation to any reader upon request.

Logan E. Mitchell, Author

ACKNOWLEDGEMENTS

The winding path of my life has taken me to a great many places where I've met amazing people and had wonderful experiences. As I stand here at the end of a major milestone along this path it is important to look back and thank those who have helped me along the way.

At the top of this list is my adviser, Ed Brook who has been a better mentor than I could have ever asked for. It was at Ed's suggestion that I applied to graduate school and he has not only patiently guided me along each step of my Ph.D. program, but he also has been a positive role model on many levels from developing professional relationships, work-life balance, writing techniques, experimental objectiveness, intellectual curiosity, etc., to name but a few. Above all else it is his kindness and graciousness to others as well as his ethic of hard work that I will always remember. It has been an honor to be your student.

Peter, it was your glacial geology class that introduced me to paleoclimatology many years ago and that class has played a pivotal role in the direction of my life since then. Someday I hope to become as good of a teacher as you are. Thank you especially for all of the encouragement you've given me over the years. Alan, thank you for having the humility and confidence to tell me and the other paleo students that no paper is perfect, not even the ones that you wrote. By encouraging us to think of constructive criticism while reading papers you helped us to grow as scientists. Andreas, even though I didn't take your modeling class, I still learned a bunch from that class through Julia and Thomas. Thank you for you continued presence and insight within the paleoclimate community. Mark, thank you for being willing to join my committee, I hope you have enjoyed learning a little bit about methane!

I have been fortunate to have awesome co-conspirators over the past few years. Thomas, you are one of the funniest and smartest people I know. I wish we could have gone to the field together! Julia, I love your voice, and I'm so excited that you have found such a good fit with science writing. I look forward to reading your articles for a

long time to come! James, where do I start? Thank you so much for all of the long hours you put into making the methane measurements and for all of your help with math over the years! I'll never be able to run as fast as you, bike as hard as you, or play Frisbee as well as you, but I can beat you at pool. The best thing though is that I can count you among my best friends. Jon, your enthusiasm is infectious! The methane line is yours now, take care of it! I can't wait to see what you turn up. Mike, it has been awesome to see your smiling face every morning over the years. Shaun, we've come a long way since that intro geology class we took a decade ago. Thanks for being an awesome TA, and for letting me copy your thesis format. Christo, of all the awesome things you've done, I'm still most impressed by you making pasta from scratch with wheat flour on Taylor Glacier. Adrian, I'll always remember your love of salad! Rachael, its been awesome to get to know you, and I hope we can continue to work together in the future!

A lot of manual labor went into producing the methane records presented here. Thanks go to Jean Ahrens who taught me how to use the methane line in the first place and Dan Berry who built the LabView program which automated the line. Thanks also to those who have helped prepare and analyze the samples: James Lee, Brad Markle, Alex Morin, Brendan Williams, Marc Nabelek, Lauren Foiles, and Jon Edwards. Matt Arsenault has played a pivotal role in the direction of my life from getting me a job with the Hi-CLIMB project to encouraging me to talk to Ed about working in the ice core lab as an undergrad. Thanks for also teaching me how to brew beer, which has been an important skill in grad school!

Thanks go to the WAIS Divide community which is responsible for drilling an excellent ice core without which this project would not be possible. This project has given me the opportunity to go to Antarctica twice, both unforgettable experiences where I've worked with amazing colleagues. Anais, Bess, Giff, John, Spruce, Tim, Brian, Natalie, Dave, Susanne, all the drillers, and the rest of the WAIS Divide crew, it was awesome!

I also wish to thank the National Science Foundation and the Oregon NASA Space Grant Fellowship for providing the financial resources to complete my Ph.D. I

also thank the College of Earth Ocean and Atmospheric Sciences (formerly Geosciences and COAS) which has been a great place to learn and grow as a scientist as well a fun department to be a part of.

My Hacienda housemates Levi, Toshi, Dafne, Jack, Jordan, and Rosie have been my closest friends and best confidants over the years. We've shared the high times, the low times, and everything in between. Through the rats, parties, fires, pool tournaments, busted pipes, and family dinners, La Hacienda endures. Jack, Rosie, and Ale, the legacy passes onto you.

My deepest thanks go to my wonderful wife, Cate. She has supported me in so many ways over past few years, most recently with the best food a person could ask for while finishing a thesis. I am looking forward to spending many adventures to come with you.

Last but not least, thanks go to my family. You have loved and supported me in everything that I've done, and I would not be here today without that.

CONTRIBUTION OF AUTHORS

Chapter 2: E. J. Brook provided the project design, assisting in methodology development, and co-wrote the manuscript. T. Sowers was a major collaborator and assisted in the data interpretation. J. R. McConnell measured mineral acidity and K. Taylor measured electrical conductivity in the ice. The mineral acidity and electrical conductivity were used to produce the chronology for the WAIS Divide shallow ice core (WDC05A).

Chapter 3: E. J. Brook assisted in the project design and co-wrote the manuscript. J. E. Lee assisted making many of the methane measurements. C. Buizert produced the gas age chronologies for the WDC06A and GISP2 ice cores. T. Sowers was a major collaborator and assisted in the data interpretation.

Chapter 4: C. Buizert developed the new stochastic parameterization for the closed porosity, conducted the firn air modeling, and co-wrote the manuscript. E. J. Brook also co-wrote the manuscript. D. Breton measured high resolution density on the WDC05A and WDC06A ice cores. J. Fegyveresi contributed to the estimate of the cut bubble correction. D. Baggenstos and A. Orsi contributed $\delta^{15}N$ isotopic measurements. J. Severinghaus, R. Alley, and M. Albert are major collaborators and contributed to the data interpretation. J. Ahn assisted in developing the conceptual framework for the project. S. Gregory contributed open porosity measurements.

TABLE OF CONTENTS

TABLE OF CONTENTS (continued)

Page

TABLE OF CONTENTS (continued)

Page

LIST OF FIGURES

LIST OF FIGURES (Continued)

LIST OF FIGURES (Continued)

LIST OF TABLES

If I have seen further it is by standing on the shoulders of giants.

- Sir Isaac Newton

A man who keeps company with glaciers comes to feel tolerably insignificant by and by.

- Mark Twain, *A Tramp Abroad*

The Late Holocene Atmospheric Methane Budget Reconstructed from Ice Cores

1.1 Background

Atmospheric methane, a greenhouse gas that exists in trace concentrations in Earth's atmosphere, is important from both societal and biogeochemical perspectives. Understanding the global methane budget has societal relevance because increases in anthropogenic methane emissions since the Industrial Revolution account for ~20% of the total increase in radiative forcing from all long lived greenhouse gases [*Forster et al.*, 2007]. Also, methane has an atmospheric lifetime of 8-10 years (e.g. [*Dentener et al.*, 2003; *Lassey et al.*, 2007]) so reductions in emissions could provide a mechanism to reduce the near future radiative forcing from greenhouse gases [*Yan et al.*, 2009]. Methane emissions from natural sources are primarily from the anaerobic decomposition of organic material by archaea in terrestrial environments (e.g. [*Khalil*, 2000]). Methane sources and sinks are sensitive to climatic variations on a range of temporal and spatial scales, linking methane to large-scale climate and biogeochemical cycles. Understanding past methane changes gives important context for the modern methane budget and helps constrain predictions of how it will change in the future.

Direct atmospheric methane measurements have greatly expanded our knowledge of the global methane budget, however these measurements do not extend far back in time and so our understanding of methane variability on timescales of decades and longer is inherently limited. Sporadic measurements of methane directly from air samples began in 1962 but these early measurements had infrequent temporal resolution, spatial coverage, and lacked widely used standards and are thus not commonly discussed in the literature [*Khalil et al.*, 1989]. Regular measurements of methane began in 1983 and continue today under the GAGE/AGAGE [*Cunnold et al.*, 2002] and NOAA ESRL GMD [*Dlugokencky et al.*, 2012] sampling networks. In addition, satellite retrievals from the SCIAMACHY instrument on board the ENVISAT satellite have greatly increased the spatial coverage of methane observations. However, these retrievals must be calibrated to flask network observations paired with a global chemical transport model, which

makes them dependent on the quality and spatial distribution of the flask sample network [*Bergamaschi et al.*, 2007; *Bergamaschi et al.*, 2009]. These sampling networks have greatly improved our understanding of the sources and sinks as well as the spatial and temporal variability of methane. However, because the data from the networks only cover three decades, they cannot provide information about methane variability on longer timescales. One of the most prominent features in the methane record over the past three decades is the reduction in growth rate beginning in the early 1990s and subsequent stabilization of its concentration since 1999 [*Bousquet et al.*, 2006; *Dlugokencky et al.*, 1998; *Dlugokencky et al.*, 1994]. The ultimate causes of the stabilization of the concentration are currently under debate, with dominant hypotheses being changes in anthropogenic, biomass burning, and wetland emissions. Recent observations show that the global methane concentration is once again increasing [*Dlugokencky et al.*, 2009]. Since the record of direct atmospheric measurements only extends three decades in the past, it is unknown if variations in the growth rate of this magnitude have occurred before this time.

Ice sheets form at the polar regions of the Earth and are unique paleoarchives because they record a number of tracers of past climate in the ice matrix as well as trapping air in bubbles which preserves a record of past atmospheric trace gas concentrations (e.g. [*Barnola et al.*, 1987; *Chappellaz et al.*, 1990; *Dansgaard et al.*, 1969; *Raynaud et al.*, 1993]). The first ice core methane measurements came from the Byrd and Camp Century ice cores, however the low preindustrial methane concentrations were discounted as resulting from chemical reactions which consumed methane in the firn [*Robbins et al.*, 1973]. The significance of the ice core record was not recognized until *Craig and Chou* [1982] made further measurements and hypothesized that ice cores faithfully preserve a record of past changes in methane concentration. Since that time there have been numerous studies documenting methane concentrations in ice cores over the past 800,000 years [*Baumgartner et al.*, 2012; *Blunier and Brook*, 2001; *Blunier et al.*, 1995; *Blunier et al.*, 1993; *Brook et al.*, 1996; *Brook et al.*, 2000; *Chappellaz et al.*, 1997a; *Chappellaz et al.*, 1990; *Chappellaz et al.*, 1993; *Chappellaz et al.*, 1997b;

Delmotte et al., 2004; *Etheridge et al.*, 1988; *Etheridge et al.*, 1992; *Etheridge et al.*, 1998; *Grachev et al.*, 2007; *Grachev et al.*, 2009; *Huber et al.*, 2006; *Kobashi et al.*, 2007; *Landais et al.*, 2003; *Loulergue et al.*, 2008; *MacFarling Meure et al.*, 2006; *Petit et al.*, 1999; *Rasmussen and Khalil*, 1984; *Raynaud et al.*, 1988; *Raynaud et al.*, 1993; *Severinghaus and Brook*, 1999; *Severinghaus et al.*, 1998; *Stauffer et al.*, 1985]. Major findings from these studies include: 1) methane concentrations are highly correlated with Greenland temperature variations [*Brook et al.*, 1996; *Brook et al.*, 2000; *Chappellaz et al.*, 1993], 2) the timing of the rapid increases in methane are nearly synchronous within a few decades with Greenland temperature increases [*Huber et al.*, 2006; *Severinghaus and Brook*, 1999; *Severinghaus et al.*, 1998], 3) glacial-interglacial changes in methane come primarily from tropical and boreal wetland sources [*Brook et al.*, 2000], 4) methane variations follow orbital scale climate change [*Delmotte et al.*, 2004; *Loulergue et al.*, 2008; *Petit et al.*, 1999]. Methane records from the high resolution Law Dome ice core records have documented the dramatic increase in methane since the start of the industrial revolution and overlap with direct atmospheric measurements, increasing the confidence that ice cores faithfully record past methane concentrations [*Etheridge et al.*, 1998; *MacFarling Meure et al.*, 2006].

Over the past few years the U.S. ice coring community has drilled a new deep ice core on the West Antarctic Ice Sheet (WAIS) Divide. One of the primary science objectives of this project is to "Develop the most detailed record of greenhouse gases possible for the last 100,000 years" (http://www.waisdivide.unh.edu/science/index.shtml). This deep ice core drilling effort has taken five field seasons to reach its depth goal of 3,405 m below the surface and was completed in January, 2012. In addition to the deep core (WDC06A), a shallow core (WDC05A) extending 300 m below the surface and 1000 years into the past was also drilled for greenhouse gas analysis and method development. Both of these cores are of excellent quality and present a unique opportunity to greatly increase our knowledge of the global methane cycle with high-resolution ice core measurements over the last glacial cycle.

Recently an analytical system for making high precision discrete measurements of methane has been developed at Oregon State University that utilizes small ice core samples [*Grachev et al.*, 2007; *Grachev et al.*, 2009]. This new extraction line is capable of an analytical precision of < 3 ppb using ~120g samples [*Mitchell et al.*, 2011] whereas the previous highest resolution measurements attained a precision of ±4.1 using 500-1500g samples [*MacFarling Meure et al.*, 2006]. The reduced sample size requirements as well as automation of a significant portion of the analysis process enabled me to make >1500 ice core methane measurements and construct the highest resolution, highest precision records of methane available over the late Holocene.

1.2 Chapter topics

Chapter two presents a 1,000 year long record of methane from WAIS Divide with a 9 year resolution that confirmed the existence of multidecadal scale variations in methane which had been previously observed in the Law Dome ice core record. I compared this record to temperature and precipitation proxies as well as past anthropogenic activities that may have affected methane emissions for a possible causal connection to the multidecadal scale methane variability. This chapter also contains a detailed description of the analytical methods I used to obtain high-precision measurements of methane including the effects of solubility, and a new chronology for the WDC05A ice core. This chapter was published in the Journal of Geophysical Research-Biogeosciences in 2011 [*Mitchell et al.*, 2011].

In the third chapter I extended the WAIS Divide record from Antarctica to 5 ka using the main deep ice borehole (WDC06A) and measured methane from a Greenland ice core (GISP2D) back to 3 ka. These records allowed me to reconstruct the first high-resolution methane inter-polar gradient (IPG), which is created by greater northern hemispheric sources. The IPG provides an important constraint on changes in the latitudinal distribution of sources over time. I used this constraint and an 8-box global methane chemical transport model to examine the Early Anthropogenic Hypothesis,

which posits that humans began influencing climate thousands of years ago and prevented the onset of the next ice age by increasing greenhouse gas emissions.

For chapter four I coordinated a multifaceted approach to investigate the processes controlling bubble closure in the region of an ice sheet where snow compacts into solid ice called the firn. That the firn is a layered medium has been known for some time, but to facilitate the modeling of air transport and occlusion of air in bubbles it has been assumed to have smoothly varying properties. I present a new parameterization for the trapping of bubbles in the firn that explicitly accounts for the additional variability imparted by density variability on short distance scales (e.g., layering). This work has implications for interpreting the smoothing parameters of ice core trace gas records. It also points to a mechanism that affects total air content records and may be responsible for poorly understood variability in air content records. I also make recommendations for future work that could better constrain these parameters.

1.3 References

Barnola, J. M., D. Raynaud, Y. S. Korotkevich, and C. Lorius (1987), VOSTOK ICE CORE PROVIDES 160,000-YEAR RECORD OF ATMOSPHERIC CO_2, *Nature*, *329*(6138), 408-414.

Baumgartner, M., A. Schilt, O. Eicher, J. Schmitt, J. Schwander, R. Spahni, H. Fischer, and T. F. Stocker (2012), High-resolution interpolar difference of atmospheric methane around the Last Glacial Maximum, *Biogeosciences*, *9*(10), 3961-3977.

Bergamaschi, P., et al. (2007), Satellite chartography of atmospheric methane from SCIAMACHY on board ENVISAT: 2. Evaluation based on inverse model simulations, *J. Geophys. Res.-Atmos.*, *112*(D2), 26.

Bergamaschi, P., et al. (2009), Inverse modeling of global and regional CH4 emissions using SCIAMACHY satellite retrievals, *J. Geophys. Res.-Atmos.*, *114*.

Blunier, T., and E. J. Brook (2001), Timing of millennial-scale climate change in Antarctica and Greenland during the last glacial period, *Science*, *291*(5501), 109-112.

Blunier, T., J. Chappellaz, J. Schwander, B. Stauffer, and D. Raynaud (1995), Variations in atmospheric methane concentration during the Holocene epoch, *Nature*, *374*(6517), 46-49.

Blunier, T., J. A. Chappellaz, J. Schwander, J. M. Barnola, T. Desperts, B. Stauffer, and D. Raynaud (1993), Atmospheric methane, record from a greenland ice core over the last 1000 year, *Geophys. Res. Let.*, *20*(20), 2219-2222.

Bousquet, P., et al. (2006), Contribution of anthropogenic and natural sources to atmospheric methane variability, *Nature*, *443*(7110), 439-443.

Brook, E. J., T. Sowers, and J. Orchardo (1996), Rapid variations in atmospheric methane concentration during the past 110,000 years, *Science*, *273*(5278), 1087-1091.

Brook, E. J., S. Harder, J. Severinghaus, E. J. Steig, and C. M. Sucher (2000), On the origin and timing of rapid changes in atmospheric methane during the last glacial period, *Glob. Biogeochem. Cycle*, *14*(2), 559-572.

Chappellaz, J., E. Brook, T. Blunier, and B. Malaize (1997a), CH_4 and $d^{18}O$ of O_2 records from Antarctic and Greenland ice: A clue for stratigraphic disturbance in the bottom part of the Greenland Ice Core Project and the Greenland Ice Sheet Project 2 ice cores, *J. Geophys. Res.-Oceans*, *102*(C12), 26547-26557.

Chappellaz, J., J. M. Barnola, D. Raynaud, Y. S. Korotkevich, and C. Lorius (1990), Ice-core record of atmospheric methane over the past 160,000 years, *Nature*, *345*(6271), 127-131.

Chappellaz, J., T. Blunier, D. Raynaud, J. M. Barnola, J. Schwander, and B. Stauffer (1993), Synchronous changes in atmospheric CH_4 and Greenland climate between 40 and 8 kyr BP, *Nature*, *366*(6454), 443-445.

Chappellaz, J., T. Blunier, S. Kints, A. Dallenbach, J. M. Barnola, J. Schwander, D. Raynaud, and B. Stauffer (1997b), Changes in the atmospheric CH_4 gradient between Greenland and Antarctica during the Holocene, *J. Geophys. Res.-Atmos.*, *102*(D13), 15987-15997.

Craig, H., and C. C. Chou (1982), METHANE - THE RECORD IN POLAR ICE CORES, *Geophys. Res. Let.*, *9*(11), 1221-1224.

Cunnold, D. M., et al. (2002), In situ measurements of atmospheric methane at GAGE/AGAGE sites during 1985-2000 and resulting source inferences, *J. Geophys. Res.-Atmos.*, *107*(D14), 20.

Dansgaard, W., S. J. Johnsen, J. Møller, and C. C. Langway, Jr. (1969), One Thousand Centuries of Climatic Record from Camp Century on the Greenland Ice Sheet, *Science*, *166*(3903), 377-381.

Delmotte, M., J. Chappellaz, E. Brook, P. Yiou, J. M. Barnola, C. Goujon, D. Raynaud, and V. I. Lipenkov (2004), Atmospheric methane during the last four glacial-interglacial cycles: Rapid changes and their link with Antarctic temperature, *J. Geophys. Res.-Atmos.*, *109*(D12), 13.

Dentener, F., W. Peters, M. Krol, M. van Weele, P. Bergamaschi, and J. Lelieveld (2003), Interannual variability and trend of CH4 lifetime as a measure for OH changes in the 1979-1993 time period, *J. Geophys. Res.-Atmos.*, *108*(D15).

Dlugokencky, E. J., K. A. Masarie, P. M. Lang, and P. P. Tans (1998), Continuing decline in the growth rate of the atmospheric methane burden, *Nature*, *393*(6684), 447-450.

Dlugokencky, E. J., P. M. Lang, A. M. Crotwell, and K. A. Masaire (2012), Atmospheric Methane Dry Air Mole Fractions from the NOAA ESRL Carbon Cycle Cooperative Global Air Sampling Network, 1983-2011, Version: 2012-09-24, Path: ftp://ftp.cmdl.noaa.gov/ccg/ch4/flask/event/, edited.

Dlugokencky, E. J., K. A. Masarie, P. M. Lang, P. P. Tans, L. P. Steele, and E. G. Nisbet (1994), A dramatic decrease in the growth rate of atmospheric methane in the northern hemisphere during 1992, *Geophys. Res. Let.*, *21*(1), 45-48.

Dlugokencky, E. J., et al. (2009), Observational constraints on recent increases in the atmospheric CH4 burden, *Geophys. Res. Let.*, *36*.

Etheridge, D. M., P. G. I., and d. S. F. (1988), Atmospheric trace-gas variations as revealed by air trapped in an ice core from Law Dome, Antarctica, *Ann. Glac.*, *10*, 28-33.

Etheridge, D. M., G. I. Pearman, and P. J. Fraser (1992), Changes in tropospheric methane between 1841 and 1978 from a high accumulation rate Antarctic ice core, *Tellus Ser. B-Chem. Phys. Meteorol.*, *44*(4), 282-294.

Etheridge, D. M., L. P. Steele, R. J. Francey, and R. L. Langenfelds (1998), Atmospheric methane between 1000 AD and present: Evidence of anthropogenic emissions and climatic variability, *J. Geophys. Res.-Atmos.*, *103*(D13), 15979-15993.

Forster, P., et al. (2007), Changes in Atmospheric Constituents and in Radiative Forcing., in *Climate Change 2007: The Physical Science Basis. Contribution of Working Group I to the Fourth Assessment Report of the Intergovernmental Panel on Climate Change*, edited by S. Solomon, D. Qin, M. Manning, Z. Chen, M. Marquis, K. B. Averyt, M. Tignor and H. L. Miller, pp. 131-234, Cambridge University Press, Cambridge, United Kingdom and New York, NY, USA.

Grachev, A. M., E. J. Brook, and J. P. Severinghaus (2007), Abrupt changes in atmospheric methane at the MIS 5b-5a transition, *Geophys. Res. Let.*, *34*(20), 5.

Grachev, A. M., E. J. Brook, J. P. Severinghaus, and N. G. Pisias (2009), Relative timing and variability of atmospheric methane and GISP2 oxygen isotopes between 68 and 86 ka, *Glob. Biogeochem. Cycle*, *23*, 10.

Huber, C., M. Leuenberger, R. Spahni, J. Fluckiger, J. Schwander, T. F. Stocker, S. Johnsen, A. Landals, and J. Jouzel (2006), Isotope calibrated Greenland temperature record over Marine Isotope Stage 3 and its relation to CH4, *Earth and Planetary Science Letters*, *243*(3-4), 504-519.

Khalil, M. A. K. (Ed.) (2000), *Atmospheric Methane: Its Role in the Global Environment*, 341 pp., Springer-Verlag, Berlin Heidelberg New York.

Khalil, M. A. K., R. A. Rasmussen, and M. J. Shearer (1989), Trends of Atmospheric Methane During the 1960s and 1970s, *J. Geophys. Res.-Atmos.*, *94*(D15), 18279-18288.

Kobashi, T., J. P. Severinghaus, E. J. Brook, J. M. Barnola, and A. M. Grachev (2007), Precise timing and characterization of abrupt climate change 8200 years ago from air trapped in polar ice, *Quat. Sci. Rev.*, *26*(9-10), 1212-1222.

Landais, A., et al. (2003), A tentative reconstruction of the last interglacial and glacial inception in Greenland based on new gas measurements in the Greenland Ice Core Project (GRIP) ice core, *J. Geophys. Res.-Atmos.*, *108*(D18), 12.

Lassey, K. R., D. M. Etheridge, D. C. Lowe, A. M. Smith, and D. F. Ferretti (2007), Centennial evolution of the atmospheric methane budget: what do the carbon isotopes tell us?, *Atmos. Chem. Phys.*, *7*(8), 2119-2139.

Loulergue, L., A. Schilt, R. Spahni, V. Masson-Delmotte, T. Blunier, B. Lemieux, J. M. Barnola, D. Raynaud, T. F. Stocker, and J. Chappellaz (2008), Orbital and millennial-scale features of atmospheric CH_4 over the past 800,000 years, *Nature*, *453*(7193), 383-386.

MacFarling Meure, C., D. Etheridge, C. Trudinger, P. Steele, R. Langenfelds, T. van Ommen, A. Smith, and J. Elkins (2006), Law Dome CO_2, CH_4 and N_2O ice core records extended to 2000 years BP, *Geophys. Res. Let.*, *33*(14), 4.

Mitchell, L. E., E. J. Brook, T. Sowers, J. R. McConnell, and K. Taylor (2011), Multidecadal variability of atmospheric methane, 1000-1800 CE, *J. Geophys. Res.-Biogeosci.*, *116*.

Petit, J. R., et al. (1999), Climate and atmospheric history of the past 420,000 years from the Vostok ice core, Antarctica, *Nature*, *399*(6735), 429-436.

Rasmussen, R. A., and M. A. K. Khalil (1984), Atmospheric Methane in the Recent and Ancient Atmospheres: Concentrations, Trends, and Interhemispheric Gradient, *J. Geophys. Res.-Atmos.*, *89*(ND7), 1599-1605.

Raynaud, D., J. Chappellaz, J. M. Barnola, Y. S. Korotkevich, and C. Lorius (1988), CLIMATIC AND CH4 CYCLE IMPLICATIONS OF GLACIAL INTERGLACIAL CH4 CHANGE IN THE VOSTOK ICE CORE, *Nature*, *333*(6174), 655-657.

Raynaud, D., J. Jouzel, J. M. Barnola, J. Chappellaz, R. J. Delmas, and C. Lorius (1993), The ice record of greenhouse gases, *Science*, *259*(5097), 926-934.

Robbins, R. C., L. A. Cavanagh, L. J. Salas, and E. Robinson (1973), ANALYSIS OF ANCIENT ATMOSPHERES, *Journal of Geophysical Research*, *78*(24), 5341-5344.

Severinghaus, J. P., and E. J. Brook (1999), Abrupt climate change at the end of the last glacial period inferred from trapped air in polar ice, *Science*, *286*(5441), 930-934.

Severinghaus, J. P., T. Sowers, E. J. Brook, R. B. Alley, and M. L. Bender (1998), Timing of abrupt climate change at the end of the Younger Dryas interval from thermally fractionated gases in polar ice, *Nature*, *391*(6663), 141-146.

Stauffer, B., G. Fischer, A. Neftel, and H. Oeschger (1985), Increase of Atmospheric Methane Recorded in Antarctic Ice Core, *Science*, *229*(4720), 1386-1388.

Yan, X. Y., H. Akiyama, K. Yagi, and H. Akimoto (2009), Global estimations of the inventory and mitigation potential of methane emissions from rice cultivation conducted using the 2006 Intergovernmental Panel on Climate Change Guidelines, *Glob. Biogeochem. Cycle*, *23*.

Multidecadal variability of atmospheric methane, 1000-1800 C.E.

Logan E. Mitchell [1], Edward J. Brook [1], Todd Sowers [2], Joseph R. McConnell [3], Kendrick Taylor [3]

[1] Oregon State University, Department of Geosciences, Corvallis, OR 97331

[2] The Earth and Environmental Systems Institute, Penn State University, University Park, PA 16802.

[3] Desert Research Institute, Nevada System of Higher Education, Reno, Nevada, USA.

Published in:
Journal of Geophysical Research – Biogeosciences
John Wiley & Sons Inc
350 Main Street
Malden MA 02148, USA
VOL. 116, G02007, doi:10.1029/2010JG001441

2.1 Abstract

We present a new high-precision, high-resolution record of atmospheric methane from the West Antarctic Ice Sheet (WAIS) Divide ice core covering 1000-1800 C.E., a time period known as the Late Preindustrial Holocene (LPIH). The results are consistent with previous measurements from the Law Dome ice core, the only other high-resolution record of methane for this time period, and confirm most of the observed variability. Multidecadal variability in methane concentrations throughout the LPIH is weakly correlated or uncorrelated with reconstructions of temperature and precipitation from a variety of geographic regions. Correlations with temperature are dominated by changes in northern hemisphere high latitude temperatures between 1400-1600 C.E. during the onset of the Little Ice Age. Times of war and plague when large population losses could have reduced anthropogenic emissions are coincident with short periods of decreasing global methane concentrations.

Index Terms: 0325 Evolution of the atmosphere, 0793 Biogeochemistry, 0490 Trace gases, 0724 Ice Cores.

2.2 Introduction

Atmospheric methane, the second most important greenhouse gas directly impacted by anthropogenic activities, accounts for 18% of the total increase in radiative forcing by all long lived greenhouse gases and varied in the past on timescales ranging from seasons to hundreds of thousands of years (e.g. [*Bousquet et al.*, 2006; *Forster et al.*, 2007; *Loulergue et al.*, 2008]). Systematic direct atmospheric measurements since 1983 from the NOAA [*Dlugokencky et al.*, 2012] and GAGE/AGAGE [*Cunnold et al.*, 2002] sampling networks reveal that methane sources and sinks are perturbed by seasonal climate cycles, atmospheric chemistry, large scale atmospheric patterns such as El Niño Sothern Oscillation (ENSO), volcanic eruptions, and anthropogenic activities [*Bousquet et al.*, 2006; *Steele et al.*, 1987]. These direct measurements also documented a surprising decrease in the methane growth rate during the 1990s and a recent resumption

of growth [*Dlugokencky et al.*, 2009]. Understanding methane variability on decadal to multidecadal timescales and discriminating between changes in natural and anthropogenic sources is difficult because of spatial and temporal variability of sources and sinks. Furthermore, direct atmospheric records are not yet long enough to assess variability on multidecadal timescales and ice core records have rarely achieved the precision and time resolution needed to observe changes on such short timescales. These limitations have made it difficult to place the decadal scale variability observed in the record of direct atmospheric measurements in a longer term context.

Air occluded in polar ice sheets provides a unique archive that enables us to extend our record of methane into the past. Accumulation rate (i.e. annual accumulation of snowfall) is one of the primary factors that limit the temporal resolution of ice core paleo-atmospheric reconstructions. Long records from low accumulation sites ($\leq$ 50 kg m^{-2} yr^{-1}) such as Vostok and Dome C have revealed orbital scale variability over the last 800,000 years (e.g. [*Delmotte et al.*, 2004; *Loulergue et al.*, 2008]), but do not preserve the detail needed to examine short term variability because diffusion in the firn smoothes the records [*Spahni et al.*, 2003]. The degree of smoothing is much smaller at sites where accumulation rates are high, and the most detailed history of methane over the last few millennia is captured in ice cores from Law Dome in East Antarctica [*Etheridge et al.*, 1998; *MacFarling Meure et al.*, 2006] where the very high accumulation rate (600-1100 kg m^{-2} yr^{-1}) allows for large sample sizes yielding precise measurements, high temporal resolution, and excellent chronological control. Furthermore the Law Dome ice core and firn air records overlap with direct atmospheric measurements and confirm that polar ice faithfully preserves past atmospheric concentrations of methane.

In this study we present a new, precise, decadally resolved ice core methane record spanning 1000-1800 C.E., a period known as the Late Preindustrial Holocene (LPIH) [*Etheridge et al.*, 1998]. The results come from the West Antarctic Ice Sheet (WAIS) Divide ice core site (core WDC05A). We confirm the magnitude and timing of multidecadal variability observed in the Law Dome methane record over this time period. We also investigate correlations between our methane concentration record and

paleoclimate and historical records relevant to methane sources to investigate the processes which likely controlled LPIH methane variations.

2.3 Methods

2.3.1 WDC05A Core Recovery

A deep ice core, the WAIS Divide Core (WDC), is located on the West Antarctic Ice Sheet divide at 79.467°S, 112.085°W, surface elevation of 1,759 m. The modern annual accumulation rate of ~200 ±34 kg m^{-2} yr^{-1}[*Banta et al.*, 2008], mean temperature of -31°C, and the simple ice flow regime at the site are ideal for high-resolution analysis of greenhouse gases over the past ~110,000 years [*Morse et al.*, 2002]. These characteristics are similar to high-resolution deep ice cores in central Greenland (GISP2, GRIP, and NGRIP) simplifying interhemispheric comparisons. The samples used here came from a 298 m shallow core that was extracted in the austral summer of 2005/2006 (WDC05A) 1.3 km northwest of the main borehole (WDC06A). It was drilled with a 10 cm electromechanical drill without drilling fluid and core quality was excellent.

2.3.2 Analytical Procedures

2.3.2.1 Methane Measurements

Samples were processed using a wet extraction technique similar to that described by [*Grachev et al.*, 2007; *Grachev et al.*, 2009] and further elaborated on here. The outer 1-2mm of ice samples was removed with a band saw in a -25˚C freezer to produce fresh ice that was not recently exposed to the modern atmosphere. This ice was divided in half along the vertical axis to produce a pair of samples with the same depth and age. Each sample had a cross sectional area of ~2.5 cm^2, height of ~10 cm, and weight of 50-63g. Samples were weighed to the nearest 0.1 g and placed in pre-cooled cylindrical glass vacuum flasks joined to stainless steel CF flanges with a glass to metal transition, manufactured by Larson Electronic Glass (Redwood City, CA, USA). Each flask was bolted to a stainless steel vacuum line assembly and sealed with a copper o-ring. Valves on the vacuum line are pneumatically actuated Swagelok bellows sealed valves with

Polychlorotrifluoroethylene (PCTFE) stem tips. The vacuum line accommodated eight flasks. The flasks were submerged in an ethanol bath maintained at -60ºC to -70ºC and ambient air was removed by pumping with a turbo molecular pump (Alcatel ATP80) backed with a dry (scroll) pump for one hour. The valves to the flasks were then closed and flasks were submerged in a warm water bath at ~50°C to completely melt the ice and release the gas into the headspace above the water. Melting was usually complete in ~15 minutes. The flasks were then re-submerged in the ethanol bath for one hour to freeze the samples and prevent water vapor from interfering with the measurements. The air in the headspace of the flasks was expanded to a 10 cc sample loop on a 6-port Valco gas sampling valve. Samples were injected on to a packed column (6 foot, 1/8" Hayesep D 80/100 mesh) in an Agilent Technologies 6890N Gas Chromatograph (GC) equipped with a flame ionization detector, using ultrapure nitrogen as a carrier gas. The pressure in the sample loop was measured using an MKS Baratron capacitance manometer (0-100 torr, 0.15% accuracy) installed in the GC oven for temperature stability. The air from each sample was analyzed four times with the pressure of the first expansion ($P_{headspace}$) typically between 35-45 torr and the last 10-20 torr. The peak area over loop pressure ratio was measured for each air sample and compared to a linear regression line fitted to the ratios from a working air standard (500.22 ppb methane on the NOAA04 methane scale [*Dlugokencky et al.*, 2005]) covering the entire range of sample pressures. Concentrations from the four measurements from each sample were then averaged to produce a mean methane concentration for each sample. Mean concentrations were averaged for each pair of samples to produce a mean concentration for each depth/age (Figure 2.1).

Calibration of daily measurements was maintained throughout the experiment by analyzing our working air standard tank 12 times each day over the pressure range of 10-50 torr. The working air standard tank was a high pressure cylinder of synthetic air prepared by Scott-Marrin Inc. that was calibrated to primary laboratory standard tanks with concentrations ranging from 380-1853 ppb, which were calibrated by the NOAA GMD Carbon Cycle Group on the NOAA04 methane scale [*Dlugokencky et al.*, 2005].

The response of the measurement system is linear to better than 1.5 ppb over the standard tank concentration range. This implies a negligible correction over the sample concentration range so we have assumed a linear response.

Over the course of this study 294 samples from 147 depths were measured. The results from two depths were rejected due to leaks. In addition, we further investigated the 5% of samples (7 depths) with the greatest disagreement between the sample pairs (> 5.9 ppb). We measured additional duplicate samples from the same or adjacent depths and in the three depths with the greatest disagreement (10.5-11.8 ppb) we observed that of the four samples measured there was good agreement between three of them and one outlier. In these three cases we suspected that the outlier was a result of contamination or a leak and rejected that pair of samples. Between September 21 and October 23, 2007 we noticed slightly higher methane levels than expected in 34 samples, and traced the contamination to a change in flask cleaning procedures after a personnel change. We detected this contamination when measurement of air-free ice (see below) indicated a contamination of 5-14 ppb. To eliminate the contamination we cleaned the flasks daily (i.e. after every use) with Alconox® detergent soap, whereas prior to October 23 we had cleaned the flasks weekly. Additional samples from identical or adjacent depths to the contaminated samples were measured after daily cleaning of flasks was implemented. Duplicate measurement of the samples analyzed prior to September 21 and after October 23, 2007 yielded consistent results. All results including leaks, outliers, and contaminated samples, are shown in Figure 2.1.

The average standard error of the four analyses for individual samples was 1.4 ppb and the pooled standard deviation between the means of the sample pairs was 1.9 ppb. These statistics exclude the rejected results described above. To quantify the long term reproducibility of the methane analysis, we measured 16 duplicate pairs of ice samples with the time between measurements ranging from days to months. These duplicates had the same depths as the original samples and should therefore have identical methane concentrations. The pooled standard deviation between the mean of the original and duplicate pairs of samples is 2.8 ppb which is the value we use to

represent the long term analytical uncertainty (1σ) for this data set. The greater variability observed in these duplicates most likely comes from subtle changes in the solubility of gases in the meltwater, discussed in greater detail below.

2.3.2.2 Corrections to Measurements

2.3.2.2.1 Blanks

To constrain the influence of leaks or other contamination in our analysis line we routinely measured air-free ice (AFI). To create AFI we boiled ultrapure, 18 MΩ water in a cylindrical stainless steel vacuum flask with a Conflat flange seal and metal bellows seal valve welded to the top flange. We affixed a ~30 cm piece of 1/8" stainless steel tubing to the outlet, and during boiling the valve remained open. The boiling drives air from the water, which is swept from the chamber by the released steam. We boiled the water for 30 minutes then sealed the bellows and slowly froze the remaining liquid from the bottom up in an ethanol bath kept at -20˚C. Sample preparation and analysis of the artificial ice was identical to ice core samples with the exception that before the artificial ice was melted in the flasks, sufficient standard air from our working air standard tank was added to the flasks so that when expanded to the sample loop it produced pressures equivalent to those from ice core samples. In this way any errors resulting from leaks or contamination of the flasks could be quantified and corrected for. Average AFI corrections were linearly interpolated between days when AFI was analyzed to create a time dependent correction to the data. The average AFI correction was 1.1 ± 0.5 (1σ) ppb.

2.3.2.2.2 Solubility of Methane in Water

Gases dissolve in liquid water with the partitioning between the air and water described by Henry's Law. Methane is ~2.5x as soluble as nitrogen and therefore the headspace methane concentration decreases when air is exposed to liquid water. As the water is re-frozen a small fraction of the air is trapped in the ice leading to a depletion of

methane in the headspace after freezing. We express a methane solubility correction factor as:

$$Correction\ Factor = \frac{[CH_4]_{Total}}{[CH_4]_{Headspace}} \quad (1)$$

where $[CH_4]_{Headspace}$ is the concentration in the headspace which we measure during our typical analysis and $[CH_4]_{Total}$ can be expressed as the molar ratio:

$$[CH_4]_{Total} = \frac{\{CH_4\}_{Headspace+Water}}{\{Ar + O_2 + N_2 + CH_4\}_{Headspace+Water}} \quad (2)$$

where $\{CH_4\}_{Headspace+Water}$ and $\{Ar+O_2+N_2+CH_4\}_{Headspace+Water}$ are the total number of moles that were in the original ice sample. Inclusion of trace atmospheric gases has a negligible effect and was ignored. At equilibrium the distribution of air constituents between the headspace and the meltwater is dictated by Henry's Law constants at 273.2 K [*Fogg*, 2003] because the majority of dissolution happens as bubbles escape from the melting ice sample and rise through the meltwater next to it. Using typical values for flask and ice volumes, the headspace air would have a methane concentration depleted by 2.1-2.2% relative to the original concentration. For example, a sample which has a measured $[CH_4]_{Headspace}$ of 700 ppb, 60 mL of water in a 134 cm^3 flask, at 273.2 K, would have a $[CH_4]_{Total}$ of 715 ppb and therefore a correction factor of 1.021.

We examined this correction factor empirically by measuring the concentration of methane in the frozen sample water ($[CH_4]_{Refreeze}$) after our typical analysis was completed for 32 samples. After the initial melt-refreeze-CH_4 measurement was completed we evacuated the headspace for one hour then another melt-refreeze-CH_4 measurement was done. $[CH_4]_{Total}$ was then calculated as follows:

$$[CH_4]_{Total} = \frac{[CH_4]_{Headspace} \times P_{Headspace} + [CH_4]_{\mathrm{Re}\ freeze} \times P_{\mathrm{Re}\ freeze}}{P_{Headspace} + P_{\mathrm{Re}\ freeze}} \quad (3)$$

where P is pressure in torr. Mean and standard deviations (1σ) from the 32 measurements were $P_{Refreeze}$ = 0.50 ± 0.06 torr and $[CH_4]_{Refreeze}$ = 1698 ±169 ppb. The correction factor from these experiments is therefore 1.0170 ± 0.0031%. Since $P_{Refreeze}$ is ~1% of $P_{Headspace}$ we expect the amount gas trapped in the ice during the second melt-refreeze cycle to be ~1% of $P_{Refreeze}$, or ~0.005 torr, and therefore negligible.

The uncertainty in the correction factor is probably caused by a variety of subtle differences between samples such as sample size, air content, and the refreezing rate. This uncertainty is inherently incorporated into our estimate of the long-term uncertainty of our measurements because it is derived from duplicate measurements from different days and should therefore represent the full range of possible variability. Given these considerations we have increased our final methane concentration values by the average empirically derived solubility correction factor of 1.0170.

The difference between the calculated and empirical correction factors is likely caused by the headspace air not reaching a solubility equilibrium with the meltwater when the samples are refrozen. This has been observed in greater detail in other studies with much larger samples [*Petrenko et al.*, 2008]. The values given above indicate that the samples reach ~80% of solubility equilibrium, presumably because of exclusion of gases during freezing. Slower re-freezing may reduce the effect at the expense of longer processing times.

2.3.2.2.3 Gravitational Fractionation

Gases within the firn undergo mass dependant fractionation due to gravity [*Craig et al.*, 1988; *Jakob Schwander*, 1989; *Jakob Schwander et al.*, 1997; *Sowers et al.*, 1989]. The magnitude of gravitational fractionation is controlled by the thickness of the diffusive air column in the firn and can be estimated by measuring the $^{15}N/^{14}N$ ratio of N_2 and reported using standard delta notation as $\delta^{15}N_2$. Because the turnover time at the

atmospheric N_2 reservoir is longer than a million years, we can assume that the $^{15}N/^{14}N$ ratio of atmospheric N_2 has remained constant over ice core timescales [*Sowers et al.*, 1992]. Measurement of $\delta^{15}N_2$ all along the main core (WDC06A) at WAIS Divide (100-300m) revealed $\delta^{15}N$ values of 0.303 ± 0.006‰ [*Severinghaus, J.*, personal communication, 2010]. Gravitational fractionation of methane concentrations results from the mass difference between methane (M = 16.04 g mol^{-1}) and dry air (M = 28.96 g mol^{-1}). The gravitational correction is therefore $\Delta M \times \delta^{15}N_2$ where ΔM = 12.92 g mol^{-1}. This results in a gravitational fractionation correction (increase of the measured concentration) of 0.39% which we have applied to all of our ice core measurements. $\delta^{15}N_2$ is not expected to be significantly different between the WDC05A and WDC06A cores.

2.3.3 WDC05A Chronology

Convective and diffusive processes move air through the firn faster than the annual accumulation of ice causing air to be younger than the surrounding ice at a given depth within the firn [*Jakob Schwander*, 1989]. The age difference between the air and the enclosing ice is termed "delta age" (Δage). The original WDC05A chronology [*Mischler et al.*, 2009], was based on annual layer counting of the non-sea salt sulfur to sodium ratio (nssS/Na) between the surface and 70 m [*Banta et al.*, 2008] and Alternative Current Electric Conductivity Measurement (ACECM) measurements from 70-298 m to establish the age of the ice. A 1-D firn air diffusion model following [*Battle et al.*, 1996] and [*Trudinger et al.*, 1997] was used to estimate the mean age of the air at the Lock in Depth (LID) which is then subtracted from the age of the ice at the LID to estimate Δage [*Mischler et al.*, 2009]. The ice chronology from 70-298 m was recently improved by optimizing correlations between the monthly resolved mineral acidity measurements from the main borehole (WDC06A) which are dominated by fallout from volcanic emissions and the WDC05A ACECM measurements. Annual layer counting of the high-resolution chemical records from the upper 70 m of WDC05A and WDC06A from ~1300 C.E. to ~2000 C.E. was confirmed by comparison with the volcanic sequence of nssS

from Law Dome, adapted from [*Palmer et al.*, 2001]. This generated 71 unique tie points between the WDC05A and WDC06A records. The annual accumulation rate from WDC06A was then mapped onto WDC05A assuming a linear change between tie points. To evaluate the uncertainty in the estimated ice age for WDC05A, we compared the estimated ice ages in the upper 70 m with those determined from high-resolution chemistry measurements on the same core. For the 231 years common to both records, the average difference between the two depth-age scales is 0.056 m_{weq} (water equivalent), with a maximum difference of 0.283 m_{weq}. The mean annual accumulation rate is ~0.20 m_{weq}, so the mean difference is 3-4 months. The maximum difference corresponds to ~1.4 years and the standard deviation between the estimated and observed depth-age scales is ~0.07 m_{weq} or ~4 months. The difference between our final ice chronology (WDC05A:2) and the original ice chronology (WDC05A:1) [*Mischler et al.*, 2009] is negligible between 0-70 m, increasing to 13 years at 148 m, and then decreasing to -36 years at 298 m.

A visible volcanic ash layer observed in both cores was also used to confirm the dating of the two cores. The ~5mm volcanic ash layer was observed at 190.83m (1248.1 C.E.) in WDC05A and 190.39m (1248.5 C.E.) in WDC06A (ages determined using the revised chronologies). Electron microprobe analysis indicates that the chemical composition, grain size and particle morphology of the two layers are nearly indistinguishable, indicating that both are from the same eruption and therefore deposited contemporaneously [*Dunbar, N.*, personal communication, 2010]. The ash layer has abundant ash particles and is relatively coarse grained with particles up to 20 μm suggesting that it has an Antarctic source. Positive chemical correlations with ash layers in the Siple Dome and Taylor Dome ice cores indicate that this ash layer is a major regional time stratigraphic marker [*Dunbar et al.*, 2003; *Dunbar et al.*, 2007].

A 1-D firn air diffusion model estimated that the mean age of the air within the open porosity at the LID (65.5 m at WDC05A) is 9.9 years for CO_2 and 7.2 years for CH_4 [*Battle, M.*, personal communication, 2009]. The difference between the mean age of CH_4 and CO_2 arises from the different diffusivities of the two gases in the firn air. The

width of the CH_4 age distribution at half height is 5.9 years. The age of the ice at the LID is 215 years which makes Δage 205.1 years for CO_2 and 207.8 years for CH_4. Since temperature [*Steig, E.*, personal communication, 2010] and accumulation at WDC05A have remained relatively constant in the LPIH we do not expect that Δage has changed significantly and for the purpose of creating a chronology have held it constant. To construct the final gas chronology we have subtracted 207.8 years from the ice chronology. The estimated uncertainty of the chronology is ± 10 years based on a detailed comparison between our record and the Law Dome methane record, discussed below. This chronology is designated WDC05A:2.

2.4 Results and Discussion

2.4.1 Comparison with Previous High-Resolution Antarctic Data from Law Dome

Replication of paleoclimate records is an important means of verifying their reliability. The methane record from Law Dome, Antarctica, a well known data set covering the last 2,000 years, is a compilation of data from three different ice cores (DSS, DE08, DE08-2) and until now has been the only high-resolution, high-precision record covering the past 1,000 years [*Etheridge et al.*, 1998; *MacFarling Meure et al.*, 2006]. The Law Dome record from 1000-1800 C.E. comes from the DSS ice core and the data are plotted with the WDC05A results in Figure 2.2, after conversion of Law Dome results to the NOAA04 calibration scale [*Dlugokencky et al.*, 2005]. Error bands are ± 2.8 ppb for WDC05A, ± 5 ppb for DSS samples reported by [*Etheridge et al.*, 1998], and ± 4.1 ppb for DSS samples reported by [*MacFarling Meure et al.*, 2006]. The Law Dome data were produced using a dry extraction technique with large samples (500-1500g) while we use a wet extraction technique with small samples (two samples, ~60g each) which requires a correction for solubility effects (discussed above).

Law Dome is located at 66.733°S, 112.833°E, with a surface elevation of 1,390 m and is over 3,500 km away from the WAIS Divide site. Since there are essentially no sources of methane in the high latitude southern hemisphere, the atmospheric

concentration around Antarctica is homogenous [*Dlugokencky et al.*, 1994] and should have been so in the past. The absolute methane concentrations in both records are very consistent (Figure 2.2). The only time interval where the records differ beyond the 1-σ envelope of analytical and temporal uncertainty is 1410-1470 C.E. where they diverge by 10-15 ppb. This is within the 2-σ level and despite the divergence both records show a peak in concentrations during this time period. We observe that the amplitude of high-precision variability in the WDC05A core is ~10-20% smaller than in Law Dome. The exact mechanisms behind the slight amplitude reduction are not currently known but we speculate that it is a result of greater mixing of air within the lock in zone during the bubble closure process, which is longer at WDC05A because of the lower accumulation rate.

The data from WDC05A and Law Dome show that atmospheric methane in the high latitude southern hemisphere averaged ~690 ppb (NOAA 04 scale) and experienced multidecadal variability during the LPIH. During the 18th century anthropogenic activities increased methane emissions and caused global concentrations to increase rapidly [*Etheridge et al.*, 1998; *MacFarling Meure et al.*, 2006]. The general trends in methane concentration during the 19th and 20th centuries have been described in greater detail elsewhere and preliminary measurements from WDC05A (not shown) support those previous conclusions [*Etheridge et al.*, 1998; *MacFarling Meure et al.*, 2006]. Here we focus on a detailed comparison with previously published high-resolution records of methane during the LPIH.

A statistical comparison of the two methane records shows a high degree of correlation ($r = 0.87$ for linear regression). The WDC05A record appears to slightly lag the Law Dome record. A maximum correlation ($r = 0.91$) between the records is obtained by shifting the WDC05A record 9 years older. While it is not possible to determine which record is "correct", the highest correlation occurs within the stated uncertainty of ±10 years for the WDC05A gas chronology [*Mischler et al.*, 2009], which is largely due to uncertainty in Δage. One possible explanation for the offset is that the firn air model used by [*Mischler et al.*, 2009] to deduce Δage for WDC05A assumes that

all bubbles close off below the Lock in Depth (LID). This assumption has been used in the past for sites with a similar temperature and accumulation rate as WAIS Divide such as Summit, Greenland but observations suggest that as much as 20% of the bubbles close above the LID [*J. Schwander et al.*, 1993]. Gradual bubble closure was included in the firn air transport model used for the Law Dome ice cores, but the large accumulation rate at this site reduces the magnitude of this effect [*Trudinger et al.*, 1997]. Qualitatively, bubble closure above the LID combined with a low to moderate accumulation rate would decrease Δage and cause additional smoothing of the gas records, consistent with our observations.

Alignment of large rapid changes in methane concentrations have been used to establish chronostratigraphic tie points between ice cores in the past because methane has a relatively short lifetime and variations recorded in polar ice cores are expected to represent global signals [*Blunier and Brook*, 2001; *Brook et al.*, 2005; *EPICA Community Members*, 2006; *Lemieux-Dudon et al.*, 2010]. This approach has generally not yet been utilized for small scale variations (≤ 50 ppb) because methane records have, until now, lacked sufficient temporal resolution and analytical precision to uniquely identify small scale variability. The high degree of correlation between the Law Dome and WDC05A methane records demonstrate that this technique could be a viable way to establish chronostratigraphic tie points between high-precision methane records from moderate to high accumulation rates.

2.4.2 Multidecadal methane variability from 1000 to 1800 C.E.

2.4.2.1 Implications for the global methane budget

At steady state the global methane budget can in simplest form be expressed as: $dB/dt = S - B/\tau$ where B is the total atmospheric burden (Tg of CH_4), S is the total source in Tg yr^{-1}, and τ is the lifetime of CH_4 in years. The average LPIH methane concentration from WDC05A is ~690 ppb and the interpolar gradient is 43 ± 5 ppb based on preliminary measurements from the Greenland ice core GISP2D (not shown) [*Mitchell and Brook*, 2009]. The global mean atmospheric concentration, weighted by surface

area, has been estimated for the LPIH as the Antarctic concentration plus 37% of the interpolar gradient [*Etheridge et al.*, 1998] and is therefore ~706 ppb from our data. Using the total mass of the dry atmosphere ($5.1352 \pm 0.0003 \times 10^{18}$ kg [*Trenberth and Smith*, 2005]) the global average atmospheric burden is calculated to be ~2008 Tg (2.844 Tg CH_4 ppb^{-1}) for the LPIH at steady state ($dB/dt = 0$). Numerous chemical modeling studies have tried to determine likely values for S & τ for the LPIH but these are sensitive to the concentration of OH, the primary sink for CH_4, and its interaction with the CH_4-CO-NO_X chemical system. These models have produced estimates of LPIH τ that range from 17% lower to 16% higher than the present day range of 8.9-9.2 years [*Dentener et al.*, 2003; *Harder et al.*, 2007; *Martinerie et al.*, 1995; *Prinn et al.*, 2001; *Shindell et al.*, 2003]. For the purposes of the discussion here we choose a LPIH τ of 8 years, implying a steady state flux of ~250 Tg CH_4 yr^{-1}.

We estimated the methane growth rate by linearly interpolating the WDC05A data annually, then determining the annual rate of change. This time series was smoothed with a 30 year Gaussian filter (Figure 2.3). The most negative growth rates occurred in the early 13th and late 16th centuries while the most positive growth rates occurred at the turn of the 16th century. The interannual variability of methane growth rates may have been greater given that the modern record of direct atmospheric measurements since 1983 record which shows variations of up to ±15 ppb CH_4 yr^{-1} [*Bousquet et al.*, 2006; *Dlugokencky et al.*, 2009], but such short term changes would not be captured by the ice core record. The overall decrease of ~10 ppb yr^{-1} over this time period [*Dlugokencky et al.*, 2009] is, however, sustained for long enough that similar changes in the past would have been preserved in the ice core record after smoothing of the firn at the WAIS Divide site. This recent change in the growth rate is therefore larger than any we observe during the LPIH.

It has been common in the ice core literature to interpret past variations as indicators of changes in climate driven methane sources, primarily wetlands, although most work has recognized the possibility that the methane sink can change [*Fischer et al.*, 2008; *Kaplan et al.*, 2006; *Valdes et al.*, 2005]. The wetland centric view is supported by

a number of model studies that appear to show that τ has changed relatively little despite the large changes in the global methane burden and sink between preindustrial and modern times [*Crutzen and Bruhl*, 1993; *Lelieveld et al.*, 1998; *Martinerie et al.*, 1995; *Shindell et al.*, 2003; *Thompson*, 1992; *Y H Wang and Jacob*, 1998]. Measurements of methyl chloroform (MCF; CH_3CCl_3) since 1978 are used to determine modern OH concentrations. These data show that while there can be significant interannual variability in OH, the longer term trend is small [*Bousquet et al.*, 2005], despite rising methane levels. This supports the contention that OH, the main sink for CH_4, has been relatively stable in the past and implies that the concentration changes we observe are likely to be the result of source changes. However, no tracer of past changes in global OH levels before MCF measurements began in 1978 currently exists and therefore the ultimate validity of this argument remains to be tested. This is important given that the magnitude of the interannual global methane sink due to reaction with OH [*Bousquet et al.*, 2006] is of a similar magnitude to the multidecadal variability seen in the LPIH.

2.4.2.2 Methane Source Variations

If we assume that the methane sink has remained relatively constant then the observed multidecadal variability would be a result of variations in source strength. Methane is primarily produced by the anaerobic decomposition of organic material by archaea (See [*Khalil*, 2000] for a review). To obtain a source distribution for the LPIH, we combined the "Holocene base" scenario from [*Harder et al.*, 2007] which estimates natural methane sources (~230 Tg CH_4 yr^{-1}) with the anthropogenic source estimate (~30 Tg CH_4 yr^{-1}) from [*Houweling et al.*, 2000] then scaled the total source to 250 Tg CH_4 yr^{-1}, as shown in Table 1. The magnitude of variability observed in the WDC05A record is ~10-34 ppb, equivalent to 4-12 Tg CH_4 yr^{-1}, or 1.4-4.8% of the total budget (Figure 2.2). As mentioned previously, ice cores record a smoothed history of atmospheric methane with the degree of smoothing being dependant on the characteristics of the ice core site. The Law Dome record appears to have recorded ~10-20% greater variability than WDC05A, so our record provides a constraint on the minimum amount of variability

possible. The variability in the WDC05A record is similar in magnitude to each of the individual non-wetland sources (Table 1). Since it is unlikely that the multidecadal variability comes from very large changes in the smaller budget terms, the most likely explanation is that the variability comes from emissions from wetlands which, given adequate carbonaceous substrate, are predominantly influenced by water table depth and soil temperature (e.g. [*Allen et al.*, 2003; *Bloom et al.*, 2010; *Christensen et al.*, 2004; *E Matthews*, 2000; *van Hulzen et al.*, 1999; *Walter et al.*, 2001a; b; *D Q Wang et al.*, 2009; *Worthy et al.*, 2000; *Zona et al.*, 2009]). Sufficient water is required to produce anoxic conditions that are a prerequisite for methanogenesis. Once anoxic conditions are present, increasing temperatures lead to higher emissions with a maximum growth temperature of 37-45°C [*Boone*, 2000]. Temperature and precipitation controls on methanogenesis operate on sub-annual timescales, so changes in these climatic variables have an immediate impact on annual emissions. The record of methane emissions is then smoothed by the atmosphere and by the firn before being trapped in polar ice sheets. Wetland emissions are thus controlled by temperature and precipitation changes and respond quickly (on sub-annual timescales) to changes in these variables, so we would expect the ice core methane record to be correlated with temperature and precipitation changes on multidecadal timescales.

In sections 2.4.2.2.1 and 2.4.2.2.2 we examine LPIH temperature and precipitation records as well as estimates of anthropogenic emissions for relationships with the WDC05A methane record. Our approach is guided by modeling studies and satellite measurements which show that precipitation exerts a dominant control on tropical (30°S-30°N) methane emission variability through its influence on water table depth and interannual OH concentrations, whereas temperature is the dominant factor in high latitude northern hemisphere (30°N-90°N) variability [*Bekki and Law*, 1997; *Bloom et al.*, 2010; *Bousquet et al.*, 2006; *Khalil and Rasmussen*, 1983; *Walter et al.*, 2001a]. Prior to comparison, the paleoclimate records and the methane record were smoothed with a bandpass filter removing periods shorter than 20 years and longer than 500 years, removing variability both higher than the Nyquist frequency of the ice core record and

lower than multicentennial frequencies due to slow changes in forcing (e.g. gradual cooling between the Medieval Warm Period and the Little Ice Age), isolating variability on multidecadal timescales. To calculate correlations and their statistical significance ($p < 0.05$, null hypothesis that $r = 0$) the smoothed paleoclimate records were then subsampled to match the ages of our methane data points (N = 89).

2.4.2.2.1 Temperature

Previous studies have documented the striking correlation between the oxygen isotope record of ice ($\delta^{18}O_{ice}$, a proxy for local temperature) from Greenland ice cores and methane during the past glacial cycle (e.g. [*Brook et al.*, 2000; *Chappellaz et al.*, 1993; *Huber et al.*, 2006; *Severinghaus and Brook*, 1999; *Severinghaus et al.*, 1998]). See Table 2 and Figure 2.4 for comparisons between methane and temperature proxies. The correlation coefficient between our methane record and the GRIP [*Johnsen et al.*, 1997] $\delta^{18}O_{ice}$ record is statistically significant, but not high ($r = 0.24$, $p = 0.03$). The correlation coefficient is even lower and not statistically significant with the NGRIP [*Vinther et al.*, 2006] $\delta^{18}O_{ice}$ record ($r = 0.06$, $p = 0.56$). A record of temperature reconstructed from $\delta^{40}Ar$ and $\delta^{15}N$ isotopes from GISP2 [*Kobashi et al.*, 2010] also does not have a statistically significant correlation with methane ($r = 0.18$, $p = 0.10$). Sliding the chronologies of these records relative to our methane record by ± 50 years does not greatly increase the correlation coefficients. We infer from this analysis that the close relationship between methane and large temperature changes during the last ice age apparently does not extend to the very small temperature variability in Greenland during the LPIH, at least to the extent that these proxies are actually recording site temperature.

We have also compared our record to three northern hemispheric land temperature reconstructions [*Mann et al.*, 2008] EIV Land ($r = -0.10$, $p = 0.37$) [*Moberg et al.*, 2005] ($r = -0.13$, $p = 0.23$) [*Hegerl et al.*, 2007] ($r = 0.03$, $p = 0.81$) (Table 2, Figure 2.4). The weakly negative correlation coefficients and lack of statistical significance indicates that hemispheric temperature variability during the LPIH did not directly control global methane concentrations. Hemispheric to global temperature

reconstructions have been used to scale methane emissions in model reconstructions for the late Holocene using the argument that emissions are temperature sensitive and because of a lack of other constraints [*Houweling et al.*, 2008]. Our results suggest that this approach will not yield accurate results.

Local to regional scale temperature reconstructions that are specific to methane source regions might be expected to have a greater correlation with global methane concentrations. Analysis of modern methane emissions indicates that Northern Hemisphere extratropical wetlands are more sensitive to temperature than tropical wetlands [*Bloom et al.*, 2010]. We examined two extratropical Northern Hemisphere temperature reconstructions [*D'Arrigo et al.*, 2006] ($r = 0.04$, $p = 0.73$) and [*Esper et al.*, 2002] ($r = 0.16$, $p = 0.13$) that utilize similar data sets and found that they both have low correlation coefficients with methane that lack statistical significance. A multiproxy Arctic temperature reconstruction [*Kaufman et al.*, 2009] ($r = 0.24$, $p = 0.03$) has a low but statistically significant correlation with methane which increases to $r = 0.34$ if the record is interpolated annually and shifted by -30 years, within the uncertainty in their chronology (~2-10%).

We also examine correlation coefficients with tropical sea surface temperature records from the Indo Pacific Warm Pool (IPWP) [*Oppo et al.*, 2009] ($r = 0.26$, $p = 0.01$) and Cariaco Basin [*Black et al.*, 2007] ($r = 0.35$, $p < 0.01$) and find statistically significant correlation coefficients that are slightly higher than with other temperature reconstructions. The record from the Cariaco basin has a high correlation ($r = 0.77$) when the record is interpolated annually and shifted forward in time by 52 years. The magnitude of this shift is near the chronological uncertainty for this record, which was determined by correlation to a nearby sediment core that utilizes AMS ^{14}C dates with uncertainties of ± 50-60 years [*Black et al.*, 1999]. This possible correlation on multidecadal timescales is compelling because Cariaco SSTs were highly correlated with methane and Greenland $\delta^{18}O$ records during the last glacial termination [*Lea et al.*, 2003]. Since temperature variations of the magnitude seen in this record would not be expected to have a direct impact on tropical methane emissions, we suggest that temperatures in

these areas are likely linked to larger scale climatic processes which control precipitation and more likely impacted emissions.

Recently [*Mann et al.*, 2009] used a diverse multiproxy network to reconstruct a global surface temperature field using a Regularized Expectation-Maximization Climate Field Reconstruction (RegEM CFR) approach. In Figure 2.5a we show the correlation coefficient field between bandpass filtered and subsampled surface temperature and methane during the LPIH. Hatching indicates statistically significant correlation ($p < 0.05$, null hypothesis is that $r = 0$) in that grid box. The highest, statistically significant correlation coefficients exist in the eastern tropical, southern, and northern Pacific, and extratropical Eurasia. Negative correlation coefficients exist over the north Atlantic. The proxy network used in this reconstruction has very few oceanic records so oceanic temperatures are dependent on the covariance relationships established with the CFR approach which assumes temporal stationarity between proxy indicators and large scale climate patterns [*Mann et al.*, 2008]. Since the ocean is a negligible source of methane, the correlations with oceanic SSTs indicate possible relationships with climate variability on multidecadal timescales associated with SSTs in those areas. The positive correlations over extratropical Eurasia are consistent with the hypothesis that temperature variability in this region is a controlling factor on emissions and impacts multidecadal variability of global methane concentrations. This same relationship has been observed on interannual and shorter timescales by satellite measurements in recent years [*Bloom et al.*, 2010].

The Pacific Decadal Oscillation (PDO) is a leading mode of variability in the North Pacific that exhibits multidecadal variability affecting regional SSTs and precipitation patterns [*Mantua and Hare*, 2002; *Mantua et al.*, 1997]. A PDO reconstruction covering the LPIH [*MacDonald and Case*, 2005] ($r = 0.35$, $p = <0.01$) has a moderate, statistically significant correlation with methane (Table 2, Figure 2.6). The positive correlations with tropical Pacific SSTs and the PDO index are puzzling since on interannual timescales La Niña conditions (when SSTs are anomalously cold in this region) are associated with greater precipitation over tropical land areas and greater tropical methane emissions [*Dlugokencky et al.*, 2009; *Gu et al.*, 2007]. We also

examined a proxy for the North Atlantic Oscillation (NAO) [*Trouet et al.*, 2009] ($r = 0.03$, $p = 0.76$) however this proxy has no correlation with methane on multidecadal timescales.

The positive correlations we observe between temperature reconstructions in some regions and the methane record appear to be driven in large part by temperature variations in the latter part of the record, particularly between 1400 and 1600 C.E. The largest feature in our methane record for the LPIH is a large increase from 1470-1520 and a subsequent decrease from 1560-1600 C.E. A similar feature is seen in many temperature reconstructions, however the temperature decline is seen most prominently in records from higher latitudes: Sweden [*Grudd et al.*, 2002]; "North (55°-70°N)" and "Eastern Hemisphere" regions in [*E R Cook et al.*, 2004]; "Northern Siberia" in [*Briffa et al.*, 2001]; "Yukon", "Central Northwest Territories", "Jaemtland", "Tornetraesk", and "Mongolia" in [*D'Arrigo et al.*, 2006]; modeled Arctic temperatures calibrated to Arctic temperature proxies [*Crespin et al.*, 2009]. The fall in methane is also coincident with the start of the "classical" climatological Little Ice Age (LIA) [*J A Matthews and Briffa*, 2005]. Using the temperature field reconstruction discussed above [*Mann et al.*, 2009], we used the annually interpolated records to calculate correlation coefficients in 200 year moving windows and found the highest correlation during the time period 1400-1600 C.E. (Figure 2.5b). During this time period the land region with the greatest spatially consistent statistically significant positive correlations is extratropical Eurasia. These observations suggest that temperature perturbations in this time period, particularly in the high latitude northern hemisphere, may have impacted global methane concentrations as has been noted previously by other workers [*Etheridge et al.*, 1998; *MacFarling Meure et al.*, 2006].

2.4.2.2.2 Precipitation

The largest areas of methane emissions from natural wetlands are the monsoon regions of East Asia, India, and South America [*Bergamaschi et al.*, 2009]. High temporal resolution records of rainfall variability in specific areas of monsoon regions

have been inferred from the oxygen isotopic composition ($\delta^{18}O$) of speleothems (cave deposits). While the correlation between speleothems from monsoon regions to Greenland temperature (e.g. [*X F Wang et al.*, 2006; *Y J Wang et al.*, 2001]) and Greenland temperature to methane (e.g. [*Brook et al.*, 2000; *Chappellaz et al.*, 1993]) have been widely reported for the last ice age, these relationships have not been explored for the late Holocene.

Speleothem $\delta^{18}O$ records that cover the LPIH with enough temporal resolution to observe multidecadal variability have been recovered from the East Asian monsoon region and Peru. Of the East Asian speleothem records, the Dongge [*Y J Wang et al.*, 2005] and Heshang [*Hu et al.*, 2008] chronologies have uncertainties of ±50 years which reduces the confidence in the timing of multidecadal variability. The Wanxiang [*P Z Zhang et al.*, 2008] chronology is much better (< ±5 years) and is highly correlated on decadal timescales with another speleothem from the Dandak cave in east-central India [*Berkelhammer et al.*, 2010] which supports the interpretation that these records represent regional precipitation. On their stated chronologies, the Heshang ($r = 0.24$, $p = 0.02$) and Wanxiang ($r = 0.28$, $p = 0.01$) speleothem $\delta^{18}O$ records have statistically significant correlation with methane, but the Dongge ($r = 0.02$, $p = 0.88$) record does not (Table 2; Figure 2.6). The speleothem $\delta^{18}O$ record from the Cascayunga cave in Peru is inversely correlated with tropical SSTs in the Cariaco basin on multidecadal timescales [*Reuter et al.*, 2009] and other South American speleothems have shown this same relationship on millennial timescales [*Cruz et al.*, 2005; *Lea et al.*, 2003]. Correlation between methane and the Cascayunga speleothem is negative and is not statistically significant on its stated chronology ($r = -0.19$, $p = 0.09$). The correlation increases to $r = -0.35$ when the annually interpolated chronology is shifted forward in time by 19 years, although this shift is larger than the uncertainty of their chronology (±4-9 years) [*Reuter et al.*, 2009]. This possible correlation on multidecadal timescales is intriguing because a negative correlation has been noted between South American speleothems and methane on millennial timescales [*Cruz et al.*, 2005].

A recent spatial reconstruction of the Asian monsoon region Palmer Drought Severity Index (PDSI) using tree rings [*E R Cook et al.*, 2010] extends back to 1300 C.E. and offers a significant advancement in that the records are annually resolved and have a broad distribution over a large wetland region. Spatial correlation coefficients and analytical uncertainty from this reconstruction were constructed in the same manner as the correlation with the temperature field reconstruction and cover 1300-1800 C.E. (Figure 2.7). Positive PDSI values indicate wetter conditions and the highest positive correlation coefficients are centered on the eastern Tibetan Plateau. This area is the source of many major Asian rivers (Yangtze, Mekong, Yellow, Pearl, and Salween rivers) which feed much of the Asian monsoon region. Modern satellite observations show that this area is also a major source of methane emissions which are positively correlated with groundwater depth and temperature on interannual and shorter timescales [*Bergamaschi et al.*, 2009; *Bloom et al.*, 2010]. Our results suggest that the relationship between methane and drought in this area holds for multidecadal timescales and may have been an important factor contributing to global methane variability during the LPIH.

2.4.2.2.3 Anthropogenic Methane Sources

The dramatic increase in atmospheric methane concentrations at the start of the industrial revolution in the mid 18th century is a result of increasing anthropogenic emissions. Before this time the contribution of anthropogenic emissions are not well constrained [*Ferretti et al.*, 2005; *Houweling et al.*, 2008; *Mischler et al.*, 2009]. A range of published LPIH anthropogenic methane emissions are shown in Table 3. These estimates are generally constructed by scaling modern anthropogenic emissions down with population and then making educated guesses about how anthropogenic activities (land use, farming practices, etc.) would have altered per capita emissions. The process involves many difficult to verify assumptions and we thus caution that the exact value of the following semi-quantitative calculations is less important than the approximate magnitudes.

The “Early Anthropogenic” hypothesis argues that human activity began altering atmospheric methane concentrations as early as 5,000 years ago with the biggest contribution coming from agricultural activities, particularly rice farming in China (see [*Ruddiman*, 2003; 2007] and sources therein). The hypothesis presumes that early rice farming techniques were inefficient resulting in disproportionately large methane emissions per capita relative to modern times. Following this line of reasoning, any large reduction in human population or agricultural production during the LPIH caused by plagues or wars, especially in areas of rice cultivation, should have reduced methane emissions on the timescales of those events. Here we use the historic record to explore the possibility that reductions in human populations, agricultural production, or land use patterns were large enough to have a demonstrative impact on global methane concentrations.

The two biggest wars in Asia during the LPIH were the Mongol invasion beginning in 1211 C.E. lasting for about three decades, and the overthrow of Ming dynasty and the establishment of the Qing dynasty in the mid 17th century. These events were associated with large losses of population estimated at 35 million (~30% or ~15% of the total Chinese or Asian population, respectively) during the Mongol invasion and 25 million (~15% or ~7% of the total Chinese or Asian population, respectively) during the transition between the Ming and Qing dynasties [*McEvedy and Jones*, 1978; *Pongratz et al.*, 2008]. [*D D Zhang et al.*, 2007] examined agricultural production associated with wars in China from 1500-1800 C.E. and concluded that the war and loss of human life associated with the transition between the Ming and Qing dynasties resulted in a sharp decrease in agricultural production. The invasion of the Mongol armies would have resulted in a similar or larger decrease in agricultural production due to the greater percentage of the population that was killed.

Assuming that essentially all preindustrial rice production occurred in Asia and given that~70% of the total world population lived in Asia [*McEvedy and Jones*, 1978], we can add 100% of the rice emissions and 70% of all other anthropogenic emissions (Table 3) to estimate Asian anthropogenic emissions. Here we will focus on the high and

low estimates of anthropogenic emissions that are commonly cited in the literature. This leads to estimates of Asian anthropogenic emissions of ~24 Tg CH_4 yr^{-1} based on [*Houweling et al.*, 2000] and ~56 Tg CH_4 yr^{-1} based on [*Ruddiman*, 2007]. Assuming a linear scaling between Asian population change and anthropogenic methane emissions, the invasion of the Mongol armies during ~1211-1241 C.E. would have resulted in a reduction of ~3.3-7.9 Tg CH_4 yr^{-1} or ~10-23 ppb for [*Houweling et al.*, 2000] and [*Ruddiman*, 2007] estimates, respectively. The WDC05A record shows that methane decreased by ~25-30 ppb from 1218-1235 C.E. Using the same argument, the transition from the Ming to Qing dynasties (1618-1662 C.E.) would have led to a reduction of ~1.6-3.7 Tg CH_4 yr^{-1} or ~5-11 ppb for [*Houweling et al.*, 2000] and [*Ruddiman*, 2007] estimates, respectively. The WDC05A record has a small gap during this time period, but there is a decrease of ~13 ppb observed in the Law Dome record. Preliminary measurements from the main borehole (WDC06A) have a decrease similar to Law Dome (not shown) in this time interval. Therefore the timing and magnitude of putative reductions in anthropogenic rice emissions resulting from war is within the chronology uncertainty of our record and represents a possible cause for these reductions in methane.

There is further anecdotal evidence that the invasion of the Mongol empire could have influenced methane emissions. After razing villages and cities, the Mongol army laboriously dismantled the irrigation systems and used their horses to churn up the soil [*Weatherford*, 2004]. This prevented people from immediately resettling after the Mongol army left and also allowed the land to revert to grasslands which have significantly lower methane emissions than irrigated farmland. Following the invasion, the governing Mongols encouraged scientific innovations which led in 1261 C.E. to the establishment of the Office for the Stimulation of Agriculture which sought to increase the agricultural output of farmlands by the diversification of crops and improvement of farming practices [*Weatherford*, 2004]. At this same time, global methane concentrations began to increase. These land use changes would have changed the areal extent of methane emissions and we speculate that it could have contributed to the rapid changes in global methane concentrations during this time period.

In the mid 14th century plague broke out and spread rapidly across Asia and Europe along the extensive Mongol trade network. Population losses in Asia and Europe were estimated to be in excess of 60 million and 20 million, respectively [*McEvedy and Jones*, 1978; *Weatherford*, 2004]. Use of the linear scaling argument above leads to a reduction of Asian anthropogenic emissions of ~6-14.3 Tg CH_4 yr^{-1} and European anthropogenic emissions of ~1.5-3.3 Tg CH_4 yr^{-1} for [*Houweling et al.*, 2000] and [*Ruddiman*, 2007] estimates, respectively. Thus the total reduction by linear scaling caused by plague would have been ~7.5-17.6 Tg CH_4 yr^{-1} or ~21-50 ppb. The WDC05A record shows that methane decreases by ~16 ppb from 1314-1359 C.E. A possible explanation for the smaller than estimated reduction in methane is that plague would not have caused the land use changes that occurred during wars. This suggests that the land use changes could have had a greater impact than population changes and might be an explanation for why the reduction in methane during the Mongol invasion is slightly greater than that estimated with a linear scaling to population.

Changes in the $\delta^{13}CH_4$ record can help identify methane sources which have divergent isotopic signatures. The $\delta^{13}CH_4$ record over the LPIH shows a large, gradual decrease from 1400-1700 C.E. however a large portion of the decrease occurs during 1560-1600 C.E. [*Ferretti et al.*, 2005; *Mischler et al.*, 2009]. This is coincident with the largest decrease in methane concentrations during the LPIH, ~32 ppb in the WDC05A record. [*Ferretti et al.*, 2005] proposed that the reduction in $\delta^{13}CH_4$ was caused by the decrease of biomass burning (an isotopically heavy source) in the Americas after the arrival of European settlers introduced disease to Native American populations causing a widespread pandemic [*N D Cook*, 1998; *Ruddiman*, 2007]. This hypothesis is consistent with a marked decrease in charcoal accumulation in global sedimentary records [*Marlon et al.*, 2008]. Estimates of LPIH biomass burning emissions range from 10-38 Tg CH_4 yr^{-1} which corresponds to 28-108 ppb (Table 3). While these estimates include some anthropogenic biomass burning that is outside of North America, [*Ferretti et al.*, 2005] argue that Native American activities provided the greatest contribution to this source. Thus a reduction in biomass burning methane emissions during this time period is

consistent with three independent lines of evidence: the decrease in methane concentrations, decreasing isotopic $\delta^{13}CH_4$ values, and widespread pandemics in the Americas associated with European invasion.

While anthropogenic activities may have had a discernable impact on multidecadal variations in methane concentrations, many uncertainties remain. Past population estimates are highly uncertain, particularly for the pre-colonial Americas and Asia. Additional work on quantifying the range of emissions from modern and preindustrial rice agriculture techniques as well as the extent of rice agriculture in the LPIH is needed. Longer high-precision methane records can place the LPIH variations in a longer term context. A coupling of methane emissions with anthropogenic activities could be an explanation for the generally low correlations with temperature and precipitation reconstructions over the LPIH discussed earlier.

2.5 Conclusion

We have presented a new high-resolution, high-precision record of atmospheric methane covering 1000-1800 C.E. from the West Antarctic Ice Sheet Divide ice core (WDC05A). The high correlation between the WDC05A and the Law Dome methane record [*Etheridge et al.*, 1998; *MacFarling Meure et al.*, 2006] confirms the variability observed in both records. We are able to uniquely identify small, high-precision scale variability demonstrating that high-resolution methane records can be used to establish chronostratigraphic tie points for ice core gas chronologies on short timescales.

We find that reconstructions of regional to hemispheric temperature are not highly correlated with methane concentrations. Correlation coefficients with a spatially resolved temperature reconstruction are highest in northern Eurasia, consistent with modern satellite observations on interannual timescales. The highest correlation coefficients with the spatial temperature reconstruction as well as many individual extratropical northern hemisphere temperature reconstructions are observed from 1400 to 1600 C.E. during the onset of the Little Ice Age. This suggests that temperature variations during this time period impacted methane variations. The correlation between proxies for East Asian

monsoon strength and methane are similarly low on multidecadal time scales, although uncertainty in the age scales prevents a definitive analysis in some cases. A spatial reconstruction of the Asian monsoon region Palmer Drought Severity Index has the greatest correlation with methane at the headwaters of major East Asian rivers, consistent with modern satellite observations. Moderate to high correlations exist with a Peruvian speleothem and tropical SSTs in the Cariaco basin if these records are shifted by the maximum amount allowed by the uncertainty in their chronologies. These possible correlations on multidecadal timescales are compelling because these relationships have been documented on millennial timescales and suggest that they could be a robust feature of the climate system. Possible explanations for the lack of high correlations with temperature and precipitation proxies are that the individual records comprising these reconstructions may not be reflecting conditions in methane source regions or that the variations were not large enough to significantly perturb methane emissions. Anthropogenic activities could have affected methane emissions based on the synchronous timing between large population losses in Asia and the Americas and decreases in methane concentrations. Our work reinforces the need for additional absolutely dated paleoclimate proxies [*Jones et al.*, 2009], particularly from methane source regions.

Future work will involve extending the high-resolution WAIS Divide methane record beyond 1000 C.E. using the main borehole WDC06A. Extension of the record will characterize the frequency of methane variability and changes in multidecadal variability that may be caused by variations in climate or anthropogenic activities. Understanding high-precision methane variability is critical for placing the recent record of atmospheric and satellite measurements in a longer term context, increasing our understanding of the range of variability in the global methane budget, and for prediction of future changes in that budget. Very high-resolution records of methane from Greenland are needed to characterize multidecadal and centennial variability in the Inter Polar Gradient which will provide another constraint on the global methane budget.

2.6 Acknowledgements

This work was supported by NSF OPP grants 0538578, 0520523, and 0538538, and by NASA/Oregon Space Grant Consortium, grant NNG05GJ85H. Glaciochemical dating of the WDC05A and WDC06A ice cores was supported by NSF OPP grants 0538427 and 0739780 to the Desert Research Institute. Thanks go to James Lee who assisted with the methane measurements, Nelia Dunbar, Mark Battle, Jeff Severinghaus, and Eric Steig who contributed preliminary results from their work, and two anonymous reviewers who provided insightful comments that improved this manuscript. The authors appreciate the support of the WAIS Divide Science Coordination Office at the Desert Research Institute of Reno Nevada for the collection and distribution of the WAIS Divide ice core and related tasks (Kendrick Taylor, NSF Grants 0440817 and 0230396). The National Science Foundation Office of Polar Programs also funds the Ice Drilling Program Office and Ice Drilling Design and Operations group for coring activities; Raytheon Polar Services for logistics support in Antarctica; and the 109th New York Air National Guard for airlift in Antarctica. The National Ice Core Laboratory, which curated the core and preformed core processing, is jointly funded by the National Science Foundation and the United States Geological Survey.

Data and description can be downloaded from the NOAA National Climate Data Center. http://www.ncdc.noaa.gov/paleo/paleo.html.

2.7 References

Allen, L. H., S. L. Albrecht, W. Colon-Guasp, S. A. Covell, J. T. Baker, D. Y. Pan, and K. J. Boote (2003), Methane emissions of rice increased by elevated carbon dioxide and temperature, *J. Environ. Qual.*, *32*(6), 1978-1991.

Banta, J. R., J. R. McConnell, M. M. Frey, R. C. Bales, and K. Taylor (2008), Spatial and temporal variability in snow accumulation at the West Antarctic Ice Sheet Divide over recent centuries, *J. Geophys. Res.-Atmos.*, *113*(D23), 8.

Battle, M., et al. (1996), Atmospheric gas concentrations over the past century measured in air from firn at the South Pole, *Nature*, *383*(6597), 231-235.

Bekki, S., and K. S. Law (1997), Sensitivity of the atmospheric CH_4 growth rate to global temperature changes observed from 1980 to 1992, *Tellus Ser. B-Chem. Phys. Meteorol.*, *49*(4), 409-416.

Bergamaschi, P., et al. (2009), Inverse modeling of global and regional CH4 emissions using SCIAMACHY satellite retrievals, *J. Geophys. Res.-Atmos.*, *114*.

Berkelhammer, M., A. Sinha, M. Mudelsee, H. Cheng, R. L. Edwards, and K. Cannariato (2010), Persistent multidecadal power of the Indian Summer Monsoon, *Earth and Planetary Science Letters*, *290*(1-2), 166-172.

Black, D. E., L. C. Peterson, J. T. Overpeck, A. Kaplan, M. N. Evans, and M. Kashgarian (1999), Eight centuries of North Atlantic Ocean atmosphere variability, *Science*, *286*(5445), 1709-1713.

Black, D. E., M. A. Abahazi, R. C. Thunell, A. Kaplan, E. J. Tappa, and L. C. Peterson (2007), An 8-century tropical Atlantic SST record from the Cariaco Basin: Baseline variability, twentieth-century warming, and Atlantic hurricane frequency, *Paleoceanography*, *22*(4), 10.

Bloom, A. A., P. I. Palmer, A. Fraser, D. S. Reay, and C. Frankenberg (2010), Large-Scale Controls of Methanogenesis Inferred from Methane and Gravity Spaceborne Data, *Science*, *327*(5963), 322-325.

Blunier, T., and E. J. Brook (2001), Timing of millennial-scale climate change in Antarctica and Greenland during the last glacial period, *Science*, *291*(5501), 109-112.

Boone, C. D. (2000), Biological formation and consumption of methane, in *Atmospheric Methane: Its Role in the Global Environment*, edited by M. A. K. Khalil, pp. 42–62, Springer-Verlag, New York, NY.

Bousquet, P., D. A. Hauglustaine, P. Peylin, C. Carouge, and P. Ciais (2005), Two decades of OH variability as inferred by an inversion of atmospheric transport and chemistry of methyl chloroform, *Atmos. Chem. Phys.*, *5*, 2635-2656.

Bousquet, P., et al. (2006), Contribution of anthropogenic and natural sources to atmospheric methane variability, *Nature*, *443*(7110), 439-443.

Briffa, K. R., T. J. Osborn, F. H. Schweingruber, I. C. Harris, P. D. Jones, S. G. Shiyatov, and E. A. Vaganov (2001), Low-frequency temperature variations from a northern tree ring density network, *J. Geophys. Res.-Atmos.*, *106*(D3), 2929-2941.

Brook, E. J., S. Harder, J. Severinghaus, E. J. Steig, and C. M. Sucher (2000), On the origin and timing of rapid changes in atmospheric methane during the last glacial period, *Glob. Biogeochem. Cycle*, *14*(2), 559-572.

Brook, E. J., J. W. C. White, A. S. M. Schilla, M. L. Bender, B. Barnett, J. P. Severinghaus, K. C. Taylor, R. B. Alley, and E. J. Steig (2005), Timing of millennial-scale climate change at Siple Dome, West Antarctica, during the last glacial period, *Quat. Sci. Rev.*, *24*(12-13), 1333-1343.

Chappellaz, J., T. Blunier, D. Raynaud, J. M. Barnola, J. Schwander, and B. Stauffer (1993), Synchronous changes in atmospheric CH_4 and Greenland climate between 40 and 8 kyr BP, *Nature*, *366*(6454), 443-445.

Christensen, T. R., T. R. Johansson, H. J. Akerman, M. Mastepanov, N. Malmer, T. Friborg, P. Crill, and B. H. Svensson (2004), Thawing sub-arctic permafrost: Effects on vegetation and methane emissions, *Geophys. Res. Let.*, *31*(4), 4.

Cook, E. R., J. Esper, and R. D. D'Arrigo (2004), Extra-tropical Northern Hemisphere land temperature variability over the past 1000 years, *Quat. Sci. Rev.*, *23*(20-22), 2063-2074.

Cook, E. R., K. J. Anchukaitis, B. M. Buckley, R. D. D'Arrigo, G. C. Jacoby, and W. E. Wright (2010), Asian Monsoon Failure and Megadrought During the Last Millennium, *Science*, *328*(5977), 486-489.

Cook, N. D. (1998), *Born to die : disease and New World conquest, 1492-1650*, xiii, 248 p. : pp., Cambridge University Press, Cambridge ; New York :.

Craig, H., Y. Horibe, and T. Sowers (1988), Gravitational Separation of Gases and Isotopes in Polar Ice Caps, *Science*, *242*(4886), 1675-1678.

Crespin, E., H. Goosse, T. Fichefet, and M. E. Mann (2009), The 15th century Arctic warming in coupled model simulations with data assimilation, *Clim. Past.*, *5*(3), 389-401.

Crutzen, P. J., and C. Bruhl (1993), A model study of atmospheric temperatures and the concentrations of ozone, hydroxyl, and some other photochemically active gases during the glacial, the pre-industrial Holocene and the present *Geophys. Res. Let.*, *20*(11), 1047-1050.

Cruz, F. W., S. J. Burns, I. Karmann, W. D. Sharp, M. Vuille, A. O. Cardoso, J. A. Ferrari, P. L. S. Dias, and O. Viana (2005), Insolation-driven changes in atmospheric circulation over the past 116,000 years in subtropical Brazil, *Nature*, *434*(7029), 63-66.

Cunnold, D. M., et al. (2002), In situ measurements of atmospheric methane at GAGE/AGAGE sites during 1985-2000 and resulting source inferences, *J. Geophys. Res.-Atmos.*, *107*(D14), 20.

D'Arrigo, R., R. Wilson, and G. Jacoby (2006), On the long-term context for late twentieth century warming, *J. Geophys. Res.-Atmos.*, *111*(D3), 12.

Delmotte, M., J. Chappellaz, E. Brook, P. Yiou, J. M. Barnola, C. Goujon, D. Raynaud, and V. I. Lipenkov (2004), Atmospheric methane during the last four glacial-interglacial cycles: Rapid changes and their link with Antarctic temperature, *J. Geophys. Res.-Atmos.*, *109*(D12), 13.

Dentener, F., W. Peters, M. Krol, M. van Weele, P. Bergamaschi, and J. Lelieveld (2003), Interannual variability and trend of CH4 lifetime as a measure for OH changes in the 1979-1993 time period, *J. Geophys. Res.-Atmos.*, *108*(D15).

Dlugokencky, E. J., L. P. Steele, P. M. Lang, and K. A. Masarie (1994), The growth rate and distribution of atmospheric methane, *J. Geophys. Res.-Atmos.*, *99*(D8), 17021-17043.

Dlugokencky, E. J., P. M. Lang, A. M. Crotwell, and K. A. Masaire (2012), Atmospheric Methane Dry Air Mole Fractions from the NOAA ESRL Carbon Cycle Cooperative Global Air Sampling Network, 1983-2011, Version: 2012-09-24, Path: ftp://ftp.cmdl.noaa.gov/ccg/ch4/flask/event/, edited.

Dlugokencky, E. J., R. C. Myers, P. M. Lang, K. A. Masarie, A. M. Crotwell, K. W. Thoning, B. D. Hall, J. W. Elkins, and L. P. Steele (2005), Conversion of NOAA atmospheric dry air CH_4 mole fractions to a gravimetrically prepared standard scale, *J. Geophys. Res.-Atmos.*, *110*(D18), 8.

Dlugokencky, E. J., et al. (2009), Observational constraints on recent increases in the atmospheric CH4 burden, *Geophys. Res. Let.*, *36*.

Dunbar, N. W., G. A. Zielinski, and D. T. Voisins (2003), Tephra layers in the Siple Dome and Taylor Dome ice cores, Antarctica: Sources and correlations, *J. Geophys. Res.-Solid Earth*, *108*(B8).

Dunbar, N. W., W. C. McIntosh, A. V. Kurbatov, and T. I. Wilch (2007), Integrated Tephrochronology of the West Antarctic Region- Implications for a potential tephra record in the West Antarctic Ice Sheet (WAIS) Divide Ice Core, paper presented at WAIS Divide Science Meeting, Tahoe, N.M.

EPICA Community Members (2006), One-to-one coupling of glacial climate variability in Greenland and Antarctica, *Nature*, *444*(7116), 195-198.

Esper, J., E. R. Cook, and F. H. Schweingruber (2002), Low-Frequency Signals in Long Tree-Ring Chronologies for Reconstructing Past Temperature Variability, *Science*, *295*(5563), 2250-2253.

Etheridge, D. M., L. P. Steele, R. J. Francey, and R. L. Langenfelds (1998), Atmospheric methane between 1000 AD and present: Evidence of anthropogenic emissions and climatic variability, *J. Geophys. Res.-Atmos.*, *103*(D13), 15979-15993.

Ferretti, D. F., et al. (2005), Unexpected Changes to the Global Methane Budget over the Past 2000 Years, *Science*, *309*(5741), 1714-1717.

Fischer, H., et al. (2008), Changing boreal methane sources and constant biomass burning during the last termination, *Nature*, *452*(7189), 864-867.

Fogg, P. G. T., Sangster, J. (2003), *Chemicals in the atmosphere : solubility, sources, and reactivity / Peter Fogg and James Sangster ; with contributions from Yin-Nan Lee, Stephen Schwartz, Peter Warneck*, ix, 453 p. : pp., J. Wiley, Hoboken, NJ :.

Forster, P., et al. (2007), Changes in Atmospheric Constituents and in Radiative Forcing., in *Climate Change 2007: The Physical Science Basis. Contribution of Working Group I to the Fourth Assessment Report of the Intergovernmental Panel on Climate Change*, edited by S. Solomon, D. Qin, M. Manning, Z. Chen, M. Marquis, K. B. Averyt, M. Tignor and H. L. Miller, pp. 131-234, Cambridge University Press, Cambridge, United Kingdom and New York, NY, USA.

Grachev, A. M., E. J. Brook, and J. P. Severinghaus (2007), Abrupt changes in atmospheric methane at the MIS 5b-5a transition, *Geophys. Res. Let.*, *34*(20), 5.

Grachev, A. M., E. J. Brook, J. P. Severinghaus, and N. G. Pisias (2009), Relative timing and variability of atmospheric methane and GISP2 oxygen isotopes between 68 and 86 ka, *Glob. Biogeochem. Cycle*, *23*, 10.

Grudd, H., K. R. Briffa, W. Karlen, T. S. Bartholin, P. D. Jones, and B. Kromer (2002), A 7400-year tree-ring chronology in northern Swedish Lapland: natural climatic variability expressed on annual to millennial timescales, *Holocene*, *12*(6), 657-665.

Gu, G. J., R. F. Adler, G. J. Huffman, and S. Curtis (2007), Tropical rainfall variability on interannual-to-interdecadal and longer time scales derived from the GPCP monthly product, *J. Clim.*, *20*(15), 4033-4046.

Harder, S. L., D. T. Shindell, G. A. Schmidt, and E. J. Brook (2007), A global climate model study of CH_4 emissions during the Holocene and glacial-interglacial transitions constrained by ice core data, *Glob. Biogeochem. Cycle*, *21*(1), 13.

Hegerl, G. C., T. J. Crowley, M. Allen, W. T. Hyde, H. N. Pollack, J. Smerdon, and E. Zorita (2007), Detection of human influence on a new, validated 1500-year temperature reconstruction, *J. Clim.*, *20*(4), 650-666.

Houweling, S., F. Dentener, and J. Lelieveld (2000), Simulation of preindustrial atmospheric methane to constrain the global source strength of natural wetlands, *J. Geophys. Res.-Atmos.*, *105*(D13), 17243-17255.

Houweling, S., G. R. van der Werf, K. K. Goldewijk, T. Rockmann, and I. Aben (2008), Early anthropogenic CH_4 emissions and the variation of CH_4 and $^{13}CH_4$ over the last millennium, *Glob. Biogeochem. Cycle*, *22*(1), 9.

Hu, C. Y., G. M. Henderson, J. H. Huang, S. Xie, Y. Sun, and K. R. Johnson (2008), Quantification of Holocene Asian monsoon rainfall from spatially separated cave records, *Earth and Planetary Science Letters*, *266*(3-4), 221-232.

Huber, C., M. Leuenberger, R. Spahni, J. Fluckiger, J. Schwander, T. F. Stocker, S. Johnsen, A. Landals, and J. Jouzel (2006), Isotope calibrated Greenland temperature record over Marine Isotope Stage 3 and its relation to CH4, *Earth and Planetary Science Letters*, *243*(3-4), 504-519.

Johnsen, S. J., et al. (1997), The delta $\delta^{18}O$ record along the Greenland Ice Core Project deep ice core and the problem of possible Eemian climatic instability, *J. Geophys. Res.-Oceans*, *102*(C12), 26397-26410.

Jones, P. D., et al. (2009), High-resolution palaeoclimatology of the last millennium: a review of current status and future prospects, *Holocene*, *19*(1), 3-49.

Kaplan, J. O., G. Folberth, and D. A. Hauglustaine (2006), Role of methane and biogenic volatile organic compound sources in late glacial and Holocene fluctuations of atmospheric methane concentrations, *Glob. Biogeochem. Cycle*, *20*(2), 16.

Kaufman, D. S., D. P. Schneider, N. P. McKay, C. M. Ammann, R. S. Bradley, K. R. Briffa, G. H. Miller, B. L. Otto-Bliesner, J. T. Overpeck, and B. M. Vinther (2009), Recent Warming Reverses Long-Term Arctic Cooling, *Science*, *325*(5945), 1236-1239.

Khalil, M. A. K. (Ed.) (2000), *Atmospheric Methane: Its Role in the Global Environment*, 341 pp., Springer-Verlag, Berlin Heidelberg New York.

Khalil, M. A. K., and R. A. Rasmussen (1983), Sources, Sinks, and Seasonal Cycles of Atmospheric Methane, *Journal of Geophysical Research-Oceans and Atmospheres*, *88*(NC9), 5131-5144.

Kobashi, T., J. P. Severinghaus, J. M. Barnola, K. Kawamura, T. Carter, and T. Nakaegawa (2010), Persistent multi-decadal Greenland temperature fluctuation through the last millennium, *Clim. Change*, *100*(3-4), 733-756.

Lea, D. W., D. K. Pak, L. C. Peterson, and K. A. Hughen (2003), Synchroneity of tropical and high-latitude Atlantic temperatures over the last glacial termination, *Science*, *301*(5638), 1361-1364.

Lelieveld, J., P. J. Crutzen, and F. J. Dentener (1998), Changing concentration, lifetime and climate forcing of atmospheric methane, *Tellus Ser. B-Chem. Phys. Meteorol.*, *50*(2), 128-150.

Lemieux-Dudon, B., E. Blayo, J. R. Petit, C. Waelbroeck, A. Svensson, C. Ritz, J. M. Barnola, B. M. Narcisi, and F. Parrenin (2010), Consistent dating for Antarctic and Greenland ice cores, *Quat. Sci. Rev.*, *29*(1-2), 8-20.

Loulergue, L., A. Schilt, R. Spahni, V. Masson-Delmotte, T. Blunier, B. Lemieux, J. M. Barnola, D. Raynaud, T. F. Stocker, and J. Chappellaz (2008), Orbital and millennial-scale features of atmospheric CH_4 over the past 800,000 years, *Nature*, *453*(7193), 383-386.

MacDonald, G. M., and R. A. Case (2005), Variations in the Pacific Decadal Oscillation over the past millennium, *Geophys. Res. Let.*, *32*(8).

MacFarling Meure, C., D. Etheridge, C. Trudinger, P. Steele, R. Langenfelds, T. van Ommen, A. Smith, and J. Elkins (2006), Law Dome CO_2, CH_4 and N_2O ice core records extended to 2000 years BP, *Geophys. Res. Let.*, *33*(14), 4.

Mann, M. E., Z. Zhang, M. K. Hughes, R. S. Bradley, S. K. Miller, S. Rutherford, and F. Ni (2008), Proxy-based reconstructions of hemispheric and global surface temperature variations over the past two millennia, *Proceedings of the National Academy of Sciences*, *105*(36), 13252-13257.

Mann, M. E., Z. H. Zhang, S. Rutherford, R. S. Bradley, M. K. Hughes, D. Shindell, C. Ammann, G. Faluvegi, and F. B. Ni (2009), Global Signatures and Dynamical Origins of the Little Ice Age and Medieval Climate Anomaly, *Science*, *326*(5957), 1256-1260.

Mantua, N. J., and S. R. Hare (2002), The Pacific decadal oscillation, *J. Oceanogr.*, *58*(1), 35-44.

Mantua, N. J., S. R. Hare, Y. Zhang, J. M. Wallace, and R. C. Francis (1997), A Pacific interdecadal climate oscillation with impacts on salmon production, *Bull. Amer. Meteorol. Soc.*, *78*(6), 1069-1079.

Marlon, J. R., P. J. Bartlein, C. Carcaillet, D. G. Gavin, S. P. Harrison, P. E. Higuera, F. Joos, M. J. Power, and I. C. Prentice (2008), Climate and human influences on global biomass burning over the past two millennia, *Nat. Geosci.*, *1*(10), 697-702.

Martinerie, P., G. P. Brasseur, and C. Granier (1995), The chemical composition of ancient atmospheres: A model study constrained by ice core data, *J. Geophys. Res.-Atmos.*, *100*(D7), 14291-14304.

Matthews, E. (2000), Wetlands, in *Atmospheric Methane: Its Role in the Global Environment*, edited by M. A. K. Khalil, pp. 202-233, Springer-Verlag, Berlin Heidelberg New York.

Matthews, J. A., and K. R. Briffa (2005), The 'Little Ice Age': Re-evaluation of an evolving concept, *Geogr. Ann. Ser. A-Phys. Geogr.*, *87A*(1), 17-36.

McEvedy, C., and R. Jones (1978), *Atlas of World Population History*, 368 pp., Penguin, London.

Mischler, J. A., T. A. Sowers, R. B. Alley, M. Battle, J. R. McConnell, L. Mitchell, T. Popp, E. Sofen, and M. K. Spencer (2009), Carbon and hydrogen isotopic composition of methane over the last 1000 years, *Glob. Biogeochem. Cycle, 23*.

Mitchell, L., and E. J. Brook (2009), New high-precision, high-resolution records of atmospheric methane from Greenland and Antarctic ice cores: 0-1800 A.D, *EOS, Trans., AGU, 90*(52), Fall Meet. Suppl., Abstract PP41B-1524.

Moberg, A., D. M. Sonechkin, K. Holmgren, N. M. Datsenko, and W. Karlen (2005), Highly variable Northern Hemisphere temperatures reconstructed from low- and high-resolution proxy data, *Nature*, *433*(7026), 613-617.

Morse, D. L., D. D. Blankenship, E. D. Waddington, and T. A. Neumann (2002), A site for deep ice coring in West Antarctica: results from aerogeophysical surveys and thermo-kinematic modeling, in *Annals of Glaciology, Vol 35*, edited, pp. 36-44, Int Glaciological Soc, Cambridge.

Oppo, D. W., Y. Rosenthal, and B. K. Linsley (2009), 2,000-year-long temperature and hydrology reconstructions from the Indo-Pacific warm pool, *Nature*, *460*(7259), 1113-1116.

Palmer, A. S., T. D. van Ommen, M. A. J. Curran, V. Morgan, J. M. Souney, and P. A. Mayewski (2001), High-precision dating of volcanic events - (AD 1301-1995) using ice cores from Law Dome, Antarctica, *J. Geophys. Res.-Atmos.*, *106*(D22), 28089-28095.

Petrenko, V. V., et al. (2008), A novel method for obtaining very large ancient air samples from ablating glacial ice for analyses of methane radiocarbon, *J. of Glaciol.*, *54*(185), 233-244.

Pongratz, J., C. Reick, T. Raddatz, and M. Claussen (2008), A reconstruction of global agricultural areas and land cover for the last millennium, *Glob. Biogeochem. Cycle*, *22*(3).

Prinn, R. G., et al. (2001), Evidence for Substantial Variations of Atmospheric Hydroxyl Radicals in the Past Two Decades, *Science*, *292*(5523), 1882-1888.

Reuter, J., L. Stott, D. Khider, A. Sinha, H. Cheng, and R. L. Edwards (2009), A new perspective on the hydroclimate variability in northern South America during the Little Ice Age, *Geophys. Res. Let.*, *36*.

Ruddiman, W. F. (2003), The anthropogenic greenhouse era began thousands of years ago, *Clim. Change*, *61*(3), 261-293.

Ruddiman, W. F. (2007), The early anthropogenic hypothesis: Challenges and responses, *Reviews of Geophysics*, *45*(3), 37.

Schwander, J. (1989), The transformation of snow to ice and the occlusion of gases, in *The Environmental Record in Glaciers and Ice Sheets*, edited by H. Oeschger and C. C. Langway, pp. 53-67, John Wiley, Chichester [England] ; New York :.

Schwander, J., T. Sowers, J. M. Barnola, T. Blunier, A. Fuchs, and B. Malaize (1997), Age scale of the air in the summit ice: Implication for glacial-interglacial temperature change, *J. Geophys. Res.-Atmos.*, *102*(D16), 19483-19493.

Schwander, J., J. M. Barnola, C. Andrie, M. Leuenberger, A. Ludin, D. Raynaud, and B. Stauffer (1993), The Age of the Air in the Firn and the Ice at Summit, Greenland, *J. Geophys. Res.-Atmos.*, *98*(D2), 2831-2838.

Severinghaus, J. P., and E. J. Brook (1999), Abrupt climate change at the end of the last glacial period inferred from trapped air in polar ice, *Science*, *286*(5441), 930-934.

Severinghaus, J. P., T. Sowers, E. J. Brook, R. B. Alley, and M. L. Bender (1998), Timing of abrupt climate change at the end of the Younger Dryas interval from thermally fractionated gases in polar ice, *Nature*, *391*(6663), 141-146.

Shindell, D. T., G. Faluvegi, and N. Bell (2003), Preindustrial-to-present-day radiative forcing by tropospheric ozone from improved simulations with the GISS chemistry-climate GCM, *Atmos. Chem. Phys.*, *3*, 1675-1702.

Sowers, T., M. Bender, and D. Raynaud (1989), Elemental and Isotopic Composition of Occluded O_2 and N_2 in Polar Ice, *J. Geophys. Res.-Atmos.*, *94*(D4), 5137-5150.

Sowers, T., M. Bender, D. Raynaud, and Y. S. Korotkevich (1992), $\delta^{15}N$ of N_2 in Air Trapped in Polar Ice: a Tracer of Gas Transport in the Fim and a Possible Constrainton Ice Age-Gas Age Differences, *J. Geophys. Res.-Atmos.*, *97*(D14), 15683-15697.

Spahni, R., J. Schwander, J. Fluckiger, B. Stauffer, J. Chappellaz, and D. Raynaud (2003), The attenuation of fast atmospheric CH_4 variations recorded in polar ice cores, *Geophys. Res. Let.*, *30*(11), 4.

Steele, L. P., P. J. Fraser, R. A. Rasmussen, M. A. K. Khalil, T. J. Conway, A. J. Crawford, R. H. Gammon, K. A. Masarie, and K. W. Thoning (1987), The Global Distribution of Methane in the Troposphere, *J. Atmos. Chem.*, *5*(2), 125-171.

Subak, S. (1994), Methane from the House of Tudor and the Ming Dynasty: Anthropogenic emissions in the sixteenth century, *Chemosphere*, *29*(5), 843-854.

Thompson, A. M. (1992), The Oxidizing Capacity of the Earth's Atmosphere: Probable Past and Future Changes *Science*, *256*(5060), 1157-1165.

Trenberth, K. E., and L. Smith (2005), The mass of the atmosphere: A constraint on global analyses, *J. Clim.*, *18*(6), 864-875.

Trouet, V., J. Esper, N. E. Graham, A. Baker, J. D. Scourse, and D. C. Frank (2009), Persistent Positive North Atlantic Oscillation Mode Dominated the Medieval Climate Anomaly, *Science*, *324*(5923), 78-80.

Trudinger, C. M., I. G. Enting, D. M. Etheridge, R. J. Francey, V. A. Levchenko, L. P. Steele, D. Raynaud, and L. Arnaud (1997), Modeling air movement and bubble trapping in firn, *J. Geophys. Res.-Atmos.*, *102*(D6), 6747-6763.

Valdes, P. J., D. J. Beerling, and C. E. Johnson (2005), The ice age methane budget, *Geophys. Res. Let.*, *32*(2), 4.

van Hulzen, J. B., R. Segers, P. M. van Bodegom, and P. A. Leffelaar (1999), Temperature effects on soil methane production: an explanation for observed variability, *Soil Biol. Biochem.*, *31*(14), 1919-1929.

Vinther, B. M., et al. (2006), A synchronized dating of three Greenland ice cores throughout the Holocene, *J. Geophys. Res.-Atmos.*, *111*(D13), 11.

Walter, B. P., M. Heimann, and E. Matthews (2001a), Modeling modern methane emissions from natural wetlands 1. Model description and results, *J. Geophys. Res.-Atmos.*, *106*(D24), 34189-34206.

Walter, B. P., M. Heimann, and E. Matthews (2001b), Modeling modern methane emissions from natural wetlands 2. Interannual variations 1982-1993, *J. Geophys. Res.-Atmos.*, *106*(D24), 34207-34219.

Wang, D. Q., Z. L. Chen, and S. Y. Xu (2009), Methane emission from Yangtze estuarine wetland, China, *J. Geophys. Res.-Biogeosci.*, *114*, 11.

Wang, X. F., A. S. Auler, R. L. Edwards, H. Cheng, E. Ito, and M. Solheid (2006), Interhemispheric anti-phasing of rainfall during the last glacial period, *Quat. Sci. Rev.*, *25*(23-24), 3391-3403.

Wang, Y. H., and D. J. Jacob (1998), Anthropogenic forcing on tropospheric ozone and OH since preindustrial times, *J. Geophys. Res.-Atmos.*, *103*(D23), 31123-31135.

Wang, Y. J., H. Cheng, R. L. Edwards, Z. S. An, J. Y. Wu, C. C. Shen, and J. A. Dorale (2001), A high-resolution absolute-dated Late Pleistocene monsoon record from Hulu Cave, China, *Science*, *294*(5550), 2345-2348.

Wang, Y. J., H. Cheng, R. L. Edwards, Y. Q. He, X. G. Kong, Z. S. An, J. Y. Wu, M. J. Kelly, C. A. Dykoski, and X. D. Li (2005), The Holocene Asian monsoon: Links to solar changes and North Atlantic climate, *Science*, *308*(5723), 854-857.

Weatherford, J. (2004), *Genghis Khan and the Making of the Modern World*, 1 ed., Crown Publishers, New York.

Worthy, D. E. J., I. Levin, F. Hopper, M. K. Ernst, and N. B. A. Trivett (2000), Evidence for a link between climate and northern wetland methane emissions, *J. Geophys. Res.-Atmos.*, *105*(D3), 4031-4038.

Zhang, D. D., P. Brecke, H. F. Lee, Y. Q. He, and J. Zhang (2007), Global climate change, war, and population decline in recent human history, *Proc. Natl. Acad. Sci. U. S. A.*, *104*(49), 19214-19219.

Zhang, P. Z., et al. (2008), A Test of Climate, Sun, and Culture Relationships from an 1810-Year Chinese Cave Record, *Science*, *322*(5903), 940-942.

Zona, D., W. C. Oechel, J. Kochendorfer, K. T. P. U, A. N. Salyuk, P. C. Olivas, S. F. Oberbauer, and D. A. Lipson (2009), Methane fluxes during the initiation of a large-scale water table manipulation experiment in the Alaskan Arctic tundra, *Glob. Biogeochem. Cycle*, *23*, 11.

2.8 Figures

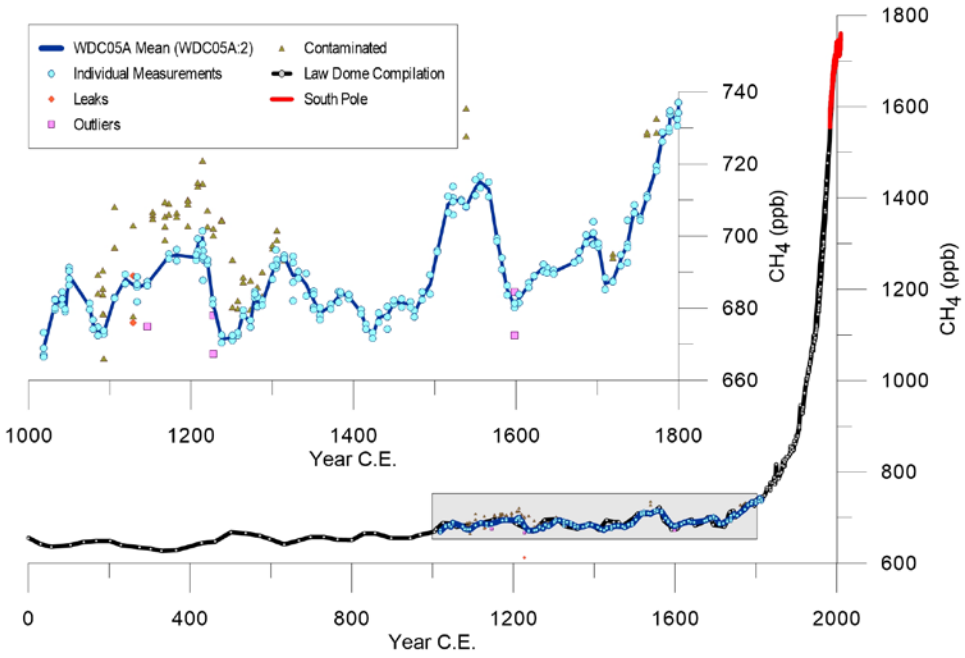

Figure 2.1. Atmospheric methane concentrations over the past two centuries from the Law Dome compilation (0-1995 C.E., black line) [*Etheridge et al.*, 1998; *MacFarling Meure et al.*, 2006], WDC05A on the WDC05A:2 chronology (1019-1814 C.E., blue line) and direct atmospheric measurements from the South Pole (1983-2010 C.E., red line) [*Dlugokencky et al.*, 2012]. Inset shows methane data from WDC05A on the WDC05A:2 chronology with the mean at each depth/age (blue line), individual measurements (light blue circles), leaks (red diamonds), outliers (pink squares), and contaminated measurements (brown triangles). All data are plotted on the NOAA04 calibration scale [*Dlugokencky et al.*, 2005].

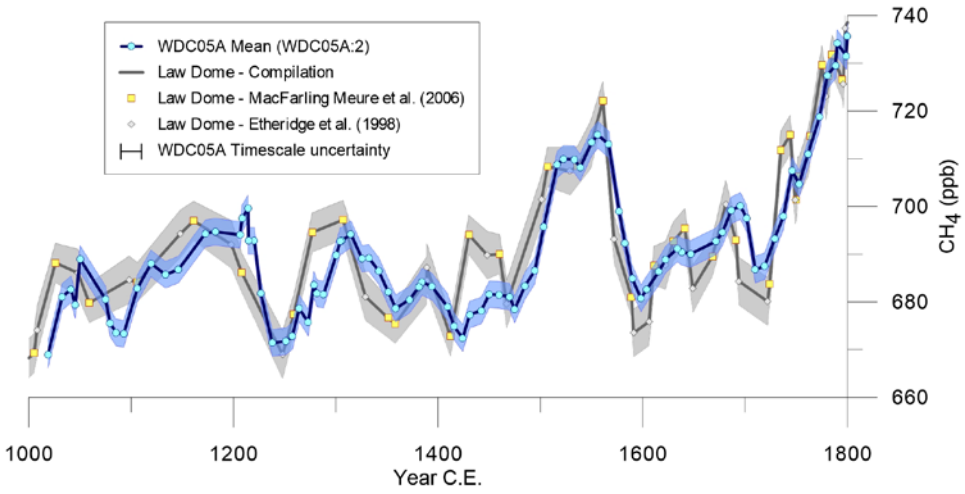

Figure 2.2. Comparison between the WDC05A (mean values) on the WDC05A:2 chronology and Law Dome methane records. Error bands are ±2.9 ppb for WDC05A, ±5 ppb for [*Etheridge et al.*, 1998], and ±4.1 ppb for [*MacFarling Meure et al.*, 2006]. All records are plotted on the NOAA04 calibration scale [*Dlugokencky et al.*, 2005]. Chronology uncertainty for WDC05A is ±10 years.

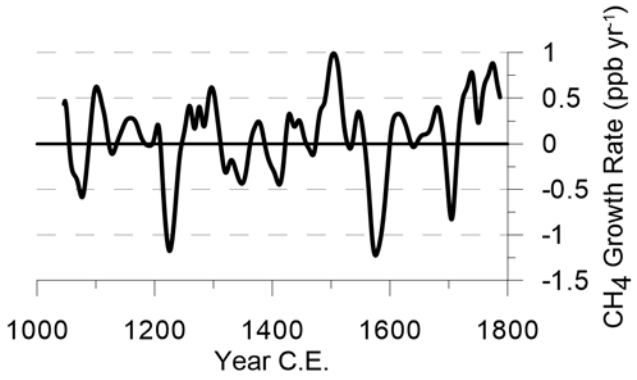

Figure 2.3. Methane growth rate computed numerically after linear interpolation between WDC05A data points then smoothed with a 30 year Gaussian filter.

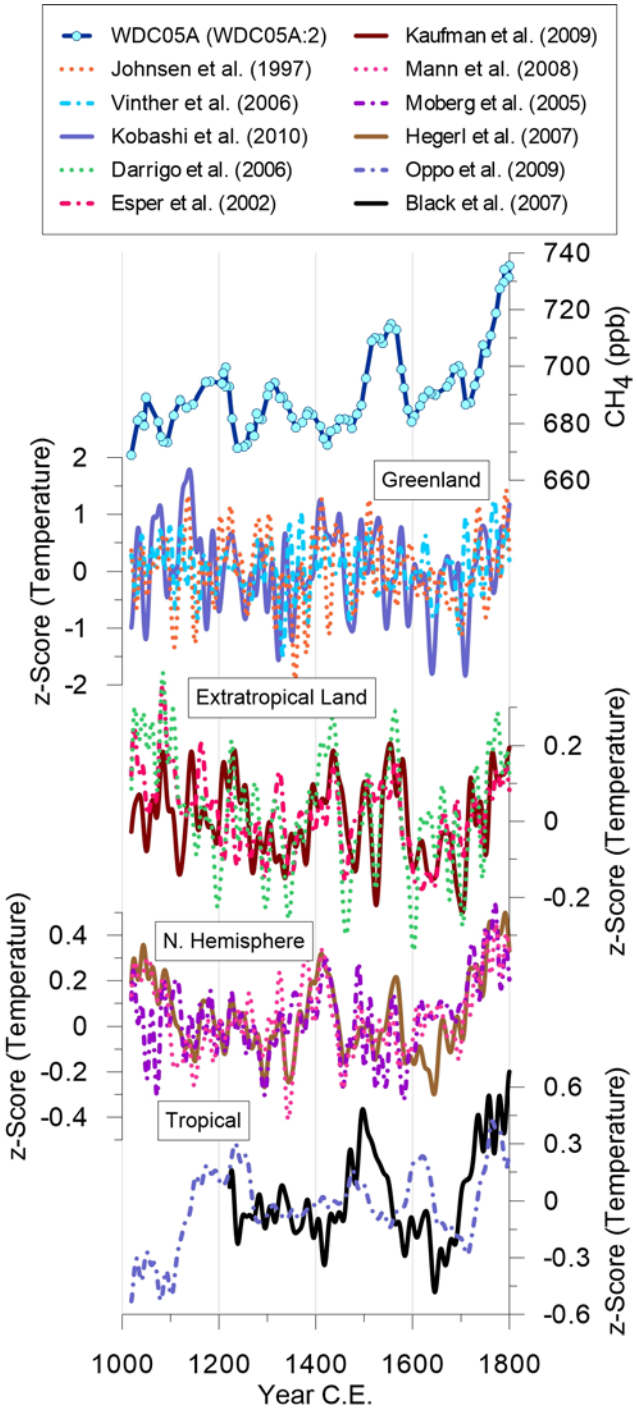

Figure 2.4. Comparison between WDC05A methane concentrations on the WDC05A:2 chronology and temperature reconstructions. Greenland: orange, dotted [*Johnsen et al.*, 1997]; light blue, dash-dot [*Vinther et al.*, 2006]; dark blue, solid [*Kobashi et al.*, 2010]. Extratropical land: green, dotted [*D'Arrigo et al.*, 2006]; light red, dash-dot [*Esper et al.*, 2002]; dark red, solid [*Kaufman et al.*, 2009]. N. Hemisphere: pink, dotted [*Mann et al.*, 2008]; purple, dash-dot [*Moberg et al.*, 2005]; brown, solid [*Hegerl et al.*, 2007]. Tropical: blue, dash-dot [*Oppo et al.*, 2009]; black, solid [*Black et al.*, 2007]. All records were smoothed with a bandpass filter with a period of 20-500 years.

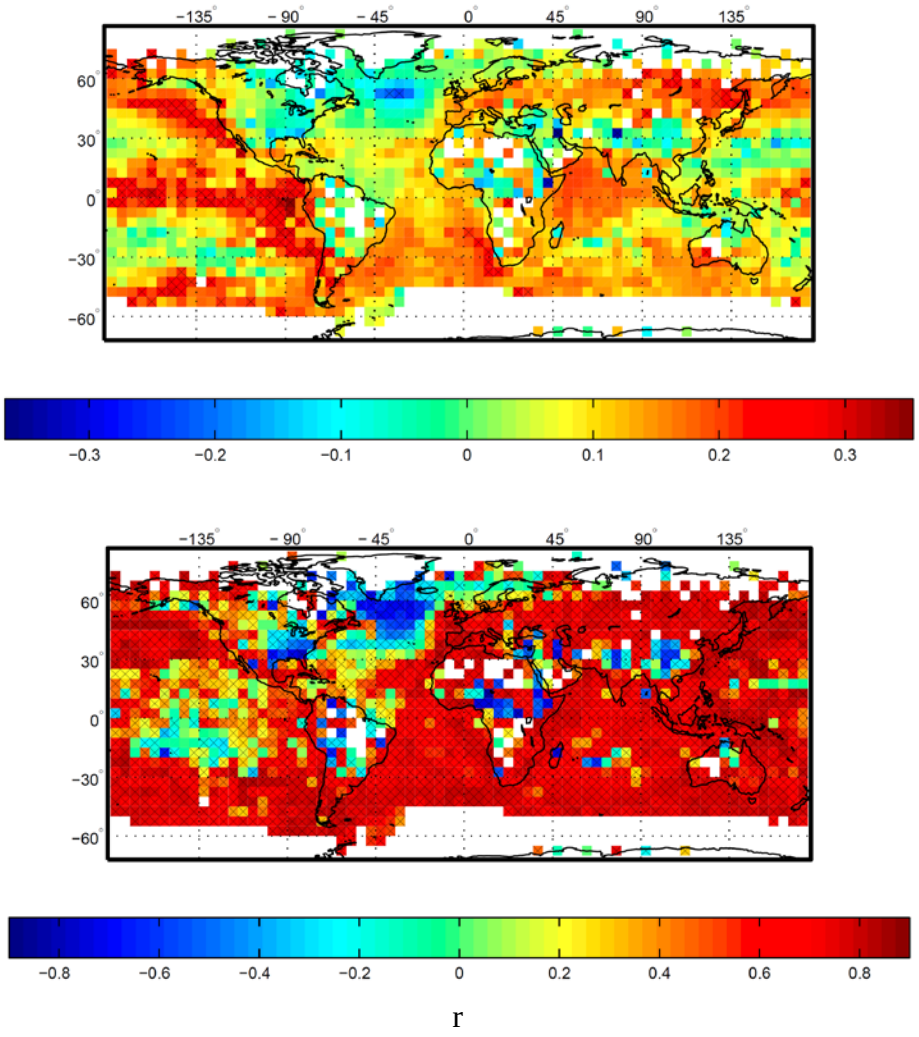

Figure 2.5. Correlation (r) between WDC05A methane concentrations on the WDC05A:2 chronology and reconstructed 5° x 5° gridded surface temperature [*Mann et al.*, 2009] for a) the LPIH (1000-1800 C.E.) and b) 1400-1600 C.E. Prior to comparison, the surface temperatures were smoothed with a bandpass filter with a period of 20 to 500 years. Hatching indicates statistically significant correlation ($p < 0.05$, null hypothesis is that $r = 0$) in that grid box.

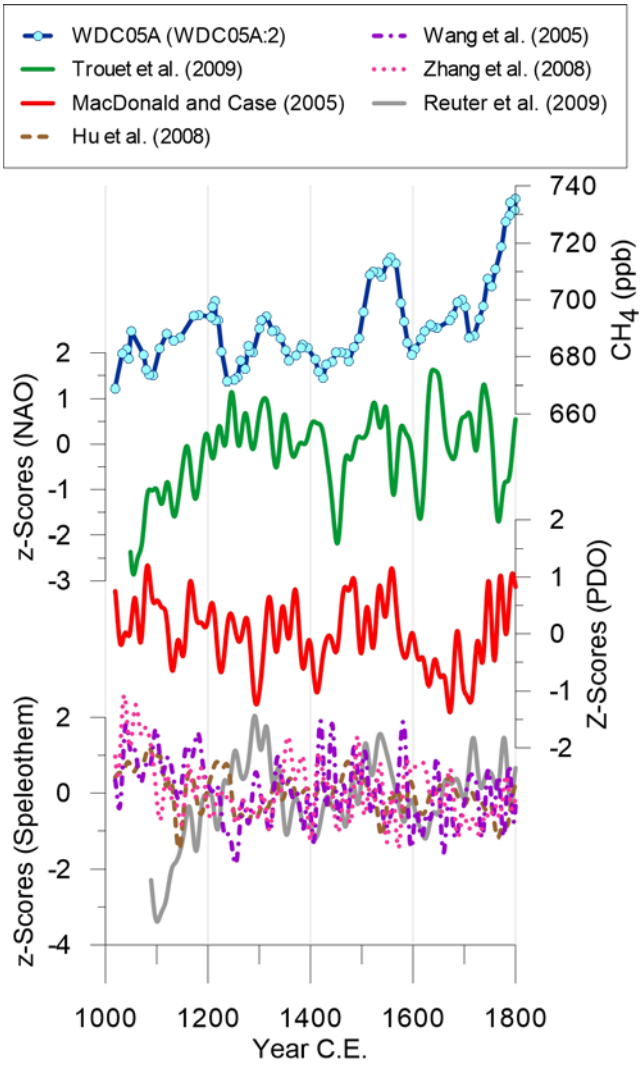

Figure 2.6. Comparison between WDC05A methane concentrations on the WDC05A:2 chronology and paleo proxies for precipitation. Smoothing applied to all records is discussed in the text. From top to bottom are: WDC05A CH_4 (this study); NAO index [*Trouet et al.*, 2009]; PDO index [*MacDonald and Case*, 2005]; Speleothem records from the East Asian Monsoon: Heshang (brown, dashed) [*Hu et al.*, 2008], Dongge (purple, dash-dot) [*Y J Wang et al.*, 2005], Wanxiang (pink, dotted) [*P Z Zhang et al.*, 2008]. Speleothem record from Peru: Cascayunga (grey) [*Reuter et al.*, 2009]. All records were smoothed with a bandpass filter with a period of 20-500 years.

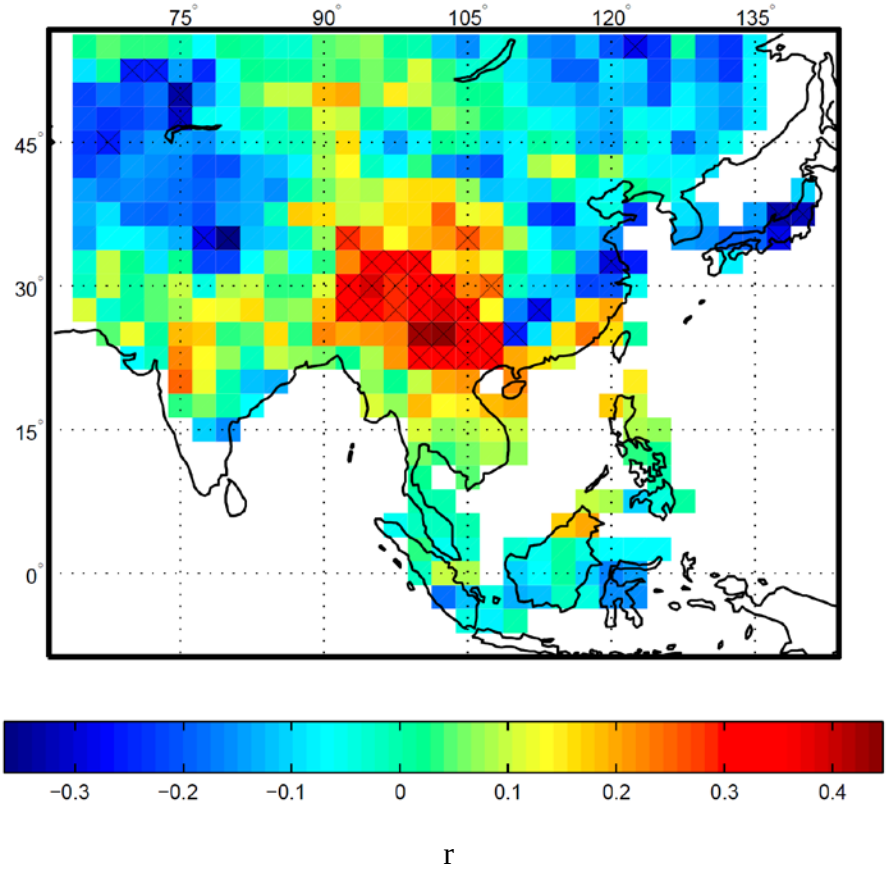

Figure 2.7. Correlation (r) between WDC05A methane concentrations on the WDC05A:2 chronology and 2.5° x 2.5° gridded Palmer Drought Severity Index (PDSI) [*E R Cook et al.*, 2010] between 1300-1800 C.E. Prior to comparison, the PDSI indices were smoothed with a bandpass filter with a period of 20 to 500 years. Hatching indicates statistically significant correlation ($p < 0.05$, null hypothesis is that $r = 0$) in that grid box.

2.9 **Tables**

Table 1. LPIH methane sources after [*Harder et al.*, 2007] and including an estimate of anthropogenic sources after [*Houweling et al.*, 2000] that has been scaled to a total of 250 Tg CH_4 yr^{-1}. See Table 3 for alternate estimates of anthropogenic sources.

Global methane sources	Tg CH_4 yr^{-1}	% of total
Animals	18.0	7.2
Termites	19.2	7.7
Ocean	12.9	5.2
Fresh water lakes	4.8	1.9
Misc ground	6.8	2.7
Biomass burning	3.8	1.5
Wetlands and tundra	155.8	62.3
Anthropogenic	28.6	11.5
Total	**250**	**100**

Table 2. Linear correlation coefficients (r) between temperature reconstructions, precipitation proxy records, and the WDC05A methane record. All records were smoothed with a bandpass filter removing periods shorter than 20 years and longer than 500 years and then subsampled to match the ages of the WDC05A methane data (N = 89). Correlation coefficients are statistically significant when $p < 0.05$ (null hypothesis is that $r = 0$).

Source	Region	r	p
Temperature proxy records and reconstructions			
[*Johnsen et al.*, 1997]	Greenland (GRIP)	0.24	0.03
[*Vinther et al.*, 2006]	Greenland (NGRIP)	0.06	0.56
[*Kobashi et al.*, 2010]	Greenland (GISP2)	0.18	0.10
[*D'Arrigo et al.*, 2006]	Extratropical N.H. 40°N-90°N	0.04	0.73
[*Esper et al.*, 2002]	Extratropical N.H. 30°N-90°N	0.16	0.13
[*Kaufman et al.*, 2009]	Extratropical N.H. 60°N-90°N	0.24	0.03
[*Mann et al.*, 2008] EIV Land	Northern Hemisphere	-0.10	0.37
[*Moberg et al.*, 2005]	Northern Hemisphere	-0.13	0.23
[*Hegerl et al.*, 2007]	Northern Hemisphere	0.03	0.81
[*Oppo et al.*, 2009]	Tropical SST (Indo-Pacific Warm Pool)	0.26	0.01
[*Black et al.*, 2007]	Tropical SST (Cariaco Basin)	0.35	< 0.01
[*Trouet et al.*, 2009]	North Atlantic Oscillation	0.03	0.76
[*MacDonald and Case*, 2005]	Pacific Decadal Oscillation	0.35	< 0.01
Precipitation proxy records			
[*Hu et al.*, 2008]	China Speleothem $\delta^{18}O$ (Heshang)	0.24	0.02
[*Y J Wang et al.*, 2005]	China Speleothem $\delta^{18}O$ (Dongge)	0.02	0.88
[*P Z Zhang et al.*, 2008]	China Speleothem $\delta^{18}O$ (Wanxiang)	0.28	0.01
[*Reuter et al.*, 2009]	Peru Speleothem $\delta^{18}O$ (Cascayunga)	-0.19	0.09

Table 3. Estimates of Anthropogenic emissions at ~1500 C.E. in Tg CH_4 yr^{-1}. Dashes indicate that the study did not estimate that source. Total budget is assumed to be 250 Tg CH_4 yr^{-1}.

	[*Houweling et al.*, 2000; *Houweling et al.*, 2008]	[*Ruddiman*, 2007]	[*Ferretti et al.*, 2005]	[*Subak*, 1994]	[*Mischler et al.*, 2009]
Rice agriculture	10	~28 (23-32)	-	15	15
Biomass burning	10	20	~20	30 (26 = biomass; 4 = wood fuel)	38
Domestic Ruminants	5	7	-	10	-
Waste	5	4	-	-	-
Climate feedbacks	-	~10 (6-15)	-	-	-
Total	30	~69 (60-78)	~20	55	53
% of Total budget	12%	~28%	~8%	22%	21%

New Constraints on the Late Holocene Anthropogenic Contribution to the Atmospheric Methane Budget

Logan Mitchell [1], Ed Brook [1], James E. Lee [1], Christo Buizert [1], Todd Sowers [2]

[1] Oregon State University, Department of Geosciences, Corvallis, OR 97331

[2] The Earth and Environmental Systems Institute, Penn State University, University Park, PA 16802

Prepared for submission to Science Magazine.

3.1 Abstract

The origin of the late pre-industrial Holocene (LPIH) increase in atmospheric methane concentrations has been much debated. Hypotheses invoking changes in solely anthropogenic sources or solely natural sources have been proposed to explain the full increase in concentrations. Here we present two new high resolution, high precision ice core methane concentration records from Greenland and Antarctica which we use to construct the first high resolution record of the methane inter-polar difference (IPD). The IPD constrains the latitudinal distribution of emissions and shows that LPIH emissions increased primarily in the tropics with secondary increases in the subtropical northern hemisphere. Anthropogenic and natural sources have different latitudinal signatures, which we exploit to demonstrate that both anthropogenic and natural sources are needed to explain the full increase in LPIH methane concentrations.

3.2 Main Body of Paper

The 2.5-fold increase in the atmospheric methane (CH_4) burden since the start of the industrial revolution accounted for ~20% of the total increase in radiative forcing over that time and motivated efforts to understand both natural methane biogeochemistry and anthropogenic impacts on methane sources and sinks [*Forster et al.,* 2007]. There has been a lively debate about the impact of early human activities on the global methane budget, based on the observation that atmospheric methane levels generally follow 30°N summer solar insolation over the last 800,000 years, but in the mid-Holocene (~5 thousand years ago, ka) there is a divergence, with methane increasing and insolation decreasing. The "early anthropogenic hypothesis" postulates that human activities were responsible for the increase in CH_4 since the mid-Holocene (and CO_2 increases since ~7ka) [*Ruddiman*, 2003] but others argue that the increase originates from natural sources [*Singarayer et al.*, 2011]. Archeological evidence supports early anthropogenic emissions, particularly from rice agriculture [*Fuller et al.*, 2011; *Ruddiman et al.*, 2008], however the magnitude of those emissions is debated [*Ruddiman et al.*, 2011; *Singarayer et al.*, 2011].

One tool for understanding methane budget changes is the methane Inter-Polar Difference (IPD) [*Brook et al.*, 2000; *Chappellaz et al.*, 1997; *Fung et al.*, 1991] which can be reconstructed from polar ice cores. The IPD results from the latitudinal source and sink distributions, as well as the interhemispheric mixing time. The prevalence of northern hemisphere (NH) sources leads to a positive IPD, with higher CH_4 levels recorded in Greenland ice cores than Antarctic ones. Recent work has shown that the sink and interhemispheric transport are second order effects [*Dlugokencky et al.*, 2009; *Lelieveld et al.*, 2008; *Montzka et al.*, 2011] leaving source changes as the dominant control on IPD variation. Since ~95% of humans lived in the NH tropics and subtropics (0-60°N) during the late pre-Industrial Holocene (LPIH) [*Goldewijk et al.*, 2010], the fingerprint of anthropogenic emissions is an increased IPD relative to the natural background. Indeed, NH anthropogenic emissions in the industrial age have increased the IPD to ~125 ppb (~7.5% of the mean global concentration), far above the 42 ppb pre-industrial background (~6.4% of the mean global concentration). Here we present decadally resolved ice core methane records from the West Antarctic Ice Sheet (WAIS) Divide and the Greenland Ice Sheet Project 2 (GISP2) ice cores (Figure 3.1), which we use to reconstruct the IPD from 800 B.C.E. to 1800 C.E. thus providing data driven constraints on the early anthropogenic hypothesis.

Our high precision methane measurements (pooled standard deviation (s.d.) ± 2.4 ppb, Information on materials and methods is available in the Supporting Online Materials.) clearly reproduce multidecadal scale variability also observed in a shallow core (WDC05A) [*Mitchell et al.*, 2011] and in the Law Dome ice core [*Etheridge et al.*, 1998; *MacFarling Meure et al.*, 2006] (SOM). We use the WAIS Divide layer counted ice chronology and a dynamic firn densification model to construct a gas-age chronology. A Monte Carlo correlation technique using the multidecadal variations is then used to create a GISP2 gas-age chronology synchronized with WAIS Divide (SOM). When comparing the synchronized GISP2 chronology to one constructed independently with our firn densification model and the layer counted ice chronology, we find a difference of 0 ± 11 years, showing our dating to be robust (SOM). The IPD is calculated by

subtracting the WAIS Divide from the GISP2 methane concentration after linear interpolation to annual spacing. Uncertainty bands (1σ) are computed with a Monte Carlo technique incorporating measurement precision and time scale uncertainties (SOM).

The IPD remains essentially constant (800 B.C.E.-1800 C.E. mean 41.8 ppb; trend 0.9 ± 0.6 ppb/ka) throughout the LPIH despite a 115 ppb (17%) increase in the global mixing ratio, broadly consistent with previous low-resolution estimates (Figure 3.6) [*Chappellaz et al.*, 1997; *Etheridge et al.*, 1998]. The record shows small (~5 ppb) centennial scale variations with a minimum around 250 B.C.E. and maximum around 1100 C.E. The end of our record captures the methane and IPD increases associated with the onset of the industrial revolution and its rapid expansion of NH anthropogenic emissions [*Etheridge et al.*, 1998].

We use an Eight Box Atmospheric Methane Model (EBAMM) after [*Marik*, 1998] to examine emission scenarios and compare modeled concentrations with our ice core records (SOM). The model has 6 tropospheric boxes covering 30° latitude each and one stratospheric box per hemisphere. We refer to these boxes as the tropical (0-30°), mid-latitude (30-60°) and high-latitude (60-90°) boxes.

The distribution of methane sources is fundamentally under-constrained by mixing ratio data from just the two poles [*Khalil and Rasmussen*, 1983]. However, the modern source distribution provides additional constraints on the relatively small emissions from the 30-90°S and 60-90°N regions (SOM). With these constraints our data can be used in the box model to solve for the source strength of two latitudinal bands at a time (Figure 3.10, SOM). We construct three "latitudinal" emission scenarios (L1-3) that balance the global budget and represent the range of realistic emissions scenarios. While keeping emissions outside the zonal bands of interest constant, we solve for SH vs. NH tropics (L1), tropical (30°S-30°N) vs. mid-latitude NH (L2), and tropical vs. mid to high-latitude NH (L3). Whenever two EBAMM boxes fall within a latitudinal band we assume a fixed emission ratio between them. L3 is equivalent to a simpler 3 box model [*Chappellaz et al.*, 1997] (SOM). Next we calculate the net change in emissions between

800 B.C.E. and 1400 C.E. in each latitudinal band using linear regression (Table 3.1). Scenarios L1-3 show global sources increased ~29 Tg/yr (~92 ppb) between 800 B.C.E-1400 C.E with the majority of that increase coming from tropical sources. We focus on the time period from 800 B.C.E.-1400 C.E. to avoid the exponential population increase after 1500 C.E and potential natural emissions reductions related to the Little Ice Age.

To our knowledge there are two model-based estimates of natural wetland methane emission changes during the LPIH that can be used to estimate the IPD through time. Scenario N1 is based on TRENCH (TRansient Emissions of Natural CH_4), a coarse grid transient model forced by global ice volume, greenhouse gases, and insolation [*Konijnendijk et al.*, 2011]. Scenario N2 used output from a fine grid methane emissions module tied to a dynamic vegetation model using the climate from the HadCM3 GCM [*Singarayer et al.*, 2011]. These models suggest that global natural methane emissions changed by -1 Tg/yr (-5 ppb) and 10 Tg/yr (32 ppb) between 800 B.C.E and 1400 C.E., respectively. Neither indicates large decreases in natural methane emissions during the late Holocene in response to declining NH insolation as proposed by the early anthropogenic hypothesis. However, neither model can explain the global increase in methane emissions of ~29 Tg/yr (~92 ppb, Table 3.1, Figure 3.2), suggesting that either these models are deficient in some way, or that some amount of anthropogenic emissions are needed to explain the full LPIH CH_4 increase.

Scenarios A1 and A2 utilize two published estimates of anthropogenic emissions for the LPIH while leaving natural emissions constant (to isolate the anthropogenic impact). Scenario A1 uses anthropogenic emission estimates from Houweling et al., (2000) (total emissions = 20 Tg/yr at 1500 C.E.) and A2 uses the maximum anthropogenic emission estimates from Ruddiman (2007) (total emissions = 43 Tg/yr at 1500 C.E.). We bin global population from the HYDE 3.1 database [*Goldewijk et al.*, 2010] into the EBAMM boxes and establish per-capita emissions based on estimates of emissions and population in 1500 C.E. The latitudinal distribution from rice agriculture is calculated using population from the rice-producing region of Asia (60-140°E and 10°S-50°N, SOM) [*Fuller et al.*, 2011; *Ruddiman et al.*, 2008]. By assigning emissions

on a per-capita basis, we find a roughly linear increase in anthropogenic emissions until ~1500 CE, consistent with recent work [*Fuller et al.*, 2011]. If anthropogenic biomass burning emissions are also scaled on a per-capita basis the $^{13}CH_4$ isotopic budget becomes too enriched with increasing population (SOM). We therefore keep all biomass burning emissions (natural and anthropogenic) constant; while some small variations are expected based on $\delta^{13}CH_4$ observations [*Sapart et al.*, 2012], these cannot be systematically tied to population changes on a per-capita basis [*Pechony and Shindell*, 2010]. A1 and A2 yield an increase in emissions of 11 Tg/yr (35 ppb) and 24 Tg/yr (74 ppb) from 800 B.C.E. to 1400 C.E., respectively. Since most of the emissions increase occurred in the NH (Table 3.1), both scenarios produce a positive slope in the IPD which is not observed in the data (Figure 3.2). However, increases and subsequent losses of population associated with the Mongol invasion and the spread of the Black Plague [*Mitchell et al.*, 2011; *Ruddiman*, 2007] create a maximum in the modeled IPD from ~1000-1400 C.E. which is evident in the data, lending support to the hypothesis that at least some of the LPIH increases in emissions were anthropogenic in origin.

Neither the anthropogenic (A1-2) nor the natural (N1-2) scenarios alone can account for the full emission increase of 29 Tg/yr (L1-3). Comparing anthropogenic emissions to L1-3, it is clear that scenarios A1-2 both have large NH emissions similar to L1-3, whereas N1-2 do not. This suggests that most of the increase in NH emissions is anthropogenic in origin, particularly in the tropical NH (N2 suggests that a small fraction of the mid-latitude NH increase could be natural). When added to natural emissions from scenarios N1 or N2, the NH emissions in A1 are lower than expected from L1-3 whereas emissions from A2 are too high. We therefore conclude that, given current NH natural emission estimates, anthropogenic emissions are intermediate between A1 and A2. In the SH, A1-2 show small increases in emissions since there are minimal population increases in the SH. However, the primary source increase in the modeling result of Singarayer et al. (2011) (scenario N2) during the LPIH are tropical SH natural wetlands, which is consistent with increases in the South American monsoon strength reconstructions [*Wang et al.*, 2006]. Since natural wetlands represent the only sizeable source for SH tropical

emissions, it likely is responsible for the majority of the SH emissions identified by L1-3. Scenario N1 does not show tropical SH increases, possibly because N1 has a lower spatial resolution and simplified climate. Based on these results we construct a "Best" estimate scenario that contains intermediate anthropogenic emissions (24 Tg/yr at 1500 C.E.) and the natural emissions from N2. We increased the tropical SH emissions of N2 to match those indicated by L1-3. This mix of natural and anthropogenic sources solves the global methane budget including the IPD over the LPIH.

In conclusion, our results suggest that increases in both SH natural wetland emissions and NH anthropogenic emissions are needed to close the LPIH global methane budget. Our dataset provides a constraint for future methane emission modeling efforts.

3.3 Acknowledgements

This work was supported by NSF OPP grants 0538578, 0520523, and 0538538 and by NASA/Oregon Space Grant Consortium grant NNG05GJ85H and the NOAA Climate and Global Change Fellowship Program, administered by the University Corporation for Atmospheric Research (Buizert). We thank Brad Markle, Alex Morin, Brendan Williams, and Jon Edwards for assisting in sample preparation and analysis; Thomas Marik who provided the original 8-box model code (BOSCAGE); Jeff Severinghaus and Giuseppe Etiope who contributed preliminary results from their work; Tiuri Konijnendijk, Jacob Van Etten, and Joy Singarayer who provided model data from their published works; the WAIS Divide Science Coordination Office at DRI, Reno, NV for the collection and distribution of the WAIS Divide ice core (Kendrick Taylor, NSF Grants 0230396, 0440817, 0944348; and 0944266 - University of New Hampshire); NSF OPP which funds the Ice Drilling Program Office and Ice Drilling Design and Operations group for coring activities; NSF which funds the National Ice Core Laboratory which curated and processed the core; Raytheon Polar Services which provided logistics support in Antarctica; and the 109th New York Air National Guard for airlift in Antarctica. Data and description can be downloaded from the NOAA National Climate

Data Center http://www.ncdc.noaa.gov/paleo/paleo.html. EBAMM model code is archived in Appendix A.

3.4 References

Brook, E. J., S. Harder, J. Severinghaus, E. J. Steig, and C. M. Sucher (2000), On the origin and timing of rapid changes in atmospheric methane during the last glacial period, *Glob. Biogeochem. Cycle*, *14*(2), 559-572.

Chappellaz, J., T. Blunier, S. Kints, A. Dallenbach, J. M. Barnola, J. Schwander, D. Raynaud, and B. Stauffer (1997), Changes in the atmospheric CH_4 gradient between Greenland and Antarctica during the Holocene, *J. Geophys. Res.-Atmos.*, *102*(D13), 15987-15997.

Dlugokencky, E. J., et al. (2009), Observational constraints on recent increases in the atmospheric CH4 burden, *Geophys. Res. Let.*, *36*.

Etheridge, D. M., L. P. Steele, R. J. Francey, and R. L. Langenfelds (1998), Atmospheric methane between 1000 AD and present: Evidence of anthropogenic emissions and climatic variability, *J. Geophys. Res.-Atmos.*, *103*(D13), 15979-15993.

Forster, P., et al. (2007), Changes in Atmospheric Constituents and in Radiative Forcing., in *Climate Change 2007: The Physical Science Basis. Contribution of Working Group I to the Fourth Assessment Report of the Intergovernmental Panel on Climate Change*, edited by S. Solomon, D. Qin, M. Manning, Z. Chen, M. Marquis, K. B. Averyt, M. Tignor and H. L. Miller, pp. 131-234, Cambridge University Press, Cambridge, United Kingdom and New York, NY, USA.

Fuller, D. Q., J. van Etten, K. Manning, C. Castillo, E. Kingwell-Banham, A. Weisskopf, L. Qin, Y. I. Sato, and R. J. Hijmans (2011), The contribution of rice agriculture and livestock pastoralism to prehistoric methane levels: An archaeological assessment, *Holocene*, *21*(5), 743-759.

Fung, I., J. John, J. Lerner, E. Matthews, M. Prather, L. P. Steele, and P. J. Fraser (1991), 3-Dimensional Model Synthesis of the Global Methane Cycle, *J. Geophys. Res.-Atmos.*, *96*(D7), 13033-13065.

Goldewijk, K. K., A. Beusen, and P. Janssen (2010), Long-term dynamic modeling of global population and built-up area in a spatially explicit way: HYDE 3.1, *Holocene*, *20*(4), 565-573.

Houweling, S., F. Dentener, and J. Lelieveld (2000), Simulation of preindustrial atmospheric methane to constrain the global source strength of natural wetlands, *J. Geophys. Res.-Atmos.*, *105*(D13), 17243-17255.

Khalil, M. A. K., and R. A. Rasmussen (1983), Sources, Sinks, and Seasonal Cycles of Atmospheric Methane, *Journal of Geophysical Research-Oceans and Atmospheres*, *88*(NC9), 5131-5144.

Konijnendijk, T. Y. M., S. L. Weber, E. Tuenter, and M. van Weele (2011), Methane variations on orbital timescales: a transient modeling experiment, *Clim. Past.*, *7*(2), 635-648.

Lelieveld, J., et al. (2008), Atmospheric oxidation capacity sustained by a tropical forest, *Nature*, *452*(7188), 737-740.

MacFarling Meure, C., D. Etheridge, C. Trudinger, P. Steele, R. Langenfelds, T. van Ommen, A. Smith, and J. Elkins (2006), Law Dome CO_2, CH_4 and N_2O ice core records extended to 2000 years BP, *Geophys. Res. Let.*, *33*(14), 4.

Marik, T. (1998), Atmospheric $d^{13}C$ and dD measurements to balance the global methane budget, Ph.D. thesis, University of Heidelberg, Heidelberg, Germany.

Mitchell, L. E., E. J. Brook, T. Sowers, J. R. McConnell, and K. Taylor (2011), Multidecadal variability of atmospheric methane, 1000-1800 CE, *J. Geophys. Res.-Biogeosci.*, *116*.

Montzka, S. A., M. Krol, E. Dlugokencky, B. Hall, P. Jockel, and J. Lelieveld (2011), Small Interannual Variability of Global Atmospheric Hydroxyl, *Science*, *331*(6013).

Pechony, O., and D. T. Shindell (2010), Driving forces of global wildfires over the past millennium and the forthcoming century, *Proc. Natl. Acad. Sci. U. S. A.*, *107*(45), 19167-19170.

Ruddiman, W. F. (2003), The anthropogenic greenhouse era began thousands of years ago, *Clim. Change*, *61*(3), 261-293.

Ruddiman, W. F. (2007), The early anthropogenic hypothesis: Challenges and responses, *Reviews of Geophysics*, *45*(3), 37.

Ruddiman, W. F., J. E. Kutzbach, and S. J. Vavrus (2011), Can natural or anthropogenic explanations of late-Holocene CO2 and CH4 increases be falsified?, *Holocene*, *21*(5), 865-879.

Ruddiman, W. F., Z. T. Guo, X. Zhou, H. B. Wu, and Y. Y. Yu (2008), Early rice farming and anomalous methane trends, *Quat. Sci. Rev.*, *27*(13-14), 1291-1295.

Sapart, C. J., et al. (2012), Natural and anthropogenic variations in methane sources during the past two millennia, *Nature*, *490*(7418), 85-88.

Singarayer, J. S., P. J. Valdes, P. Friedlingstein, S. Nelson, and D. J. Beerling (2011), Late Holocene methane rise caused by orbitally controlled increase in tropical sources, *Nature*, *470*(7332), 82-U91.

Wang, X. F., A. S. Auler, R. L. Edwards, H. Cheng, E. Ito, and M. Solheid (2006), Interhemispheric anti-phasing of rainfall during the last glacial period, *Quat. Sci. Rev.*, *25*(23-24), 3391-3403.

3.5 Figures

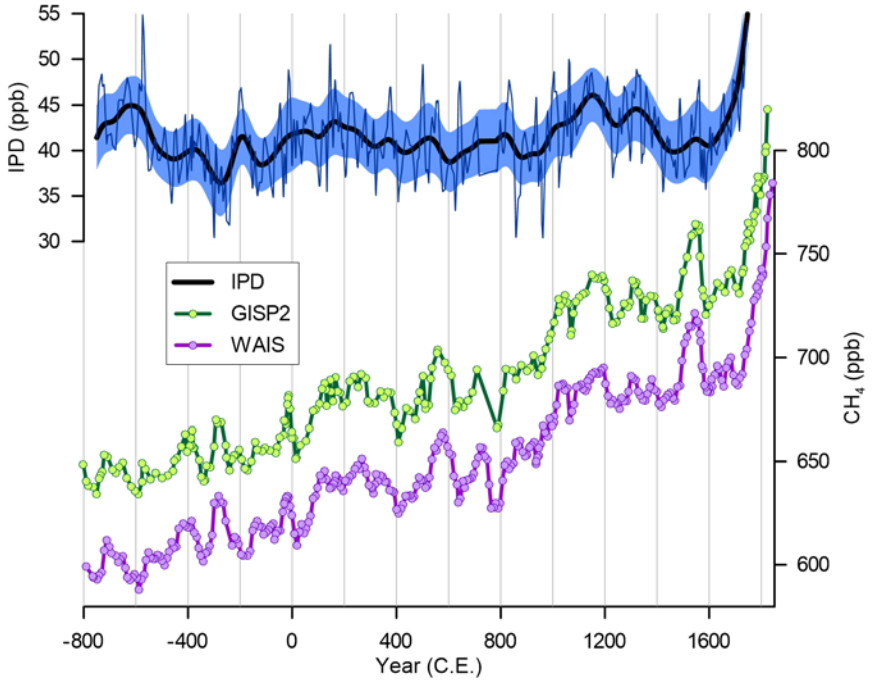

Figure 3.1. Methane and IPD records. Data points are the mean concentration from replicate samples measured at that depth. Thin line shows IPD obtained by linear interpolation between ice core measurements at an annual spacing. Smoothed heavy line was computed using a 20-year lowpass filter. IPD 1σ error bands were obtained using a Monte Carlo procedure accounting for analytical uncertainty of the measurements and chronologic uncertainty of the tie points (SOM).

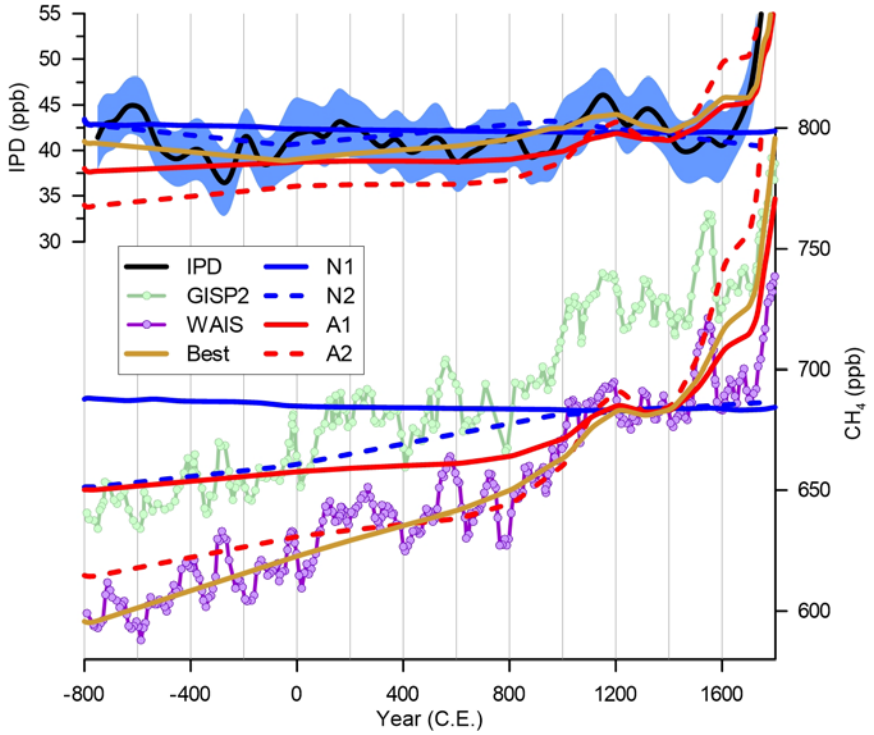

Figure 3.2. Model scenarios N1, N2, A1, A2, and Best. All scenarios are tuned to match the concentration and IPD at ~1400 CE. Emission histories used to produce these scenarios are shown in supplemental Figure 3.12. Model concentrations from Greenland are omitted for clarity.

3.6 Tables

Table 3.1. Modeled change in zonal methane emissions between 800 B.C.E. and 1400 C.E. (Tg/yr).

EBAMM Box (latitude)	L1*	L2*	L3*	N1	N2	A1	A2	Best
6 (60-90°N)	0	0	1 ± 1	0	-1	0	0	0
5 (30-60°N)	0	6 ± 6	3 ± 3	-1	3	4	8	8
4 (0-30°N)	22 ± 9	11 ± 3	12 ± 2	-1	1	7	15	8
3 (0-30°S)	8 ± 7	12 ± 3	13 ± 2	0	7	1	1	12
2 (30-60°S)	0	0	0	0	0	0	0	0
1 (60-90°S)	0	0	0	0	0	0	0	0
Total change	30 ± 5	29 ± 5	29 ± 5	(-2)	10	12	24	28
CH_4 increase (ppb)	92	92	92	(-5)	32	35	74	90

* The difference in the zonal methane emissions between 800 B.C.E. and 1400 C.E. (± 2 times the 1 standard deviation of the prediction interval) after calculating the linear regression of emissions from the global methane budget solved for tropical and subtropical NH emissions. In L1-3 we solve for the zonal bands indicated by the colors; when there are two boxes within a band we assume a fixed emission ratio between them. See SOM for details.

3.7 Supporting Online Materials (SOM)

3.7.1 Analytical Methods

3.7.1.1 Sample measurement

We measured samples using a wet extraction technique described in detail elsewhere [*Grachev et al.*, 2007; *Grachev et al.*, 2009; *Mitchell et al.*, 2011]. Briefly, a ~10 cm tall slab of ice was divided into two samples with cross sectional area of ~2.5 cm x 2.5 cm each. We trimmed the outer 1-2 mm of the sample yielding a mean weight of ~60.5 g. Samples were placed in a pre-chilled glass flask with a glass to metal transition and Conlflat flange and then the flasks were sealed to the extraction line with a copper gasket. While on the extraction line we submerged the flasks in a chilled ethanol bath maintained at -70°C. Ambient air was pumped from the samples for one hour using a turbo molecular pump, then the samples were melted by submersion of the flasks in a hot water bath, releasing the air from the ice into the flask headspace. The flasks were then re-submerged in the ethanol bath to freeze the sample and lower the water vapor pressure in the headspace. We expanded the air from each flask into the sample loop of a gas chromatograph (GC) equipped with a flame ionization detector four times and the concentrations were averaged. We then averaged the mean values for each pair of samples to produce a mean concentration for each depth (Figure 3.3).

We calculated the methane concentrations by placing the sample peak area over pressure on a linear regression line fitted to the peak area over pressure from a working air standard (500.2 ppb methane on the NOAA04 methane scale [*Dlugokencky et al.*, 2005]). The concentration of our working air standard was periodically calibrated to primary laboratory standard tanks with concentrations ranging from 380 to 1853 ppb, which were in turn calibrated by the NOAA GMD Carbon Cycle Group on the NOAA04 methane scale.

In the summer of 2009 we rebuilt the extraction line to increase the throughput from 8 samples per day to 12 samples per day. In the fall of 2010 we added foam insulation around the bath and extraction line which reduced the thermal gradient inside

the flasks and decreased the blank corrections of the rebuilt extraction line by ~2 ppb, otherwise the apparatus remained unchanged.

In total we measured 1,616 individual samples from 709 depths. Of these, 247 depths (578 individual samples) came from the Greenland Ice Sheet Project 2 (GISP2, 72.6° N, 38.5° W) ice core covering 811 B.C.E to 1824 C.E. yielding a mean sampling resolution of 11 years. There is a gap from 708 C.E. to 785 C.E. as no ice was available between 345-359 m. 389 depths (880 individual samples) were measured from the WAIS Divide deep ice core (WDC06A, 79.4676°S, 112.0865°W) covering 2,604 B.C.E. to 1783 C.E. We combined our WDC06A record with data from 18 depths (38 individual samples, 14 of which were previously published and 24 are new) from the WDC05A shallow ice core [*Mitchell et al.*, 2011] from 1784-1909 C.E. to yield a complete WAIS Divide record from 2,604 B.C.E. to 1909 C.E with a combined mean sampling resolution of 11 years. 44 sample pairs (88 individual samples, 5% of the total number of samples) were rejected because of problems with the extraction line, leaks, extreme disagreement between replicates (>4 standard deviations), and samples with cracks in the ice. Finally, samples from 11 more depths (33 individual samples) were excluded due to suspected in-situ methane production, discussed in detail below. The pooled standard deviation of the pairs of samples measured on the same day is 2.0 ppb (excluding the rejected measurements). All of these data are plotted in Figure 3.3.

To establish our analytical precision we measured a duplicate pair of samples from 98 sample depths (47 from GISP2 and 51 from WAIS Divide). The pooled standard deviation between duplicate pairs of samples is 2.4 ppb. This is slightly higher than the pooled standard deviation between pairs of samples because it incorporates the additional uncertainty from slight changes in day-to-day procedures, solubility, and blank ice corrections. We take this as our best estimate of the 1σ uncertainty of the complete data set.

3.7.1.2 Blank correction

To constrain the influence of leaks or other contamination we routinely measured air-free ice (AFI, see [*Mitchell et al.*, 2011] for a description of how we produce AFI). Sample preparation and analysis with AFI is identical to our typical samples except that after ambient air was pumped out of the flasks we added our working standard over the AFI to a pressure of ~50 torr. Average AFI corrections were linearly interpolated between days when AFI was analyzed to create a time-dependent correction. Occasionally, we measured AFI along with real ice core samples and in those cases we used the mean AFI concentrations from that day to correct the samples instead of interpolated values. The mean and standard deviation AFI correction to the data was 2.5 ± 1.6 ppb.

3.7.1.3 Gravitational fractionation correction

Within the firn, gasses undergo a mass dependent fractionation due to gravity [*Craig et al.*, 1988; *Schwander*, 1989; *Sowers et al.*, 1989]. The magnitude of this fractionation is controlled by the thickness of the diffusive column of the firn. Since the atmospheric N_2 ($\delta^{15}N$) has remained constant over timescales relevant to ice cores [*Sowers et al.*, 1992] we can use the measured $\delta^{15}N$ to correct for this gravitational fractionation. Methane (M = 16.04 g mol^{-1}) is fractionated relative to dry air (M = 28.96 g mol^{-1}) and the gravitational fractionation is therefore $\Delta M \times \delta^{15}N$. We have used linear interpolation between $\delta^{15}N$ measurements from both the WAIS Divide ice core [Severinghaus, J., personal communication 2012] and the GISP2 ice core [*Takuro Kobashi et al.*, 2010] to obtain $\delta^{15}N$ values at the depths of our samples. The mean correction factor for WAIS Divide samples is 1.00397 and for GISP2D it is 1.00396.

3.7.1.4 Solubility correction

When air is exposed to liquid water, a portion of it dissolves into the water in a ratio that is described by Henry's Law. While methane has about the same solubility as oxygen, it is ~2.5x as soluble as nitrogen and therefore the headspace methane

concentration decreases during sample analysis when the air is exposed to the melting sample water. We followed [*Mitchell et al.*, 2011] who empirically determined a methane solubility correction factor of 1.0170 ± 0.0031.

3.7.2 In-situ methane production in the GISP2 ice core.

We measured a number of GISP2 samples that had methane concentrations elevated relative to both nearby samples and to values expected based on the WAIS Divide record (constant IPD added). For five of the depths we had enough ice to make a second measurement on a different day. In all cases we obtained good agreement between both days, confirming that the measurements represent the real concentration of methane in the ice. To investigate the possibility that these signals represent extremely abrupt atmospheric events, we measured additional samples close to the elevated samples (usually within about ± 1 m, corresponding to ± 5 years). We did not find any similarly elevated values. Because the firn air diffusion and bubble trapping processes act as a smoothing filter of the atmospheric signal on the order of 20-40 years, it is impossible for these one-point elevated values to represent real atmospheric events. We therefore tentatively conclude that the elevated methane levels must be the result of in-situ methane production, probably by microbial metabolism [*Rohde et al.*, 2008]. To objectively identify which samples contain elevated concentrations we followed the approach of [*Schilt et al.*, 2010] who used a spline fit to the data to identify samples containing in-situ production of N_2O. This is better suited than a lowpass filter because it can be created using the raw time series data while a lowpass filter requires evenly spaced (interpolated) data. We used the Matlab function "csaps" with a smoothing parameter (p) of 0.011, roughly equivalent to a lowpass filter with a cutoff frequency of 3 years [*de Boor*, 2001]. We identified the sample with the highest elevation above the spline fit and exclude it, refit the spline, and repeated the process until there are no samples which are elevated more than 2 σ (4.8 ppb). This procedure identified 11 points in our record which are shown in Figure 3.4 along with the final spline fit.

To search for the source of in-situ methane production by microbial metabolism, we looked for a correlation between our elevated methane concentrations and the trace element chemical records from GISP2 [*Mayewski et al.*, 1997]. We observed that some, but not all, of the samples with elevated methane concentrations also had elevated concentrations of ammonium (NH_4^+). There was no notable correlation between methane artifacts and any other chemical species. Our analysis was severely limited, however, by the fact that the GISP2 chemistry data generally had a ~44 cm sample resolution, whereas our samples are 10 cm long and abrupt changes in chemistry can occur on centimeter scales at this depth range [*Mayewski et al.*, 1997]. In a few select areas high-resolution (2 cm) chemical analysis was performed [*Mayewski et al.*, 1997]. One of these high resolution chemical transects overlaps the methane sample at 583.6-583.7 m that had the largest methane spike (elevated ~70 ppb over nearby samples and the spline fit) and reveals a very large spike in NH_4^+ in the middle of the methane sample. The low resolution NH_4^+ record shows a concentration of 43.9 ppb in a 40 cm long sample whereas the high resolution NH_4^+ record shows peak concentrations of 154 ppb and 78 ppb in two 3 cm long samples located in the middle of the depth interval encompassing our methane sample and lower concentrations (~5 ppb) surrounding. After making our measurement we were able to examine the ice archive at this depth in the National Ice Core Laboratory and observed a ~2 cm thick cloudy band in the ice at the same depth of the high resolution NH_4^+ peak, but we are currently unsure of its origin (Figure 3.5). Although these observations offer compelling evidence for organic based in-situ production, we are not able to unambiguously determine the cause.

Recently Rhodes et al., (*in press*) [*Rhodes et al.*, Submitted] used continuous flow analysis of methane and trace elements on the NEEM S1 ice core from NW Greenland to examine these relationships in greater detail. This study also observed reproducible, abrupt, high amplitude methane spikes that could not have been atmospheric in origin. They observe that these spikes are closely associated with black carbon, NH_4^+, and NO_3^-, but they do not have a consistent relationship with inorganic chemical species derived from mineral dust. Since the NEEM S1 core is located ~650 km northwest of GISP2 it is

possible that these methane spikes are the result of a widespread event which deposits the organisms and trace elements which are necessary for in-situ methane production over a large portion of the Greenland ice sheet. This hypothesis will be examined as other ice cores from Greenland are analyzed in greater detail in the future.

These observations raise the possibility that methane could be produced in-situ throughout the core, not only in the isolated areas discussed previously. This would elevate the baseline methane concentration and also the methane IPD. We here argue this is highly unlikely for two reasons. First, microbial CH4 production would require the simultaneous presence of both methanogenic microbes as well as nutrients, the deposition of which has a very high temporal variability associated with northern hemispheric weather events and seasonal patterns (Figure 3.4) [*Mayewski et al.*, 1997]. Since the magnitude of suspected in-situ methane production is 7-70 ppb, we would expect that if present, the contamination would obscure the multidecadal variability of methane which has a magnitude of 10-40 ppb. However the multidecadal scale variability is similar in both records as can be seen in the very high correlation coefficient between the bandpass (pass band = 20-100 years) filtered methane records ($r^2 = 0.85$). Second, if the small amplitude, high frequency trace chemical variations were causing smaller in-situ contamination (< 7 ppb) the high frequency variability of the GISP2 methane record would increase relative to the WAIS Divide record. However, the standard deviation of the high pass (high pass cutoff = 5 years) filtered records is similar (GISP2 = 1.4 ppb, WAIS = 1.7 ppb).

Given these observations, the only possible type of in-situ production that could be affecting our record is a small, constant amount of methane production throughout the core. Since microbial metabolism is the only known possible source of in-situ methane production and since this source would depend on the highly variable trace chemical deposition on the surface of the ice sheet, we feel that a small, constant amount of methane production throughout the core is highly improbable. The ultimate confirmation that Greenlandic ice core records do not contain methane concentrations elevated by a small amount awaits a new Greenlandic ice core with a high enough accumulation rate to

overlap the northern hemispheric record of direct atmospheric methane measurements, which began in 1983.

3.7.3 Chronologies

To construct the IPD, the chronologies of both ice cores need to be synchronized. The multidecadal events observed in both ice core records must have occurred simultaneously since the duration of the events is much larger than the atmospheric mixing time (~1 year). We therefore take one ice core record as our "reference" and use a wiggle matching technique to obtain an ideal match based on the multidecadal variability – this works provided that the offset between the initial independent chronologies of both cores is smaller than the duration of multidecadal methane variations used in the synchronization.

We used a coupled heat diffusion-firn densification model to determine the ice age-gas age (Δage) difference in the WAIS Divide and GISP2 ice cores. Accumulation rates were reconstructed for each core using measured annual layer thickness records with a simple 2-D ice flow model to correct for strain due to ice flow [*Alley et al.*, 1997; *K. M. Cuffey and Clow*, 1997]. GISP2 temperatures were obtained from Kobashi et al., (2011); WAIS temperatures were based on a combination of the borehole temperature record and stable water isotopes [*Fegyveresi et al.*, 2011; *Orsi et al.*, 2012]. Modern day CO_2 Δage values of 205 and 190 years for WAIS and GISP2, respectively, were determined using firn air sampling data from WAIS and Summit station [*Battle et al.*, 2011; *Buizert et al.*, 2012; *Witrant et al.*, 2011]. Because methane diffuses more quickly through the firn column than CO_2 does, we added two years to the modern day (CO_2 based) Δage estimates [*Buizert et al.*, 2013]. The firn densification model is a dynamical version of the Herron and Langway model [*Herron and Langway*, 1980] using ice thermal properties [*K.M. Cuffey and Paterson*, 2010]. $\delta^{15}N$ data were used to verify that the firn column thickness predicted by the densification model was correct.

We used these chronologies as starting points for an iterative Monte Carlo analysis which maximizes the correlations between the bandpass filtered GISP2 and

WAIS Divide records. The WAIS Divide layer counted chronology is probably more accurate as it is based on a combination of multi-parameter high-resolution chemistry records and electrical conductivity measurements. Therefore we chose to use the WAIS Divide chronology as our "reference" chronology and tie the GISP2 record to the WAIS Divide record.

Our iterative Monte Carlo procedure is as follows. Step 1: Choose tie points between the methane records with an even spacing of 200 years. Step 2: Performed the following procedure 1000 times: randomly perturb the depth of the tie points (standard deviation of 4 m, equivalent to ~20 years) to produce a new depth-age scale, apply a bandpass filter to the records (passband of 20-100 years), and calculate the correlation coefficient over the whole record. Each tie point therefore has 1000 results consisting of the depth and the correlation of the whole record. Step 3: we took the mean tie point depth of the 20% of records with the highest correlation coefficients. Step 4: Iterate through steps two and three 50 times, which allows the Monte Carlo procedure to converge on stable depth-age values for GISP2. However, there were still small differences between individual iterations, so for Step 5 we took the mean depth of the final 25 iterations. Step 6: We shifted all of the tie points by 20 years and performed steps one to five again. We repeated step six until we had 10 independent chronologies consisting of tie points that were spaced 200 years apart. Step 7: We combined the 10 independent chronologies into one final chronology. This final chronology is shown in Figure 3.6 along with colored symbols that correspond to the 10 individual chronologies.

We performed a number of sensitivity tests to examine the robustness of our chronology. We used the GISP2 chronology as a "reference" and this gave equivalent results. We also constructed timescales with tie points spaced every 50 and 100 years. The closer spacing allowed the procedure to over fit the data and created very large oscillations in Δage which are unrealistic. These sensitivity tests demonstrate that 1) our method of establishing the chronology has yielded closely spaced tie points which provide detailed information about Δage variability and 2) the 200 year tie point spacing

of the individual component timescales prevented the procedure from over fitting the data.

Our analysis provides an independent check for the accuracy of the original chronologies (Figure 3.6). We find that the methane synchronized GISP2 chronology is 0 ± 11 years different from the gas chronology found from by employing the dynamic firn model and the Meese/Sowers layer counted ice chronology [*Meese et al.*, 1994]. This offset is well within the estimated uncertainty of the layer counting (± 25 years) and firn densification modeling (± 20 years).

3.7.4 Comparison with other ice core records

Our new high-resolution records compare well with previous high-resolution methane records from WAIS Divide (WDC05A) [*Mitchell et al.*, 2011] and Law Dome [*Etheridge et al.*, 1998; *MacFarling Meure et al.*, 2006]. The WDC05A shallow ice core was drilled at WAIS Divide ~1.3 km away from the main borehole (WDC06A) in the 2005/2006 drilling season. This core was drilled to a depth of 298 m (gas age ~1000 CE) without the use of mechanical drilling fluid. For this comparison we have plotted the WDC05A samples using the chronology for WDC06A since they show nearly identical trends on a depth scale indicating that there is little difference in timescales [*Mitchell et al.*, 2011]. The WDC05A record has a similar temporal resolution as our WDC06A record and excellently reproduces the variability. Over the time period where we have data for both ice cores (1002-1780 CE) the correlation coefficient after linear interpolation between the mean of each sample is $r^2 = 0.92$.

The Law Dome ice core was drilled on the coast of Antarctica (66.733°S, 112.833°E) and since there are essentially no methane emissions in the high latitude Southern Hemisphere (SH) we expect that the atmospheric history derived from both cores should be the same [*Dlugokencky et al.*, 1994]. In reality there may be slight differences owing to different smoothing from diffusion in the firn and bubble trapping processes, but the differences between Law Dome and WAIS Divide shouldn't be large since both sites have a moderate to high accumulation rate. Overall there is excellent

agreement between the WAIS Divide and Law Dome records (Figure 3.3, all records are on the NOAA04 calibration scale [*Dlugokencky et al.*, 2005]). Mitchell et al., (2011) noted that the largest discrepancy between the WDC05A and Law Dome record over the past 1000 years was the multidecadal event from 1410-1470 CE which has a 10-15 ppb larger magnitude in the Law Dome record than the WDC05A record. The WDC06A and GISP2 records both confirm the magnitude of the event seen in the WDC05A record and suggest that the data for the three samples comprising this event in the Law Dome record may be elevated. Between 0-1000 CE the Law Dome record diverges from the WDC06A record, however it appears that this is due to a shift in the chronology. There is a large oscillation in the Law Dome record at ~300-500 CE that would clearly match the WAIS Divide record if it was shifted ~80 years (Figure 3.3).

3.7.5 Monte Carlo Error Analysis of the IPD

To determine error bands around our IPD record we performed a Monte Carlo analysis which incorporated our 1σ analytical measurement uncertainty of ± 2.4 ppb and a temporal uncertainty of ± 5 years for each of our tie points. We randomly perturbed the measurements and the tie points then used a lowpass filter with a cutoff frequency of 20 years to smooth the records 1000 times. We then took the standard deviation of the 1000 perturbed records to obtain the uncertainty through time. The average 1σ uncertainty for the IPD is ± 3.3 ppb, as indicated with the blue shaded area in Figure 3.1 of the main text.

3.7.6 Comparison with previous IPD estimates

Previous estimates of the IPD during the LPIH are shown in Figure 3.7 [*Chappellaz et al.*, 1997; *Etheridge et al.*, 1998]. Given the lower precision and temporal resolution of the earlier records, the three reconstructions are consistent with each other in the period 1000-1800 C.E. The additional variability seen in Etheridge et al., (1998) could have been caused by aliasing the multidecadal scale variability. Chappellaz et al., (1997) estimated the IPD in the time period 2.5-5 ka of 50 ± 3 ppb.

3.7.7 Atmospheric box modeling

To evaluate how emission scenarios affect the IPD we used an Eight Box Atmospheric Methane Model (EBAMM). This model consists of six tropospheric boxes covering 30° latitude each and one stratospheric box in each hemisphere with the tropopause located at ~200 hPa (Figure 3.8). This model was chosen because it can resolve the latitudinal distribution of methane yet is simple enough to model methane concentrations over thousands of years using a personal computer. The original structure of EBAMM was developed in Simulink and was called BOSCAGE-8 (8-BOx SF_6 CAlibrated Global Euler transport model) [*Marik*, 1998]. We reprogrammed and optimized the model in Matlab retaining the original box structure, transport terms, and sink characteristics from BOSCAGE-8.

Each box contains a constant mass of air and the molar ratios of methane isotopologues are changed by the sources, sinks, and transport between the boxes. Since we examined variations in methane on decadal and longer timescales we did not use seasonal variability in the sources. Atmospheric transport between the boxes was calibrated against modern SF_6 observations using singular value decomposition (SVD) [*Marik*, 1998]. The sink distribution and fractionation factors from OH and soil uptake were taken from BOSCAGE-8 and were originally taken from the 3D model (TM2) [*Hein et al.*, 1997]. In addition we incorporated a self-feedback into the sink term of 10% after Hopcroft et al., (2011). This causes a 100% change in source strength to yield a 110% change in concentration. We assumed that the late Holocene changes in temperature, humidity, and volatile organic compounds (VOCs) were not large and their impact on OH can therefore be neglected over this time period. The lifetime of methane was set to 8 years at 1500 C.E. which is broadly consistent with modeling estimates which range from a decrease of 17% to an increase of 16% from the modern lifetime of ~9 years [*Dentener et al.*, 2003; *Harder et al.*, 2007; *Lassey et al.*, 2007; *Martinerie et al.*, 1995; *Prinn et al.*, 2001; *Shindell et al.*, 2003]. The EBAMM source code has been attached to this supplement.

The detailed source scenarios and changes through time are described below. Unless otherwise noted, the natural sources have latitudinal distributions that remain constant throughout the model runs and are listed in Table 3.2. The parameterization of anthropogenic emissions is also described below. Our modeled distribution of sources compares well with more complex models of the pre-industrial latitudinal distribution of sources from Harder et al., (2007) Figure 2b, and also with zonal concentrations modeled in Kaplan et al., (2006) Figure 8. Furthermore we experimented with modifying our latitudinal distributions within reasonable limits and found that our conclusions are not sensitive to slight changes in the baseline latitudinal distribution of sources.

Since EBAMM simulates atmospheric methane concentrations we passed the concentrations from Boxes 1 and 6 through firn air smoothing filters to represent the smoothing of the atmospheric signal through the upper layer of the ice sheet known as the firn (e.g. [*Buizert et al.*, 2011; *Trudinger et al.*, 1997]). The firn air filters were determined with a firn air transport model and are shown in Figure 3.9. The firn air model was calibrated using firn air measurements of reference tracers with known atmospheric history at WAIS and Summit, Greenland. We used Summit to represent GISP2 since there are many more firn air measurements from Summit and since Summit is only ~28 km away from GISP2 and should therefore have similar characteristics. Since this work is focused on changes in methane concentrations which occur on a much longer timescale than the width of the firn smoothing filters, the details of the filters have a negligible effect on our conclusions.

3.7.8 Model Scenarios

We created model scenarios to explore different hypotheses for the late preindustrial Holocene (LPIH) increase in methane concentrations. We first examine latitudinal constraints the IPD imposes on methane sources by calculating the source strength of a limited number of individual boxes. Next we will compare this result to that from a 3-box model. Finally we will discuss two natural (N1 and N2) and two anthropogenic (A1 and A2) scenarios that are based on specific hypotheses for changes in

the LPIH methane sources. For each model run we allowed the model to spin up for 50 years to allow the sources and sinks to reach steady state.

3.7.8.1 Constraining the latitudinal changes in LPIH sources

Since we have two constraints (Greenland and Antarctic concentrations) we can use the global methane budget to solve for two unknown parameters. We can also make use of the modern distribution of sources to provide additional constraints. In addition to the sink distribution and interhemispheric transport constraints discussed earlier, work on the modern distribution of sources has shown that emissions south of 30°S are ~11-15 Tg CH_4/yr and emissions north of 60°N are ~15 Tg CH_4/yr [*Bergamaschi et al.*, 2009; *Fung et al.*, 1991; *Hein et al.*, 1997]. These modern distributions include some anthropogenic sources and provide an upper boundary for LPIH sources from these latitudes.

In Figure 3.10 we show the results from three different Latitudinal Scenarios (L1-3) which are solved with the annually interpolated methane concentrations. In L1 the global methane budget is solved using the tropical NH and SH boxes (box 3 [0-30°S] vs. box 4 [0-30°N]) while all other parameters (sources, sinks, transport) are left constant. It would be surprising if the entire budget was controlled by changes in only tropical sources, so we view this scenario as an end member. In L2 we solved the global methane budget using the combined source strength from the tropical boxes (3-4 [30°S-30°N]) vs. the subtropical NH box 5 [30-60°N]. To do this we assumed a fixed ratio between the tropical boxes with box 3 [0-30°S] accounting for 51% of the tropical emissions and box 4 [0-30°N] accounting for 49% of the tropical emissions. Lastly, in L3 we solved the global methane budget using the combined source strength from the tropical boxes (3-4 [30°S-30°N]) vs. the combined source strength of the NH extratropical boxes (5-6 [30-90°N]). The ratio between the tropical boxes is the same as in L2 and the ratio between the NH extratropical boxes is 76% in box 5 [30-60°N] and 24% in box 6 [60-90°N]. These latitudinal scenarios encompass all the solvable realistic combinations of source emissions that could explain the observations of a globally increasing methane budget while maintaining a roughly constant IPD. They demonstrate that the net source changes

in the late Holocene involved predominantly increasing sources from the tropics and overall constant sources in the extratropical NH with some centennial scale variability. To obtain the "Observed" values in Table 3.1 of the main paper we calculated the change in emissions from 800 BCE to 1400 CE using the linear regression of the calculated emissions through time from L1-3 from each latitude band. We used the linear regression because the lowpass filtered results contained multidecadal scale variability and in this case we are interested in the multicentennial scale change.

Our latitudinal scenarios did not examine scenarios where extratropical SH sources changed because they are a small proportion of the total budget (~5%) and could thus not have had a large impact on LPIH source distributions. Qualitatively, however, if source changes did occur in the extratropical SH they would have to be equal in magnitude but of the opposite sign in the extratropical NH in order to obtain the same IPD and the tropical sources would also respond with the opposite sign in order to maintain the global concentration.

3.7.8.2 Comparison with a 3-box model

It is useful to compare our model results discussed above with a previously published model. In Figure 3.11 we present the results from a 3-box model [*Chappellaz et al.*, 1997]. This model assumes a constant source strength in the SH extratropical regions (30°S-90°S) and then solves for tropical and NH extratropical sources using the global methane budget and the observed polar concentrations. We changed the lifetimes in the boxes to 11.1, 5.9, and 19.5 years for the NH, tropical, and SH boxes respectively (with a global average lifetime of 8.2 years) and the SH source strength to 10 Tg/yr to be consistent with EBAMM parameters. This approach is equivalent to our L3 discussed above when the EBAMM boxes are combined to yield the same zonal regions as the 3 box model. The calculated tropical and NH extratropical emissions are essentially identical which shows that the LPIH increase in emissions must come from tropical regions.

3.7.8.3 Scenarios for LPIH source histories based on estimates from the literature

There are four scenarios discussed in the main text, two having only natural emissions (N1 & N2) [*Konijnendijk et al.*, 2011; *Singarayer et al.*, 2011] and two having constant natural emissions and variable anthropogenic emissions (A1 & A2) [*Houweling et al.*, 2000; *Ruddiman*, 2007]. Since these literature estimates do not all include the same set of base natural sources and in some cases recent research has indicated that previous assumptions about particular sources have been inaccurate, we use a consistent set of base natural sources in all of the scenarios. Our base sources include wild animals (15 Tg/yr), termites (20 Tg/yr), ocean (1 Tg/yr), geologic (30 Tg/yr), and biomass burning (25 Tg/yr). The estimate for wild animals and termite emissions come from Houweling et al., (2000). The estimate for ocean emissions comes from Rhee et al., (2009). Recent estimates of geologic and biomass burning emissions vary widely so we have chosen emissions that are roughly in the middle of previous estimates and which also balance the $\delta^{13}CH_4$ budget [*Etiope et al.*, 2008a; *Etiope et al.*, 2008b; *Ferretti et al.*, 2005; *Mischler et al.*, 2009; *Sapart et al.*, 2012] (Figure 3.13). The latitudinal distribution of these natural emissions is shown in Table 3.2. Additionally, in A1-2 we use the estimate for rice agriculture, domestic ruminants, and landfills from the literature cited. For each of these scenarios we first adjust our model's tropical vs. boreal wetland source strength so that the total source distribution produces the correct concentration and IPD values at ~1400 CE. Then for scenarios N1-2 we use the anomaly of the wetland source from the literature estimate to drive the scenario through time. In scenarios A1-2 the change in anthropogenic emissions is driven by changes in population (described in greater detail below). The concentration and IPD from these model runs are shown in Figure 3.2 and Table 3.1 of the main text and the emissions for each model run are plotted in Figure 3.12.

3.7.8.3.1 Scenario N1: TRENCH wetland emissions from *Konijnendijk et al.*, [2011]

TRENCH (TRansient Emissions of Natural CH_4) is a coarse grid transient model forced by global ice volume, greenhouse gases, and insolation and was used to estimate orbital timescale variations in global wetland emissions over the past 650 ka [*Konijnendijk et al.*, 2011]. TRENCH used the climate output from the CLIMAte and BiosphERe model (CLIMBER-2, [*Petoukhov et al.*, 2000]) which contained atmosphere, ocean, and vegetation components. These models have a resolution of 10° latitude by 51.43° longitude and we combined the emissions from this grid into 30° zonal bands to match the resolution of EBAMM.

3.7.8.3.2 Scenario N2: Natural emissions from *Singarayer et al.*, [2011]

Singarayer et al., (2011) produced model snapshots at 1 ka intervals over the past 130 ka using the coupled ocean-atmosphere Hadley Centre climate model (HadCM3) and then used the resulting climatologies as input to the Sheffield Dynamic Global Vegetation Model (SDGVM) coupled to a wetland methane emission model that predicts the location of vegetation, wetlands, methane emissions, and Volatile Organic Compound (VOC) emissions. In addition to wetlands the SDGVM has a fire module which contributes to methane emissions from biomass burning. Their models are forced by varying orbital configurations, greenhouse gases (CO_2, CH_4, and N_2O), ice sheet extent and sea level. Since we are primarily interested in the changing latitudinal distribution of sources, we placed all of the methane emissions in the "wetlands" category of EBAMM. We combined the emissions from the original model grid into 30° zonal bands to match the resolution of EBAMM.

3.7.8.3.3 Scenario A1: Natural and anthropogenic emissions after *Houweling et al.*, [2000]

Houweling et al., (2000) provide a holistic estimate of the pre-industrial methane budget in order to constrain the magnitude of wetland methane emissions. Their study

focuses on the average concentration between 1500-1800 C.E. and many of the individual source estimates are for the year 1500 C.E. To get the model to produce the correct concentration and IPD values at 1400 CE we set tropical wetlands to 128 Tg/yr and boreal wetlands to 31 Tg/yr yielding total wetland emissions of 159 Tg/yr. This compares well with their estimate of 163 Tg/yr (± 2σ range of 130-194 Tg/yr). We coupled the latitudinal distribution of anthropogenic sources to the time dependent latitudinal distribution of population by binning global population from the HYDE 3.1 database [*Goldewijk et al.*, 2010; *Goldewijk et al.*, 2011] into the 30° zonal distribution of EBAMM, then interpolating those values for each time step and, finally, normalizing this to the global total population at that time step. The strength of the anthropogenic source is then multiplied by these normalized values to obtain the latitudinal distribution of each source at each time step. Since there is no evidence of pre-industrial rice emissions outside of Asia, we have treated this source separately from other anthropogenic emissions and binned population from 60-140°E and 10°S-50°N [*Fuller et al.*, 2011] into EBAMM boxes 3, 4 and 5 and used this distribution for rice emissions in the same manner as for other global anthropogenic emissions. We also examined the impact of using our per-capita scaling for anthropogenic biomass burning emissions (Figure 3.13). We find that scaling anthropogenic biomass burning to population causes $\delta^{13}CH_4$ to become less depleted through time which is inconsistent with the ice core $\delta^{13}CH_4$ data from Greenland (NEEM [*Sapart et al.*, 2012]) and Antarctica (WDC05A [*Mischler et al.*, 2009]; Law Dome [*Ferretti et al.*, 2005]). As noted previously [*Sapart et al.*, 2012], the long term late Holocene change in $\delta^{13}CH_4$ is consistent with a predominantly biogenic increase in sources. By leaving all (natural and anthropogenic) biomass burning emissions constant we are able to fit the millennial scale $\delta^{13}CH_4$ trend which in the model is caused by increasing emissions from wetlands and rice.

3.7.8.3.4 Scenario A2: Natural and anthropogenic emissions after *Ruddiman* [2007]

The early anthropogenic hypothesis provides an upper level estimate of anthropogenic emissions in the LPIH. This scenario is based on estimates of emissions from Table 5 in *Ruddiman* [2007] and we used the rice agriculture upper limit of 32 Tg/yr in 1500 CE. The per-capita scaling scheme is the same as in Scenario A1. As in previous scenarios, we then use tropical and boreal wetland emissions to adjust the concentration and IPD to fit the data at 1400 CE. This yields tropical wetland emissions of 109 Tg/yr and boreal wetland emissions of 7 Tg/yr for total wetland emissions of 116 Tg/yr at 1500 CE. We again do not include anthropogenic biomass burning because of its impact on the modeled $\delta^{13}CH_4$.

The full early anthropogenic hypothesis includes decreasing natural sources and uses increasing anthropogenic sources to balance the budget. However, this decrease in natural emissions is not predicted by either of the models incorporating only natural emissions. Also, if natural emissions were decreasing, there would need to be an even larger increase in anthropogenic emissions with time. This could only be possible through large changes in per-capita emissions, the analysis of which is beyond the scope of the present work. It would also give the IPD a positive slope which is not supported by the data (unless the decrease in natural emissions was in boreal latitudes). We have therefore opted to keep natural sources constant in this scenario to illustrate the effect that increasing anthropogenic emissions would have on the concentrations and IPD.

3.7.8.3.5 Scenario Best

This scenario is described in the main text. It contains intermediate anthropogenic emissions (24 Tg/yr at 1500 C.E.) and the natural emissions from N2. We increased the tropical SH (Box 3) emissions by 1.7 times to attain the emissions levels indicated by L1-3.

3.7.9 References

Alley, R. B., et al. (1997), Visual-stratigraphic dating of the GISP2 ice core: Basis, reproducibility, and application, *J. Geophys. Res.-Oceans*, *102*(C12), 26367-26381.

Bates, T. S., K. C. Kelly, J. E. Johnson, and R. H. Gammon (1996), A reevaluation of the open ocean source of methane to the atmosphere, *J. Geophys. Res.-Atmos.*, *101*(D3), 6953-6961.

Battle, M. O., J. P. Severinghaus, E. D. Sofen, D. Plotkin, A. J. Orsi, M. Aydin, S. A. Montzka, T. Sowers, and P. P. Tans (2011), Controls on the movement and composition of firn air at the West Antarctic Ice Sheet Divide, *Atmos. Chem. Phys.*, *11*(21), 11007-11021.

Bergamaschi, P., et al. (2009), Inverse modeling of global and regional CH4 emissions using SCIAMACHY satellite retrievals, *J. Geophys. Res.-Atmos.*, *114*.

Buizert, C., T. Sowers, and T. Blunier (2013), Assessment of diffusive isotopic fractionation in polar firn, and application to ice core trace gas records, *Earth and Planetary Science Letters*, *361*(0), 110-119.

Buizert, C., et al. (2011), Gas transport in firn: multiple-tracer characterisation and model intercomparison for NEEM, Northern Greenland, *Atmos. Chem. Phys. Discuss.*, *11*(5), 15975-16021.

Buizert, C., et al. (2012), Gas transport in firn: multiple-tracer characterisation and model intercomparison for NEEM, Northern Greenland, *Atmos. Chem. Phys.*, *12*(9), 4259-4277.

Chappellaz, J., T. Blunier, S. Kints, A. Dallenbach, J. M. Barnola, J. Schwander, D. Raynaud, and B. Stauffer (1997), Changes in the atmospheric CH_4 gradient between Greenland and Antarctica during the Holocene, *J. Geophys. Res.-Atmos.*, *102*(D13), 15987-15997.

Craig, H., Y. Horibe, and T. Sowers (1988), Gravitational Separation of Gases and Isotopes in Polar Ice Caps, *Science*, *242*(4886), 1675-1678.

Cuffey, K. M., and G. D. Clow (1997), Temperature, accumulation, and ice sheet elevation in central Greenland through the last deglacial transition, *J. Geophys. Res.-Oceans*, *102*(C12), 26383-26396.

Cuffey, K. M., and W. Paterson (2010), *The physics of glaciers*, Academic Press.

de Boor, C. (2001), *A Practical Guide to Splines*, Springer, New York.

Dentener, F., W. Peters, M. Krol, M. van Weele, P. Bergamaschi, and J. Lelieveld (2003), Interannual variability and trend of CH4 lifetime as a measure for OH changes in the 1979-1993 time period, *J. Geophys. Res.-Atmos.*, *108*(D15).

Dlugokencky, E. J., P. M. Lang, A. M. Crotwell, and K. A. Masaire (2012), Atmospheric Methane Dry Air Mole Fractions from the NOAA ESRL Carbon Cycle Cooperative Global Air Sampling Network, 1983-2011, Version: 2012-09-24, Path: ftp://ftp.cmdl.noaa.gov/ccg/ch4/flask/event/, edited.

Dlugokencky, E. J., K. A. Masarie, P. M. Lang, P. P. Tans, L. P. Steele, and E. G. Nisbet (1994), A dramatic decrease in the growth rate of atmospheric methane in the northern hemisphere during 1992, *Geophys. Res. Let.*, *21*(1), 45-48.

Dlugokencky, E. J., R. C. Myers, P. M. Lang, K. A. Masarie, A. M. Crotwell, K. W. Thoning, B. D. Hall, J. W. Elkins, and L. P. Steele (2005), Conversion of NOAA atmospheric dry air CH_4 mole fractions to a gravimetrically prepared standard scale, *J. Geophys. Res.-Atmos.*, *110*(D18), 8.

Etheridge, D. M., L. P. Steele, R. J. Francey, and R. L. Langenfelds (1998), Atmospheric methane between 1000 AD and present: Evidence of anthropogenic emissions and climatic variability, *J. Geophys. Res.-Atmos.*, *103*(D13), 15979-15993.

Etiope, G., A. V. Milkov, and E. Derbyshire (2008a), Did geologic emissions of methane play any role in Quaternary climate change?, *Glob. Planet. Change*, *61*(1-2), 79-88.

Etiope, G., K. R. Lassey, R. W. Klusman, and E. Boschi (2008b), Reappraisal of the fossil methane budget and related emission from geologic sources, *Geophys. Res. Let.*, *35*(9).

Fegyveresi, J. M., R. B. Alley, M. K. Spencer, J. J. Fitzpatrick, E. J. Steig, J. W. C. White, J. R. McConnell, and K. C. Taylor (2011), Late-Holocene climate evolution at the WAIS Divide site, West Antarctica: bubble number-density estimates, *J. of Glaciol.*, *57*(204), 629-638.

Ferretti, D. F., et al. (2005), Unexpected Changes to the Global Methane Budget over the Past 2000 Years, *Science*, *309*(5741), 1714-1717.

Fuller, D. Q., J. van Etten, K. Manning, C. Castillo, E. Kingwell-Banham, A. Weisskopf, L. Qin, Y. I. Sato, and R. J. Hijmans (2011), The contribution of rice agriculture and livestock pastoralism to prehistoric methane levels: An archaeological assessment, *Holocene*, *21*(5), 743-759.

Fung, I., J. John, J. Lerner, E. Matthews, M. Prather, L. P. Steele, and P. J. Fraser (1991), 3-Dimensional Model Synthesis of the Global Methane Cycle, *J. Geophys. Res.-Atmos.*, *96*(D7), 13033-13065.

Goldewijk, K. K., A. Beusen, and P. Janssen (2010), Long-term dynamic modeling of global population and built-up area in a spatially explicit way: HYDE 3.1, *Holocene*, *20*(4), 565-573.

Goldewijk, K. K., A. Beusen, G. van Drecht, and M. de Vos (2011), The HYDE 3.1 spatially explicit database of human-induced global land-use change over the past 12,000 years, *Glob. Ecol. Biogeogr.*, *20*(1), 73-86.

Grachev, A. M., E. J. Brook, and J. P. Severinghaus (2007), Abrupt changes in atmospheric methane at the MIS 5b-5a transition, *Geophys. Res. Let.*, *34*(20), 5.

Grachev, A. M., E. J. Brook, J. P. Severinghaus, and N. G. Pisias (2009), Relative timing and variability of atmospheric methane and GISP2 oxygen isotopes between 68 and 86 ka, *Glob. Biogeochem. Cycle*, *23*, 10.

Harder, S. L., D. T. Shindell, G. A. Schmidt, and E. J. Brook (2007), A global climate model study of CH_4 emissions during the Holocene and glacial-interglacial transitions constrained by ice core data, *Glob. Biogeochem. Cycle*, *21*(1), 13.

Hein, R., P. J. Crutzen, and M. Heimann (1997), An inverse modeling approach to investigate the global atmospheric methane cycle, *Glob. Biogeochem. Cycle*, *11*(1), 43-76.

Herron, M. M., and C. C. Langway (1980), Firn Densification: An Empirical Model, *J. of Glaciol.*, *25*(93), 373-385.

Hopcroft, P. O., P. J. Valdes, and D. J. Beerling (2011), Simulating idealized Dansgaard-Oeschger events and their potential impacts on the global methane cycle, *Quat. Sci. Rev.*, *30*(23-24), 3258-3268.

Houweling, S., F. Dentener, and J. Lelieveld (2000), Simulation of preindustrial atmospheric methane to constrain the global source strength of natural wetlands, *J. Geophys. Res.-Atmos.*, *105*(D13), 17243-17255.

Kaplan, J. O., G. Folberth, and D. A. Hauglustaine (2006), Role of methane and biogenic volatile organic compound sources in late glacial and Holocene fluctuations of atmospheric methane concentrations, *Glob. Biogeochem. Cycle*, *20*(2), 16.

Kobashi, T., J. P. Severinghaus, J. M. Barnola, K. Kawamura, T. Carter, and T. Nakaegawa (2010), Persistent multi-decadal Greenland temperature fluctuation through the last millennium, *Clim. Change*, *100*(3-4), 733-756.

Kobashi, T., K. Kawamura, J. P. Severinghaus, J. M. Barnola, T. Nakaegawa, B. M. Vinther, S. J. Johnsen, and J. E. Box (2011), High variability of Greenland surface temperature over the past 4000 years estimated from trapped air in an ice core, *Geophys. Res. Let.*, *38*.

Konijnendijk, T. Y. M., S. L. Weber, E. Tuenter, and M. van Weele (2011), Methane variations on orbital timescales: a transient modeling experiment, *Clim. Past.*, *7*(2), 635-648.

Lassey, K. R., D. M. Etheridge, D. C. Lowe, A. M. Smith, and D. F. Ferretti (2007), Centennial evolution of the atmospheric methane budget: what do the carbon isotopes tell us?, *Atmos. Chem. Phys.*, *7*(8), 2119-2139.

MacFarling Meure, C., D. Etheridge, C. Trudinger, P. Steele, R. Langenfelds, T. van Ommen, A. Smith, and J. Elkins (2006), Law Dome CO_2, CH_4 and N_2O ice core records extended to 2000 years BP, *Geophys. Res. Let.*, *33*(14), 4.

Marik, T. (1998), Atmospheric $d^{13}C$ and dD measurements to balance the global methane budget, Ph.D. thesis, University of Heidelberg, Heidelberg, Germany.

Martinerie, P., G. P. Brasseur, and C. Granier (1995), The chemical composition of ancient atmospheres: A model study constrained by ice core data, *J. Geophys. Res.-Atmos.*, *100*(D7), 14291-14304.

Mayewski, P. A., L. D. Meeker, M. S. Twickler, S. Whitlow, Q. Z. Yang, W. B. Lyons, and M. Prentice (1997), Major features and forcing of high-latitude northern hemisphere atmospheric circulation using a 110,000-year-long glaciochemical series, *J. Geophys. Res.-Oceans*, *102*(C12), 26345-26366.

Meese, D. A., A. J. Gow, P. Grootes, P. A. Mayewski, M. Ram, M. Stuiver, K. C. Taylor, E. D. Waddington, and G. A. Zielinski (1994), The Accumulation Record from the GISP2 Core as an Indicator of Climate Change Throughout the Holocene, *Science*, *266*(5191), 1680-1682.

Mischler, J. A., T. A. Sowers, R. B. Alley, M. Battle, J. R. McConnell, L. Mitchell, T. Popp, E. Sofen, and M. K. Spencer (2009), Carbon and hydrogen isotopic composition of methane over the last 1000 years, *Glob. Biogeochem. Cycle*, *23*.

Mitchell, L. E., E. J. Brook, T. Sowers, J. R. McConnell, and K. Taylor (2011), Multidecadal variability of atmospheric methane, 1000-1800 CE, *J. Geophys. Res.-Biogeosci.*, *116*.

Orsi, A. J., B. D. Cornuelle, and J. P. Severinghaus (2012), Little Ice Age cold interval in West Antarctica: Evidence from borehole temperature at the West Antarctic Ice Sheet (WAIS) Divide, *Geophys. Res. Let.*, *39*(9), L09710.

Petoukhov, V., A. Ganopolski, V. Brovkin, M. Claussen, A. Eliseev, C. Kubatzki, and S. Rahmstorf (2000), CLIMBER-2: a climate system model of intermediate complexity. Part I: model description and performance for present climate, *Clim. Dyn.*, *16*(1), 1-17.

Prinn, R. G., et al. (2001), Evidence for Substantial Variations of Atmospheric Hydroxyl Radicals in the Past Two Decades, *Science*, *292*(5523), 1882-1888.

Rhee, T. S., A. J. Kettle, and M. O. Andreae (2009), Methane and nitrous oxide emissions from the ocean: A reassessment using basin-wide observations in the Atlantic, *J. Geophys. Res.-Atmos.*, *114*.

Rhodes, R. H., X. Faïn, C. Stowasser, T. Blunier, J. Chappellaz, J. R. McConnell, L. E. Mitchell, and E. Brook (Submitted), Continuous ice core methane measurements: atmospheric and in-situ signals, *Earth and Planetary Science Letters*.

Rohde, R. A., P. B. Price, R. C. Bay, and N. E. Bramall (2008), In situ microbial metabolism as a cause of gas anomalies in ice, *Proc. Natl. Acad. Sci. U. S. A.*, *105*(25), 8667-8672.

Ruddiman, W. F. (2007), The early anthropogenic hypothesis: Challenges and responses, *Reviews of Geophysics*, *45*(3), 37.

Sapart, C. J., et al. (2012), Natural and anthropogenic variations in methane sources during the past two millennia, *Nature*, *490*(7418), 85-88.

Schilt, A., et al. (2010), Atmospheric nitrous oxide during the last 140,000 years, *Earth and Planetary Science Letters*, *300*(1-2), 33-43.

Schwander, J. (1989), The transformation of snow to ice and the occlusion of gases, in *The Environmental Record in Glaciers and Ice Sheets*, edited by H. Oeschger and C. C. Langway, pp. 53-67, John Wiley, Chichester [England] ; New York :.

Shindell, D. T., G. Faluvegi, and N. Bell (2003), Preindustrial-to-present-day radiative forcing by tropospheric ozone from improved simulations with the GISS chemistry-climate GCM, *Atmos. Chem. Phys.*, *3*, 1675-1702.

Singarayer, J. S., P. J. Valdes, P. Friedlingstein, S. Nelson, and D. J. Beerling (2011), Late Holocene methane rise caused by orbitally controlled increase in tropical sources, *Nature*, *470*(7332), 82-U91.

Sowers, T., M. Bender, and D. Raynaud (1989), Elemental and Isotopic Composition of Occluded O_2 and N_2 in Polar Ice, *J. Geophys. Res.-Atmos.*, *94*(D4), 5137-5150.

Sowers, T., M. Bender, D. Raynaud, and Y. S. Korotkevich (1992), $d^{15}N$ of N_2 in Air Trapped in Polar Ice: a Tracer of Gas Transport in the Fim and a Possible Constraint on Ice Age-Gas Age Differences, *J. Geophys. Res.-Atmos.*, *97*(D14), 15683-15697.

Trudinger, C. M., I. G. Enting, D. M. Etheridge, R. J. Francey, V. A. Levchenko, L. P. Steele, D. Raynaud, and L. Arnaud (1997), Modeling air movement and bubble trapping in firn, *J. Geophys. Res.-Atmos.*, *102*(D6), 6747-6763.

Witrant, E., et al. (2011), A new multi-gas constrained model of trace gas non-homogeneous transport in firn: evaluation and behavior at eleven polar sites, *Atmos. Chem. Phys. Discuss.*, *11*(8), 23029-23080.

Zhuang, Q., J. M. Melillo, D. W. Kicklighter, R. G. Prinn, A. D. McGuire, P. A. Steudler, B. S. Felzer, and S. Hu (2004), Methane fluxes between terrestrial ecosystems and the atmosphere at northern high latitudes during the past century: A retrospective analysis with a process-based biogeochemistry model, *Glob. Biogeochem. Cycle*, *18*(3).

3.7.10 Figures

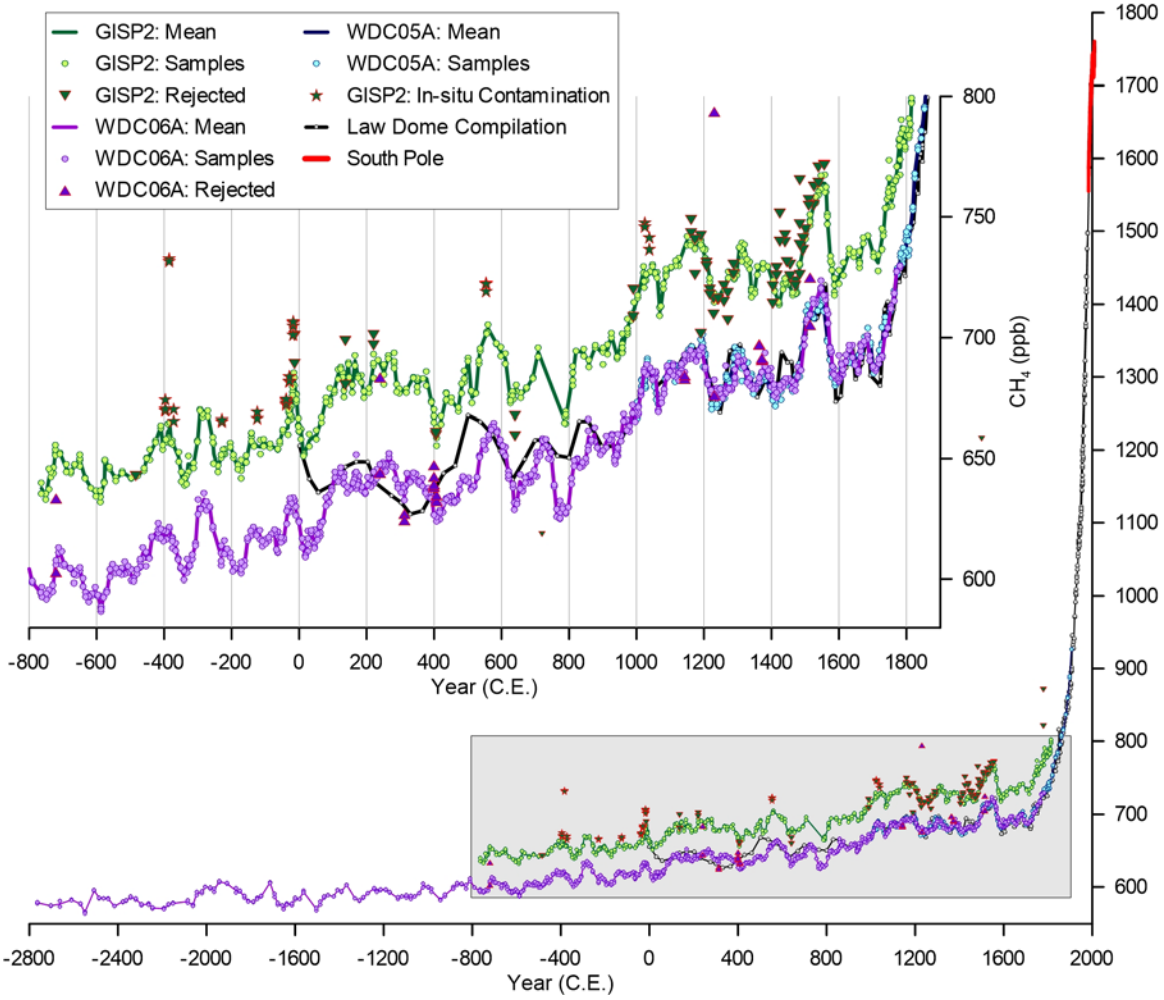

Figure 3.3. Methane measurements from GISP2 (green), WAIS Divide (the main borehole WDC06A [purple] and the shallow borehole WDC05A [blue] [*Mitchell et al.*, 2011]), Law Dome (black) [*Etheridge et al.*, 1998; *MacFarling Meure et al.*, 2006], and South Pole (red) [*Dlugokencky et al.*, 2012]. Circles represent individual samples and the line is linearly interpolated through the mean concentration from each depth/age. The WAIS Divide records are on a gas-age chronology derived from the WDC06A-7 layer counted ice-age chronology (Fudge et al., (*in review*)) and a dynamic firn air densification model. The GISP2 timescale has been optimized to match the WAIS Divide timescale using an iterative Monte Carlo correlation technique. Also shown are rejected samples (WAIS: upwards pointing triangles, GISP: downwards pointing triangles) and GISP2 samples which we suspect of containing in-situ contamination (stars). All methane measurements are plotted on the NOAA04 calibration scale [*Dlugokencky et al.*, 2005]. Shaded box indicates the time period for this study.

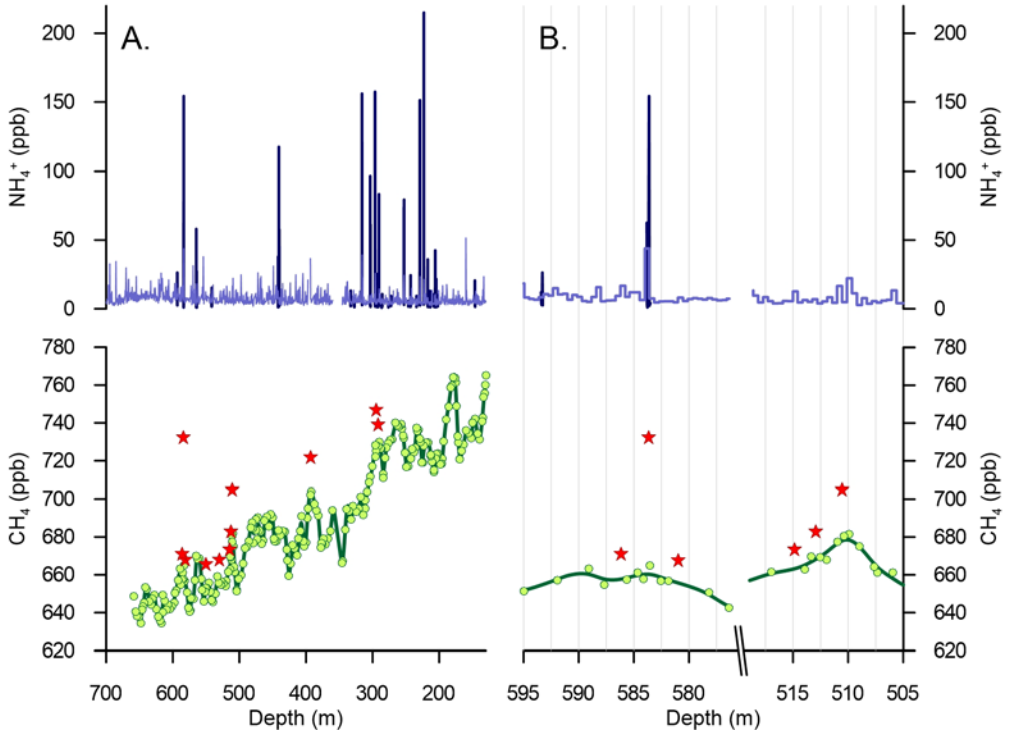

Figure 3.4. GISP2 CH_4 and NH_4^+ [*Mayewski et al.*, 1997] records in the late pre-industrial Holocene (A.), and detailed views of samples at ~510 and ~585m (B.). The line between the data points in (B.) is a spline fit to the data as discussed in the text.

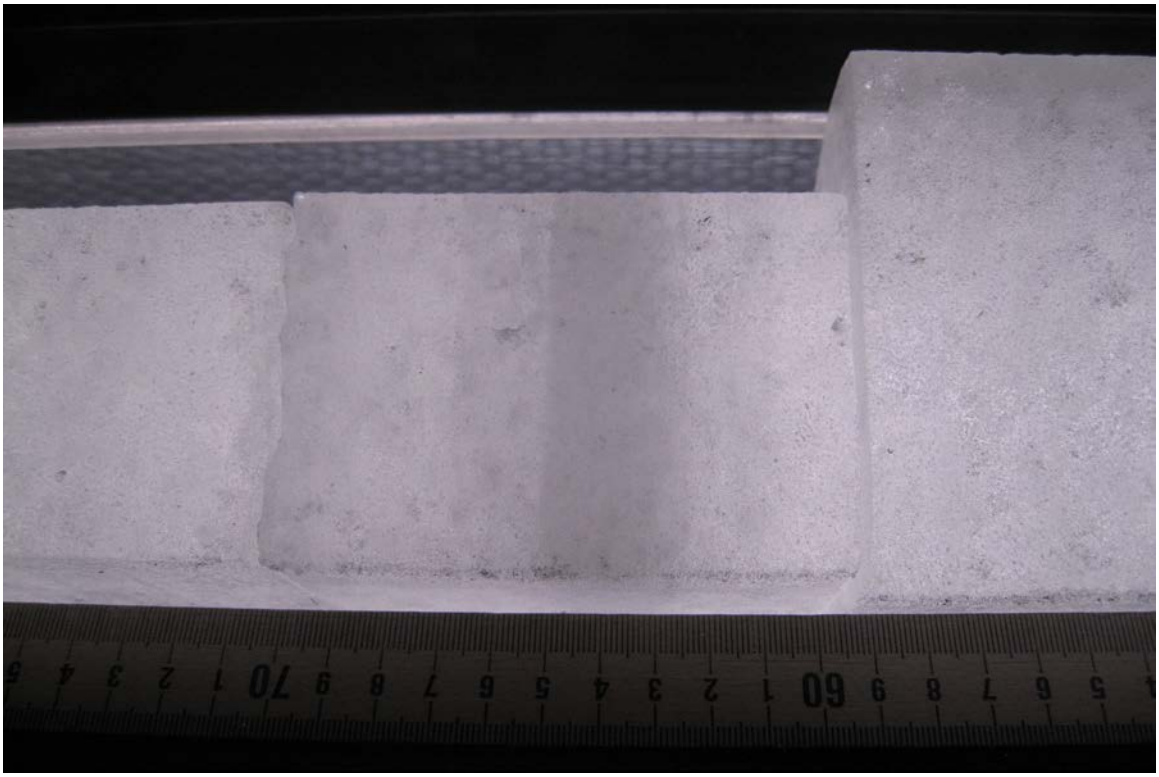

Figure 3.5. Cloudy band in the GISP2 methane sample which had methane concentrations ~70 ppb higher than nearby samples. The sample depths are 583.6-583.7 m and the cloudy band associated with the NH_4^+ spike is visible from 583.63-583.65 m.

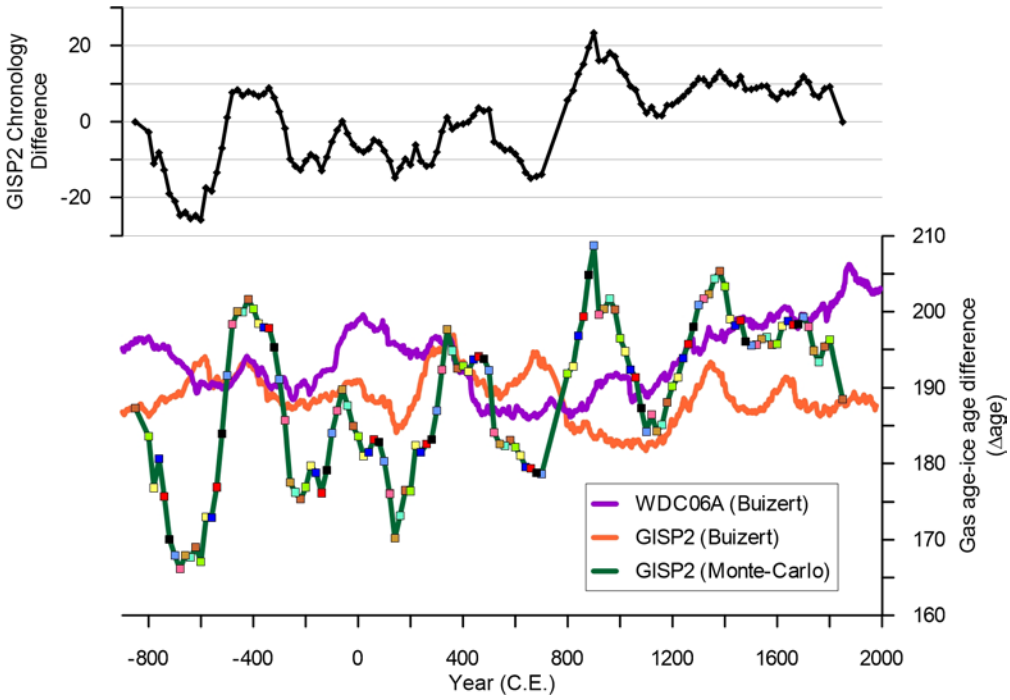

Figure 3.6. The difference between the GISP2 (Buizert) and GISP2 (Monte-Carlo) chronologies (top) and Gas age-ice age difference (Δage) for the GISP2 and WAIS Divide ice cores (bottom). Gas age chronologies for "GISP2 (Buizert)" (orange) and "WDC06A (Buizert)" (purple) were determined with a dynamic firn air model. Our "GISP2 (Monte-Carlo)" (green with symbols) chronology has 10 different symbol colors corresponding to the tie points of the 10 different iterative Monte Carlo chronologies which each have a spacing of 200 years. The combined chronology thus has tie points which are spaced 20 years apart.

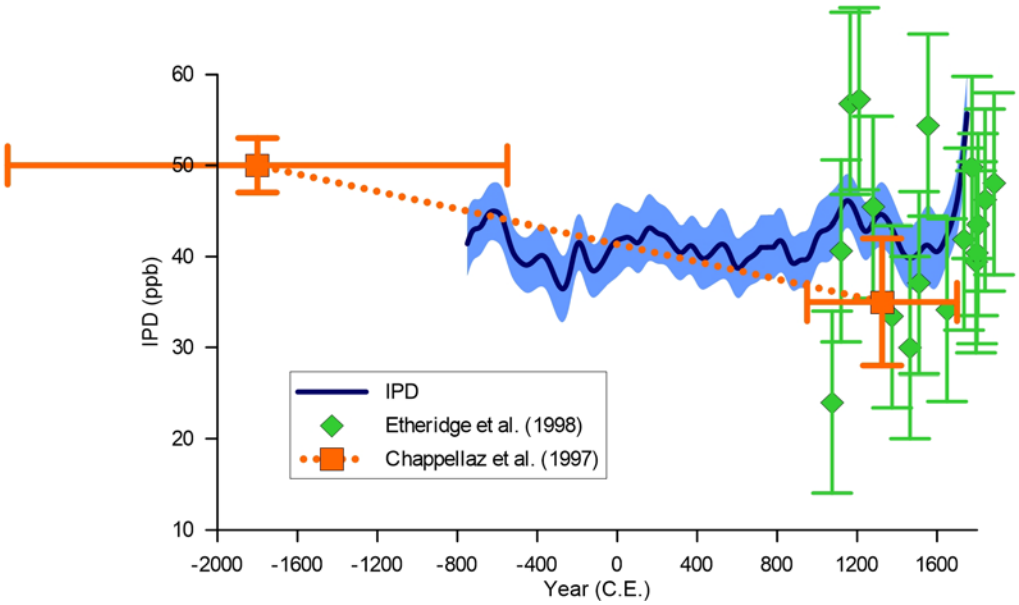

Figure 3.7. Comparison with previously published estimates of the late Holocene IPD [*Chappellaz et al.*, 1997; *Etheridge et al.*, 1998]. Our IPD record has been smoothed with a 100 year lowpass filter and the shaded 2σ error was determined with a Monte Carlo procedure (SOM). Horizontal line indicates the mean IPD.

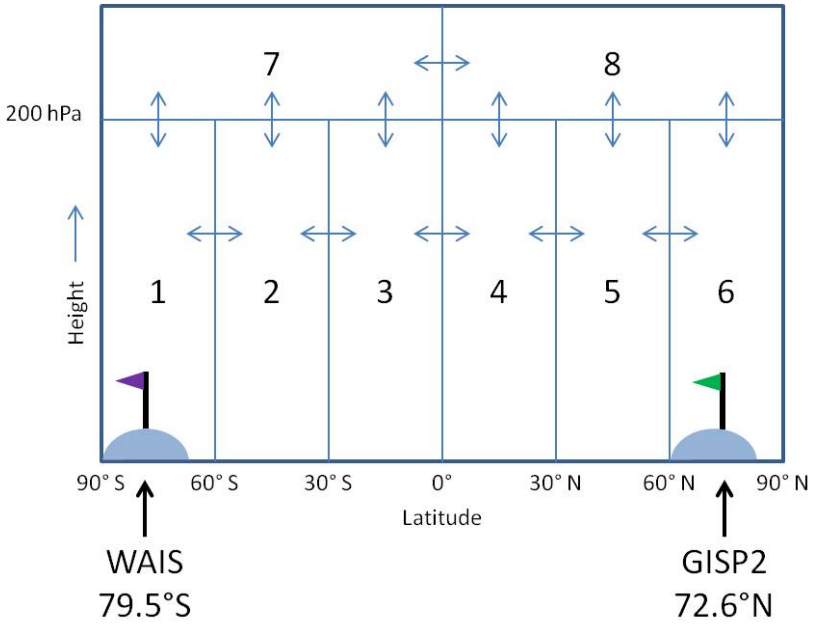

Figure 3.8. Schematic diagram of the EBAMM model space. There are 6 tropospheric boxes and two stratospheric boxes separated by the tropopause at 200 hPa. We take Box 1 and Box 6 to represent the concentrations of WAIS Divide and GISP2, respectively.

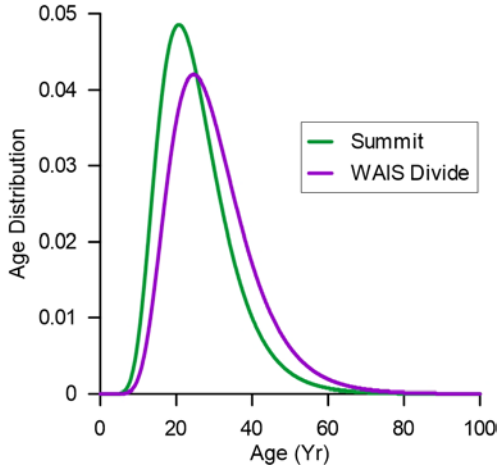

Figure 3.9. Age distribution for Summit Greenland and WAIS Divide. Summit, Greenland was used instead of GISP2 because of the availability of many trace gases being measured in the Summit firn air. The Summit ice core is ~28 km away from GISP2 and should therefore have very similar smoothing characteristics.

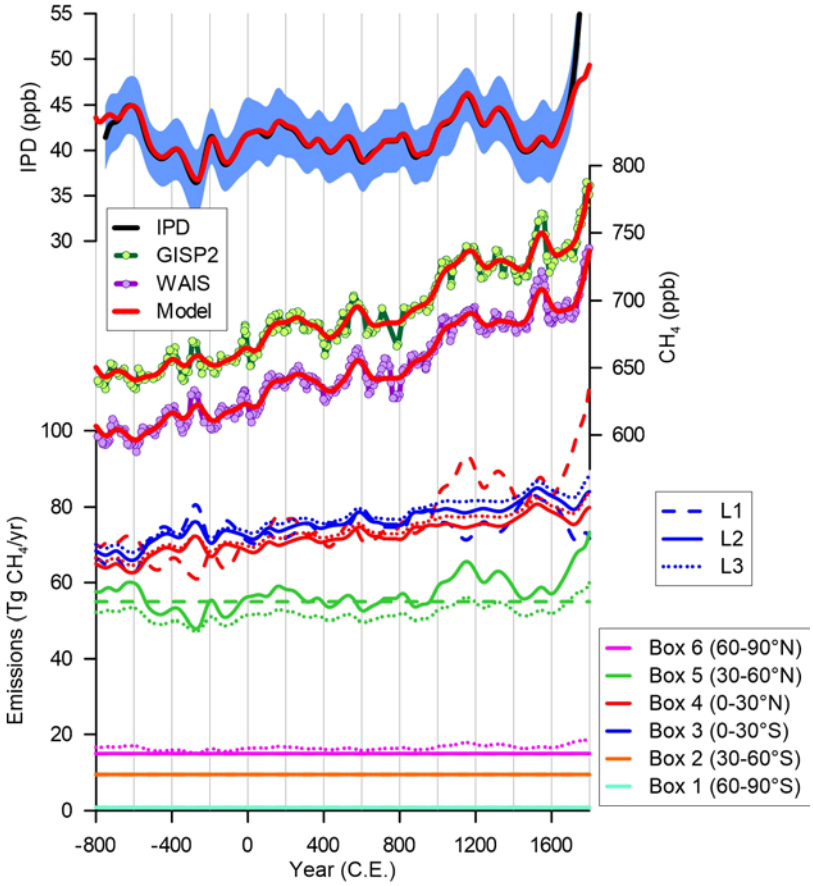

Figure 3.10. EBAMM latitude scenarios 1-3 (L1-3). Each of the 3 scenarios obtains the same concentration and IPD results. The colors correspond to EBAMM boxes while the pattern of the line indicates scenarios L1-3.

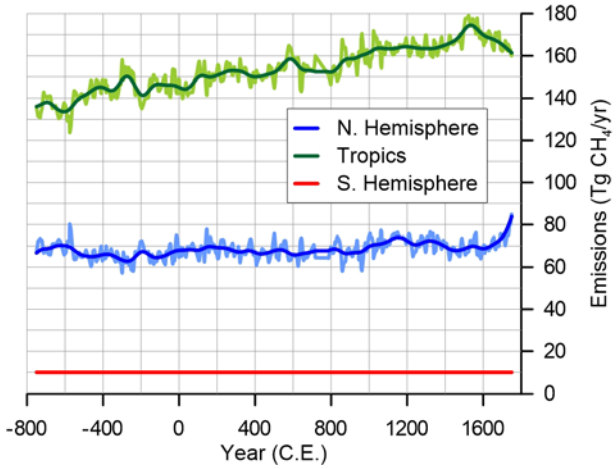

Figure 3.11. 3 box model results. Model is described in [*Chappellaz et al.*, 1997]. The light lines are the model results solved for the annually interpolated data and the darker lines are the model results solved for the 100 year lowpass filtered results.

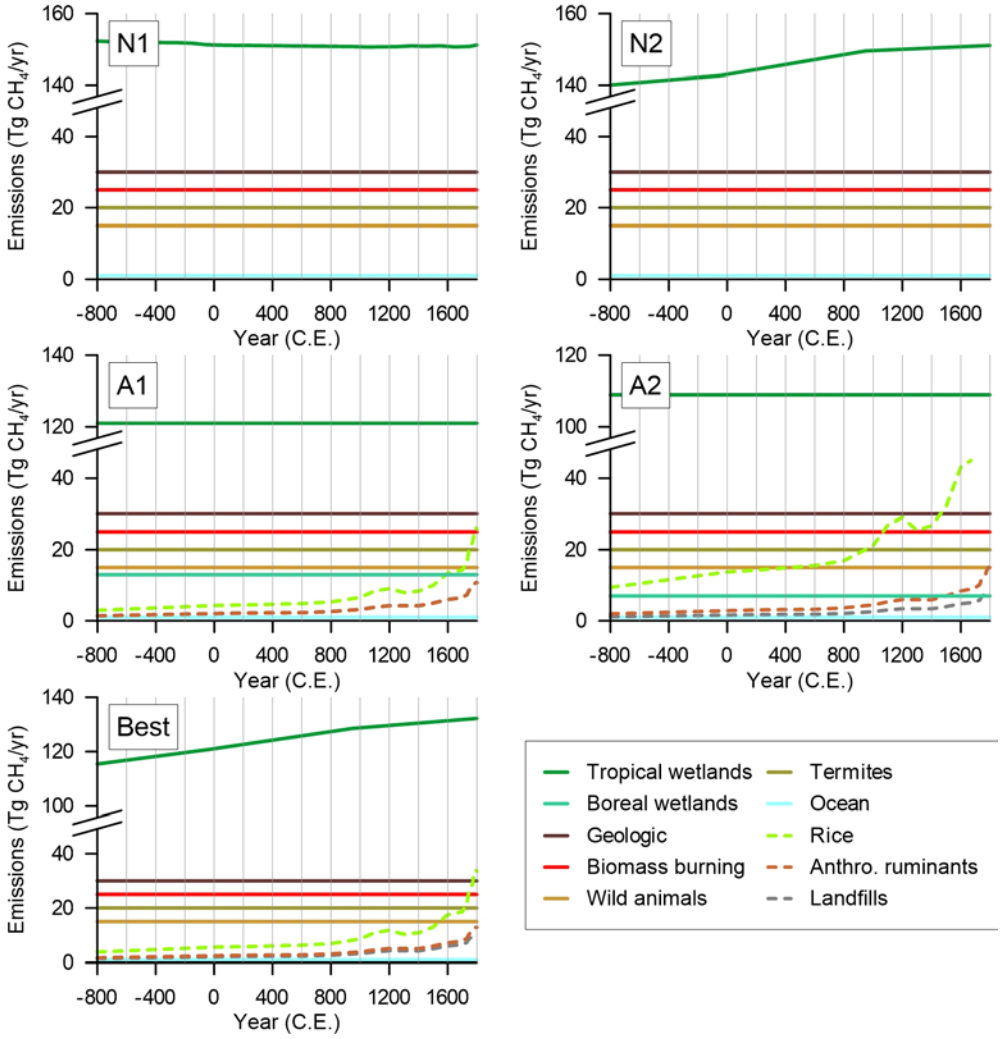

Figure 3.12. Emissions for scenarios N1-2 and A1-2 from Figure 3.2 of the main text. Note the broken vertical axes. Latitudinal distributions of natural sources are specified in Table 3.2 and are described for anthropogenic emissions under the description for Scenario A1. In scenarios N1-2 all of the wetland emissions are combined into one "wetlands" source, however scenarios A1-2 have both a "Tropical wetland" and "Boreal wetland" source.

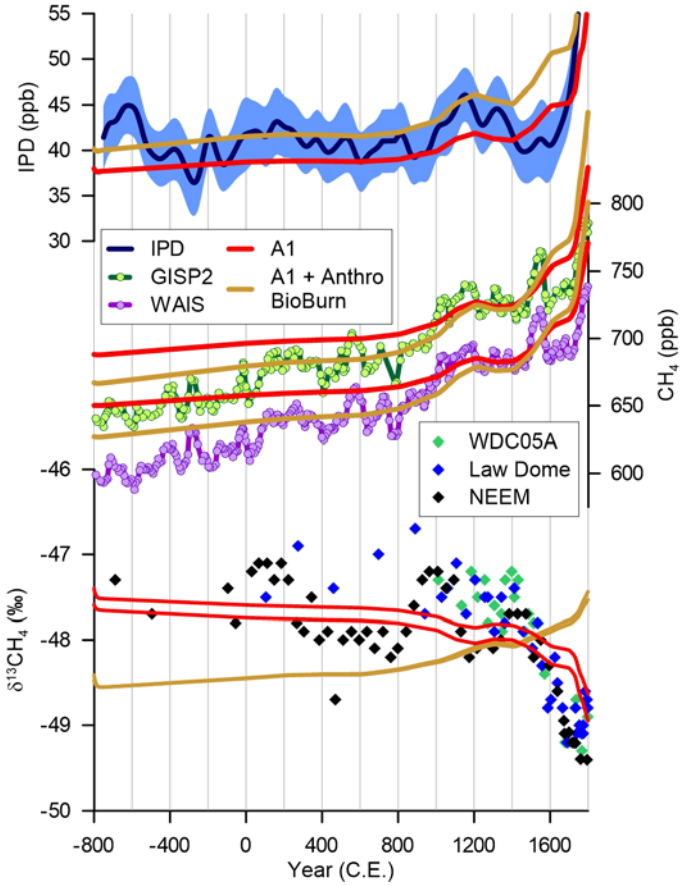

Figure 3.13 – Model results from Scenario A1 if biomass burning emissions are included. In this modified scenario we set natural biomass burning emissions to 15 Tg/yr (instead of 25 Tg/yr in our base scenario) and anthropogenic biomass burning emissions to 10 Tg/yr in the year 1500 CE [*Houweling et al.*, 2000] and allow our per-capita scaling technique to change emissions through time.

3.7.11 Tables

Table 3.2. Latitudinal distribution of natural sources in EBAMM (% of total)

Source	90-60°S	60-30°S	30S-0°	0-30°N	30-60°N	60-90°N
Boreal Wetlands [a]	0	0	0	0	59	41
Tropical Wetlands [b]	0	2.9	50.2	38.4	8.2	0
Wild Animals [b]	0	5	18.7	41.1	35.2	0
Termites [c]	0	2.3	40.5	37.1	2	0
Biomass Burning [b]	0	0.2	56	43.9	0	0
Ocean [d]	0	21	47	32	0	0
Geologic [e]	0	0	4.9	7.4	62.2	25.1

[a] – [*Zhuang et al.*, 2004]
[b] – BOSCAGE-8 [*Marik*, 1998]
[c] – [*Fung et al.*, 1991]
[d] – [*Bates et al.*, 1996]
[e] – Global Onshore Gas-Oil Seeps Dataset (GLOGOS) (version APR11) Etiope, G., (Personal Communication, 2012)

Observing and modeling the influence of layering on bubble trapping in polar firn

Logan Mitchell [1], Christo Buizert [1], Edward Brook [1], Daniel Breton [2], John Fegyveresi [3], Daniel Baggenstos [4], Anais Orsi [4], Jeffrey Severinghaus [4], Richard Alley [3], Mary Albert [2], Jinho Ahn [5], Stephanie Gregory [2]

[1] Oregon State University, Department of Geosciences, Corvallis, OR 97331

[2] University of Maine, Department of Physics and Astronomy, Orono, ME 04469, and, University of Maine, Climate Change Institute, Orono, ME 04469

[3] Department of Geosciences, and Earth and Environmental Systems Institute, Pennsylvania State University, University Park, PA 16802

[4] Scripps Institution of Oceanography, University of California, San Diego, CA 92093-0244, USA

[5] School of Earth and Environmental Sciences, Seoul National University, Seoul, South Korea.

Prepared for submission to Climate of the Past.

4.1 Abstract

Interpretation of ice core trace gas records depends on an accurate understanding of the processes that smooth the atmospheric signal in the firn. Much work has been done to understand the processes affecting air transport in the open porosity, but a paucity of data from the closed porosity in the firn-ice transition region has limited the ability to constrain the effect of bubble closure processes. Here we present high-resolution measurements of firn density, methane mixing ratios, nitrogen isotopes, and total air content that all show evidence for strong layering in the firn-ice transition region at the WAIS Divide ice core site in West Antarctica. These measurements are used to show that common parameterizations of the bubble closure process have not accounted for high frequency density variability in the firn. We present a new parameterization that accounts for layering and discuss the implications for the interpretation of the age distribution of air trapped in ice sheets and total air content records.

4.2 Introduction

Ice cores preserve a unique archive of ancient air in bubbles that allows us to reconstruct the history of atmospheric trace gases back to 800,000 years ago (e.g. [*Loulergue et al.*, 2008; *Luthi et al.*, 2008]). The air trapped in ice sheets is not a direct record of the past atmospheric history, however, because the air must first pass through the permeable upper 50-100 m layer of the ice sheet known as the firn. The firn acts as a low-pass filter that attenuates high frequency atmospheric signals such as the annual cycle of trace gases [*Trudinger et al.*, 1997]. For example, [*Spahni et al.*, 2003] found that firn smoothing had reduced the magnitude of the methane response to the abrupt 8.2 ka climate event by 34-59% in the EPICA Dome C ice core. It is therefore important to understand the processes that affect the atmospheric signal in order to accurately interpret trace gas records measured in ice cores. The two processes that cause smoothing of the atmospheric signal are diffusive transport of air through the open pores and gradual bubble closure that physically traps the air in bubbles. Diffusion of air through the open pores has been extensively studied elsewhere (e.g. [*Buizert et al.*, 2012; *J. Schwander et*

al., 1993; *Trudinger et al.*, 1997; *Witrant et al.*, 2012]) and this paper will focus on the process of gradual bubble closure.

An interesting paradox is that the bubbles are known to close off over a vertical range that corresponds to roughly 10% of the gas age-ice age difference, yet the observed smoothing of the trapped gas record often appears to be less than would be expected from this rate of gradual bubble closure. This suggests that other poorly-understood processes exist, which limit the extent of smoothing. The need to shed light on these processes motivates our current study.

The firn column is commonly divided into three zones that are defined by the dominant mechanism of air transport: the convective zone, the diffusive zone, and the lock-in zone, from top to bottom [*Sowers et al.*, 1992]. The convective zone contains air that is well mixed with the overlying atmosphere. This zone is typically less than a few meters thick except in very windy locations [*Kawamura et al.*, 2006], or in the situation where extremely low accumulation allows deep cracks to form in the firn [*Severinghaus et al.*, 2010]. In the diffusive zone air movement is dominated by molecular diffusion and the effective diffusivity decreases with depth as the pore volume decreases and the pore space becomes increasingly tortuous. Vertical diffusion of air effectively ceases at the lock-in depth (LID), below which advection with the surrounding ice dominates air transport within the lock-in-zone (LIZ). There is a finite amount of remnant diffusivity within the LIZ, the nature of which is poorly constrained by observations [*Buizert et al.*, 2012]. At the base of the LIZ all of the air is trapped in bubbles within the ice.

Air-entrapment and bubble-closure processes are not understood as well as air transport through open pores. Pycnometric measurements of the volume of closed pores [*J. Schwander et al.*, 1993; *Trudinger et al.*, 1997] have shown that the process of bubble closure occurs gradually, and is primarily controlled by density. To date, these measurements provide the best constraint on the depth where bubble closure occurs at any given firn site. Weather events create variable surface snow conditions which are preserved at depth causing variability in density with depth (e.g. [*Hörhold et al.*, 2011]), leading to corresponding layering in closed porosity. The importance of density layering

on bubble trapping was realized early on (e.g. [*Raynaud and Whillans,* 1982]). *Martinerie et al.* [1992] noted that at Summit, Greenland, the high density (winter) layers sealed before (i.e. at a shallower depth than) the low density (summer) layers. In addition, *Etheridge et al.* [1992] found that the ice age-gas age difference (Δage) at Law Dome, Antarctica was on average two years smaller in denser winter layers than in the summer layers. Although these observations are decades old, a quantitative framework for relating density layering and bubble trapping to the smoothing of trace gas records has been lacking. The primary reasons for this are the paucity of trace gas records from the closed pores of the LIZ and, for the records that do exist, the contamination of those records with post-coring entrapment of modern air [*Aydin et al.*, 2010].

Here we present the first high-resolution discrete measurements of methane (CH_4) mixing ratios and air content (V) in the LIZ closed porosity from the firn at the West Antarctic Ice Sheet (WAIS) Divide deep ice coring site. These measurements are corrected for contamination from post-coring entrapment of modern air based on the isotopic ratio of N_2 ($\delta^{15}N$), which is a sensitive tracer for this process. We also present high-resolution density measurements of the ice. We use these measurements to show that the typical application of bubble closure parameterizations based on mean ice properties leads to slight inaccuracies in the modeled concentration and age of trace gases in the closed pores. We present a new parameterization for bubble closure that accounts for high-frequency layering imparted by density variations, which provides an improved fit to the data. This work provides a constraint on the age distribution of air in the closed porosity and has implications for the interpretation of total air content measurements in deep ice cores.

4.3 Methods

4.3.1 WAIS Divide site description

The WAIS Divide Core (WDC) is located near the West Antarctic Ice Sheet flow divide at 79° 28.058’ S, 112° 05.189’ W, at a surface elevation of 1766 m. The core site has a modern annual accumulation rate of ~200 ± 34 kg m^{-2} yr^{-1} [*Banta et al.*, 2008],

and mean temperature of -30°C [*Orsi et al.*, 2012]. The trace gas (CH_4, $\delta^{15}N$) and total air content (*V*) samples presented here came from a 298 m shallow core that was extracted in the austral summer of 2005/2006 (WDC05A) 1.3 km northwest of the main borehole (WDC06A). WDC05A was drilled with a 10 cm diameter electromechanical drill without drilling fluid and core quality was excellent. CH_4 measurements in mature ice (i.e. ice below the firn) are presented elsewhere (WDC05: [*Mitchell et al.*, 2011]; WDC06A: [*Mitchell et al.*, submitted]).

4.3.2 Sample Integrity

The trace gas and total air content methods involve placing a sample in a high vacuum chamber for approximately one hour, which removes the ambient air and any remaining air in the open porosity. The samples are then melted and refrozen to release the air trapped in the closed porosity into the headspace, which is then measured by the methods described below. Previous workers have hypothesized that subjecting firn samples to a high vacuum would cause some of the recently closed air bubbles to break open since they could have very thin ice walls and the pressure difference between the inside and outside of the bubble would be large (e.g. [*J. Schwander and Stauffer*, 1984; *Stauffer et al.*, 1985]). We have no way to confirm or reject this hypothesis but instead point to model-data agreement shown below that suggests that this phenomenon was small to negligible.

4.3.3 CH_4

Air from 182 discrete ice core samples was extracted using a typical wet extraction technique and then the methane concentration was measured by injection into a gas chromatograph (GC) equipped with a flame ionization detector. The methods are described in detail elsewhere [*Mitchell et al.*, 2011; Mitchell et al., submitted]. There are two types of samples discussed here. First, our low-resolution samples had a cross-sectional area of 2.5 cm × 2.5 cm and covered a depth of ~10 cm (26 samples from 11 different depths). This orientation is what we typically use for deeper ice core samples

because it allows us to measure 2-4 samples from each depth. Second, our high-resolution samples had a cross-sectional area of 2.5 cm × 8 cm and covered a depth of only 3 cm (156 samples). At each high-resolution sample depth only one sample was measured due to limited sample availability. Since the mean annual layer thickness in the LIZ is 24 ± 5 cm yr^{-1}, we were able to measure ~8 high-resolution samples per annual layer vs. only ~2.4 samples per annual layer using our low-resolution sample orientation.

Our previously reported analytical uncertainty for CH_4 samples is ± 2.4 ppb based on the pooled standard deviation of replicate samples [*Mitchell et al.*, submitted]. However, the LIZ samples presented here were not measured in replicate and the extremely large variability (100-200 ppb) observed between them would make replicate comparisons difficult, so we have no direct measure of the analytical uncertainty for these samples. For each sample we expand the air into the GC four times and the standard error obtained from these expansions is slightly higher (1.6 ppb) than from typical ice core samples (1.2 ppb) because the samples within the LIZ have significantly lower total air content than typical ice core samples (discussed below). We therefore estimate that our analytical uncertainty is of the same order of magnitude as our typical ice core samples, but slightly higher for samples with lower air content.

The CH_4 data are corrected for blanks (using air-free ice), solubility, and gravitational fractionation after [*Mitchell et al.*, 2011]. In addition we have estimated a correction for post-coring bubble closure based on $\delta^{15}N$ of N_2 that is discussed in Appendix A.

4.3.4 Total Air Content (*V*)

Total air content (*V*) measurements are obtained simultaneously with the methane measurements [*Martinerie et al.*, 1994]. To measure *V*, we used the sample weight, pressure measurements, the volume of the vacuum flasks and vacuum line, and the temperature of the vacuum line to determine *V* at standard temperature and pressure (STP) in units of $mL_{air}\ kg^{-1}_{ice}$. The weight of the samples was determined with an electronic balance with a precision of 0.1 g. The volumes of the flask and extraction line

were determined by expanding air from a large flask with a known volume at a constant room temperature. The flask and extraction line were not isothermal, so we calculated the effective temperature (T_e) according to the following equation:

$$T_e = \frac{[(T_{GC} \cdot V_{GC}) \cdot (1-c)] + [(T_f \cdot (V_f - V_s) + T_l \cdot V_l) \cdot c]}{V_{GC} + V_f - V_s + V_l} \quad (1)$$

where T_{GC}, T_f, T_l are the temperature of the GC oven containing the sample loop (50°C), flask (a.k.a. the measured ethanol bath temperature), and exposed portion of extraction line (room temperature, ~22°C); V_{GC}, V_f, V_s, V_l are the volumes of the GC, flask, sample, and extraction line; c is a dimensionless constant. V_s is derived by $V_s = M_{sample}/\rho_{ice}$ where ρ_{ice} = 917 kg m^{-3}. The dimensionless constant c represents the relative contribution of T_f and T_l vs. T_{GC} to the T_e of the entire extraction line. We adjust c so that our *V* results are consistent with those obtained using a different method which utilizes a known temperature and pressure [*Lipenkov et al.*, 1995; *Martinerie et al.*, 1994]. To calibrate c we first determined the expected air content at WAIS Divide and a Greenlandic ice core (GISP2) based on the relationship between site temperature and *V* [*Delmotte et al.*, 1999; *Martinerie et al.*, 1994]. We then adjusted c until the difference between the expected *V* (at GISP2 and WAIS Divide) and the sample *V* from mature ice (mean of samples from 100-200 m at GISP2 and WAIS Divide) was minimized (not shown). The value of c was recalibrated when changes were made to the configuration of the extraction line [*Mitchell et al.*, submitted]. The sample *V* was then calculated by:

$$total\ air\ content\ (V) = \frac{(V_{GC} + V_f - V_s + V_l) \cdot P_1}{T_e} \cdot \frac{273.15}{760} \Big/ M_{ice} \quad (2)$$

where P_1 was the pressure of the sample when it is expanded into the GC sample loop (in units of torr) and M_{ice} was the mass of the ice sample (kg). We corrected for solubility of air in liquid water by increasing P_1 by 1.3% which is the percentage of the total amount of air which is trapped in the sample ice during the sample refreezing step. We also

estimated a correction for post-coring bubble closure based on $\delta^{15}N$ (Appendix A). After correcting for post-coring bubble closure we increased *V* by 7% to account for a cut bubble correction.

The pooled standard deviation of replicate *V* samples of mature ice from WAIS Divide and GISP2 is 1.1 $mL_{air}\ kg^{-1}_{ice}$ (n = 93) or ~1.1% of the air content (not shown). As for the CH_4 samples, we have no replicates from the LIZ; however, it is reasonable to assume that our precision is similar to that from mature ice. This analytical precision is comparable to previous workers [*Martinerie et al.,* 1994; *Raynaud et al.,* 1997]; however, since our method relies on calibrating T_e using the *V* vs. site temperature relationship [*Delmotte et al.,* 1999], it has an estimated absolute accuracy of ± 5% [*Martinerie et al.,* 1994].

4.3.5 $\delta^{15}N$

We measured the isotopic ratios of $^{15}N/^{14}N$ on 33 samples with depths adjacent to high-resolution CH_4 samples, using a Finnigan MAT Delta V mass spectrometer with methods detailed in [*Petrenko et al.,* 2006] and based broadly on [*Sowers et al.,* 1989]. As with the CH_4 and *V* measurements, there were no replicates from the LIZ, so we assume that the analytical uncertainty is of the same order of magnitude as in previous work (pooled standard deviation of 0.005 ‰ [*Severinghaus et al.,* 2009]). These measurements are used to provide a correction for contamination from post-coring entrapment of modern air, which is described in Appendix A.

4.3.6 Density

High-resolution density was measured over the whole firn column in the WDC06A ice core as well as along the WDC05A ice core LIZ sample depths presented here at a resolution of 3.3 mm using the Maine Automated Density Gauge Experiment (MADGE) instrument following the methods described in [*Breton et al.,* 2009]. MADGE uses a ^{241}Am gamma-ray source to measure the density of ice non-destructively. One meter of the WDC06A data (72.4-73.4) was lost during processing and was

reconstructed based on the correlation with optical brightness and the mean density at this depth. The density of the WDC05A LIZ samples was on average lower than the average density observed in WDC06A. We have therefore increased the WDC05A density by 7.2 kg m^{-3} to correct for this. Analytical uncertainty (1σ) for the density measurements is ± 4.4 kg m^{-3}.

4.3.7 Model description

To interpret the measurements we used the Center for Ice and Climate (CIC), University of Copenhagen firn air transport model [*Buizert et al.*, 2012]. The model solves the second order diffusion-advection equation in an Eulerian (i.e. static) reference frame using implicit Crank-Nicolson time stepping. The physical processes included in the model are: convection and wind pumping in the upper firn [*Kawamura et al.*, 2006], molecular diffusion, downward advection with the ice matrix, dispersive mixing in the deep firn, bubble trapping and compaction of closed bubbles. We assume a steady state, isothermal firn at -31°C. Mean annual atmospheric pressure at WAIS is P = 780 hPa. The effective diffusivity with depth is calibrated using seven transport tracers with known atmospheric history (CH_4, CO_2, SF_6, $\delta^{15}N$, CFC-11, CFC-12 and HFC-134a) [*Battle et al.*, 2011; *Buizert et al.*, 2012]. The fit to WAIS firn air data with this model is shown in figures 5 and A1, as well as elsewhere [*Buizert et al.*, 2013].

4.4 Results

4.4.1 Observations

Methane mixing ratios in the firn air samples show a characteristic overall pattern similar to that at other firn sampling sites [*Buizert et al.*, 2012; *J. Schwander et al.*, 1993; *Trudinger et al.*, 1997]. Within the diffusive zone, concentrations are nearly constant due to rapid transport of air and the relatively stable atmospheric concentrations over the past decade. The lock-in depth (LID) is found at z_{LID} = 67 m [*Battle et al.*, 2011], below which the CH_4 mixing ratios drop quickly with depth, reflecting both the rapidly

increasing atmospheric CH_4 burden prior to 1998, as well as the slow LIZ transport that is dominated by advection (Figure 4.1).

The isotopic ratio of N_2 ($\delta^{15}N$) is a sensitive tracer for post-coring entrapment of modern air. We measured $\delta^{15}N$ in 33 of our shallower samples (70.75-73.15 m) which have the greatest amount of open porosity and therefore the greatest likelihood of post-coring entrapment of modern air. The results show convincing evidence for post-coring entrapment of modern air. Based on a mass balance calculation, 10.6 ± 6.1 % of the air in these samples came from modern air (Appendix A). Furthermore, there is a strong correlation between the air content in the sample and the percent of modern air contamination, with samples that contain more air having less contamination and vice versa. We used the linear regression of this relationship to derive a correction for post-coring contamination from entrapment of modern air for all of our CH_4 and *V* samples (Appendix A).

Our corrected *V* and CH_4 measurements exhibit strong variability that is indicative of non-uniform trapping with depth (Figure 4.2, mid and lower panels). They are anti-correlated ($r = -0.43$, $p < 0.01$), consistent with the interpretation that layers containing more air closed off at an earlier time when the CH_4 concentrations in the open porosity were lower, and vice versa (Figure 4.2 and Appendix A). The magnitudes of the variations are notably large. The *V* variations of 60-80 $mL_{air}\ kg^{-1}_{ice}$ can be compared with the mean and standard deviation in mature ice of 112 ± 2 $mL_{air}\ kg^{-1}_{ice}$ (from 100-200 m). The methane variations of 100-200 ppb can be compared to the annual rate of methane increase during the past half century of ~10-17 ppb yr^{-1} [*Etheridge et al.*, 1998]. These large variations imply that adjacent samples have mean gas ages ~10 years different from each other, despite having ice age differences of only a few months. As densification continues and more bubbles are isolated, the magnitude of the variations is not expected to decrease since the air in the open porosity has a high CH_4 concentration but the air in the closed porosity samples with low CH_4 concentrations already have high air content. Note that the annual cycle of ~30 ppb should not be visible within the LIZ due to smoothing in the diffusive column [*Trudinger et al.*, 1997], and that this cannot be the

origin of the observed variability. Similar variations are observed in a new methane record from the NEEM S1 (Greenland) ice core using a continuous melting system [*Rhodes et al.*, in press]. The variations observed with this system have a quasi-annual frequency and are anti-correlated with trace elements. Some of these CH_4 measurements have a higher concentration than those in the open pores at this site and so must be influenced by an unknown fraction of modern air that was assimilated either during the melting process or from post-coring entrapment of modern air. Without a method of quantifying the fraction of modern air, it is impossible to confirm to what extent the variability observed in LIZ samples using this technique are a result of bubble trapping processes vs. being a result of contamination from modern air. Based on our WAIS Divide observations, however, it is likely that most of the observed variability in the NEEM S1 data is a result of the bubble trapping processes.

We also measured the density of ice adjacent to the high-resolution CH_4 and V samples. The density measurements have a resolution of 3.3 mm and in Figure 4.2 we show these as well as the mean density over the depth range of the CH_4 and V samples (~3 cm). There is a high correlation between the mean sample density and V ($r = 0.87$, $p < 0.01$, Figure 4.2), which is discussed in greater detail below.

4.4.2 A stochastic description of bubble trapping in layered firn

Traditionally firn air models reconstruct the mean parameters of the firn. However, here we use the high-resolution density profile from WDC06A [*Kreutz et al.*, 2011] to reconstruct and compare both the mean parameters and also the high-resolution variability in those parameters. We used WDC06A because density was measured over the whole firn column whereas in WDC05A it was only measured on our select LIZ samples. In the following discussion we distinguish between the true, layered density profile $\rho(z)$ as it exists at a given moment in time, and the averaged density profile $\langle\rho(z)\rangle$, which is assumed stationary on time scales considered here. We shall refer to ρ and $\langle\rho\rangle$ as the local and bulk densities, respectively. The bulk densities $\langle\rho(z)\rangle$ used in this study are obtained from a smoothed spline fit to the high-resolution local density measurements

from WDC06A (Figure 4.1). The same distinction is made for the porosity, where we have the local porosity $s = 1-\rho/\rho_{ice}$ and the bulk porosity $\langle s\rangle = 1-\langle\rho\rangle/\rho_{ice}$. The porosity is a combination of open and closed pores ($s = s_{op}+s_{cl}$), with the former still interconnected with each other and the overlying atmosphere and the latter consisting of isolated bubbles. Two parameterizations of closed porosity can be found in the literature, the first by [*Jakob Schwander*, 1989]

$$s_{cl} = \begin{cases} s \cdot \exp[\lambda(\rho - \rho_{co})] & \text{for } \rho < \rho_{co} \\ s & \text{for } \rho \geq \rho_{co} \end{cases} \quad (3)$$

with $\lambda = 75/\rho_{co}$ and the close off density $\rho_{co} = 830$ kg m^{-3} at Summit station, Greenland. A slightly modified version of the Schwander parameterization is given in [*Severinghaus and Battle*, 2006]. The second one is the Barnola parameterization [*Goujon et al.*, 2003]:

$$s_{cl} = 0.37 \cdot s \cdot \left(\frac{s}{\overline{s_{co}}}\right)^{-7.6}$$

with

$$\overline{s_{co}} = 1 - \overline{\rho_{co}}/\rho_{ice} \quad (4)$$

$$\overline{\rho_{co}} = \left(\frac{1}{\rho_{ice}} + 6.95 \cdot 10^{-7}T - 4.3 \cdot 10^{-5}\right)^{-1}$$

where $\overline{s_{co}}$ is the mean close-off porosity, $\overline{\rho_{co}}$ is the mean close-off density [*Martinerie et al.*, 1992; *Martinerie et al.*, 1994]. Note that the close-off density (ρ_{co}) in Equation (3) has a slightly different meaning and value from the mean close-off density ($\overline{\rho_{co}}$) in Equation (4).

It is important to realize that both parameterizations were derived from porosity measurements on centimeter scale samples, and therefore give a relationship between local s_{cl} and local ρ. Like the local firn density, the local (closed) porosity and *V* exhibit strong variability with depth due to layering. This is illustrated in Figure 4.3 for the Greenland Summit, Antarctic DE08 (Law Dome), and WDC05A ice cores. The left panels show the fraction of closed pores and *V* in a sample (s_{cl}/s, V/V_{mature}) as a function of the (local) sample density. Some of the plotted s_{cl} data are greater than one because they have been corrected for post-coring bubble closure by increasing the values by 7%.

There is little scatter in the data, indicating that to first order the local density controls bubble closure and *V*, since *V* is directly related to the closed pore volume (after correction for bubble compression from firn densification). When the same data are plotted versus the bulk density at sampling depth (right panel) we observe strong scatter due to layering (the bulk density is equivalent to depth given the monotonic depth-$<\rho(z)>$ relationship). At the high-accumulation DE08 site it is possible to clearly distinguish between summer (blue dots) and winter (black dots) layers. On average summer layers close off deeper than the winter layers do at this high accumulation site.

For many modeling purposes the effect of layering is neglected and the bulk firn properties are used instead of the local ones. For example, in firn air modeling the firn properties are assumed stationary e.g. [*Trudinger et al.*, 1997]; this is a necessary assumption given the strong spatial and temporal variability of real firn. It is common practice to start from $<\rho>$ to obtain $<s>$, and then use these bulk properties in Eqs (3) and (4) to obtain bulk $<s_{cl}>$. We want to point out that this is approach is strictly speaking invalid, given that the parameterizations were derived on local properties and cannot be expected to apply to bulk properties as well. The correct approach would be to start from high-resolution ρ measurements to obtain local s_{cl} values, which can subsequently be averaged to find $<s_{cl}>$. This difference is subtle but important. The strong layering of firn causes the first bubbles to close-off before this is expected based on $<\rho>$ alone, and allows for open pores to be present when $<\rho> \geq \rho_{co}$.

We now derive a new closed porosity parameterization that includes the effect of firn layering on bubble trapping in a stochastic sense. We start by modifying Eq. (3) to improve the fit to the Summit and DE08 data in Figure 4.3. The Schwander parameterization of Eq. (3) is given by the green line, and it appears that the parameterization closes bubbles too abruptly. To make the transition smoother we convolve the Schwander parameterization with a Gaussian of width σ_{co} which yields an improved fit to the data (Appendix B). This convolved equation is expressed as follows:

$$s_{cl} = s \cdot \left(1 - \Phi(u, 0, v) + \exp\left[-u + \frac{v^2}{2} + \ln\{\Phi(u, v^2, v)\}\right]\right) \qquad (5)$$

with

$$\Phi(x, \mu, \Sigma) = \frac{1}{2} + \frac{1}{2}\,\mathrm{erf}\left(\frac{x-\mu}{\sqrt{2\Sigma^2}}\right)$$

$$u = \lambda(\rho - \rho_{co})$$

$$v = \lambda \cdot \sigma_{co}$$

where erf(.) denotes the error function and $\lambda = 75/\rho_{co}$ as before. Contrary to Equation (3), this parameterization is valid for all ρ, and does not have a discontinuity at ρ_{co}. Equation (5) is the cumulative distribution function of the exponentially modified Gaussian function that is used frequently in gas chromatography (e.g. [*Kalambet et al.*, 2011]). The best fit to DE08 and Summit data (red curve in left panels of Figure 4.3) is observed for $\sigma_{co} = 7$ kg m^{-3} (Appendix B); close-off densities are given in the figure caption and were chosen to optimize the fit. When fitting the data it is important to consider the measurement uncertainties; details of the fitting procedure are outlined in Appendix B. In the limit $\sigma_{co} \rightarrow 0$, Eq. (5) is equal to the Schwander parameterization.

Although lacking the mathematical simplicity of other porosity parameterizations, the form of Eq. (5) allows us to easily include the effects of layering. We assume that ρ(z) is a stochastic variable with mean value <ρ(z)> and standard deviation σ_{layer} due to layering. The bulk closed porosity can now be obtained by convolving Eq. (5) with a Gaussian of width σ_{layer}, giving:

$$< s_{cl} >=< s >\cdot \left(1 - \Phi(u, 0, v) + \exp\left[-u + \frac{v^2}{2} + \ln\{\Phi(u, v^2, v)\}\right]\right) \qquad (6)$$

with $\quad v = \lambda \cdot \sqrt{\sigma_{co}^2 + \sigma_{layer}^2}$

and Φ, u as in Eq. (5). Note that Eq. (6) is nearly identical to Eq. (5), the difference being that local properties s and s_{cl} are replaced by bulk properties <s> and <s_{cl}>, and that the width of the distribution has increased from σ_{co} to $\left(\sigma_{co}^2 + \sigma_{layer}^2\right)^{1/2}$. By setting $\sigma_{co} = 0$ in Eq. (6) one obtains the Schwander parameterization corrected for density layering. The fit of Eq. (6) to DE08 and Summit data is shown in the right panels of Figure 4.3, where σ_{layer} was derived from density measurements at the sites. The shaded area indicates the magnitude of the layering (<ρ>±1σ) at both sites. [*Severinghaus and Battle*, 2006] modified the Schwander equation to better describe the enrichment of fugitive

gases ($\delta O_2/N_2$, $\delta Ar/N_2$, $\delta Ne/N_2$) in the open porosity of the lock-in zone (Figure 4.3). Their result agrees fairly well with our Eq. (6), leading us to speculate that our parameterization would work well with the permeation model implemented in [*Severinghaus and Battle*, 2006]. We recommend the following parameters be used in Eqs. (5) and (6):

$$\rho_{co} = \frac{1}{1-1/75} \cdot \left(\frac{1}{\rho_{ice}} + 7.02 \cdot 10^{-7} T - 4.5 \cdot 10^{-5}\right)^{-1} \quad (7)$$

$$\sigma_{co} = 7 \text{ kg m}^{-3} \quad (8)$$

$$\sigma_{layer} = \sqrt{\frac{1}{N} \sum_{LIZ} (\rho_i - <\rho>_i)^2} \quad (9)$$

Equation (7) is based on the mean close-off density from [*Delmotte et al.*, 1999], corrected for the skewness of the trapping distribution (the mean of the trapping distribution occurs in our parameterization at $\rho_{co} - 1/\lambda$). In Figure 4.3 we used ρ_{co} values which are different from those calculated with Eq. (7) to optimize the fit to the porosity data; Eq. (7) is therefore recommended when no porosity data is available. Equation (9) gives the standard deviation of (centimeter scale) density data in the LIZ after subtracting bulk densities, with N the number of data points going into the calculation. We find that the value of σ_{layer} is mostly insensitive to the exact choice of the depth interval used in Eq. 9; when using sparse data sets the depth interval can be increased to obtain a statistically more robust value (in Figure 4.3 we use the 60-90 m depth interval for the σ_{layer} calculations).

We now apply the new parameterization to the WAIS site; following Eqs. (7)-(9) we use ρ_{co} = 837 kg m^{-3} and σ_{layer} = 12.5 kg m^{-3} obtained from the $\rho(z)$ data in Figure 4.1 over the 60-80 m depth interval. In Figure 4.4 we compare Eq. (6) to the Schwander and Barnola parameterizations. As we mentioned earlier, it is not technically accurate to use the $<\rho>$ in the latter two parameterizations and here we do it only because it is the common practice in the literature. Using the Schwander and Barnola parameterizations we get full bubble closure (s_{op}=0) around 71.5 and 74 m depth, respectively (Figure 4.4c). This is incompatible with the field observation that it was possible to pump air from the open porosity of the firn to a depth of 76.5 m, indicating that a large, interconnected pore

space must still exist below 74 m [*Battle et al.*, 2011] (Figure 4.2). Therefore we added a modified Barnola parameterization (blue dashed line) for which the mean close-off porosity $\overline{s_{co}}$ in Eq. (4) was adjusted to yield full bubble closure at 77 m depth; this adjustment is more commonly made in firn air modeling studies (e.g. [*Buizert et al.*, 2012; *Witrant et al.*, 2012]) that focus on the modeling of trace gases in the open porosity alone.

Figure 4.4a shows the bubble trapping rate $d(\langle s_{cl}\rangle/\langle s\rangle)/dz$. It is clear that by including layering, our method gives gas occlusion over a much wider depth range than the parameterizations without layering. Also, the trapping distribution is smooth and does not show a discontinuity at the close-off depth. While the modification to the Barnola parameterization is commonly made for modeling trace gases in the open porosity, this modification causes the mean depth of the bubble trapping to occur much deeper than with the other parameterizations. Figures 4b and 4c show the closed- and open porosities, respectively. The light grey line gives local $s_{cl}(z)$ and $s_{op}(z)$ calculated from the high-resolution $\rho(z)$ data from WDC06A using Eq. (5), with a 200-point moving average shown in dark grey. Contrary to the common practice of applying the classical parameterizations on bulk density, the $s_{cl}(z)$ and $s_{op}(z)$ curves shown in light and dark grey do not show a sudden close-off horizon below which no open pores exist; note that this is a consequence of the layering, and that the same result would have been found irrespective of which closed porosity parameterization is used since we are examining density and porosity at the local scale. Both the reconstructed $s_{op}(z)$, as well as our $\langle s_{op}\rangle$ curve have finite open porosity at 76.5 m depth, in agreement with the deepest firn air sample extraction. This means our parameterization can be used with firn air modeling without ad-hoc modifications to the closed porosity (such as the modified Barnola parameterization shown here). In Figure 4.4d we plot the air content with depth. To convert closed porosity (units of cm^3) to air content (units of $mL_{air}\ kg^{-1}{}_{ice}$) we need to 1.) convert the site temperature and pressure to standard temperature and pressure (STP) using the ideal gas law, and 2.) multiply it by the mean closed bubble pressure, which is above ambient as densification compacts bubbles after they have closed. We calculate

bubble pressure using the method outlined in [*Buizert*, 2011], which is based on the assumptions that the firn column is in steady state, and that closed pores are compacted at the same fractional rate as the total porosity. Using Eq. (6) we model a final air content of 108.8 mL STP kg^{-1}, in good agreement with the 109.4 mL STP kg^{-1} expected from [*Delmotte et al.*, 1999], and the amplitude of air content variability in the data agrees well with our reconstructed air content in light grey (Figure 4.4d). In the bottom panels of Figure 4.3 we plot the modeled local and bulk air content vs. density in red which shows good agreement to the data.

To summarize, our new s_{cl} and $<s_{cl}>$ parameterizations give a good fit to DE08 and Summit closed porosity measurements (Figure 4.3), reconstructed high-resolution $s_{cl}(z)$ and $s_{op}(z)$ profiles, and LIZ air content measurements (Figure 4.4). The site-dependent magnitude of density variability from layering is introduced through a single parameter. Our parameterization is also consistent with the deepest firn air open porosity sampling depth without the need for ad hoc adjustments.

4.5 Discussion

4.5.1 Age Distribution

One important application of our new stochastic parameterization, CH_4, and *V* measurements is the first experimental verification of the age distribution of air in the closed porosity as originally suggested by [*Jakob Schwander*, 1989]. The modeled gas-age distribution reflects the integrated impacts of the firn's smoothing properties on a particular trace gas and it is important to quantify this because it determines the maximum frequencies at which the atmospheric signal is recorded in the ice core. While previous studies have used trace gas concentrations in the open porosity to constrain the age distribution of air in the open porosity at the LID, (e.g. [*Buizert et al.*, 2012; *J. Schwander et al.*, 1993; *Trudinger et al.*, 1997]) before now there have been few constraints on the age distribution of the air trapped in bubbles. Figure 4.5a shows the age distribution of air in the closed porosity at 85 m and 5b shows the modeled methane concentration with depth using the four parameterizations. In addition, Table 4.1 reports

the mean age and spectral width (Δ, a measure of the width of the age distribution [*Trudinger et al.*, 2002]) of the age distributions at 85 m. First we will discuss how CH_4 constrains the mean age through the LIZ, then we will look at the impact of layering, and finally discuss the implications for relating physical properties of the firn to gas transport and trapping.

The differences in concentration are large at the top of the LIZ (~67 m) because the Barnola parameterization uses a polynomial form compared to the exponential form by Schwander, with the former causing shallower bubble trapping. However, these differences are not meaningful because the amount of air trapped at this depth is very small, and we do not have any data at this depth to compare with the model results. In the deeper portion of the LIZ the concentrations from the modified Barnola parameterization are higher than the other parameterization as well as the measurements. This is because the bubble trapping in the modified Barnola parameterization occurs too deeply throughout the LIZ (Figure 4.4d). Deeper trapping causes the mean age with the modified Barnola parameterization to be ~4 years younger than with our stochastic parameterization (Table 4.1). With atmospheric growth rates of ~10 ppb yr^{-1} during the past half century, this translates to a modeled CH_4 difference of ~40 ppb, which is observed between the stochastic and Barnola-modified parameterizations through the deeper portion of the LIZ (Figure 4.5b). Our stochastic parameterization appears to have a similar mean age as the Schwander parameterization (Table 4.1). However, the Schwander parameterization uses ρ_{co} = 830 whereas the stochastic parameterization uses ρ_{co} = 837. For comparison, Table 4.1 also gives the mean age and spectral width of the Schwander parameterization using ρ_{co} = 837 which provides a more direct comparison with our stochastic parameterization. While the 2-4 year mean age differences between the parameterizations are important for improving the chronologies of high-resolution ice core records, it is smaller than the estimate of the uncertainty of the method (±20 years) and as such, does not require a re-evaluation of past work.

The mean age distributions shown in Figure 4.5a are calculated from the firn model using the bulk s_{cl} curve, but we can also use the local s_{cl} to examine the high-

resolution variations of the local mean age of the air, which shows variability from density layering. To examine the variability in the local mean age of the air we subtracted the local mean age of the air modeled with the high-resolution density values from the bulk mean age of the air modeled with the bulk density curve (Figure 4.6). This high-resolution mean age anomaly reconstruction has a resolution of 0.5 cm (light grey line) and in addition we show a six point (black line) and 20 point (blue line) smoothing curve to represent the magnitude of variability expected in samples spanning a depth of ~3 cm and ~10 cm, respectively. We also calculated the mean age anomaly in our high-resolution CH_4 samples using the Law Dome methane time series to determine the age of the air in our samples, then subtracted this age from the mean age of the air modeled with the bulk density curve from WDC06A. Figure 4.6 shows that the mean age of air within the LIZ has peak-to-peak variations of ~10 years at the 3 cm scale, consistent with our high-resolution data. Note that the modeling is based on WDC06A density data, whereas the samples are from WDC05A and, therefore, an exact model-data match is not expected. The figure merely indicates that modeling and data give a similar magnitude of mean age variability in adjacent layers. These results are consistent with the observation at DE08 that summer layers contain air that is ~1.8 years younger than the surrounding winter layers [*Etheridge et al.*, 1992], with the smaller variability being a result of the very high accumulation rate (modern accumulation rate at DE08 is ~1100 kg m^{-2} yr^{-1}). In addition, [*Rhodes et al.*, in press] observed small, quasi-annual variations in mature ice from the NEEM S1 (Greenland) ice core, which has a similar accumulation rate to WAIS Divide. The variations from ~1550 C.E. occur during a decrease in overall methane concentrations of ~2 ppb yr^{-1}. The peak-to-peak magnitude of these quasi-annual methane variations is ~24 ppb, which indicates that adjacent layers have mean age peak-to-peak variations of ~12 years. The results from these three sites are all consistent with the interpretation that density variability is affecting the mean age of samples and it confirms that the high-resolution variations observed in continuous methane records are not atmospheric in origin, but are instead a relic of density variability in the firn [*Rhodes et al.*, in press].

As discussed above, the exact location of the LID is an important feature for understanding the age distribution and spectral width of trace gases. The LID has been identified as the depth at which gravitational enrichment of $\delta^{15}N$ ceases, indicating that the density in the firn has increased to a point where the air in subsequent layers is isolated from the overlying atmosphere. It has not been possible, however, to quantitatively relate the LID to a particular density. We find that the LID at WAIS Divide occurs at $<\rho> = \rho_{co} - 0.77 \times \sigma_{layer}$, and the deepest firn sampling depth occurs at $<\rho> = \rho_{co} + 0.71 \times \sigma_{layer}$. At WAIS the LIZ is therefore spanned by a bulk density range of $\sim 1.5 \times \sigma_{layer}$. We hypothesize that this relationship could hold for other sites as well. This implies that, mechanistically, the thickness of the LIZ is controlled by the magnitude of density variability (σ_{layer}). This hypothesis is qualitatively supported by other recent observations. *Hörhold et al.* [2011] noted a positive correlation between the magnitude of density variability in the LIZ and site temperature and accumulation rate. Therefore, thicker LIZs should be observed at warmer, high accumulation sites and thinner LIZs observed at cold, low accumulation sites. This relationship is consistent with recent observations [*Witrant et al.*, 2012].

Similar to the mean ages discussed above, the differences between the spectral widths of the different parameterizations are small (Table 4.1). The traditional explanation for this is that the slight differences are caused primarily by differing amounts of air being trapped above the LIZ, since once in the LIZ the air is advected with the ice and there is little change in the spectral width. This effect causes the Barnola parameterization to give a wider age distribution in the bubbles than both the Schwander parameterization and our stochastic parameterization because it has shallower trapping, as discussed above. However, a thick LIZ could lead to additional diffusive smoothing of the atmospheric record due to continued gas mixing during the long residence time of gases within the LIZ [*Buizert et al.*, 2012]. Future work should examine the impacts of these two processes at sites with a variety of LIZ thicknesses.

4.5.2 Air Content

The final air content is controlled primarily by the depth at which bubbles seal. Shallow trapping (i.e. with lower ρ and higher total porosity) leads to a higher air content, and vice versa. The different parameterizations each trap bubbles at different depths (Figure 4.4a), which leads to different predictions of final air content in mature ice. The observation that the depth of bubble closure controls the magnitude of the resulting air content has important implications for total air content studies.

First, the magnitude of density variability affects the final air content value because a higher degree of variability causes air to be trapped at a shallower depth. Thus the thickness of the LIZ should be considered when interpreting the air content from ice cores.

Second, our parameterization does not consider interaction between adjacent firn layers, which will occur in real firn. *Stauffer et al.* [1985] observed that dense winter layers can form impermeable layers that trap the air in the open summer layers below, causing the latter to have higher air content. By drilling and cutting of firn samples, pore clusters can be opened that were effectively sealed in the undisturbed firn. The parameterizations give the closed porosity in disturbed samples rather than in real firn. Layering will lead to an effective sealing depth that is shallower than the depth where full closure is predicted in our parameterization. The deepest firn sampling depth may not be a reliable gauge for the effective sealing depth, given that extensive lateral connectivity (from which air can be pumped) can remain below such sealing layers. The sealing effect implies that strongly layered firn retains more air than firn which is more homogenous.

Third, the magnitude of density variability might be a confounding variable that introduces noise into the linear relationship between the mature air content and the mean site temperature [*Delmotte et al.*, 1999; *Martinerie et al.*, 1994]. A new parameterization that corrects for the magnitude of density variability and then relates air content to mean site temperature could yield a higher correlation.

Finally, recent work on high-resolution density records suggest that densification rates could be controlled by chemical impurities in the ice [*Hörhold et al.*, 2012]. Since

chemical impurities vary by orders of magnitude on glacial-interglacial timescales it is possible that these impurities are impacting total air content through changes in the magnitude of density variability. This complicates the interpretation of air content as a surface elevation proxy.

4.5.3 Future Recommendations

The experiment and samples measured here were obtained fortuitously because the WDC05A LIZ ice was not allocated for specific work, which allowed us to obtain large, continuous samples. These initial results call for further investigation and the following are recommended modifications to the experimental design. 1.) Field based CH_4 analysis using a discrete sampling technique would reduce the possibility of post-coring entrapment of modern air and could be compared with lab based results of CH_4 and $\delta^{15}N$ conducted later to accurately quantify the degree of post-coring contamination. Extremely high-precision (<5 ppb) is not necessary for the field based measurements since the variations are on the order of 100-200 ppb. Packing samples in a vacuum container in the field for latter analysis in the lab could accomplish the same goals. 2.) Co-located measurements of chemical impurities in the ice would allow for a detailed investigation of the impact on total air content. 3.) Co-located measurements of pore volume would allow for a comparison with total air content and verify the bubble compaction parameterization. 4.) These measurements should be conducted at sites with a range of temperature, accumulation, density variability, LIZ thickness, and trace element loading characteristics in order to validate the parameterization over a range of climatic conditions.

4.6 Conclusions

Measurements of methane and total air content (V) from within the Lock-in Zone (LIZ) in a WAIS Divide core reveal large variations that are anti-correlated with each other, indicating that layering is causing bubble trapping to occur in a staggered manner over a range of depths. Thus far there have been no attempts to incorporate layering into

firn air models. Previous work on firn air modeling used parameterizations for bubble trapping based on cm scale samples representing local ice properties (ρ, s) and applied these parameterizations to bulk ice properties ($<\rho>$, $<s>$). This approach is invalid because high frequency layering within the firn causes bubble trapping to occur over a wider depth range than predicted by the bulk density profile alone. We use the original parameterization for local closed porosity (s_{cl}) convolved with a Gaussian distribution with a width defined by the magnitude of density variability to represent the effects of high frequency layering. This new stochastic parameterization has a physical basis, is computationally inexpensive, and yields an improved fit to a variety of bulk firn parameters including bulk closed pore volume ($<s_{cl}>$), total air content (V), and CH_4 in the closed porosity. It also correctly predicts that there is finite open porosity at the depth of the deepest extraction of air from the open porosity, as opposed to the other parameterizations which predict that all of the pores are fully closed at that depth, and thus need an ad-hoc modification in order to be used in firn air modeling. Our CH_4 data provide a constraint on the mean age of the air in the closed porosity at the base of the LIZ and shows that the ad-hoc parameterization affects the depth at which bubbles close and yields a mean age that is too young. We can also calculate the variability of the mean age from the high-resolution density and we show that this causes peak-to-peak variations in the sample mean gas age of ~10 years. This is consistent with observations from other ice cores and indicates that high-resolution (centimeter scale) measurements of methane showing semi-annual variations is a result of density layering in the firn and is not an atmospheric signal.

Our stochastic parameterization also has implications for the interpretation of ice core total air content records and estimates of past ice sheet thickness. The total air content is affected by the depth at which bubbles close and by the magnitude of density variability in the ice. Relating these observations to chemical impurities in the ice and detailed firn microstructure could help explain some of the observed variability in air content records.

4.7 Acknowledgements

This work was supported by NSF OPP grants 0538578, 0520523, 0538538 and 0944343 (to J.P.S.), by NASA/Oregon Space Grant Consortium grant NNG05GJ85H, and the NOAA Climate and Global Change Fellowship Program, administered by the University Corporation for Atmospheric Research, and Polar Academic Program (PAP, PD12010) of Korea Polar Research Institute (KOPRI). We thank Brendan Williams, James Lee, and Jon Edwards for assisting in sample preparation and analysis; Jakob Schwander and David Etheridge for useful discussions and sharing porosity data, and Steve Montzka for sharing WAIS halocarbon firn air data; the WAIS Divide Science Coordination Office at DRI, Reno, NV for the collection and distribution of the WAIS Divide ice core (Kendrick Taylor, NSF Grants 0230396, 0440817, 0944348; and 0944266 - University of New Hampshire); NSF OPP which funds the Ice Drilling Program Office and Ice Drilling Design and Operations group for coring activities; NSF which funds the National Ice Core Laboratory which curated and processed the core; Raytheon Polar Services which provided logistics support in Antarctica; and the 109th New York Air National Guard for airlift in Antarctica. Data and description can be downloaded from the NOAA National Climate Data Center http://www.ncdc.noaa.gov/paleo/paleo.html.

4.8 Appendices

4.8.1 Appendix A: Post-coring entrapment of air

The CH_4 and *V* measurements are inversely correlated with each other ($r = -0.78$, $p < 0.01$, after de-trending with a spline fit) and there are two hypotheses to explain this relationship. The first hypothesis is that they are real variations, i.e. depths that contain a greater amount of air began trapping air at a relatively shallow depth, containing older air with a lower methane concentration and depths that contain less air began trapping air at a relatively deeper depth, containing younger air with a higher methane concentration. Conversely, the inverse relationship could be caused by post-coring bubble closure whereby depths that contain a greater amount of air have had less contamination and lower methane concentration and depths that contain less air have more open porosity

which is susceptible to post-coring bubble closure and therefore trap more modern air and have a higher methane concentration.

To investigate the possibility of post-coring bubble closure, we measured $\delta^{15}N$ at the exact same depths as some of our CH_4 samples. $\delta^{15}N$ is a sensitive tracer to post-coring bubble closure for two reasons. First, throughout the diffusive column, gravitational fractionation causes a linear increase in $\delta^{15}N$ with depth. This ceases within the LIZ since there is no vertical diffusion of air. Since most of the bubble trapping occurs within the LIZ, and only a small amount occurs just above the LIZ, there should be little natural variability of $\delta^{15}N$ in the closed pores in the LIZ. Second, there are no other sources of enriched ^{15}N that could contaminate the signal.

We measured 33 $\delta^{15}N$ samples and rejected 4 because the air content did not agree with the CH_4 samples at the same depth. There was a high correlation ($R^2 = 0.95$) in the air content between the remaining $\delta^{15}N$ and CH_4 data indicating that both sets of samples should have recorded the same signals. The samples had a $\delta^{15}N$ of 0.266 ± 0.018 ‰ which is lower and more variable than the model predicted value of 0.300 ± 0.005 ‰ (between 70-80m, Figure 4.7). To analyze the possibility of post-coring contamination, we plot $\delta^{15}N$ vs. CH_4 (Figure 4.8). If the low $\delta^{15}N$ values were authentic they would indicate that the air was isolated in bubbles at a shallow depth and would therefore have to contain old air that would also have a low CH_4 concentration, yielding a positive relationship between $\delta^{15}N$ and CH_4. However, we observe a negative relationship ($r = -0.76$, $p < 0.01$) indicating that the low $\delta^{15}N$ values must be caused by entrapment of some modern air by post-coring bubble closure (Figure 4.8). A comparison between $\delta^{15}N$ and *V* reveals a positive relationship ($r = 0.85$, $p < 0.01$) indicating that the amount of contamination is related to the air content and, by extension, the amount of open porosity in the sample (Figure 4.8). Therefore, samples with more open pores had a greater amount of total contamination.

To correct for the post-coring contamination we assumed that the $\delta^{15}N$ should be equal to that expected in the LIZ. We used the model predicted value of $\delta^{15}N$ between 70-80 m, $\delta^{15}N_{real} = 0.300 \pm 0.005$ ‰. This is consistent with $\delta^{15}N$ measurements between

80-200 m of 0.304 ± 0.006 ‰. We assumed that the contaminant was modern atmospheric air ($\delta^{15}N_{cont}$ = 0 ‰), then used a mass balance calculation to derive the amount of contaminated air content (V_{cont}):

$$\delta^{15}\mathrm{N}_{\mathrm{cont}}V_{\mathrm{cont}} = \delta^{15}\mathrm{N}_{\mathrm{meas}}V_{\mathrm{meas}} - \delta^{15}\mathrm{N}_{\mathrm{real}}V_{\mathrm{real}} \qquad \text{A-1}$$
$$V_{\mathrm{real}} = V_{\mathrm{meas}} - V_{\mathrm{cont}}$$

where $\delta^{15}N_{meas}$ and V_{meas} are the measured values. This calculation reveals that 10.6 ± 6.1 % of the V_{meas} was from post-coring contamination. Since we did not measure $\delta^{15}N$ at all of the depths where we have CH_4 measurements we fit a linear regression to the percent of contamination ($100 \cdot V_{cont}/V_{meas}$) vs. V_{meas} (r^2 = 0.75, Figure 4.9) and used this relationship to calculate the V_{cont} based on the V_{meas} in the samples. We applied this linear fit to our $\delta^{15}N$ measurements and note that the fit does not account for all of the variability, leading to some uncertainty in our correction (Figure 4.7). We then assume that the modern air that is being trapped in the ice has a concentration of 2000 ppb. This is a reasonable assumption based on preliminary methane concentrations observed at the NOAA Boulder Atmospheric Observatory (designated BAO in the NOAA data base) air sampling station that average ~1900 ppb but have frequent spikes in excess of 2100 ppb during the time period when these cores were stored at the National Ice Core Laboratory (NICL) in Lakewood, CO. We can then calculate the corrected CH_4 ($CH_{4\text{-corr}}$) by:

$$\mathrm{CH}_{4-\mathrm{corr}} = \frac{\mathrm{CH}_{4-\mathrm{meas}} \cdot V_{\mathrm{meas}} - \mathrm{CH}_{4-\mathrm{cont}} \cdot V_{\mathrm{cont}}}{V_{\mathrm{meas}} - V_{\mathrm{cont}}} \qquad \text{A-2}$$

The original and corrected CH_4 measurements are shown in Figure 4.10. Since there is a significant amount of uncertainty in the estimation of the amount of contaminated air, the absolute concentration of the CH_4 in the firn is uncertain. In Figure 4.10 we show a shaded region of methane concentrations that assumes the contaminated CH_4 has a concentration of 1800 ppb to 2400 ppb, corresponding to end member estimates of the contaminated methane concentrations. Note that the range of the shaded correction

region scales with the amount of air content. The correction also affects the relative changes between the samples and causes the observed anti-correlation between CH_4 and *V* to decrease to r = -0.43, p < 0.01.

The CH_4 and *V* samples were measured in three batches in 2008, 2009 and 2012. Some sample depths from 2008 and 2009 were re-measured in 2012 and yielding consistent results suggesting that at least over this time there was not a significant amount of post-coring bubble closure. Therefore, most of the post-coring bubble closure must have occurred between the time of drilling during the 2005/2006 field season and 2008.

4.8.2 Appendix B: Propagating uncertainty in fitting s_{cl}/s vs. local ρ

When fitting the s_{cl}/s vs. local ρ curves in the left panels of Figure 4.3, we must bear in mind that the ρ data themselves are subject to additional measurement and sampling uncertainties (σ_{meas}), which also contribute to broadening of features in the data. We consider two contributions to σ_{meas} that we assume to be independent. The first is the measurement precision, which can be estimated from replicate measurements. The second is the finite size of the samples, having potentially larger dimensions (5 cm) than the underlying density variability. We evaluated this by taking half of the average density difference between adjacent samples, which is the density variability in half a sample. We multiplied this value by $\sqrt{2}$, assuming density in both halves of the sample can vary independently from each other. In this way we found σ_{meas}= 9.4 kg m^{-3} for the Summit data, and σ_{meas}= 7.1 kg m^{-3} for the DE08-2 data.

The red curves in the left panels of Figure 4.3 were fitted with Eq. (5), where we used $v = \lambda \cdot \sqrt{\sigma_{co}^2 + \sigma_{meas}^2}$, with σ_{meas} values as given above. Fitting was done by eye; the best fit to both curves was obtained with σ_{co}= 7 kg m^{-3}. We therefore recommend this value be used at other sites as well.

4.9 References

Aydin, M., et al. (2010), Post-coring entrapment of modern air in some shallow ice cores collected near the firn-ice transition: evidence from CFC-12 measurements in Antarctic firn air and ice cores, *Atmos. Chem. Phys.*, *10*(11), 5135-5144.

Banta, J. R., J. R. McConnell, M. M. Frey, R. C. Bales, and K. Taylor (2008), Spatial and temporal variability in snow accumulation at the West Antarctic Ice Sheet Divide over recent centuries, *J. Geophys. Res.-Atmos.*, *113*(D23), 8.

Battle, M. O., J. P. Severinghaus, E. D. Sofen, D. Plotkin, A. J. Orsi, M. Aydin, S. A. Montzka, T. Sowers, and P. P. Tans (2011), Controls on the movement and composition of firn air at the West Antarctic Ice Sheet Divide, *Atmos. Chem. Phys.*, *11*(21), 11007-11021.

Breton, D. J., G. S. Hamilton, and C. T. Hess (2009), Design, optimization and calibration of an automated density gauge for firn and ice cores, *J. of Glaciol.*, *55*, 1092-1100.

Buizert, C. (2011), The influence of firn air transport processes and radiocarbon production on gas records from polar firn and ice, Universtity of Copenhagen.

Buizert, C., T. Sowers, and T. Blunier (2013), Assessment of diffusive isotopic fractionation in polar firn, and application to ice core trace gas records, *Earth and Planetary Science Letters*, *361*(0), 110-119.

Buizert, C., et al. (2012), Gas transport in firn: multiple-tracer characterisation and model intercomparison for NEEM, Northern Greenland, *Atmos. Chem. Phys.*, *12*(9), 4259-4277.

Delmotte, M., D. Raynaud, V. Morgan, and J. Jouzel (1999), Climatic and glaciological information inferred from air-content measurements of a Law Dome (East Antarctica) ice core, *J. of Glaciol.*, *45*(150), 255-263.

Etheridge, D. M., G. I. Pearman, and P. J. Fraser (1992), Changes in tropospheric methane between 1841 and 1978 from a high accumulation rate Antarctic ice core, *Tellus Ser. B-Chem. Phys. Meteorol.*, *44*(4), 282-294.

Etheridge, D. M., L. P. Steele, R. J. Francey, and R. L. Langenfelds (1998), Atmospheric methane between 1000 AD and present: Evidence of anthropogenic emissions and climatic variability, *J. Geophys. Res.-Atmos.*, *103*(D13), 15979-15993.

Goujon, C., J. M. Barnola, and C. Ritz (2003), Modeling the densification of polar firn including heat diffusion: Application to close-off characteristics and gas isotopic fractionation for Antarctica and Greenland sites, *J. Geophys. Res.-Atmos.*, *108*(D24), 18.

Hörhold, M. W., S. Kipfstuhl, F. Wilhelms, J. Freitag, and A. Frenzel (2011), The densification of layered polar firn, *J. Geophys. Res.-Earth Surf.*, *116*.

Hörhold, M. W., T. Laepple, J. Freitag, M. Bigler, H. Fischer, and S. Kipfstuhl (2012), On the impact of impurities on the densification of polar firn, *Earth and Planetary Science Letters*, *325–326*(0), 93-99.

Kalambet, Y., Y. Kozmin, K. Mikhailova, I. Nagaev, and P. Tikhonov (2011), Reconstruction of chromatographic peaks using the exponentially modified Gaussian function, *Journal of Chemometrics*, *25*(7), 352-356.

Kawamura, K., J. P. Severinghaus, S. Ishidoya, S. Sugawara, G. Hashida, H. Motoyama, Y. Fujii, S. Aoki, and T. Nakazawa (2006), Convective mixing of air in firn at four polar sites, *Earth and Planetary Science Letters*, *244*(3–4), 672-682.

Kreutz, K., B. Koffman, D. Breton, and G. S. Hamilton (2011), Microparticle, Conductivity, and Density Measurements from the WAIS Divide Deep Ice Core, Antarctica.

Lipenkov, V., F. Candaudap, J. Ravoire, E. Dulac, and D. Raynaud (1995), A new device for the measurement of air content in polar ice, *J. of Glaciol.*, *41*(138), 423-429.

Loulergue, L., A. Schilt, R. Spahni, V. Masson-Delmotte, T. Blunier, B. Lemieux, J. M. Barnola, D. Raynaud, T. F. Stocker, and J. Chappellaz (2008), Orbital and millennial-scale features of atmospheric CH_4 over the past 800,000 years, *Nature*, *453*(7193), 383-386.

Luthi, D., et al. (2008), High-resolution carbon dioxide concentration record 650,000-800,000 years before present, *Nature*, *453*(7193), 379-382.

Martinerie, P., D. Raynaud, D. M. Etheridge, J. M. Barnola, and D. Mazaudier (1992), Physical and climatic parameters which influence the air content in polar ice, *Earth and Planetary Science Letters*, *112*(1-4), 1-13.

Martinerie, P., V. Y. Lipenkov, D. Raynaud, J. Chappellaz, N. I. Barkov, and C. Lorius (1994), Air content paleo record in the Vostok ice core (Antarctica): A mixed record of climatic and glaciological parameters, *J. Geophys. Res.-Atmos.*, *99*(D5), 10565-10576.

Mitchell, L. E., E. J. Brook, T. Sowers, J. R. McConnell, and K. Taylor (2011), Multidecadal variability of atmospheric methane, 1000-1800 CE, *J. Geophys. Res.-Biogeosci.*, *116*.

Orsi, A. J., B. D. Cornuelle, and J. P. Severinghaus (2012), Little Ice Age cold interval in West Antarctica: Evidence from borehole temperature at the West Antarctic Ice Sheet (WAIS) Divide, *Geophys. Res. Let.*, *39*(9), L09710.

Petrenko, V. V., J. P. Severinghaus, E. J. Brook, N. Reeh, and H. Schaefer (2006), Gas records from the West Greenland ice margin covering the Last Glacial Termination: a horizontal ice core, *Quat. Sci. Rev.*, *25*(9-10), 865-875.

Raynaud, D., and I. M. Whillans (1982), AIR CONTENT OF THE BYRD CORE AND PAST CHANGES IN THE WEST ANTARCTIC ICE SHEET, *Ann. Glac.*, *3*, 269-273.

Raynaud, D., J. Chappellaz, C. Ritz, and P. Martinerie (1997), Air content along the Greenland Ice Core Project core: A record of surface climatic parameters and elevation in central Greenland, *J. Geophys. Res.-Oceans*, *102*(C12), 26607-26613.

Schwander, J. (1989), The transformation of snow to ice and the occlusion of gases, in *The Environmental Record in Glaciers and Ice Sheets*, edited by H. Oeschger and C. C. Langway, pp. 53-67, John Wiley, Chichester [England] ; New York :.

Schwander, J., and B. Stauffer (1984), Age difference between polar ice and the air trapped in its bubbles, *Nature*, *311*(5981), 45-47.

Schwander, J., J. M. Barnola, C. Andrie, M. Leuenberger, A. Ludin, D. Raynaud, and B. Stauffer (1993), The Age of the Air in the Firn and the Ice at Summit, Greenland, *J. Geophys. Res.-Atmos.*, *98*(D2), 2831-2838.

Severinghaus, J. P., and M. O. Battle (2006), Fractionation of gases in polar ice during bubble close-off: New constraints from firn air Ne, Kr and Xe observations, *Earth and Planetary Science Letters*, *244*(1-2), 474-500.

Severinghaus, J. P., R. Beaudette, M. A. Headly, K. Taylor, and E. J. Brook (2009), Oxygen-18 of O_2 Records the Impact of Abrupt Climate Change on the Terrestrial Biosphere, *Science*, *324*(5933), 1431-1434.

Severinghaus, J. P., et al. (2010), Deep air convection in the firn at a zero-accumulation site, central Antarctica, *Earth and Planetary Science Letters*, *293*(3-4), 359-367.

Sowers, T., M. Bender, and D. Raynaud (1989), Elemental and Isotopic Composition of Occluded O_2 and N_2 in Polar Ice, *J. Geophys. Res.-Atmos.*, *94*(D4), 5137-5150.

Sowers, T., M. Bender, D. Raynaud, and Y. S. Korotkevich (1992), $d^{15}N$ of N_2 in Air Trapped in Polar Ice: a Tracer of Gas Transport in the Fim and a Possible Constraint on Ice Age-Gas Age Differences, *J. Geophys. Res.-Atmos.*, *97*(D14), 15683-15697.

Spahni, R., J. Schwander, J. Fluckiger, B. Stauffer, J. Chappellaz, and D. Raynaud (2003), The attenuation of fast atmospheric CH_4 variations recorded in polar ice cores, *Geophys. Res. Let.*, *30*(11), 4.

Stauffer, B., J. Schwander, and H. Oeschger (1985), Enclosure of air during metamorphosis of dry firn to ice, *Ann. Glac.*, *6*, 108-112.

Trudinger, C. M., I. G. Enting, and P. J. Rayner (2002), Kalman filter analysis of ice core data - 1. Method development and testing the statistics, *J. Geophys. Res.-Atmos.*, *107*(D20).

Trudinger, C. M., I. G. Enting, D. M. Etheridge, R. J. Francey, V. A. Levchenko, L. P. Steele, D. Raynaud, and L. Arnaud (1997), Modeling air movement and bubble trapping in firn, *J. Geophys. Res.-Atmos.*, *102*(D6), 6747-6763.

Witrant, E., et al. (2012), A new multi-gas constrained model of trace gas non-homogeneous transport in firn: evaluation and behaviour at eleven polar sites, *Atmos. Chem. Phys.*, *12*(23), 11465-11483.

4.10 Figures

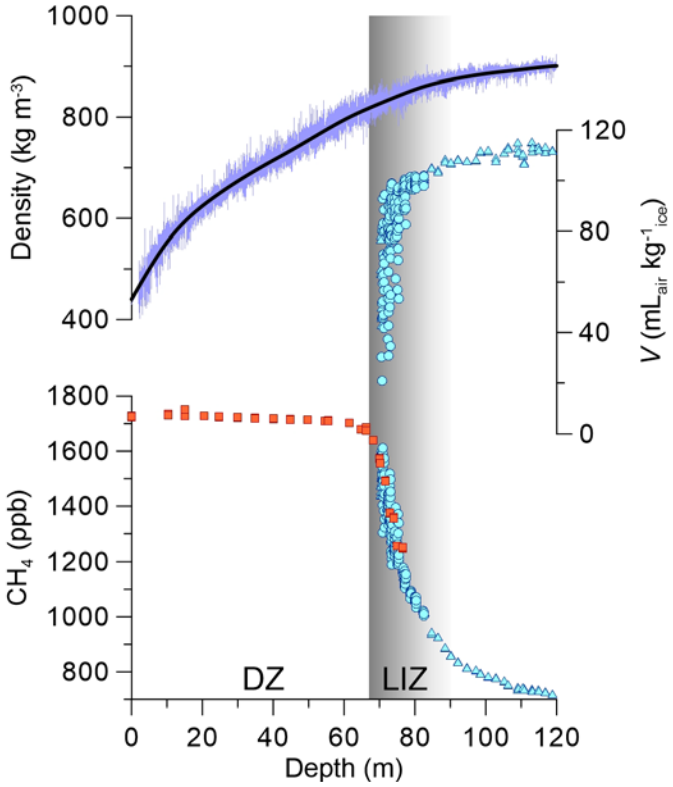

Figure 4.1. Overview of the firn at WAIS Divide. High resolution local ρ (light purple) and bulk <ρ> (black) density from WDC06A (top). Air content (*V*, middle) and CH_4 (bottom) come from WDC05A. Orange squares are CH_4 in the open pores [*Battle et al.*, 2011] while the blue circles are the closed pore data. Blue circles are high-resolution data (covering 3 cm depth) and blue triangles are low-resolution data (covering 10 cm depth). DZ and LIZ (shaded region) are the diffusive zone and lock-in-zone, respectively.

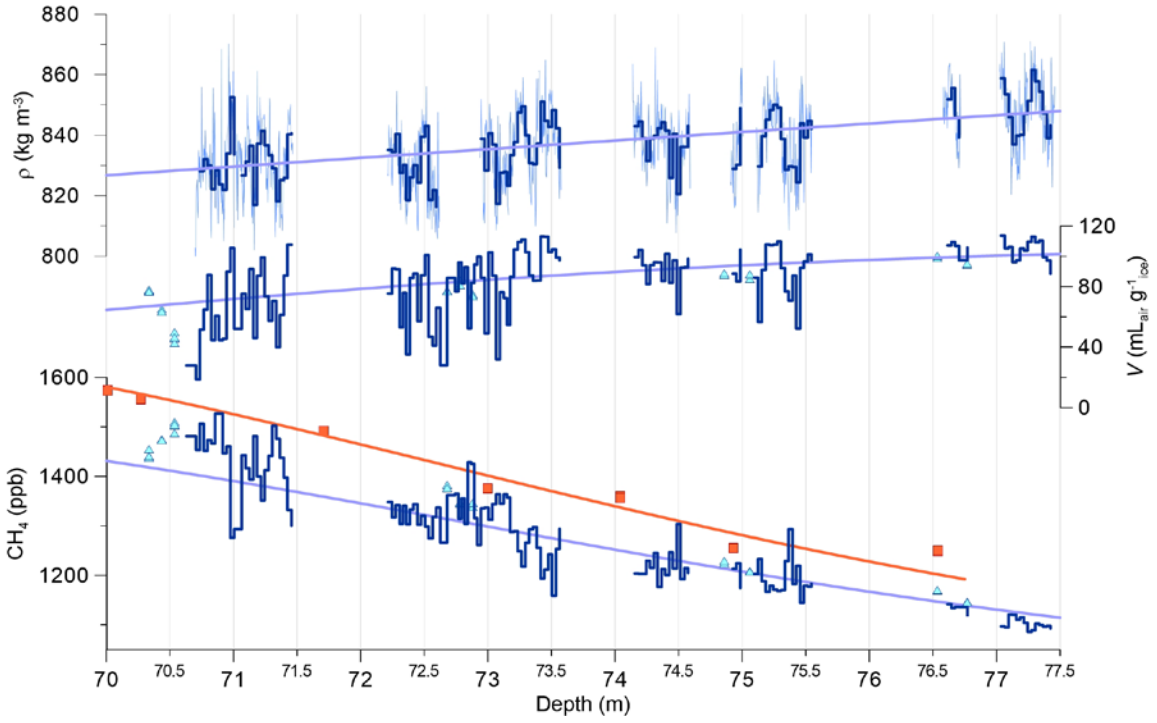

Figure 4.2. Density (top), air content (V, middle), and methane (CH_4, bottom) from WDC05A. The raw density measurements are shown with the light blue line and the average density over the depth of the high-resolution CH_4 samples is shown by the dark blue line. High-resolution CH_4 and *V* measurements are shown by the dark blue line. Low-resolution CH_4 and *V* measurements are triangle symbols. The smooth light blue lines show the spline fit to the WDC06A density (top), and modeled results for air content (middle) and CH_4 (lower). Orange squares [*Battle et al.*, 2011] and line are the observations and model for the open porosity, respectively.

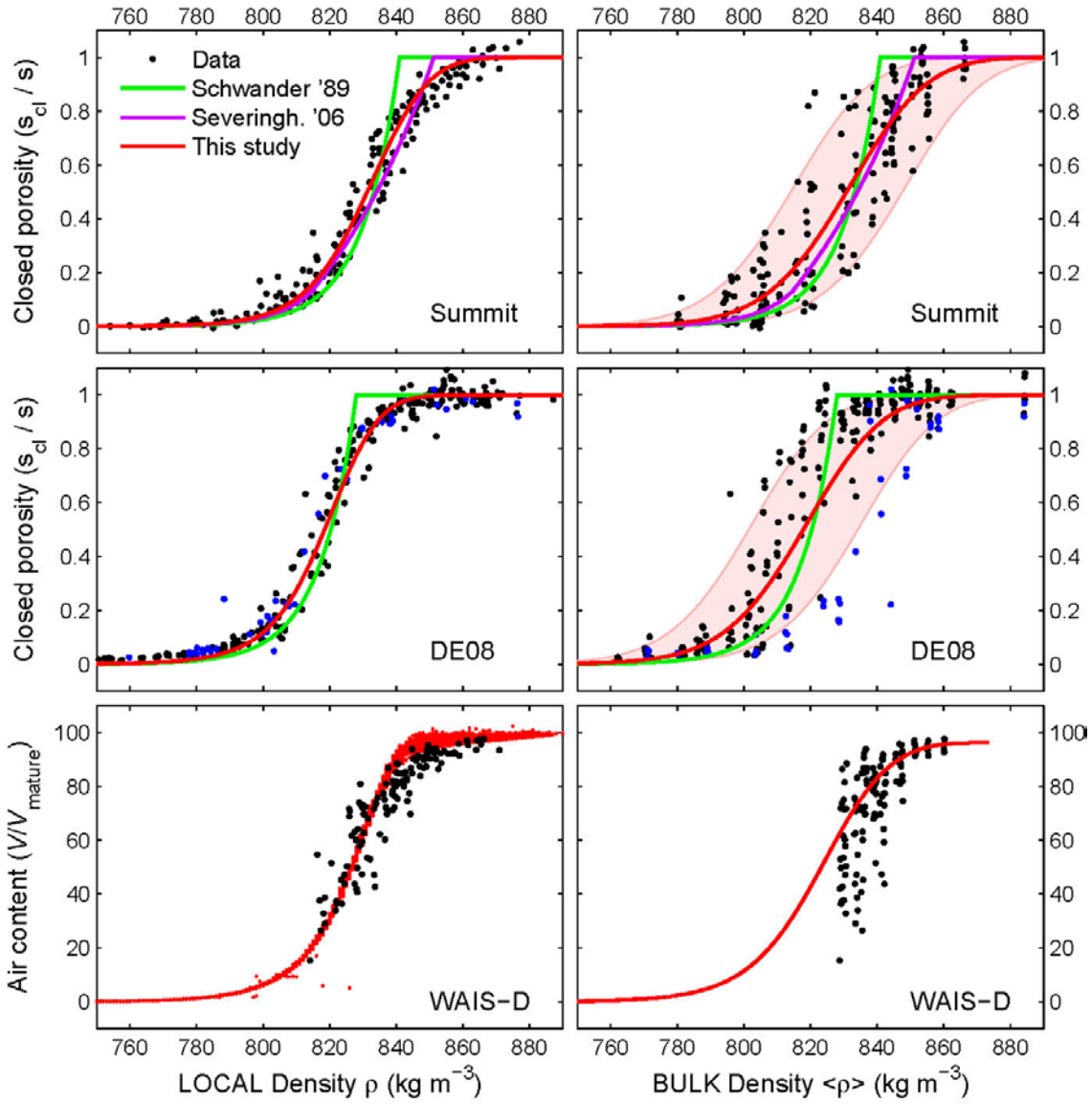

Figure 4.3. Closed porosity measurements at Summit, Greenland [*J. Schwander et al.*, 1993] and DE08-2, Law Dome, Antarctica [*Trudinger et al.*, 1997]. At DE08-2, the black dots are from winter layers and the blue dots are from summer layers. Left panels: fraction of closed pores vs. sample (i.e. local) density; red curves follow Eq. (5) where we include a measurement error σ_{meas} (see Appendix B for details). Right panels: fraction of closed pores vs. bulk density at sampling depth; red curves show Eq. (6) using σ_{layer}=12 kg m^{-3} at Summit and σ_{layer}=13 kg m^{-3} at DE08-2, as obtained from Eq. (9). Bulk density $<\rho>$ obtained with a spline fit to sample density data. Green lines show Eq. (5) applied to ρ (left panels) and to $<\rho>$ (right panels). In all parameterizations we use ρ_{co}= 841 kg m^{-3} at Summit, ρ_{co}= 828 kg m^{-3} at DE08-2, and ρ_{co} = 837 kg m^{-3} at WAIS Divide. Purple lines give modified Schwander parameterization from [*Severinghaus and Battle*, 2006].

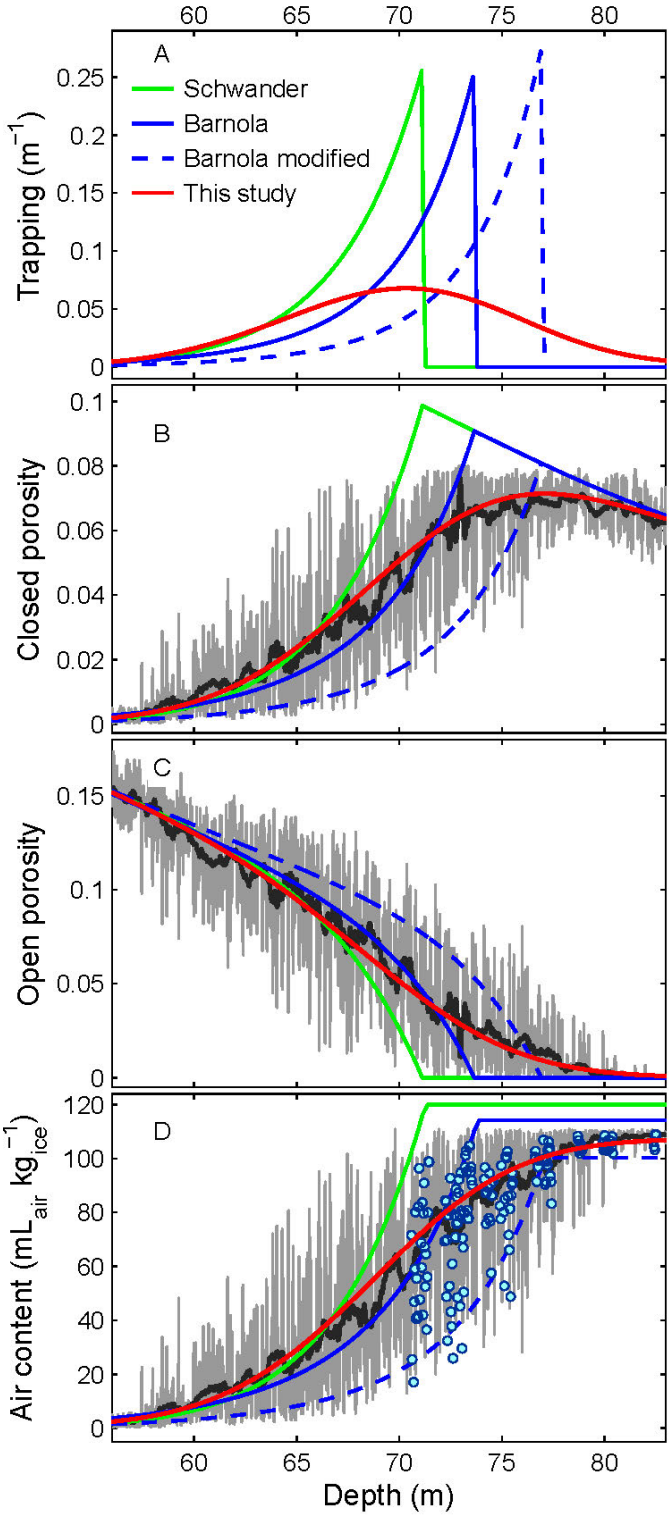

Figure 4.4. Porosity parameterizations applied to the WAIS site. The Schwander, Barnola, modified Barnola and Eq. (8) parameterizations use ρ_{co}= 830 [*Jakob Schwander*, 1989], $\overline{\rho_{co}}$= 825.6 [*Martinerie et al.*, 1994], $\overline{\rho_{co}}$= 836 and ρ_{co}= 837 kg m^{-3}, respectively. A) trapping rate d(<s_{cl}>/<s>)/dz. B) and C) closed and open porosities, with in light grey local s_{cl} and s_{op} reconstructed from ρ(z) using Eq. (7), with 200 point running average (dark grey). D) Air content, with local air (light grey), running mean (dark grey) and high-resolution air content data (blue circles). Air content in the model is calculated as $s_{cl} \cdot P_{cl}\ /1013.25 \cdot 273.15/T \cdot \rho^{-1}$, where P_{cl} is the mean pressure in closed bubbles, which exceeds the open pore pressure due to continued pore compaction after close-off; see [*Buizert*, 2011] for details.

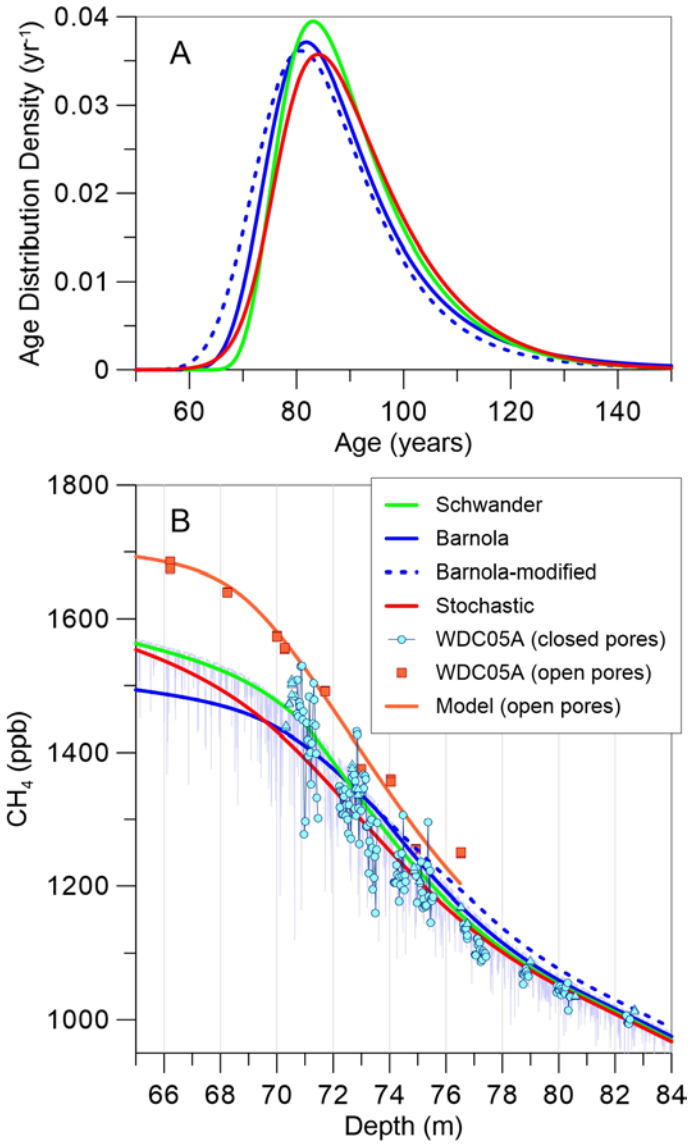

Figure 4.5. Age distribution (top) and modeled CH_4 concentrations (bottom) using the different parameterizations. The green, blue, blue dashed, and red lines show the modeled age distribution and CH_4 in the closed porosity using the Schwander, Barnola, Barnola-modified, and Stochastic parameterizations. The orange line and squares show the modeled and measured [*Battle et al.*, 2011] CH_4 in the open porosity. Blue circles are the high-resolution measurements and blue triangles show the low resolution measurements. Light grey line shows the modeled CH_4 using the WDC06A density.

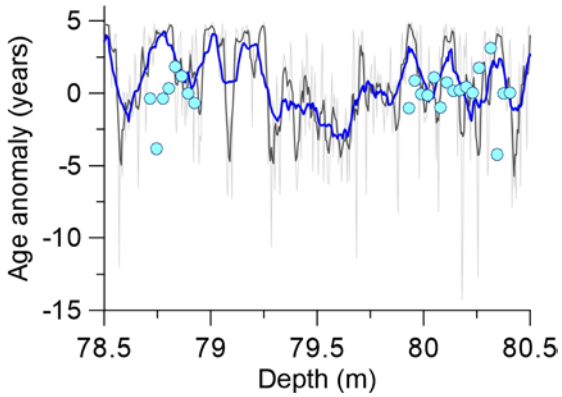

Figure 4.6. Age anomalies of air at the base of the LIZ. The light grey line is calculated from the 5 mm high resolution density data, and in addition we show a 6 point (black) and a 20 point (blue) smoothing curve representing a 3 cm and 10 cm sample, respectively. The calculation of the age of the samples (blue circles) is described in the text.

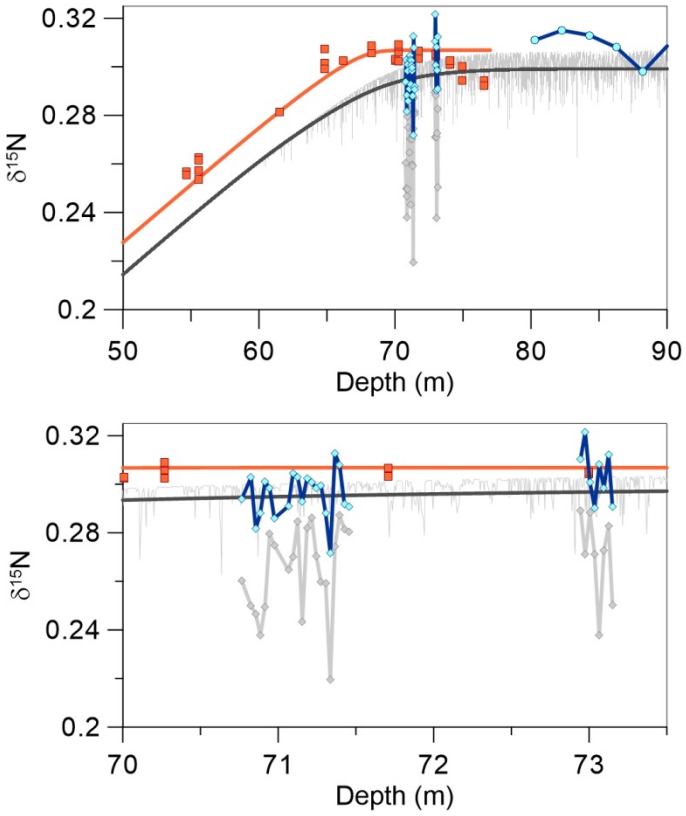

Figure 4.7. Overview of $\delta^{15}N$ (top) and detailed view of the data (bottom). Orange squares and line are the measured [*Battle et al.*, 2011] and modeled $\delta^{15}N$ from the open porosity. Grey circles and thick line are the originally measured values. Blue circles are the corrected $\delta^{15}N$. Thin grey and black lines are the modeled $\delta^{15}N$ based on local and bulk densities.

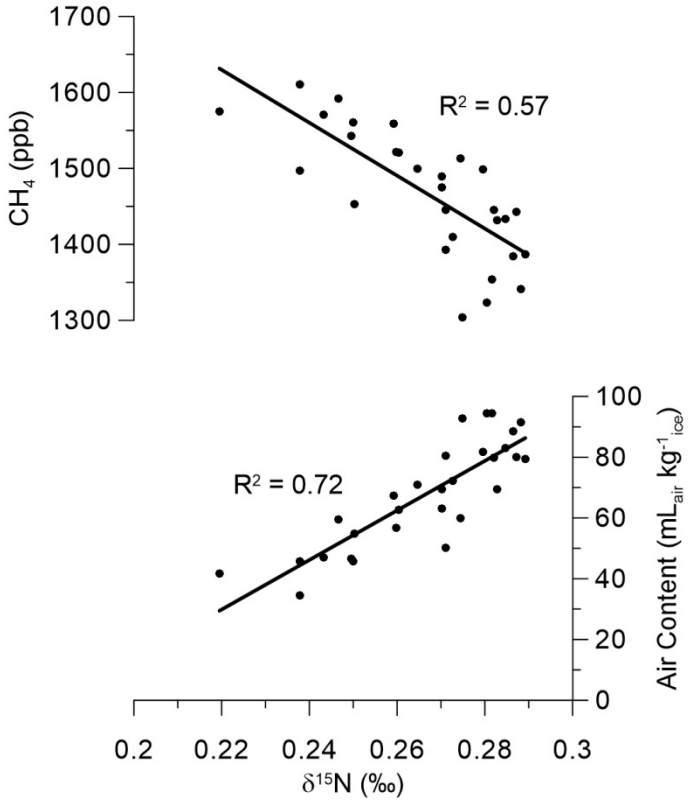

Figure 4.8. $\delta^{15}N$ vs. methane (CH_4, top) and air content (*V*, bottom).

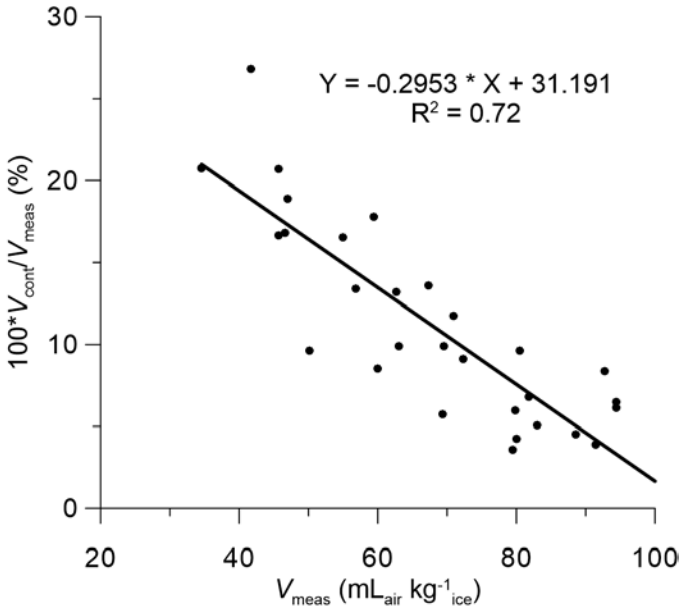

Figure 4.9. Relative amount of contaminated air vs. measured air content and the linear fit used to correct the CH_4, and *V* data.

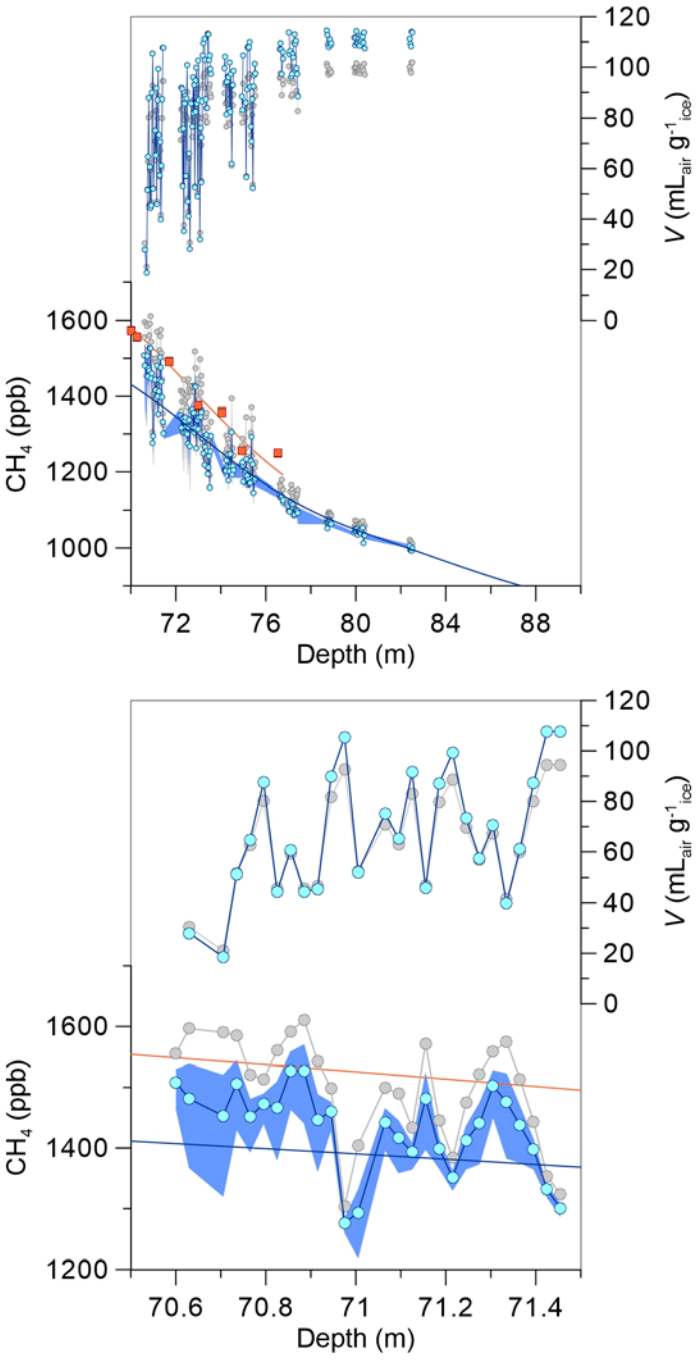

Figure 4.10. Overview of original and corrected values (top) as well as an expanded section (bottom). Orange squares and line are the open porosity measurements [*Battle et al.*, 2011] and model. Blue line is the model CH_4 in the closed porosity using the new stochastic parameterization. Grey circles are the original measurements. Blue circles are the measurements corrected for post-coring contamination (*V* and CH_4) and the cut bubble effect (*V* only). The light blue shaded region is the range of possible CH_4 values determined by assuming the contaminated CH_4 values range from 1800 ppb to 2400 ppb.

4.11 Tables

Table 4.1. Age distribution characteristics of the closed porosity at the bottom of the LIZ (z = 85 m) including the mean age and spectral width (a measure of the width of the age distribution). All values are given in years.

Parameterization	Mean	Δ
Barnola	89.9	11.4
Barnola-modified	86.9	10.2
Schwander (ρ_{co} = 830)	90.5	9.2
Schwander (ρ_{co} = 837)	87.8	8.7
Stochastic (this study)	91.0	9.7

General Conclusions

Paleoclimate research aims to expand our knowledge of the past climate system in part to improve our understanding of the modern climate and inform projections of future climate changes. Within paleoclimatological data collection there are two overarching themes, one, to extend records further back in time and two, to increase the detail of existing records in terms of both analytical precision as well as temporal resolution. The work presented here investigating the late Holocene global methane budget and advancing our knowledge of the processes controlling air entrapment in ice sheets thus is a logical progression of the latter theme. Here I summarize the key findings from this work and also discuss the prospects for future related work.

The second chapter describes the air extraction and methane analysis line that was used to produce the measurements in this thesis. This system was used to construct the highest resolution time series of methane variations to date for the time period from 1000-1800 C.E., from the shallow WAIS Divide Core (WDC05A). This record confirmed that the multidecadal scale variability originally observed in the Law Dome ice core was real [*Etheridge et al.*, 1998; *MacFarling Meure et al.*, 2006]. The variations in WDC05A had a magnitude of 10-34 ppb, translating to source changes of 4-12 Tg CH_4^{-1}, assuming that the global sink remained constant. The confirmation of the multidecadal scale variability naturally led to a broad search for correlations with other paleoclimate records which are proxies for factors that influence methane emissions, for example temperature and precipitation and examinations of historical records for possible influence from anthropogenic activities. I found that the multidecadal scale variability in methane concentrations was weakly correlated or uncorrelated with temperature and precipitation reconstructions from a range of geographic regions. The greatest correlations among a spatially resolved temperature reconstructions was for northern Eurasia, consistent with modern satellite observations of methane concentrations and surface air temperature on interannual timescales [*Bloom et al.*, 2010]. In addition, while the overall temporal correlation was not high, the time period with the highest

correlations was 1400-1600 C.E., during the onset of the Little Ice Age. I also found that the correlation with proxies for East Asian monsoon strength, a large methane source region, are low on multidecadal timescales, although chronologic uncertainties may have impacted this result. A comparison with a spatial reconstruction of the Palmer Drought Severity Index revealed the greatest correlation at the headwaters of major East Asian rivers, consistent with modern satellite observations. There are moderate to high correlations with proxies for the South American Summer Monsoon and tropical SSTs in the Cariaco basin, but these records need to be shifted by the maximum amount allowed by the uncertainty in their chronologies. The possible linkage with these proxy records on multidecadal timescales is important because the proxies are believed to represent broad aspects of the climate system, which have, in turn, been shown to correlate with millennial scale methane variability and could therefore be robust features in the climate system. It is possible that the lack of high correlations between these proxies and multidecadal scale methane variations is caused by the proxies not reflecting conditions over broad methane source regions, or that the variations were not large enough to significantly affect emissions at the multidecadal scale. I also examined anthropogenic activities that have been hypothesized to have impacted methane emissions and found that the synchronous timing between large population losses in Asia and the Americas with decreases in methane concentrations suggests that anthropogenic activities could have affected multidecadal scale methane variations.

In the third chapter I expand the set of methane measurements to the main borehole from WAIS Divide (WDC06A) back to 5 ka and from the Greenland GISP2 ice core back to 3 ka. The multidecadal scale variations are again clearly visible in both of these cores which allowed us to synchronize the chronologies with unprecedented precision. With synchronized ice core records from both polar regions in hand I constructed the first high resolution methane inter-polar difference (IPD) over the past 3 ka. The IPD constrains the latitudinal distribution of sources through time and by solving the global methane budget for this latitudinal distribution I found that the majority of the

increase in late Holocene methane emissions must have come from the tropics with a smaller contribution coming from northern hemisphere extratropical regions. I then used two temporal estimates of natural emissions and two estimates of anthropogenic emissions in a 8-box atmospheric methane model (EBAMM) to determine the predicted effects on the IPD over time. I found that by using the natural or anthropogenic emission estimates alone it is impossible to account for the full increase in global methane concentrations and the IPD. The anthropogenic scenarios produce a peak in the IPD from ~1000-1400 C.E. which is the result of an increase and subsequent decrease in population. This feature is also visible in the IPD record, which lends support to the anthropogenic hypothesis. However, the higher estimate of anthropogenic emissions causes an increase in the IPD over time which is not observed in the data. I then constructed a "Best" scenario which combines natural and anthropogenic emission scenarios. This scenario argues for anthropogenic emissions that are at the low end of those in the literature and natural emissions that are larger than those cited in the literature.

In the fourth chapter I coordinated an investigation to examine how the processes of air occlusion in bubbles in the ice sheet affects trace gas records trapped in the ice core. The novel data that instigated this investigation were CH_4 and total air content measurements I made from within the lock-in-zone (LIZ) at the WAIS Divide site. This study also includes measurements of the isotopic ratio of N_2 ($\delta^{15}N$) which constrained the amount of post-coring contamination, and high-resolution ice density which shows a tight relationship with discrete total air content measurements. I used these measurements to show that a common parameterizations for the occlusion of air is not technically correct since it was defined by the relationship between local density and pore space, but has been used to relate bulk density to pore space. I proposed a new parameterization that analytically accounts for the high-resolution density variability in the firn (e.g., layering). This new parameterization yields an improved model fit to many firn parameters such as closed/open porosity, total air content, and CH_4. It shows that our previous

understanding of the mean age of the air and age distribution was approximately correct, but offers a refined estimate that is constrained by observations. It has implications for the interpretation of total air content since the magnitude of density variability changes the depth at which air bubbles form which affects the final air content value in the ice core, which may help interpret glacial-interglacial changes in total air content records.

There are promising prospects for the continuation of the research themes presented in this work. Ice core methane measurements are increasingly being done with a new method involving continuous melting of the core coupled with laser spectroscopy. This method is significantly faster than making discrete measurements and, for example, construction of a multi-thousand year long record can be accomplished in a matter of weeks instead of multiple months using a discrete sample analysis technique. However, this new method suffers from a significant solubility correction that makes accompanying discrete measurements essential in order to quantify the absolute magnitude of the concentration. This will be important as further efforts are made to extend the IPD record present here further into the past. Also, for extremely high-resolution measurements (centimeter scale variations), discrete samples still provide higher resolution, and discrete measurements are better suited for measuring samples within the lock-in-zone (LIZ) where open porosity is present and it is possible to trap ambient air using a continuous melting technique. Furthermore, the discrete measurements obtain total air content measurements along with the CH_4 results, which is not yet possible with the continuous melting technique.

Naturally the IPD record that I have presented should be extended into the mid and early Holocene. Doing this could resolve the latitudinal distribution of natural methane emissions through the Holocene, which would be a valuable constraint for modeling studies. Also, a detailed modeling study of the final portion of the present record from 1500 C.E. to present would be valuable. There may be enough information in paleoclimate and historical records to reconstruct anthropogenic methane emissions in greater detail than possible for the earlier time and also examine the effects of possibly

changing per-capita emissions as well as the effect of cooling from the Little Ice Age on global methane concentrations.

With regard to firn air modeling, plans are already underway to repeat the experiment I conducted in greater detail at an ice coring location in Greenland, and it is also being proposed for an ice core drilling site at the South Pole. Ideally this should be done at a variety of locations so that the parameterization could be generalized to fit a variety of site characteristics, particularly at low accumulation sites in East Antarctica.

5.1 References

Bloom, A. A., P. I. Palmer, A. Fraser, D. S. Reay, and C. Frankenberg (2010), Large-Scale Controls of Methanogenesis Inferred from Methane and Gravity Spaceborne Data, *Science*, *327*(5963), 322-325.

Etheridge, D. M., L. P. Steele, R. J. Francey, and R. L. Langenfelds (1998), Atmospheric methane between 1000 AD and present: Evidence of anthropogenic emissions and climatic variability, *J. Geophys. Res.-Atmos.*, *103*(D13), 15979-15993.

MacFarling Meure, C., D. Etheridge, C. Trudinger, P. Steele, R. Langenfelds, T. van Ommen, A. Smith, and J. Elkins (2006), Law Dome CO_2, CH_4 and N_2O ice core records extended to 2000 years BP, *Geophys. Res. Let.*, *33*(14), 4.

Bibliography

Allen, L. H., S. L. Albrecht, W. Colon-Guasp, S. A. Covell, J. T. Baker, D. Y. Pan, and K. J. Boote (2003), Methane emissions of rice increased by elevated carbon dioxide and temperature, *J. Environ. Qual.*, *32*(6), 1978-1991.

Alley, R. B., et al. (1997), Visual-stratigraphic dating of the GISP2 ice core: Basis, reproducibility, and application, *J. Geophys. Res.-Oceans*, *102*(C12), 26367-26381.

Aydin, M., et al. (2010), Post-coring entrapment of modern air in some shallow ice cores collected near the firn-ice transition: evidence from CFC-12 measurements in Antarctic firn air and ice cores, *Atmos. Chem. Phys.*, *10*(11), 5135-5144.

Banta, J. R., J. R. McConnell, M. M. Frey, R. C. Bales, and K. Taylor (2008), Spatial and temporal variability in snow accumulation at the West Antarctic Ice Sheet Divide over recent centuries, *J. Geophys. Res.-Atmos.*, *113*(D23), 8.

Barnola, J. M., D. Raynaud, Y. S. Korotkevich, and C. Lorius (1987), VOSTOK ICE CORE PROVIDES 160,000-YEAR RECORD OF ATMOSPHERIC CO_2, *Nature*, *329*(6138), 408-414.

Bates, T. S., K. C. Kelly, J. E. Johnson, and R. H. Gammon (1996), A reevaluation of the open ocean source of methane to the atmosphere, *J. Geophys. Res.-Atmos.*, *101*(D3), 6953-6961.

Battle, M., et al. (1996), Atmospheric gas concentrations over the past century measured in air from firn at the South Pole, *Nature*, *383*(6597), 231-235.

Battle, M. O., J. P. Severinghaus, E. D. Sofen, D. Plotkin, A. J. Orsi, M. Aydin, S. A. Montzka, T. Sowers, and P. P. Tans (2011), Controls on the movement and composition of firn air at the West Antarctic Ice Sheet Divide, *Atmos. Chem. Phys.*, *11*(21), 11007-11021.

Baumgartner, M., A. Schilt, O. Eicher, J. Schmitt, J. Schwander, R. Spahni, H. Fischer, and T. F. Stocker (2012), High-resolution interpolar difference of atmospheric methane around the Last Glacial Maximum, *Biogeosciences*, *9*(10), 3961-3977.

Bekki, S., and K. S. Law (1997), Sensitivity of the atmospheric CH_4 growth rate to global temperature changes observed from 1980 to 1992, *Tellus Ser. B-Chem. Phys. Meteorol.*, *49*(4), 409-416.

Bergamaschi, P., et al. (2007), Satellite chartography of atmospheric methane from SCIAMACHY on board ENVISAT: 2. Evaluation based on inverse model simulations, *J. Geophys. Res.-Atmos.*, *112*(D2), 26.

Bergamaschi, P., et al. (2009), Inverse modeling of global and regional CH4 emissions using SCIAMACHY satellite retrievals, *J. Geophys. Res.-Atmos.*, *114*.

Berkelhammer, M., A. Sinha, M. Mudelsee, H. Cheng, R. L. Edwards, and K. Cannariato (2010), Persistent multidecadal power of the Indian Summer Monsoon, *Earth and Planetary Science Letters*, *290*(1-2), 166-172.

Black, D. E., L. C. Peterson, J. T. Overpeck, A. Kaplan, M. N. Evans, and M. Kashgarian (1999), Eight centuries of North Atlantic Ocean atmosphere variability, *Science*, *286*(5445), 1709-1713.

Black, D. E., M. A. Abahazi, R. C. Thunell, A. Kaplan, E. J. Tappa, and L. C. Peterson (2007), An 8-century tropical Atlantic SST record from the Cariaco Basin: Baseline variability, twentieth-century warming, and Atlantic hurricane frequency, *Paleoceanography*, *22*(4), 10.

Bloom, A. A., P. I. Palmer, A. Fraser, D. S. Reay, and C. Frankenberg (2010), Large-Scale Controls of Methanogenesis Inferred from Methane and Gravity Spaceborne Data, *Science*, *327*(5963), 322-325.

Blunier, T., J. Chappellaz, J. Schwander, B. Stauffer, and D. Raynaud (1995), Variations in atmospheric methane concentration during the Holocene epoch, *Nature*, *374*(6517), 46-49.

Blunier, T., J. A. Chappellaz, J. Schwander, J. M. Barnola, T. Desperts, B. Stauffer, and D. Raynaud (1993), Atmospheric methane, record from a greenland ice core over the last 1000 year, *Geophys. Res. Let.*, *20*(20), 2219-2222.

Blunier, T., and E. J. Brook (2001), Timing of millennial-scale climate change in Antarctica and Greenland during the last glacial period, *Science*, *291*(5501), 109-112.

Boone, C. D. (2000), Biological formation and consumption of methane, in *Atmospheric Methane: Its Role in the Global Environment*, edited by M. A. K. Khalil, pp. 42–62, Springer-Verlag, New York, NY.

Bousquet, P., D. A. Hauglustaine, P. Peylin, C. Carouge, and P. Ciais (2005), Two decades of OH variability as inferred by an inversion of atmospheric transport and chemistry of methyl chloroform, *Atmos. Chem. Phys.*, *5*, 2635-2656.

Bousquet, P., et al. (2006), Contribution of anthropogenic and natural sources to atmospheric methane variability, *Nature*, *443*(7110), 439-443.

Breton, D. J., G. S. Hamilton, and C. T. Hess (2009), Design, optimization and calibration of an automated density gauge for firn and ice cores, *J. of Glaciol.*, *55*, 1092-1100.

Briffa, K. R., T. J. Osborn, F. H. Schweingruber, I. C. Harris, P. D. Jones, S. G. Shiyatov, and E. A. Vaganov (2001), Low-frequency temperature variations from a northern tree ring density network, *J. Geophys. Res.-Atmos.*, *106*(D3), 2929-2941.

Brook, E. J., T. Sowers, and J. Orchardo (1996), Rapid variations in atmospheric methane concentration during the past 110,000 years, *Science*, *273*(5278), 1087-1091.

Brook, E. J., S. Harder, J. Severinghaus, E. J. Steig, and C. M. Sucher (2000), On the origin and timing of rapid changes in atmospheric methane during the last glacial period, *Glob. Biogeochem. Cycle*, *14*(2), 559-572.

Brook, E. J., J. W. C. White, A. S. M. Schilla, M. L. Bender, B. Barnett, J. P. Severinghaus, K. C. Taylor, R. B. Alley, and E. J. Steig (2005), Timing of millennial-scale climate change at Siple Dome, West Antarctica, during the last glacial period, *Quat. Sci. Rev.*, *24*(12-13), 1333-1343.

Buizert, C. (2011), The influence of firn air transport processes and radiocarbon production on gas records from polar firn and ice, Universtity of Copenhagen.

Buizert, C., T. Sowers, and T. Blunier (2013), Assessment of diffusive isotopic fractionation in polar firn, and application to ice core trace gas records, *Earth and Planetary Science Letters*, *361*(0), 110-119.

Buizert, C., et al. (2011), Gas transport in firn: multiple-tracer characterisation and model intercomparison for NEEM, Northern Greenland, *Atmos. Chem. Phys. Discuss.*, *11*(5), 15975-16021.

Buizert, C., et al. (2012), Gas transport in firn: multiple-tracer characterisation and model intercomparison for NEEM, Northern Greenland, *Atmos. Chem. Phys.*, *12*(9), 4259-4277.

Chappellaz, J., E. Brook, T. Blunier, and B. Malaize (1997a), CH_4 and $d^{18}O$ of O_2 records from Antarctic and Greenland ice: A clue for stratigraphic disturbance in the bottom part of the Greenland Ice Core Project and the Greenland Ice Sheet Project 2 ice cores, *J. Geophys. Res.-Oceans*, *102*(C12), 26547-26557.

Chappellaz, J., J. M. Barnola, D. Raynaud, Y. S. Korotkevich, and C. Lorius (1990), Ice-core record of atmospheric methane over the past 160,000 years, *Nature*, *345*(6271), 127-131.

Chappellaz, J., T. Blunier, D. Raynaud, J. M. Barnola, J. Schwander, and B. Stauffer (1993), Synchronous changes in atmospheric CH_4 and Greenland climate between 40 and 8 kyr BP, *Nature*, *366*(6454), 443-445.

Chappellaz, J., T. Blunier, S. Kints, A. Dallenbach, J. M. Barnola, J. Schwander, D. Raynaud, and B. Stauffer (1997b), Changes in the atmospheric CH_4 gradient between Greenland and Antarctica during the Holocene, *J. Geophys. Res.-Atmos.*, *102*(D13), 15987-15997.

Christensen, T. R., T. R. Johansson, H. J. Akerman, M. Mastepanov, N. Malmer, T. Friborg, P. Crill, and B. H. Svensson (2004), Thawing sub-arctic permafrost: Effects on vegetation and methane emissions, *Geophys. Res. Let.*, *31*(4), 4.

Cook, E. R., J. Esper, and R. D. D'Arrigo (2004), Extra-tropical Northern Hemisphere land temperature variability over the past 1000 years, *Quat. Sci. Rev.*, *23*(20-22), 2063-2074.

Cook, E. R., K. J. Anchukaitis, B. M. Buckley, R. D. D'Arrigo, G. C. Jacoby, and W. E. Wright (2010), Asian Monsoon Failure and Megadrought During the Last Millennium, *Science*, *328*(5977), 486-489.

Cook, N. D. (1998), *Born to die : disease and New World conquest, 1492-1650*, xiii, 248 p. : pp., Cambridge University Press, Cambridge ; New York :.

Craig, H., and C. C. Chou (1982), METHANE - THE RECORD IN POLAR ICE CORES, *Geophys. Res. Let.*, *9*(11), 1221-1224.

Craig, H., Y. Horibe, and T. Sowers (1988), Gravitational Separation of Gases and Isotopes in Polar Ice Caps, *Science*, *242*(4886), 1675-1678.

Crespin, E., H. Goosse, T. Fichefet, and M. E. Mann (2009), The 15th century Arctic warming in coupled model simulations with data assimilation, *Clim. Past.*, *5*(3), 389-401.

Crutzen, P. J., and C. Bruhl (1993), A model study of atmospheric temperatures and the concentrations of ozone, hydroxyl, and some other photochemically active gases during the glacial, the pre-industrial Holocene and the present *Geophys. Res. Let.*, *20*(11), 1047-1050.

Cruz, F. W., S. J. Burns, I. Karmann, W. D. Sharp, M. Vuille, A. O. Cardoso, J. A. Ferrari, P. L. S. Dias, and O. Viana (2005), Insolation-driven changes in atmospheric circulation over the past 116,000 years in subtropical Brazil, *Nature*, *434*(7029), 63-66.

Cuffey, K. M., and G. D. Clow (1997), Temperature, accumulation, and ice sheet elevation in central Greenland through the last deglacial transition, *J. Geophys. Res.-Oceans*, *102*(C12), 26383-26396.

Cuffey, K. M., and W. Paterson (2010), *The physics of glaciers*, Academic Press.

Cunnold, D. M., et al. (2002), In situ measurements of atmospheric methane at GAGE/AGAGE sites during 1985-2000 and resulting source inferences, *J. Geophys. Res.-Atmos.*, *107*(D14), 20.

D'Arrigo, R., R. Wilson, and G. Jacoby (2006), On the long-term context for late twentieth century warming, *J. Geophys. Res.-Atmos.*, *111*(D3), 12.

Dansgaard, W., S. J. Johnsen, J. Møller, and C. C. Langway, Jr. (1969), One Thousand Centuries of Climatic Record from Camp Century on the Greenland Ice Sheet, *Science*, *166*(3903), 377-381.

de Boor, C. (2001), *A Practical Guide to Splines*, Springer, New York.

Delmotte, M., J. Chappellaz, E. Brook, P. Yiou, J. M. Barnola, C. Goujon, D. Raynaud, and V. I. Lipenkov (2004), Atmospheric methane during the last four glacial-interglacial cycles: Rapid changes and their link with Antarctic temperature, *J. Geophys. Res.-Atmos.*, *109*(D12), 13.

Delmotte, M., D. Raynaud, V. Morgan, and J. Jouzel (1999), Climatic and glaciological information inferred from air-content measurements of a Law Dome (East Antarctica) ice core, *J. of Glaciol.*, *45*(150), 255-263.

Dentener, F., W. Peters, M. Krol, M. van Weele, P. Bergamaschi, and J. Lelieveld (2003), Interannual variability and trend of CH4 lifetime as a measure for OH changes in the 1979-1993 time period, *J. Geophys. Res.-Atmos.*, *108*(D15).

Dlugokencky, E. J., L. P. Steele, P. M. Lang, and K. A. Masarie (1994), The growth rate and distribution of atmospheric methane, *J. Geophys. Res.-Atmos.*, *99*(D8), 17021-17043.

Dlugokencky, E. J., K. A. Masarie, P. M. Lang, and P. P. Tans (1998), Continuing decline in the growth rate of the atmospheric methane burden, *Nature*, *393*(6684), 447-450.

Dlugokencky, E. J., P. M. Lang, A. M. Crotwell, and K. A. Masaire (2012), Atmospheric Methane Dry Air Mole Fractions from the NOAA ESRL Carbon Cycle Cooperative Global Air Sampling Network, 1983-2011, Version: 2012-09-24, Path: ftp://ftp.cmdl.noaa.gov/ccg/ch4/flask/event/, edited.

Dlugokencky, E. J., K. A. Masarie, P. M. Lang, P. P. Tans, L. P. Steele, and E. G. Nisbet (1994), A dramatic decrease in the growth rate of atmospheric methane in the northern hemisphere during 1992, *Geophys. Res. Let.*, *21*(1), 45-48.

Dlugokencky, E. J., R. C. Myers, P. M. Lang, K. A. Masarie, A. M. Crotwell, K. W. Thoning, B. D. Hall, J. W. Elkins, and L. P. Steele (2005), Conversion of NOAA atmospheric dry air CH_4 mole fractions to a gravimetrically prepared standard scale, *J. Geophys. Res.-Atmos.*, *110*(D18), 8.

Dlugokencky, E. J., et al. (2009), Observational constraints on recent increases in the atmospheric CH4 burden, *Geophys. Res. Let.*, *36*.

Dunbar, N. W., G. A. Zielinski, and D. T. Voisins (2003), Tephra layers in the Siple Dome and Taylor Dome ice cores, Antarctica: Sources and correlations, *J. Geophys. Res.-Solid Earth*, *108*(B8).

Dunbar, N. W., W. C. McIntosh, A. V. Kurbatov, and T. I. Wilch (2007), Integrated Tephrochronology of the West Antarctic Region- Implications for a potential tephra record in the West Antarctic Ice Sheet (WAIS) Divide Ice Core, paper presented at WAIS Divide Science Meeting, Tahoe, N.M.

EPICA Community Members (2006), One-to-one coupling of glacial climate variability in Greenland and Antarctica, *Nature*, *444*(7116), 195-198.

Esper, J., E. R. Cook, and F. H. Schweingruber (2002), Low-Frequency Signals in Long Tree-Ring Chronologies for Reconstructing Past Temperature Variability, *Science*, *295*(5563), 2250-2253.

Etheridge, D. M., P. G. I., and d. S. F. (1988), Atmospheric trace-gas variations as revealed by air trapped in an ice core from Law Dome, Antarctica, *Ann. Glac.*, *10*, 28-33.

Etheridge, D. M., G. I. Pearman, and P. J. Fraser (1992), Changes in tropospheric methane between 1841 and 1978 from a high accumulation rate Antarctic ice core, *Tellus Ser. B-Chem. Phys. Meteorol.*, *44*(4), 282-294.

Etheridge, D. M., L. P. Steele, R. J. Francey, and R. L. Langenfelds (1998), Atmospheric methane between 1000 AD and present: Evidence of anthropogenic emissions and climatic variability, *J. Geophys. Res.-Atmos.*, *103*(D13), 15979-15993.

Etiope, G., A. V. Milkov, and E. Derbyshire (2008a), Did geologic emissions of methane play any role in Quaternary climate change?, *Glob. Planet. Change*, *61*(1-2), 79-88.

Etiope, G., K. R. Lassey, R. W. Klusman, and E. Boschi (2008b), Reappraisal of the fossil methane budget and related emission from geologic sources, *Geophys. Res. Let.*, *35*(9).

Fegyveresi, J. M., R. B. Alley, M. K. Spencer, J. J. Fitzpatrick, E. J. Steig, J. W. C. White, J. R. McConnell, and K. C. Taylor (2011), Late-Holocene climate evolution at the WAIS Divide site, West Antarctica: bubble number-density estimates, *J. of Glaciol.*, *57*(204), 629-638.

Ferretti, D. F., et al. (2005), Unexpected Changes to the Global Methane Budget over the Past 2000 Years, *Science*, *309*(5741), 1714-1717.

Fischer, H., et al. (2008), Changing boreal methane sources and constant biomass burning during the last termination, *Nature*, *452*(7189), 864-867.

Fogg, P. G. T., Sangster, J. (2003), *Chemicals in the atmosphere : solubility, sources, and reactivity / Peter Fogg and James Sangster ; with contributions from Yin-Nan Lee, Stephen Schwartz, Peter Warneck*, ix, 453 p. : pp., J. Wiley, Hoboken, NJ :.

Forster, P., et al. (2007), Changes in Atmospheric Constituents and in Radiative Forcing., in *Climate Change 2007: The Physical Science Basis. Contribution of Working Group I to the Fourth Assessment Report of the Intergovernmental Panel on Climate Change*, edited by S. Solomon, D. Qin, M. Manning, Z. Chen, M. Marquis, K. B. Averyt, M. Tignor and H. L. Miller, pp. 131-234, Cambridge University Press, Cambridge, United Kingdom and New York, NY, USA.

Fuller, D. Q., J. van Etten, K. Manning, C. Castillo, E. Kingwell-Banham, A. Weisskopf, L. Qin, Y. I. Sato, and R. J. Hijmans (2011), The contribution of rice agriculture and livestock pastoralism to prehistoric methane levels: An archaeological assessment, *Holocene*, *21*(5), 743-759.

Fung, I., J. John, J. Lerner, E. Matthews, M. Prather, L. P. Steele, and P. J. Fraser (1991), 3-Dimensional Model Synthesis of the Global Methane Cycle, *J. Geophys. Res.-Atmos.*, *96*(D7), 13033-13065.

Goldewijk, K. K., A. Beusen, and P. Janssen (2010), Long-term dynamic modeling of global population and built-up area in a spatially explicit way: HYDE 3.1, *Holocene*, *20*(4), 565-573.

Goldewijk, K. K., A. Beusen, G. van Drecht, and M. de Vos (2011), The HYDE 3.1 spatially explicit database of human-induced global land-use change over the past 12,000 years, *Glob. Ecol. Biogeogr.*, *20*(1), 73-86.

Goujon, C., J. M. Barnola, and C. Ritz (2003), Modeling the densification of polar firn including heat diffusion: Application to close-off characteristics and gas isotopic fractionation for Antarctica and Greenland sites, *J. Geophys. Res.-Atmos.*, *108*(D24), 18.

Grachev, A. M., E. J. Brook, and J. P. Severinghaus (2007), Abrupt changes in atmospheric methane at the MIS 5b-5a transition, *Geophys. Res. Let.*, *34*(20), 5.

Grachev, A. M., E. J. Brook, J. P. Severinghaus, and N. G. Pisias (2009), Relative timing and variability of atmospheric methane and GISP2 oxygen isotopes between 68 and 86 ka, *Glob. Biogeochem. Cycle*, *23*, 10.

Grudd, H., K. R. Briffa, W. Karlen, T. S. Bartholin, P. D. Jones, and B. Kromer (2002), A 7400-year tree-ring chronology in northern Swedish Lapland: natural climatic variability expressed on annual to millennial timescales, *Holocene*, *12*(6), 657-665.

Gu, G. J., R. F. Adler, G. J. Huffman, and S. Curtis (2007), Tropical rainfall variability on interannual-to-interdecadal and longer time scales derived from the GPCP monthly product, *J. Clim.*, *20*(15), 4033-4046.

Harder, S. L., D. T. Shindell, G. A. Schmidt, and E. J. Brook (2007), A global climate model study of CH_4 emissions during the Holocene and glacial-interglacial transitions constrained by ice core data, *Glob. Biogeochem. Cycle*, *21*(1), 13.

Hegerl, G. C., T. J. Crowley, M. Allen, W. T. Hyde, H. N. Pollack, J. Smerdon, and E. Zorita (2007), Detection of human influence on a new, validated 1500-year temperature reconstruction, *J. Clim.*, *20*(4), 650-666.

Hein, R., P. J. Crutzen, and M. Heimann (1997), An inverse modeling approach to investigate the global atmospheric methane cycle, *Glob. Biogeochem. Cycle*, *11*(1), 43-76.

Herron, M. M., and C. C. Langway (1980), Firn Densification: An Empirical Model, *J. of Glaciol.*, *25*(93), 373-385.

Hörhold, M. W., S. Kipfstuhl, F. Wilhelms, J. Freitag, and A. Frenzel (2011), The densification of layered polar firn, *J. Geophys. Res.-Earth Surf.*, *116*.

Hörhold, M. W., T. Laepple, J. Freitag, M. Bigler, H. Fischer, and S. Kipfstuhl (2012), On the impact of impurities on the densification of polar firn, *Earth and Planetary Science Letters*, *325–326*(0), 93-99.

Hopcroft, P. O., P. J. Valdes, and D. J. Beerling (2011), Simulating idealized Dansgaard-Oeschger events and their potential impacts on the global methane cycle, *Quat. Sci. Rev.*, *30*(23-24), 3258-3268.

Houweling, S., F. Dentener, and J. Lelieveld (2000), Simulation of preindustrial atmospheric methane to constrain the global source strength of natural wetlands, *J. Geophys. Res.-Atmos.*, *105*(D13), 17243-17255.

Houweling, S., G. R. van der Werf, K. K. Goldewijk, T. Rockmann, and I. Aben (2008), Early anthropogenic CH_4 emissions and the variation of CH_4 and $^{13}CH_4$ over the last millennium, *Glob. Biogeochem. Cycle*, *22*(1), 9.

Hu, C. Y., G. M. Henderson, J. H. Huang, S. Xie, Y. Sun, and K. R. Johnson (2008), Quantification of Holocene Asian monsoon rainfall from spatially separated cave records, *Earth and Planetary Science Letters*, *266*(3-4), 221-232.

Huber, C., M. Leuenberger, R. Spahni, J. Fluckiger, J. Schwander, T. F. Stocker, S. Johnsen, A. Landals, and J. Jouzel (2006), Isotope calibrated Greenland temperature record over Marine Isotope Stage 3 and its relation to CH4, *Earth and Planetary Science Letters*, *243*(3-4), 504-519.

Johnsen, S. J., et al. (1997), The delta $\delta^{18}O$ record along the Greenland Ice Core Project deep ice core and the problem of possible Eemian climatic instability, *J. Geophys. Res.-Oceans*, *102*(C12), 26397-26410.

Jones, P. D., et al. (2009), High-resolution palaeoclimatology of the last millennium: a review of current status and future prospects, *Holocene*, *19*(1), 3-49.

Kalambet, Y., Y. Kozmin, K. Mikhailova, I. Nagaev, and P. Tikhonov (2011), Reconstruction of chromatographic peaks using the exponentially modified Gaussian function, *Journal of Chemometrics*, *25*(7), 352-356.

Kaplan, J. O., G. Folberth, and D. A. Hauglustaine (2006), Role of methane and biogenic volatile organic compound sources in late glacial and Holocene fluctuations of atmospheric methane concentrations, *Glob. Biogeochem. Cycle*, *20*(2), 16.

Kaufman, D. S., D. P. Schneider, N. P. McKay, C. M. Ammann, R. S. Bradley, K. R. Briffa, G. H. Miller, B. L. Otto-Bliesner, J. T. Overpeck, and B. M. Vinther

(2009), Recent Warming Reverses Long-Term Arctic Cooling, *Science*, *325*(5945), 1236-1239.

Kawamura, K., J. P. Severinghaus, S. Ishidoya, S. Sugawara, G. Hashida, H. Motoyama, Y. Fujii, S. Aoki, and T. Nakazawa (2006), Convective mixing of air in firn at four polar sites, *Earth and Planetary Science Letters*, *244*(3–4), 672-682.

Khalil, M. A. K. (Ed.) (2000), *Atmospheric Methane: Its Role in the Global Environment*, 341 pp., Springer-Verlag, Berlin Heidelberg New York.

Khalil, M. A. K., and R. A. Rasmussen (1983), Sources, Sinks, and Seasonal Cycles of Atmospheric Methane, *Journal of Geophysical Research-Oceans and Atmospheres*, *88*(NC9), 5131-5144.

Khalil, M. A. K., R. A. Rasmussen, and M. J. Shearer (1989), Trends of Atmospheric Methane During the 1960s and 1970s, *J. Geophys. Res.-Atmos.*, *94*(D15), 18279-18288.

Kobashi, T., J. P. Severinghaus, E. J. Brook, J. M. Barnola, and A. M. Grachev (2007), Precise timing and characterization of abrupt climate change 8200 years ago from air trapped in polar ice, *Quat. Sci. Rev.*, *26*(9-10), 1212-1222.

Kobashi, T., J. P. Severinghaus, J. M. Barnola, K. Kawamura, T. Carter, and T. Nakaegawa (2010), Persistent multi-decadal Greenland temperature fluctuation through the last millennium, *Clim. Change*, *100*(3-4), 733-756.

Kobashi, T., K. Kawamura, J. P. Severinghaus, J. M. Barnola, T. Nakaegawa, B. M. Vinther, S. J. Johnsen, and J. E. Box (2011), High variability of Greenland surface temperature over the past 4000 years estimated from trapped air in an ice core, *Geophys. Res. Let.*, *38*.

Konijnendijk, T. Y. M., S. L. Weber, E. Tuenter, and M. van Weele (2011), Methane variations on orbital timescales: a transient modeling experiment, *Clim. Past.*, *7*(2), 635-648.

Kreutz, K., B. Koffman, D. Breton, and G. S. Hamilton (2011), Microparticle, Conductivity, and Density Measurements from the WAIS Divide Deep Ice Core, Antarctica.

Landais, A., et al. (2003), A tentative reconstruction of the last interglacial and glacial inception in Greenland based on new gas measurements in the Greenland Ice Core Project (GRIP) ice core, *J. Geophys. Res.-Atmos.*, *108*(D18), 12.

Lassey, K. R., D. M. Etheridge, D. C. Lowe, A. M. Smith, and D. F. Ferretti (2007), Centennial evolution of the atmospheric methane budget: what do the carbon isotopes tell us?, *Atmos. Chem. Phys.*, *7*(8), 2119-2139.

Lea, D. W., D. K. Pak, L. C. Peterson, and K. A. Hughen (2003), Synchroneity of tropical and high-latitude Atlantic temperatures over the last glacial termination, *Science*, *301*(5638), 1361-1364.

Lelieveld, J., P. J. Crutzen, and F. J. Dentener (1998), Changing concentration, lifetime and climate forcing of atmospheric methane, *Tellus Ser. B-Chem. Phys. Meteorol.*, *50*(2), 128-150.

Lelieveld, J., et al. (2008), Atmospheric oxidation capacity sustained by a tropical forest, *Nature*, *452*(7188), 737-740.

Lemieux-Dudon, B., E. Blayo, J. R. Petit, C. Waelbroeck, A. Svensson, C. Ritz, J. M. Barnola, B. M. Narcisi, and F. Parrenin (2010), Consistent dating for Antarctic and Greenland ice cores, *Quat. Sci. Rev.*, *29*(1-2), 8-20.

Lipenkov, V., F. Candaudap, J. Ravoire, E. Dulac, and D. Raynaud (1995), A new device for the measurement of air content in polar ice, *J. of Glaciol.*, *41*(138), 423-429.

Loulergue, L., A. Schilt, R. Spahni, V. Masson-Delmotte, T. Blunier, B. Lemieux, J. M. Barnola, D. Raynaud, T. F. Stocker, and J. Chappellaz (2008), Orbital and millennial-scale features of atmospheric CH_4 over the past 800,000 years, *Nature*, *453*(7193), 383-386.

Luthi, D., et al. (2008), High-resolution carbon dioxide concentration record 650,000-800,000 years before present, *Nature*, *453*(7193), 379-382.

MacDonald, G. M., and R. A. Case (2005), Variations in the Pacific Decadal Oscillation over the past millennium, *Geophys. Res. Let.*, *32*(8).

MacFarling Meure, C., D. Etheridge, C. Trudinger, P. Steele, R. Langenfelds, T. van Ommen, A. Smith, and J. Elkins (2006), Law Dome CO_2, CH_4 and N_2O ice core records extended to 2000 years BP, *Geophys. Res. Let.*, *33*(14), 4.

Mann, M. E., Z. Zhang, M. K. Hughes, R. S. Bradley, S. K. Miller, S. Rutherford, and F. Ni (2008), Proxy-based reconstructions of hemispheric and global surface temperature variations over the past two millennia, *Proceedings of the National Academy of Sciences*, *105*(36), 13252-13257.

Mann, M. E., Z. H. Zhang, S. Rutherford, R. S. Bradley, M. K. Hughes, D. Shindell, C. Ammann, G. Faluvegi, and F. B. Ni (2009), Global Signatures and Dynamical Origins of the Little Ice Age and Medieval Climate Anomaly, *Science*, *326*(5957), 1256-1260.

Mantua, N. J., and S. R. Hare (2002), The Pacific decadal oscillation, *J. Oceanogr.*, *58*(1), 35-44.

Mantua, N. J., S. R. Hare, Y. Zhang, J. M. Wallace, and R. C. Francis (1997), A Pacific interdecadal climate oscillation with impacts on salmon production, *Bull. Amer. Meteorol. Soc.*, *78*(6), 1069-1079.

Marik, T. (1998), Atmospheric $d^{13}C$ and dD measurements to balance the global methane budget, Ph.D. thesis, University of Heidelberg, Heidelberg, Germany.

Marlon, J. R., P. J. Bartlein, C. Carcaillet, D. G. Gavin, S. P. Harrison, P. E. Higuera, F. Joos, M. J. Power, and I. C. Prentice (2008), Climate and human influences on global biomass burning over the past two millennia, *Nat. Geosci.*, *1*(10), 697-702.

Martinerie, P., D. Raynaud, D. M. Etheridge, J. M. Barnola, and D. Mazaudier (1992), Physical and climatic parameters which influence the air content in polar ice, *Earth and Planetary Science Letters*, *112*(1-4), 1-13.

Martinerie, P., V. Y. Lipenkov, D. Raynaud, J. Chappellaz, N. I. Barkov, and C. Lorius (1994), Air content paleo record in the Vostok ice core (Antarctica): A mixed record of climatic and glaciological parameters, *J. Geophys. Res.-Atmos.*, *99*(D5), 10565-10576.

Martinerie, P., G. P. Brasseur, and C. Granier (1995), The chemical composition of ancient atmospheres: A model study constrained by ice core data, *J. Geophys. Res.-Atmos.*, *100*(D7), 14291-14304.

Matthews, E. (2000), Wetlands, in *Atmospheric Methane: Its Role in the Global Environment*, edited by M. A. K. Khalil, pp. 202-233, Springer-Verlag, Berlin Heidelberg New York.

Matthews, J. A., and K. R. Briffa (2005), The 'Little Ice Age': Re-evaluation of an evolving concept, *Geogr. Ann. Ser. A-Phys. Geogr.*, *87A*(1), 17-36.

Mayewski, P. A., L. D. Meeker, M. S. Twickler, S. Whitlow, Q. Z. Yang, W. B. Lyons, and M. Prentice (1997), Major features and forcing of high-latitude northern hemisphere atmospheric circulation using a 110,000-year-long glaciochemical series, *J. Geophys. Res.-Oceans*, *102*(C12), 26345-26366.

McEvedy, C., and R. Jones (1978), *Atlas of World Population History*, 368 pp., Penguin, London.

Meese, D. A., A. J. Gow, P. Grootes, P. A. Mayewski, M. Ram, M. Stuiver, K. C. Taylor, E. D. Waddington, and G. A. Zielinski (1994), The Accumulation Record from the GISP2 Core as an Indicator of Climate Change Throughout the Holocene, *Science*, *266*(5191), 1680-1682.

Mischler, J. A., T. A. Sowers, R. B. Alley, M. Battle, J. R. McConnell, L. Mitchell, T. Popp, E. Sofen, and M. K. Spencer (2009), Carbon and hydrogen isotopic composition of methane over the last 1000 years, *Glob. Biogeochem. Cycle*, *23*.

Mitchell, L., and E. J. Brook (2009), New high-precision, high-resolution records of atmospheric methane from Greenland and Antarctic ice cores: 0-1800 A.D, *EOS, Trans., AGU*, *90*(52), Fall Meet. Suppl., Abstract PP41B-1524.

Mitchell, L. E., E. J. Brook, T. Sowers, J. R. McConnell, and K. Taylor (2011), Multidecadal variability of atmospheric methane, 1000-1800 CE, *J. Geophys. Res.-Biogeosci.*, *116*.

Moberg, A., D. M. Sonechkin, K. Holmgren, N. M. Datsenko, and W. Karlen (2005), Highly variable Northern Hemisphere temperatures reconstructed from low- and high-resolution proxy data, *Nature*, *433*(7026), 613-617.

Montzka, S. A., M. Krol, E. Dlugokencky, B. Hall, P. Jockel, and J. Lelieveld (2011), Small Interannual Variability of Global Atmospheric Hydroxyl, *Science*, *331*(6013).

Morse, D. L., D. D. Blankenship, E. D. Waddington, and T. A. Neumann (2002), A site for deep ice coring in West Antarctica: results from aerogeophysical surveys and thermo-kinematic modeling, in *Annals of Glaciology, Vol 35*, edited, pp. 36-44, Int Glaciological Soc, Cambridge.

Oppo, D. W., Y. Rosenthal, and B. K. Linsley (2009), 2,000-year-long temperature and hydrology reconstructions from the Indo-Pacific warm pool, *Nature*, *460*(7259), 1113-1116.

Orsi, A. J., B. D. Cornuelle, and J. P. Severinghaus (2012), Little Ice Age cold interval in West Antarctica: Evidence from borehole temperature at the West Antarctic Ice Sheet (WAIS) Divide, *Geophys. Res. Let.*, *39*(9), L09710.

Palmer, A. S., T. D. van Ommen, M. A. J. Curran, V. Morgan, J. M. Souney, and P. A. Mayewski (2001), High-precision dating of volcanic events - (AD 1301-1995) using ice cores from Law Dome, Antarctica, *J. Geophys. Res.-Atmos.*, *106*(D22), 28089-28095.

Pechony, O., and D. T. Shindell (2010), Driving forces of global wildfires over the past millennium and the forthcoming century, *Proc. Natl. Acad. Sci. U. S. A.*, *107*(45), 19167-19170.

Petit, J. R., et al. (1999), Climate and atmospheric history of the past 420,000 years from the Vostok ice core, Antarctica, *Nature*, *399*(6735), 429-436.

Petoukhov, V., A. Ganopolski, V. Brovkin, M. Claussen, A. Eliseev, C. Kubatzki, and S. Rahmstorf (2000), CLIMBER-2: a climate system model of intermediate complexity. Part I: model description and performance for present climate, *Clim. Dyn.*, *16*(1), 1-17.

Petrenko, V. V., J. P. Severinghaus, E. J. Brook, N. Reeh, and H. Schaefer (2006), Gas records from the West Greenland ice margin covering the Last Glacial Termination: a horizontal ice core, *Quat. Sci. Rev.*, *25*(9-10), 865-875.

Petrenko, V. V., et al. (2008), A novel method for obtaining very large ancient air samples from ablating glacial ice for analyses of methane radiocarbon, *J. of Glaciol.*, *54*(185), 233-244.

Pongratz, J., C. Reick, T. Raddatz, and M. Claussen (2008), A reconstruction of global agricultural areas and land cover for the last millennium, *Glob. Biogeochem. Cycle*, *22*(3).

Prinn, R. G., et al. (2001), Evidence for Substantial Variations of Atmospheric Hydroxyl Radicals in the Past Two Decades, *Science*, *292*(5523), 1882-1888.

Rasmussen, R. A., and M. A. K. Khalil (1984), Atmospheric Methane in the Recent and Ancient Atmospheres: Concentrations, Trends, and Interhemispheric Gradient, *J. Geophys. Res.-Atmos.*, *89*(ND7), 1599-1605.

Raynaud, D., and I. M. Whillans (1982), AIR CONTENT OF THE BYRD CORE AND PAST CHANGES IN THE WEST ANTARCTIC ICE SHEET, *Ann. Glac.*, *3*, 269-273.

Raynaud, D., J. Chappellaz, J. M. Barnola, Y. S. Korotkevich, and C. Lorius (1988), CLIMATIC AND CH4 CYCLE IMPLICATIONS OF GLACIAL INTERGLACIAL CH4 CHANGE IN THE VOSTOK ICE CORE, *Nature*, *333*(6174), 655-657.

Raynaud, D., J. Jouzel, J. M. Barnola, J. Chappellaz, R. J. Delmas, and C. Lorius (1993), The ice record of greenhouse gases, *Science*, *259*(5097), 926-934.

Raynaud, D., J. Chappellaz, C. Ritz, and P. Martinerie (1997), Air content along the Greenland Ice Core Project core: A record of surface climatic parameters and elevation in central Greenland, *J. Geophys. Res.-Oceans*, *102*(C12), 26607-26613.

Reuter, J., L. Stott, D. Khider, A. Sinha, H. Cheng, and R. L. Edwards (2009), A new perspective on the hydroclimate variability in northern South America during the Little Ice Age, *Geophys. Res. Let.*, *36*.

Rhee, T. S., A. J. Kettle, and M. O. Andreae (2009), Methane and nitrous oxide emissions from the ocean: A reassessment using basin-wide observations in the Atlantic, *J. Geophys. Res.-Atmos.*, *114*.

Rhodes, R. H., X. Faïn, C. Stowasser, T. Blunier, J. Chappellaz, J. R. McConnell, L. E. Mitchell, and E. Brook (Submitted), Continuous ice core methane measurements: atmospheric and in-situ signals, *Earth and Planetary Science Letters*.

Robbins, R. C., L. A. Cavanagh, L. J. Salas, and E. Robinson (1973), ANALYSIS OF ANCIENT ATMOSPHERES, *Journal of Geophysical Research, 78*(24), 5341-5344.

Rohde, R. A., P. B. Price, R. C. Bay, and N. E. Bramall (2008), In situ microbial metabolism as a cause of gas anomalies in ice, *Proc. Natl. Acad. Sci. U. S. A.*, *105*(25), 8667-8672.

Ruddiman, W. F. (2003), The anthropogenic greenhouse era began thousands of years ago, *Clim. Change*, *61*(3), 261-293.

Ruddiman, W. F. (2007), The early anthropogenic hypothesis: Challenges and responses, *Reviews of Geophysics*, *45*(3), 37.

Ruddiman, W. F., J. E. Kutzbach, and S. J. Vavrus (2011), Can natural or anthropogenic explanations of late-Holocene CO2 and CH4 increases be falsified?, *Holocene*, *21*(5), 865-879.

Ruddiman, W. F., Z. T. Guo, X. Zhou, H. B. Wu, and Y. Y. Yu (2008), Early rice farming and anomalous methane trends, *Quat. Sci. Rev.*, *27*(13-14), 1291-1295.

Sapart, C. J., et al. (2012), Natural and anthropogenic variations in methane sources during the past two millennia, *Nature*, *490*(7418), 85-88.

Schilt, A., et al. (2010), Atmospheric nitrous oxide during the last 140,000 years, *Earth and Planetary Science Letters*, *300*(1-2), 33-43.

Schwander, J. (1989), The transformation of snow to ice and the occlusion of gases, in *The Environmental Record in Glaciers and Ice Sheets*, edited by H. Oeschger and C. C. Langway, pp. 53-67, John Wiley, Chichester [England] ; New York :.

Schwander, J., and B. Stauffer (1984), Age difference between polar ice and the air trapped in its bubbles, *Nature*, *311*(5981), 45-47.

Schwander, J., T. Sowers, J. M. Barnola, T. Blunier, A. Fuchs, and B. Malaize (1997), Age scale of the air in the summit ice: Implication for glacial-interglacial temperature change, *J. Geophys. Res.-Atmos.*, *102*(D16), 19483-19493.

Schwander, J., J. M. Barnola, C. Andrie, M. Leuenberger, A. Ludin, D. Raynaud, and B. Stauffer (1993), The Age of the Air in the Firn and the Ice at Summit, Greenland, *J. Geophys. Res.-Atmos.*, *98*(D2), 2831-2838.

Severinghaus, J. P., and E. J. Brook (1999), Abrupt climate change at the end of the last glacial period inferred from trapped air in polar ice, *Science*, *286*(5441), 930-934.

Severinghaus, J. P., T. Sowers, E. J. Brook, R. B. Alley, and M. L. Bender (1998), Timing of abrupt climate change at the end of the Younger Dryas interval from thermally fractionated gases in polar ice, *Nature*, *391*(6663), 141-146.

Severinghaus, J. P., and M. O. Battle (2006), Fractionation of gases in polar ice during bubble close-off: New constraints from firn air Ne, Kr and Xe observations, *Earth and Planetary Science Letters*, *244*(1-2), 474-500.

Severinghaus, J. P., R. Beaudette, M. A. Headly, K. Taylor, and E. J. Brook (2009), Oxygen-18 of O_2 Records the Impact of Abrupt Climate Change on the Terrestrial Biosphere, *Science*, *324*(5933), 1431-1434.

Severinghaus, J. P., et al. (2010), Deep air convection in the firn at a zero-accumulation site, central Antarctica, *Earth and Planetary Science Letters*, *293*(3-4), 359-367.

Shindell, D. T., G. Faluvegi, and N. Bell (2003), Preindustrial-to-present-day radiative forcing by tropospheric ozone from improved simulations with the GISS chemistry-climate GCM, *Atmos. Chem. Phys.*, *3*, 1675-1702.

Singarayer, J. S., P. J. Valdes, P. Friedlingstein, S. Nelson, and D. J. Beerling (2011), Late Holocene methane rise caused by orbitally controlled increase in tropical sources, *Nature*, *470*(7332), 82-U91.

Sowers, T., M. Bender, and D. Raynaud (1989), Elemental and Isotopic Composition of Occluded O_2 and N_2 in Polar Ice, *J. Geophys. Res.-Atmos.*, *94*(D4), 5137-5150.

Sowers, T., M. Bender, D. Raynaud, and Y. S. Korotkevich (1992), $\delta^{15}N$ of N_2 in Air Trapped in Polar Ice: a Tracer of Gas Transport in the Fim and a Possible Constrainton Ice Age-Gas Age Differences, *J. Geophys. Res.-Atmos.*, *97*(D14), 15683-15697.

Spahni, R., J. Schwander, J. Fluckiger, B. Stauffer, J. Chappellaz, and D. Raynaud (2003), The attenuation of fast atmospheric CH_4 variations recorded in polar ice cores, *Geophys. Res. Let.*, *30*(11), 4.

Stauffer, B., J. Schwander, and H. Oeschger (1985), Enclosure of air during metamorphosis of dry firn to ice, *Ann. Glac.*, *6*, 108-112.

Steele, L. P., P. J. Fraser, R. A. Rasmussen, M. A. K. Khalil, T. J. Conway, A. J. Crawford, R. H. Gammon, K. A. Masarie, and K. W. Thoning (1987), The Global Distribution of Methane in the Troposphere, *J. Atmos. Chem.*, *5*(2), 125-171.

Subak, S. (1994), Methane from the House of Tudor and the Ming Dynasty: Anthropogenic emissions in the sixteenth century, *Chemosphere*, *29*(5), 843-854.

Thompson, A. M. (1992), The Oxidizing Capacity of the Earth's Atmosphere: Probable Past and Future Changes *Science*, *256*(5060), 1157-1165.

Trenberth, K. E., and L. Smith (2005), The mass of the atmosphere: A constraint on global analyses, *J. Clim.*, *18*(6), 864-875.

Trouet, V., J. Esper, N. E. Graham, A. Baker, J. D. Scourse, and D. C. Frank (2009), Persistent Positive North Atlantic Oscillation Mode Dominated the Medieval Climate Anomaly, *Science*, *324*(5923), 78-80.

Trudinger, C. M., I. G. Enting, and P. J. Rayner (2002), Kalman filter analysis of ice core data - 1. Method development and testing the statistics, *J. Geophys. Res.-Atmos.*, *107*(D20).

Trudinger, C. M., I. G. Enting, D. M. Etheridge, R. J. Francey, V. A. Levchenko, L. P. Steele, D. Raynaud, and L. Arnaud (1997), Modeling air movement and bubble trapping in firn, *J. Geophys. Res.-Atmos.*, *102*(D6), 6747-6763.

Valdes, P. J., D. J. Beerling, and C. E. Johnson (2005), The ice age methane budget, *Geophys. Res. Let.*, *32*(2), 4.

van Hulzen, J. B., R. Segers, P. M. van Bodegom, and P. A. Leffelaar (1999), Temperature effects on soil methane production: an explanation for observed variability, *Soil Biol. Biochem.*, *31*(14), 1919-1929.

Vinther, B. M., et al. (2006), A synchronized dating of three Greenland ice cores throughout the Holocene, *J. Geophys. Res.-Atmos.*, *111*(D13), 11.

Walter, B. P., M. Heimann, and E. Matthews (2001a), Modeling modern methane emissions from natural wetlands 1. Model description and results, *J. Geophys. Res.-Atmos.*, *106*(D24), 34189-34206.

Walter, B. P., M. Heimann, and E. Matthews (2001b), Modeling modern methane emissions from natural wetlands 2. Interannual variations 1982-1993, *J. Geophys. Res.-Atmos.*, *106*(D24), 34207-34219.

Wang, D. Q., Z. L. Chen, and S. Y. Xu (2009), Methane emission from Yangtze estuarine wetland, China, *J. Geophys. Res.-Biogeosci.*, *114*, 11.

Wang, X. F., A. S. Auler, R. L. Edwards, H. Cheng, E. Ito, and M. Solheid (2006), Interhemispheric anti-phasing of rainfall during the last glacial period, *Quat. Sci. Rev.*, *25*(23-24), 3391-3403.

Wang, Y. H., and D. J. Jacob (1998), Anthropogenic forcing on tropospheric ozone and OH since preindustrial times, *J. Geophys. Res.-Atmos.*, *103*(D23), 31123-31135.

Wang, Y. J., H. Cheng, R. L. Edwards, Z. S. An, J. Y. Wu, C. C. Shen, and J. A. Dorale (2001), A high-resolution absolute-dated Late Pleistocene monsoon record from Hulu Cave, China, *Science*, *294*(5550), 2345-2348.

Wang, Y. J., H. Cheng, R. L. Edwards, Y. Q. He, X. G. Kong, Z. S. An, J. Y. Wu, M. J. Kelly, C. A. Dykoski, and X. D. Li (2005), The Holocene Asian monsoon: Links to solar changes and North Atlantic climate, *Science*, *308*(5723), 854-857.

Witrant, E., et al. (2011), A new multi-gas constrained model of trace gas non-homogeneous transport in firn: evaluation and behavior at eleven polar sites, *Atmos. Chem. Phys. Discuss.*, *11*(8), 23029-23080.

Witrant, E., et al. (2012), A new multi-gas constrained model of trace gas non-homogeneous transport in firn: evaluation and behaviour at eleven polar sites, *Atmos. Chem. Phys.*, *12*(23), 11465-11483.

Weatherford, J. (2004), *Genghis Khan and the Making of the Modern World*, 1 ed., Crown Publishers, New York.

Worthy, D. E. J., I. Levin, F. Hopper, M. K. Ernst, and N. B. A. Trivett (2000), Evidence for a link between climate and northern wetland methane emissions, *J. Geophys. Res.-Atmos.*, *105*(D3), 4031-4038.

Yan, X. Y., H. Akiyama, K. Yagi, and H. Akimoto (2009), Global estimations of the inventory and mitigation potential of methane emissions from rice cultivation conducted using the 2006 Intergovernmental Panel on Climate Change Guidelines, *Glob. Biogeochem. Cycle*, *23*.

Zhang, D. D., P. Brecke, H. F. Lee, Y. Q. He, and J. Zhang (2007), Global climate change, war, and population decline in recent human history, *Proc. Natl. Acad. Sci. U. S. A.*, *104*(49), 19214-19219.

Zhang, P. Z., et al. (2008), A Test of Climate, Sun, and Culture Relationships from an 1810-Year Chinese Cave Record, *Science*, *322*(5903), 940-942.

Zhuang, Q., J. M. Melillo, D. W. Kicklighter, R. G. Prinn, A. D. McGuire, P. A. Steudler, B. S. Felzer, and S. Hu (2004), Methane fluxes between terrestrial ecosystems and the atmosphere at northern high latitudes during the past century: A retrospective analysis with a process-based biogeochemistry model, *Glob. Biogeochem. Cycle*, *18*(3).

Zona, D., W. C. Oechel, J. Kochendorfer, K. T. P. U, A. N. Salyuk, P. C. Olivas, S. F. Oberbauer, and D. A. Lipson (2009), Methane fluxes during the initiation of a large-scale water table manipulation experiment in the Alaskan Arctic tundra, *Glob. Biogeochem. Cycle*, *23*, 11.

Appendix

Appendix A. Matlab code for EBAMM (Eight Box Atmospheric Methane Model)

There are five files which are required to run EBAMM (Eight Box Atmospheric Methane Model). They are named as follows:

1.) ebamm.m
2.) ebammSource.m
3.) ebammODE45.m
4.) saveData.m
5.) ebammFigures.m

In addition to these files, the raw input data is needed to run the model. This data will be archived at the NOAA National Climate Data Center http://www.ncdc.noaa.gov/paleo/paleo.html.

File: ebamm.m

```
clear all
%close all
set(0,'DefaultFigureWindowStyle','docked')

global inputIndex inputSource inputSink stepYear

eval('ebammSource')

%% Model Input

% iso is a file full of constants that define the
% constants for combining the sources and for the sinks.
%iso = load('Data/quellen.txt');

% This scales the OH sink.  The parameterization in the original
BOSCAGE
% model has OH being reduced between 1885-1978 which causes the
lifetime to
% increase during this time period.
%ohScalar = load('Data/ohlauf.txt');
```

```
%ohScalar = [1000 1.236; 1885 1.236; 1978 1; 2100 1]; % The original
values used in the model.
%ohScalar = [-1000 0.966; 1885 0.966; 1978 1; 2100 1]; % The one i've
been using.
ohScalar = [-1000 0.966; 1885 0.966; 1900 0.86; 2100 0.86]; % Used for
modern conc.


%% Preparing the variables

% The following emission, OH, etc time series will be interpolated so
that
% they have a common time frame.  This is done because the ode45
function
% uses an interp1q call to find the values of each of these parameters
at
% every time step, so it is called a lot.  It is about as fast to
% interpolate values in a matrix as it is to interpolate values in a
single
% column vector, so it is significantly faster to use a single matrix
% instead of many individual column vectors.  Note that the source time
% resolution is established here.  Currently it is set at annual
% resolution.  If you want it higher it could slow down the model.
I've
% tested it at 0.1 year and its only marginally slower (~10 slower).
c.InterpYear = (yearStart:1:yearEnd)';

% Interpolated population time series.

% Columns 1-6 are population in the boxes. Column 7-12 is population in
rice emitting regions.
c.Interp(:,1:12) = interp1(HYDEboxYear,[HYDEboxPop
HYDEricePop],c.InterpYear,'linear','extrap');

c.Interp(c.Interp(:,1:12)<0) = 0; % Checks to make sure no population
figures are below 0.

% Scalar for OH.
c.Interp(:,13) =
interp1(ohScalar(:,1),ohScalar(:,2),c.InterpYear,'linear','extrap');

% Interpolated values for the source histories.
for i = 1:c.numSources
    c.Interp(:,13+i) =
interp1(c.source.(c.sourceNames{i}).hx(:,1),c.source.(c.sourceNames{i})
.hx(:,2),c.InterpYear,'linear','extrap')/16.04;
end

r13st =  0.011237;
rDst =  6.23e-004;
```

```
sourceIso =
1./(1+(r13st*(sourceIsoRatio(:,1)/1000+1))+(rDst*(sourceIsoRatio(:,2)/1
000+1)));
sourceIso(:,2:3) =
[sourceIso(:,1).*(r13st*(sourceIsoRatio(:,1)/1000+1)) ...
    sourceIso(:,1).*(rDst*(sourceIsoRatio(:,2)/1000+1))];

r12 = repmat(sourceIso(:,1)',6,1);
r13 = repmat(sourceIso(:,2)',6,1);
rD = repmat(sourceIso(:,3)',6,1);

% Check this and make sure it is zero!!  If its not that means that
what
% I'm putting in the model is not what I'm getting out.
%sourceSig(:,1:2) = [(1000*(r13(1,:)./r12(1,:)/r13st-1))'
(1000*(rD(1,:)./r12(1,:)/rDst-1))'];
%[sourceSig-sourceIsoRatio]

% Values from the original model:
%br12=repmat(iso(2,4:12),6,1);
%br13=repmat(iso(3,4:12),6,1);
%brD=repmat(iso(4,4:12),6,1);
%bsourceSig(:,1:2) = [(1000*(br13(1,:)./br12(1,:)/r13st-1))'
(1000*(brD(1,:)./br12(1,:)/rDst-1))'];
%[sourceSig-bsourceSig]

% iso(2:4,4:12)'

%   0.989134820000000   0.010436899000000   0.000428280540000
%   0.989137870000000   0.010436931000000   0.000425200700000
%   0.989178140000000   0.010415125000000   0.000406730270000
%   0.989137870000000   0.010436931000000   0.000425200700000
%   0.988980380000000   0.010557514000000   0.000462101080000
%   0.988687420000000   0.010832134000000   0.000480442770000
%   0.988739960000000   0.010754936000000   0.000505107690000
%   0.988781200000000   0.010719829000000   0.000498968660000
%   0.988963960000000   0.010546226000000   0.000489819010000

%sum(iso(2:4,4:12)',2)
% This is the sum of each of the sources.  The
%values are pretty close to 1 with the only difference being in the 9th
%decimal place.  This is much smaller than the variation in each of the
%columns above (variation in the 4th-5th decimal place) so I think that
%effectively the sum of each of them should be 1.

cm=[1.590,  1.590,  1.610,  1.650,  1.690,  1.690,  1.390,  1.450   ];
% Methane concentration in the boxes in ppm; Methankonzentration in den
Boxen in ppm
cm=cm-0.85; %0.890; % What is this for?  Is it the pre-industrial
starting concentration?
```

```
d13C=[-47.1, -47.1, -47.15, -47.4, -47.4, -47.5, -45.3, -45.7];  % dc13
isotope; c13-isotopie
d13C=d13C-1.95; % preindustrial statring condition?
dD=[-82, -82, -82, -90, -92, -99, -68, -75]; %dD-Isotopie
dD=dD+20; % preindustrial starting condition?
k12=1;%iso(9,4);
k13=9.9462900e-001;%iso(10,4);
kD=7.4349442e-001;%iso(11,4);
k13st=9.8814229e-001;%iso(10,6);
kDst=8.4033613e-001;%iso(11,6);
k_soil12=1;%iso(9,8);
k_soil13=9.8231827e-001;%iso(10,8);
k_soilD=9.3808630e-001;%iso(11,8);
r13box=(d13C/1000+1)*r13st;
rdbox=(dD/1000+1)*rDst;
cm12=cm./(1+r13box+rdbox);
cm13=cm12.*r13box;
cmd=cm12.*rdbox;

% OH-Radikale
oh=[0.00986,    0.0475, 0.201,  0.2222, 0.0969, 0.0245, 0.0577, 0.0488
]; % 1/tau_oh in 1/year with chlorine; 1/tau_oh in 1/jahr mit clor

% Transport constants for all of the boxes.  In boxes 1, 2, 5, and 6
there
% are two extra terms.  This is because there is an additional
frequency of
% variability in these boxes.
s_trans=[   oh(1),  1.462,  -0.05,  0,  0.580,  0.01;
            oh(2),  0.836,  0.0,    0,  0.102,  0.15;
            oh(3),  0.354,  -0.03,  0,  0,      0;
            oh(4),  0.45,   0.517,  0,  0,      0;
            oh(5),  1.109,  0.528,  0,  0.308,  0.10;
            oh(6),  1.57,   0.515,  0,  0.788,  0.04;
            oh(7),  0.6,    0,      0,  0,      0;
            oh(8),  0.6,    0.525,  0,  0,      0];

% Bodensenke (Boden senke = Soil sink)
soil=33.2/3800*4*1.115; % Sink strength = reduction / (tropospheric of
methane quantity a box); Senkenstärke= Abbau/(troposphärische
Methanmenge einer Box)

m_soil=[    0,  0.01,   0.272,  0.303,  0.35,   0.06]*soil;
% there are only 6 boxes touching the soil, so this has only 6 values


% This is used as the values to scale the sink feedback factor against.
It
% was determined with a model run for the budget at 1500 CE with a
lifetime
```

```
% of ~8 years and should be approximately correct for other scenarios.
To
% get new values just run the model to the desired year (eg 1500 CE)
and
% then stop it and get the values from the bStep variable.
% See Hopcroft et al 2011 (QSR) for a discussion of this effect.

c.bStep1500CE = [
    5.9686    0.0639    0.0033
   16.7276    0.1791    0.0093
   25.2206    0.2701    0.0140
   25.5316    0.2734    0.0141
   17.3503    0.1857    0.0095
    6.2965    0.0674    0.0034
   10.2260    0.1097    0.0058
   10.5906    0.1136    0.0060];

c.bStepTrop1500CE = c.bStep1500CE(1:6,:);
c.bStepStrat1500CE = c.bStep1500CE(7:8,:);


%%

% Mass of the atmosphere in x10^18 mols of dry air.  Equiv to 5.13e18
kg.
% This compares well with the value I used of 5.1352e18 +/- 0.0003 from
% Trenberth and Smith, 2005.
M = 177; % e18 mols of dry air.
% Note, I think this should be 178.  In the paper it says that the mass
of
% the atm is 5.13e18 but that water vapor is 1.3e16, so they subtract
the
% water vapor then devide by the dry air molecular mass of 28.82g/mol.
In
% Trenberth's paper he says that the total mass of the atm is 5.1479e18
kg
% with the dry air mass being 5.1352e18 kg and mean water vapor being
1.27e16 kg.
% If you divide the dry air mass by the molecular mass, you get 178e18
mol of dry air.


% Transport parameters for the BOSCAGE-8 model fitted to the
seasonality of
% SF6 at Neumayer, Cape Grim, Izana, and Alert.  The parameters are
sorted
% south to north.  t_nm means the transport parameter set fo the air
mass
% transport between boxes n and m.  The function for the transport is
% F(t) = F0(1+A1*cos(w(t-phi1))+A2*cos(2*w(t-phi2)))
% with w = 2*pi and t in years.
```

```
% t_nm = [Flow, F0 (Global air mass/year); Amplitude, A1; Phase, phi1
% (year^-1); Aplitude, A2; Phase, phi2 (year^-1)]
t_12 = [0.6*M    0.1440    0.7500    0.3110    0.0930];
t_23 = [0.9*M    0.4000    0.4510    0.4000    0.7870];
t_34 = [0.6*M    0.1770    0.8480    0.2500    0.9840];
t_45 = [0.9*M    0.4000    0.4510    0.6000    0.0050];
t_56 = [0.25*M   0.3560    0.0680    0.4040    0.9050];
t_17 = [0.5310    0.3800    0.2500         0    0.4500];
t_27 = [1.4160    0.3800    0.2500         0    0.3200];
t_37 = [3.5400    0.5000    0.5000         0    0.3200];
t_48 = [3.5400    0.5000         0         0         0];
t_58 = [1.4160    0.7500    0.5000         0         0];
t_68 = [0.7080    0.5000    0.5000         0    0.1000];
t_78 = [1.7700         0    0.5000         0    0.2500];

% Constants that will be used in the ode function.
c.r12 = r12;
c.r13 = r13;
c.rD = rD;
c.k12 = k12;
c.k13 = k13; % Update from Saueressig 2001 = 1/1.0039.  Does not work
well.
c.k13st = k13st; % stratosphere
c.kD = kD; % Update from Saueressig 2001 = 1/1.294.  Does not work
well.
c.kDst = kDst; % stratosphere
c.s_trans = s_trans;
c.s_transTrop = c.s_trans(1:6,:);
c.s_transStrat = c.s_trans(7:8,:);
c.m_soil = m_soil;
c.k_soil12 = k_soil12;
c.k_soil13 = k_soil13;
c.k_soilD = k_soilD;
c.t_12 = t_12;
c.t_17 = t_17;
c.t_23 = t_23;
c.t_27 = t_27;
c.t_34 = t_34;
c.t_37 = t_37;
c.t_45 = t_45;
c.t_48 = t_48;
c.t_56 = t_56;
c.t_58 = t_58;
c.t_68 = t_68;
c.t_78 = t_78;
c.boxMass = [8.85; 24.78; 37.17; 37.17; 24.78; 8.85; 17.7; 17.7]; %
based on a total of 177.
c.stepTotSourceStrengthOnes = ones(6,1); % can get rid of this.
c.stepTotSourceStrength = ones(6,c.numSources);

%% Load data for figures and calculate the IPD
```

```
ts.ch4Atm = load('Data/CH4-Atm.txt');
meas.gisp = load('Data/CH4-GISP2D.txt');
meas.gispLow = load('Data/CH4-GISP2D_low.txt');
meas.wdc = load('Data/CH4-WDC.txt');
meas.wdc06a = load('Data/CH4-WDC06A.txt');
meas.wdc05a = load('Data/CH4-WDC05A.txt');
chron.wdcBuizert = load('Data/AgeControl-WDC06A-
Gas_Age_Buizert_2012.09.19.txt');
chron.wdcBuizert(:,2) = chron.wdcBuizert(:,2)+2;
chron.wdc = [chron.wdcBuizert(:,1) 1950-chron.wdcBuizert(:,2)];
chron.gisp = load('Data/AgeControl-GISP-MonteCarlo.txt');
chron.gisp = chron.gisp(~isnan(chron.gisp(:,2)),:);
chron.wdc = chron.wdc(~isnan(chron.wdc(:,2)),:);
chron.gispLow = load('Data/AgeControl-GISP-Gas_Age_Kobashi2010.txt');
chron.gispLow = [chron.gispLow(:,1),1950-chron.gispLow(:,2)];
ts.d13cLD = load('Data/d13C-LD-Ferretti.txt');
ts.d13cNEEM = load('Data/d13C-NEEM.txt');
ts.d13cGISP = load('Data/d13C-GISP2D.txt');
ts.dDGISP = load('Data/dD-GISP2D.txt');
meas.d13cWDC05A = load('Data/d13C-WDC05A.txt');
meas.dDWDC05A = load('Data/dD-WDC05A.txt');
IPDsmoothError = load('Data/IPDsmoothError100yr.txt'); % This is output
from ipgGaussianPlusAge.m

ts.d13cNEEM = sortrows(ts.d13cNEEM,1);

if yearStart<min(ts.d13cNEEM(:,1))
    ts.d13cNEEM = [yearStart,ts.d13cNEEM(1,2);ts.d13cNEEM];
end

% Creates a time series for the GISP and WAIS data from the
chronologies.
ts.wdc =
[interp1(chron.wdc(:,1),chron.wdc(:,2),meas.wdc(:,1),'linear','extrap')
meas.wdc(:,3)];
ts.gisp =
[interp1(chron.gisp(:,1),chron.gisp(:,2),meas.gisp(:,1),'linear','extra
p') meas.gisp(:,3)];
ts.gispLow =
[interp1(chron.gispLow(:,1),chron.gispLow(:,2),meas.gispLow(:,1),'linea
r','extrap') meas.gispLow(:,3)];
ts.wdc05a =
[interp1(chron.wdc(:,1),chron.wdc(:,2),meas.wdc05a(:,1),'linear','extra
p') meas.wdc05a(:,3)];
ts.wdc06a =
[interp1(chron.wdc(:,1),chron.wdc(:,2),meas.wdc06a(:,1),'linear','extra
p') meas.wdc06a(:,3)];

% WDC05A/WDC06A comparison
%wdc05a_06ayear =
(min(ceil(ts.wdc05a(:,1))):1:max(floor(ts.wdc06a(:,1))))';
```

```
%corr(interp1(ts.wdc05a(:,1),ts.wdc05a(:,2),wdc05a_06ayear),...
%    interp1(ts.wdc06a(:,1),ts.wdc06a(:,2),wdc05a_06ayear))^2

% This creates a new timescale for the CH4 isotope data.
dc13WDC05AageMask = meas.d13cWDC05A(:,1)>chron.wdc(1,1);
ts.d13cWDC05A = [meas.d13cWDC05A(~dc13WDC05AageMask,2)
meas.d13cWDC05A(~dc13WDC05AageMask,3);...

interp1(chron.wdc(:,1),chron.wdc(:,2),meas.d13cWDC05A(dc13WDC05AageMask
,1)) meas.d13cWDC05A(dc13WDC05AageMask,3)];

dDWDC05AageMask = find(meas.dDWDC05A(:,1)>chron.wdc(1,1));
ts.dDWDC05A = [meas.dDWDC05A(~dDWDC05AageMask,2)
meas.dDWDC05A(~dDWDC05AageMask,3);...

interp1(chron.wdc(:,1),chron.wdc(:,2),meas.dDWDC05A(dDWDC05AageMask,1))
meas.dDWDC05A(dDWDC05AageMask,3)];

% Find the common time interval
%maxIPDyear = 1750; % I am setting this to be just after the start of
the anthro rise.
% The data extends to 1808, but I don't think the chronology should be
extended this far.

maxIPDyear = floor(min(max(ts.gisp(:,1)),max(ts.wdc(:,1)))); % based on
the data.
minIPDyear = ceil(max(min(ts.gisp(:,1)),min(ts.wdc(:,1))));
%minIPDyear = -750; % This is to prevent the preturbed time series from
not reaching the end of the record.

missingGISPyears = [717 783];%[758 825];

ts.ipdYear =
[(minIPDyear:1:missingGISPyears(1))';(missingGISPyears(2):1:maxIPDyear)
'];
ts.wdcInterp =
[ts.ipdYear,interp1(ts.wdc(:,1),ts.wdc(:,2),ts.ipdYear)];
ts.gispInterp =
[ts.ipdYear,interp1(ts.gisp(:,1),ts.gisp(:,2),ts.ipdYear)];
IPD = [ts.ipdYear ts.gispInterp(:,2)-ts.wdcInterp(:,2)];


ts.gispLowSpline = [(-2900:10:1800)'
csaps(ts.gispLow(:,1),ts.gispLow(:,2),1e-8,(-2900:10:1800)')];
ts.wdcLowSpline = [(-2900:10:1800)' csaps(ts.wdc(:,1),ts.wdc(:,2),1e-
8,(-2900:10:1800)')];
IPDLowSpline = [ts.wdcLowSpline(:,1),ts.gispLowSpline(:,2)-
ts.wdcLowSpline(:,2)];
```

```
% data = [(-2900:10:1800)',zeros(size((-2900:10:1800)'))];
% data(dsearchn(data(:,1),0),2) = 1;
% f = [(-2900:10:1800)' csaps(data(:,1),data(:,2),1e-8,(-
2900:10:1800)')];
% figure(99)
% plot(f(:,1),f(:,2))

%interpOutput = [IPD(:,1), ts.gispInterp, ts.wdcInterp];
%save('GISP+WDC_CH4.txt','interpOutput','-ASCII') % Output for my
simple 3 box model


% This is a lowpass filter for the IPD data.  Alternatly I could filter
the
% conc data and then calc the smooth IPD
%lowpassFilterDesign=fdesign.lowpass('Fp,Fst,Ap,Ast',2*pi/1000000,1/20,
0.001,60);
%lowpassFilter = design(lowpassFilterDesign,'equiripple');
%save('Data/lowpassFilter20yr.mat','lowpassFilter')
load('Data/lowpassFilter20yr.mat') % this is the same every time and it
takes a few seconds to make the filter.

%max(length(lowpassFilter.Numerator)-1,length(1)-1) % This is the
filter order.
%fvtool(lowpassFilter); % Displays the designed filter.
ts.gispLowpass(:,1)=filtfilt(lowpassFilter.Numerator,1,ts.gispInterp(:,
2)); % Use filtfilt because it does not phase shift the signal as
opposed to filter.
ts.wdcLowpass(:,1)=filtfilt(lowpassFilter.Numerator,1,ts.wdcInterp(:,2)
); % Use filtfilt because it does not phase shift the signal as opposed
to filter.
ts.gispLowpass(:,1) = ts.gispLowpass-mean(ts.gispLowpass-
ts.gispInterp(:,2)); % Takes care of any offset that the filtering may
cause.
ts.wdcLowpass(:,1) = ts.wdcLowpass-mean(ts.wdcLowpass-
ts.wdcInterp(:,2));
ts.ipdLowpass = ts.gispLowpass-ts.wdcLowpass;
%figure(99);clf;
%plot(IPD(:,1),IPD(:,2),'k-',IPD(:,1),ts.ipdLowpass(:,1),'b-
',IPDsmooth(:,1),IPDsmooth(:,2),'r-')
%axis([-80 80 35 55])

% The concentration is turned into burden (terra Moles, used in the
model) for boxes 1 & 6.
% c.burden = [(yearStart:1:yearEnd+10)' ...
%
interp1(ts.ipdYear,(ts.wdcInterp(:,2)/1000)*c.boxMass(1),(yearStart:1:y
earEnd+10)','linear','extrap') ...
%
interp1(ts.ipdYear,(ts.gispInterp(:,2)/1000)*c.boxMass(6),(yearStart:1:
```

```
yearEnd+10)','linear','extrap')]; % the 1000 converts ppb (1e9) to
terra (1e12)
c.burden = [(yearStart:1:yearEnd+10)' ...

interp1(ts.ipdYear,(ts.wdcLowpass(:,1)/1000)*c.boxMass(1),(yearStart:1:
yearEnd+10)','linear','extrap') ...

interp1(ts.ipdYear,(ts.gispLowpass(:,1)/1000)*c.boxMass(6),(yearStart:1
:yearEnd+10)','linear','extrap')]; % the 1000 converts ppb (1e9) to
terra (1e12)

c.d13Cts = ts.d13cNEEM;



%% Now comes the actual model.


% Initial conitions for the boxes.  These are fluxes in terra
moles/year with
% the columns being d12C, d13C, and dD
binit = [6.4760 0.0692 0.0038;...
    18.1328 0.1938 0.0106;...
    27.9344 0.2985 0.0163;...
    29.4048 0.3141 0.0170;...
    20.5834 0.2199 0.0119;...
    7.3513 0.0785 0.0042;...
    9.4512 0.1012 0.0056;...
    10.5014 0.1124 0.0062];

% When you do not specify a max time step, ode45 appears to make some
bad
% decisions and maybe it is taking too large of a time step.  The model
% result does seem to be affected this, so it is a good idea to specify
the
% maximum time step.
% The original model had a max time step of 0.04166667 which is 1/24 of
a
% year, or just over 2 weeks.  When running the model for ~170 years it
% takes ~40 seconds to do this at this time step (whereas the original
% model took ~109 seconds).  However, I can make the
% max time step be 10/24 and the data does not seem to be significantly
% affected and it only takes ~7 seconds to run the model which is
% essentially as fast as it runs without any time step constratins.
This
% seems like a good compramise while I'm testing the model, but once
I'm
% comparing it or trying to get data out of it, I may want to decrease
this
% a little to 5/24 or something like that.  The ODE45 help file
suggested
```

```
% that it is better to adjust the error tolerance than fiddle with the
time
% step, so that may be something to look into also.
% After some experimenting it seems that 3/24 is the fastest max time
step.
%  I think this is because when it is higher it obtains some
predictions
%  outside of its error tolerance and it has to go back...but this step
%  size is small enough that this may not be happening as much.  This
is
%  just a theory, but 3/24 is definitely the fastest combination, and
the
%  data looks good (but still not as detailed as 1/24).
%
% It can be 4/24 if there is no seasonality in the sources, sinks or
% transport and it runs even faster.

myStepSize = 3/24;%3/24;

% Initialize some variables
inputIndex = 1;
inputSource = zeros((yearEnd-yearStart)/myStepSize+1,c.numSources*6+1);
inputSink = zeros((yearEnd-yearStart)/myStepSize+1,25);


options =
odeset('MaxStep',myStepSize,'OutputFcn',@saveData,'Refine',4,'RelTol',1
e-3);%5e-5);


stepYear = yearStart;
c.yearString = '\b';
numDigits = max([length(num2str(floor(yearStart)))
length(num2str(floor(yearEnd)))]);
for i = 1:numDigits-1
    c.yearString = [c.yearString '\b'];
end
c.yearString = [c.yearString '%' num2str(numDigits) '.0f'];

fprintf(['Model range: %' num2str(numDigits) '.0f to %'
num2str(numDigits) '.0f\n'],yearStart,yearEnd)
fprintf(['Current year: %' num2str(numDigits) '.0f'],yearStart) % This
field is updated in the ode45 loop.
tic
[mT mB] = ode45(@(t,b) ebammODE45(t,b,c),[yearStart
yearEnd],binit,options);
fprintf('\n')
toc
% Note: The ODE option "refine" allows ODE45 to calculate intermediat
data
```

```
% points between integration time steps at very little computing cost.
It
% allows the mT and mB variables to have N times more data points
(where N
% is the Refine value).  However, the saveData function only saves data
at
% the end of every time step, so the varaibles in it will have fewer
data
% points.  To compare output from mT or mB with output from saveData,
use
% the mask which is defined here:

% I'm not sure why, but the first value in these variables is set to
the
% last value.  It is an easy fix...just set them to the start year.
inputSource(1,1) = yearStart;
inputSink(1,1) = yearStart;

[mask(:,1) mask(:,2) mask(:,3)] = intersect(inputSource(:,1),mT(:,1));

% Saving the mB variables in easier to use/remember variable names.
boxCH4conc(:,1:8) =
1000*((mB(:,1:8)+mB(:,9:16)+mB(:,17:24))./repmat(c.boxMass',length(mB),
1)); % 1e3 is the diff btw ppb (1e9) & terra (1e12)
boxBurden(:,1:8) = mB(:,1:8)+mB(:,9:16)+mB(:,17:24);
globalCH4conc(:,1) = 1000*sum(boxBurden,2)/sum(c.boxMass);
tropCH4conc(:,1) = 1000*sum(boxBurden(:,1:6),2)/sum(c.boxMass(1:6,1));
% Concentration of the Troposphere.
boxdC13(:,1:8) = 1000*(mB(:,9:16)./mB(:,1:8)/r13st-1);
boxdD(:,1:8) = 1000*(mB(:,17:24)./mB(:,1:8)/rDst-1);

% Total emissions of each of the 9 sources in all of the 6 latitudinal
boxes.
inputSourceSum = zeros(size(inputSource,1),c.numSources);

for i = 1:c.numSources
    c.sourceMask(:,i) = (i:c.numSources:6*c.numSources+i-1);
end

for i = 1:c.numSources
    inputSourceSum(:,i) = sum(inputSource(:,c.sourceMask(:,i)+1),2);
end

% Total emissions of all of the sources in each of the 6 latitudinal
boxes.
inputSourceLatSum = zeros(size(inputSource,1),6);
for i = 1:6
    n = 1+(1+(i-1)*c.numSources);
    inputSourceLatSum(:,i) = sum(inputSource(:,n:n+c.numSources-1),2);
end
```

```
% Total sink in each of the 8 boxes.
inputSinkSum = zeros(size(inputSink,1),8);
for i = 1:8
    inputSinkSum(:,i) = sum(inputSink(:,i*3-1:i*3+1),2);
end

% Units are Terra moles CH4 per year.  Multiply by 16.04 g/mol to get
Tg CH4 per year
totalSource = sum(inputSource(:,2:end),2);
totalSink = sum(inputSink(:,2:end),2);
totalBurden = sum(boxBurden,2);

lifetime = totalBurden(mask(:,3),1)./totalSink;
lifetimeBox = boxBurden(mask(:,3),:)./inputSinkSum;
% Note, Burden comes from mB whereas flux comes from saveData, so the
mask is used.



% This interpolates the results onto a time series with equal time
steps.
tt.Step = 0.05;
tt.Year= (yearStart:tt.Step:yearEnd)';
tt.BoxCH4conc = interp1q(mT,boxCH4conc,tt.Year);
tt.GlobalCH4conc = interp1q(mT,globalCH4conc,tt.Year);
tt.TropCH4conc = interp1q(mT,tropCH4conc,tt.Year);
tt.BoxdC13 = interp1q(mT,boxdC13,tt.Year);
tt.BoxdD = interp1q(mT,boxdD,tt.Year);
tt.InputSource =
interp1q(inputSource(:,1),inputSource(:,2:end),tt.Year);
tt.Source = interp1q(inputSource(:,1),inputSourceSum,tt.Year);
tt.SourceLat = interp1q(inputSource(:,1),inputSourceLatSum,tt.Year);
tt.Sink = interp1q(inputSink(:,1),inputSinkSum,tt.Year);
tt.Lifetime = interp1q(inputSink(:,1),lifetime,tt.Year);

% Ice core firn air filter.
load('Data/firnAgeDist.mat')
firnAgeDist.summitInterp = [(0:tt.Step:100)'
interp1(firnAgeDist.summit(:,1),firnAgeDist.summit(:,2),(0:tt.Step:100)
')];
firnAgeDist.waisInterp = [(0:tt.Step:100)'
interp1(firnAgeDist.wais(:,1),firnAgeDist.wais(:,2),(0:tt.Step:100)')];
firnAgeDist.summitInterp(firnAgeDist.summitInterp(:,2)<0,2) = 0;
firnAgeDist.waisInterp(firnAgeDist.waisInterp(:,2)<0,2) = 0;

% Mean age of the air in the filter.  Subtract this from the age in the
figures.
%firnAgeDist.waisMeanAge =
sum(firnAgeDist.waisInterp(:,1).*firnAgeDist.waisInterp(:,2)./sum(firnA
geDist.waisInterp(:,2)));
```

```
%firnAgeDist.summitMeanAge =
sum(firnAgeDist.summitInterp(:,1).*firnAgeDist.summitInterp(:,2)./sum(f
irnAgeDist.summitInterp(:,2)));

% Median age of the air in the filter.
[a b] = max(firnAgeDist.waisInterp(:,2));
firnAgeDist.waisMeanAge = firnAgeDist.waisInterp(b,1);
[a b] = max(firnAgeDist.summitInterp(:,2));
firnAgeDist.summitMeanAge = firnAgeDist.summitInterp(b,1);
%figure(99)
%plot(firnAgeDist.summit(:,1)-
firnAgeDist.summitMeanAge,firnAgeDist.summit(:,2),firnAgeDist.wais(:,1)
-firnAgeDist.waisMeanAge,firnAgeDist.wais(:,2))

tt.BoxCH4Filter(:,1) =
filter(firnAgeDist.waisInterp(:,2),sum(firnAgeDist.waisInterp(:,2)),tt.
BoxCH4conc(:,1));
tt.BoxCH4Filter(:,6) =
filter(firnAgeDist.summitInterp(:,2),sum(firnAgeDist.summitInterp(:,2))
,tt.BoxCH4conc(:,6));
tt.BoxdC13Filter(:,1) =
filter(firnAgeDist.waisInterp(:,2),sum(firnAgeDist.waisInterp(:,2)),tt.
BoxdC13(:,1));
tt.BoxdC13Filter(:,6) =
filter(firnAgeDist.summitInterp(:,2),sum(firnAgeDist.summitInterp(:,2))
,tt.BoxdC13(:,6));
tt.BoxdDFilter(:,1) =
filter(firnAgeDist.waisInterp(:,2),sum(firnAgeDist.waisInterp(:,2)),tt.
BoxdD(:,1));
tt.BoxdDFilter(:,6) =
filter(firnAgeDist.summitInterp(:,2),sum(firnAgeDist.summitInterp(:,2))
,tt.BoxdD(:,6));

% This step corrects for the mean (or median, depending on the code
above) age of the firn air filter.
tt.BoxCH4Filter(:,1) = interp1(tt.Year-
firnAgeDist.waisMeanAge,tt.BoxCH4Filter(:,1),tt.Year,'linear','extrap')
;
tt.BoxCH4Filter(:,6) = interp1(tt.Year-
firnAgeDist.summitMeanAge,tt.BoxCH4Filter(:,6),tt.Year,'linear','extrap
');
tt.BoxdC13Filter(:,1) = interp1(tt.Year-
firnAgeDist.waisMeanAge,tt.BoxdC13Filter(:,1),tt.Year,'linear','extrap'
);
tt.BoxdC13Filter(:,6) = interp1(tt.Year-
firnAgeDist.summitMeanAge,tt.BoxdC13Filter(:,6),tt.Year,'linear','extra
p');
tt.BoxdDFilter(:,1) = interp1(tt.Year-
firnAgeDist.waisMeanAge,tt.BoxdDFilter(:,1),tt.Year,'linear','extrap');
tt.BoxdDFilter(:,6) = interp1(tt.Year-
firnAgeDist.summitMeanAge,tt.BoxdDFilter(:,6),tt.Year,'linear','extrap'
);
```

```
tt.BoxIPDFilter = tt.BoxCH4Filter(:,6)-tt.BoxCH4Filter(:,1);

% This calculates the annual mean of the time series.
tt.Mean = (yearStart:1:yearEnd-1)';
tt.BoxCH4concMean = zeros(length(tt.Mean),8);
tt.BoxCH4FilterMean = zeros(length(tt.Mean),6);
tt.GlobalCH4concMean = zeros(length(tt.Mean),1);
%tt.GlobalCH4FilterMean = zeros(length(tt.Mean),1);
tt.TropCH4concMean = zeros(length(tt.Mean),1);
%tt.TropCH4FilterMean = zeros(length(tt.Mean),1);
tt.BoxdC13Mean = zeros(length(tt.Mean),8);
tt.BoxdC13FilterMean = zeros(length(tt.Mean),6);
tt.BoxdDMean = zeros(length(tt.Mean),8);
tt.BoxdDFilterMean = zeros(length(tt.Mean),6);
tt.InputSourceMean = zeros(length(tt.Mean),c.numSources*6);
tt.SourceMean = zeros(length(tt.Mean),c.numSources);
tt.SourceLatMean = zeros(length(tt.Mean),6);
tt.SinkMean = zeros(length(tt.Mean),8);
tt.LifetimeMean = zeros(length(tt.Mean),1);
tt.BoxIPDFilterMean = zeros(length(tt.Mean),1);

for i = 1:length(tt.Mean) % Note, this code is written for tt.Step =
0.05.
    tt.BoxCH4concMean(i,1:8) = sum(tt.BoxCH4conc(i*20-
19:i*20,1:8))*tt.Step;
    tt.BoxCH4FilterMean(i,[1 6]) = sum(tt.BoxCH4Filter(i*20-19:i*20,[1
6]))*tt.Step;
    tt.GlobalCH4concMean(i,1) = sum(tt.GlobalCH4conc(i*20-
19:i*20,1))*tt.Step;
    %tt.GlobalCH4FilterMean(i,1) = sum(tt.GlobalCH4Filter(i*20-
19:i*20,1))*tt.Step;
    tt.TropCH4concMean(i,1) = sum(tt.TropCH4conc(i*20-
19:i*20,1))*tt.Step;
    %tt.TropCH4FilterMean(i,1) = sum(tt.TropCH4Filter(i*20-
19:i*20,1))*tt.Step;
    tt.BoxdC13Mean(i,1:8) = sum(tt.BoxdC13(i*20-19:i*20,1:8))*tt.Step;
    tt.BoxdC13FilterMean(i,[1 6]) = sum(tt.BoxdC13Filter(i*20-
19:i*20,[1 6]))*tt.Step;
    tt.BoxdDMean(i,1:8) = sum(tt.BoxdD(i*20-19:i*20,1:8))*tt.Step;
    tt.BoxdDFilterMean(i,[1 6]) = sum(tt.BoxdDFilter(i*20-19:i*20,[1
6]))*tt.Step;
    tt.InputSourceMean(i,1:c.numSources*6) = sum(tt.InputSource(i*20-
19:i*20,1:c.numSources*6))*tt.Step;
    tt.SourceMean(i,1:c.numSources) = sum(tt.Source(i*20-
19:i*20,1:c.numSources))*tt.Step;
    tt.SourceLatMean(i,1:6) = sum(tt.SourceLat(i*20-
19:i*20,1:6))*tt.Step;
    tt.SinkMean(i,1:8) = sum(tt.Sink(i*20-19:i*20,1:8))*tt.Step;
    tt.LifetimeMean(i,1) = sum(tt.Lifetime(i*20-19:i*20,1))*tt.Step;
    tt.BoxIPDFilterMean(i,1) = sum(tt.BoxIPDFilter(i*20-
19:i*20,1))*tt.Step;
```

```
end

eval('ebammFigures')
```

File: ebammSource.m

```
%% EBAMM Model Scenarios

% The following are time series scenarios of model sources.  The model
will
% only use the sources which have a source history (hx) defined.  The
full
% list of sources available for use are below along with parameters
that
% are specific to each source.  The PIHBaseSources are a list of common
% base Pre-Industrial Holocene sources.

% The sources are all in Tg CH4/year.



scenario = 'L1';
fprintf(['Scenario ' scenario ': ']);

if strcmp(scenario,'L1')
    fprintf('Balancing the IPD with only the tropics.\n');

    dist = [0.004 0.044 0.32 0.305 0.257 0.07];
    if sum(dist)~=1; fprintf('Error: sum(dist) must = 1.'); return;
end;
    te = 213.8; % level of emissions which match -800 C.E.

    dist = dist*te;
    c.source.Box1.hx = [-1000 dist(1); 2000 dist(1)]; % This is the box
# and source column # of the added source.
    c.source.Box2.hx = [-1000 dist(2); -800 dist(2); 930 dist(2)*1;
1030 dist(2)*1; 1700 dist(2)*1];
    c.source.Box3.hx = [-900 dist(3); -800 dist(3); 930 dist(3)*1.133;
1030 dist(3)*1.089; 1700 dist(3)*1.173];
    c.source.Box4.hx = [-900 dist(4); -800 dist(4); 930 dist(4)*1.133;
1030 dist(4)*1.299; 1700 dist(4)*1.273];
    c.source.Box5.hx = [-900 dist(5); -800 dist(5); 930 dist(5); 1030
dist(5); 1700 dist(5)];
    c.source.Box6.hx = [-900 dist(6); -800 dist(6); 930 dist(6); 1030
dist(6);  1700 dist(6)];

    yearStart = -850;
    yearEnd = 1800;
    %saveScenarioOutput = 'y';
    saveScenarioSources = 'n';
    usePrevScenarioSources = 'n';
    c.sinkType = 'Feedback';
    c.transport = 'NoSeason';
```

```
    c.RealLatSolver = '3-4';
    %sum([dist(1:2),dist(3)*1.173,dist(4)*1.273,dist(5:6)])-te

elseif strcmp(scenario,'L2') % box scenario balancing tropics with box
5.
    fprintf('Balancing the tropics and box 5.\n');

    dist = [0.004 0.044 0.34 0.323 0.22 0.07];
    te = 213.8; % level of emissions which match -800 C.E.

    dist = dist*te;
    c.source.Box1.hx = [-900 dist(1); 2000 dist(1)]; % This is the box
# and source column # of the added source.
    c.source.Box2.hx = [-900 dist(2); -800 dist(2); 930 dist(2)*1; 1030
dist(2)*1; 1700 dist(2)*1];
    c.source.Box3.hx = [-900 dist(3); -800 dist(3); 930 dist(3)*1.132;
1030 dist(3)*1.141; 1700 dist(3)*1.198];
    c.source.Box4.hx = [-900 dist(4); -800 dist(4); 930 dist(4)*1.132;
1030 dist(4)*1.141; 1700 dist(4)*1.198];
    c.source.Box5.hx = [-900 dist(5); -800 dist(5); 930 dist(5)*1.000;
1030 dist(5)*1.145; 1700 dist(5)*1.068];
    c.source.Box6.hx = [-900 dist(6); -800 dist(6); 930 dist(6)*1.000;
1030 dist(6)*1; 1700 dist(6)*1];

    yearStart = -850;
    yearEnd = 1800;
    %saveScenarioOutput = 'y';
    saveScenarioSources = 'n';
    usePrevScenarioSources = 'n';
    c.sinkType = 'Feedback';
    c.transport = 'NoSeason';
    c.RealLatSolver = '34-5';
    %sum([dist(1:2),dist(3)*1.173,dist(4)*1.273,dist(5:6)])-te

elseif strcmp(scenario,'L3') % box scenario balancing tropics with box
5 & 6.
    fprintf('Balancing the tropics and boxes 5 and 6.\n');

    dist = [0.004 0.044 0.34 0.323 0.22 0.07];
    te = 213.8; % level of emissions which match -800 C.E.

    dist = dist*te;
    c.source.Box1.hx = [-900 dist(1); 2000 dist(1)]; % This is the box
# and source column # of the added source.
    c.source.Box2.hx = [-900 dist(2); -800 dist(2); 930 dist(2)*1; 1030
dist(2)*1; 1700 dist(2)*1];
    c.source.Box3.hx = [-900 dist(3); -800 dist(3); 930 dist(3)*1.133;
1030 dist(3)*1.153; 1700 dist(3)*1.204];
    c.source.Box4.hx = [-900 dist(4); -800 dist(4); 930 dist(4)*1.133;
1030 dist(4)*1.153; 1700 dist(4)*1.204];
```

```
    c.source.Box5.hx = [-900 dist(5); -800 dist(5); 930 dist(5)*0.998;
1030 dist(5)*1.078; 1700 dist(5)*1.036];
    c.source.Box6.hx = [-900 dist(6); -800 dist(6); 930 dist(6)*0.998;
1030 dist(6)*1.078; 1700 dist(6)*1.036];
    yearStart = -850;
    yearEnd = 1800;
    %saveScenarioOutput = 'y';
    saveScenarioSources = 'n';
    usePrevScenarioSources = 'n';
    c.sinkType = 'Feedback';
    c.transport = 'NoSeason';
    c.RealLatSolver = '34-56';

elseif strcmp(scenario,'N1')
    fprintf('Wetland emissions from Konijnendijk et al 2011.\n')
    yearStart = -850;
    yearEnd = 1800;

    % Uses the anomaly emissions from TRENCH:
    trench = load('Data\TRENCH_wetland_emissions_anomaly.txt');
    c.source.TropicalWetlands.hx = [-900 115; 2000 115];
    c.source.BorealWetlands.hx = [-3000 2; 2000 2];

    % Uses the actual numbers from TRENCH:
    %c.source.TropicalWetlands.hx = [-900 9; 2000 9]; % This is needed
to decrease the IPD slightly.
    %c.source.BorealWetlands.hx = [-3000 0; 2000 0];
    %trench = load('Data\TRENCH_wetland_emissions.txt');
    %trench(:,2:7) = trench(:,2:7)*.95;%.83;

    c.source.Box1.hx = [trench(:,1) trench(:,2)];
    c.source.Box2.hx = [trench(:,1) trench(:,3)];
    c.source.Box3.hx = [trench(:,1) trench(:,4)];
    c.source.Box4.hx = [trench(:,1) trench(:,5)];
    c.source.Box5.hx = [trench(:,1) trench(:,6)];
    c.source.Box6.hx = [trench(:,1) trench(:,7)];

    c.source.WildAnimals.hx = [-10000 15; 2000 15];
    c.source.Termites.hx = [-10000 20; 2000 20];
    c.source.Ocean.hx = [-10000 1; 2000 1]; % Rhee et al 2009, Bates et
al 1996
    c.source.Geologic.hx = [-10000 30; 2000 30];
    c.source.BiomassBurning.hx = [-10000 25; 2000 25];
    combineWetlandOutput = 'y';
    %saveScenarioOutput = 'y';

elseif strcmp(scenario,'N2')
    fprintf('Consistent with Singarayer Model results.\n')
    yearStart = -850;
    yearEnd = 1800;
    %PIHBaseSources = 'y';
```

```
    % Option 1: Source specification by box (estimated from Singarayer
figs):
    %c.source.Box3.hx = [-1000 0; 2000 11.2];
    %c.source.Box4.hx = [-1000 1.05; 2000 0];
    %c.source.Box5.hx = [-1000 0.35; 2000 0];
    %c.source.Box3.hx = [-3000 0; -2000 6.4; -1000 5; 2000
16];%11.2];%15];% 11.2];
    %c.source.Box4.hx = [-3000 1.5; 2000 0];
    %c.source.Box5.hx = [-3000 0.5; 2000 0];
    %c.source.BorealWetlands.hx =   [-3000 21; 2000 21];
    %c.source.TropicalWetlands.hx = [-3000 115; 2000 115];

    % Option 2: Singarayer's emissions
    %singarayer = load('Data\Singarayer et al 2011-emissions.txt');

    % Option 3: Singarayer anomaly with my tropical and boreal
emissions to
    % balance the IPD.
    singarayer = load('Data\Singarayer et al 2011-anomaly.txt');
    c.source.TropicalWetlands.hx = [-900 113; 2000 113]; %98
    c.source.BorealWetlands.hx = [-3000 19; 2000 19];

    c.source.Box1.hx = [singarayer(:,1) singarayer(:,7)];
    c.source.Box2.hx = [singarayer(:,1) singarayer(:,6)];
    c.source.Box3.hx = [singarayer(:,1) singarayer(:,5)];
    c.source.Box4.hx = [singarayer(:,1) singarayer(:,4)];
    c.source.Box5.hx = [singarayer(:,1) singarayer(:,3)];
    c.source.Box6.hx = [singarayer(:,1) singarayer(:,2)];

    c.source.WildAnimals.hx = [-10000 15; 2000 15];
    c.source.Termites.hx = [-10000 20; 2000 20];
    c.source.Ocean.hx = [-10000 1; 2000 1]; % Rhee et al 2009, Bates et
al 1996
    c.source.Geologic.hx = [-10000 30; 2000 30];
    c.source.BiomassBurning.hx = [-10000 25; 2000 25];
    combineWetlandOutput = 'y';
    %saveScenarioOutput = 'y';

elseif strcmp(scenario,'N21')
    fprintf('Consistent with Singarayer Model results-absolute
values.\n')
    yearStart = -850;
    yearEnd = 1800;

    singarayer = load('Data\Singarayer et al 2011-emissions.txt');

    singarayer(:,2:7) = singarayer(:,2:7)*.83;
```

```
    % This 15% reduction in emissions makes sense.  I think they
included
    % biomass buring emissions in their model and this 15% results in a
~25
    % Tg/yr reduction which is about the right amount of biomass buring
    % emissions that I have below.  Cool, or lucky.

    c.source.Box1.hx = [singarayer(:,1) singarayer(:,7)];
    c.source.Box2.hx = [singarayer(:,1) singarayer(:,6)];
    c.source.Box3.hx = [singarayer(:,1) singarayer(:,5)];
    c.source.Box4.hx = [singarayer(:,1) singarayer(:,4)];
    c.source.Box5.hx = [singarayer(:,1) singarayer(:,3)];
    c.source.Box6.hx = [singarayer(:,1) singarayer(:,2)];

    %c.source.TropicalWetlands.hx = [-900 95; 2000 95];
    %c.source.BorealWetlands.hx = [-3000 18; 2000 18];
    c.source.WildAnimals.hx = [-10000 15; 2000 15];
    c.source.Termites.hx = [-10000 20; 2000 20];
    c.source.Ocean.hx = [-10000 1; 2000 1]; % Rhee et al 2009, Bates et
al 1996
    c.source.Geologic.hx = [-10000 30; 2000 30];
    c.source.BiomassBurning.hx = [-10000 25; 2000 25];
    combineWetlandOutput = 'y';
    %saveScenarioOutput = 'y';

elseif strcmp(scenario,'N22')
    fprintf('Consistent with Singarayer Model results - estimated from
Singarayer figures.\n')
    yearStart = -850;
    yearEnd = 1800;

    % Option 1: Source specification by box (estimated from Singarayer
figs):
    c.source.Box3.hx = [-3000 0; -2000 6.4; -1000 5; 2000
16];%11.2];%15];% 11.2];
    c.source.Box4.hx = [-3000 1.5; 2000 0];
    c.source.Box5.hx = [-3000 0.5; 2000 0];
    c.source.BorealWetlands.hx =   [-3000 21; 2000 21];
    c.source.TropicalWetlands.hx = [-3000 115; 2000 115];

    c.source.WildAnimals.hx = [-10000 15; 2000 15];
    c.source.Termites.hx = [-10000 20; 2000 20];
    c.source.Ocean.hx = [-10000 1; 2000 1]; % Rhee et al 2009, Bates et
al 1996
    c.source.Geologic.hx = [-10000 30; 2000 30];
    c.source.BiomassBurning.hx = [-10000 25; 2000 25];
    combineWetlandOutput = 'y';
    %saveScenarioOutput = 'y';

elseif strcmp(scenario,'A1')
```

```
    fprintf('Houweling et al 2000 + isotope edits + budget updates.\n')
% Looks pretty good!!
    c.source.BorealWetlands.hx = [-900  13; 2000 13];
    c.source.TropicalWetlands.hx = [-900 121; 2000 121];
    c.source.Rice.hx = [-900 10; 1500 10; 2000 10];
    c.source.Rice.scaling = 'PerCapita';
    sourceAllAnthroScaling = 'PerCapita';
    c.source.ARuminants.hx = [-900 5; 1500 5; 2000 5];
    %c.source.ABiomassBurning.hx = [-900 10; 1500 10; 2000 10]; %
editited, should be 10.  checking C13
    c.source.Landfills.hx = [-900 5; 2000 5];

    c.source.WildAnimals.hx = [-10000 15; 2000 15];
    c.source.Termites.hx = [-10000 20; 2000 20];
    c.source.Ocean.hx = [-10000 1; 2000 1]; % Rhee et al 2009, Bates et
al 1996
    c.source.Geologic.hx = [-10000 30; 2000 30];
    c.source.BiomassBurning.hx = [-10000 25; 2000 25];

    sourceAnthroPerCapitaYear = 1500;
    yearStart = -850;
    yearEnd = 1800;
    %saveScenarioOutput = 'y';

elseif strcmp(scenario,'A11')
    fprintf('Houweling et al 2000 + isotope edits + budget updates +
Singarayer.\n') % Looks pretty good!!
    c.source.BorealWetlands.hx = [-900  14; 2000 14];
    c.source.TropicalWetlands.hx = [-900 101; 2000 101];%101 when
Singarayer anomaly is *1 % 92 when Singarayer anomaly is *1.5
    c.source.Rice.hx = [-900 10; 1500 10; 2000 10];
    c.source.Rice.scaling = 'PerCapita';
    sourceAllAnthroScaling = 'PerCapita';
    c.source.ARuminants.hx = [-900 5; 1500 5; 2000 5];
    %c.source.ABiomassBurning.hx = [-900 10; 1500 10; 2000 10]; %
editited, should be 10.  checking C13
    c.source.Landfills.hx = [-900 5; 2000 5];
    c.source.Termites.hx = [-900 20; 2000 20];
    c.source.BiomassBurning.hx = [-900 25; 2000 25]; % should be 5.
    c.source.Ocean.hx = [-900 1; 2000 1];
    c.source.Geologic.hx = [-900 30; 2000 30];
    c.source.WildAnimals.hx = [-900 15; 2000 15];
    sourceAnthroPerCapitaYear = 1500;

    %singarayer = load('Data\Singarayer et al 2011-emissions.txt');
    singarayer = load('Data\Singarayer et al 2011-anomaly.txt');
    singarayer(:,2:7) = singarayer(:,2:7)*1;
    c.source.Box1.hx = [singarayer(:,1) singarayer(:,7)];
    c.source.Box2.hx = [singarayer(:,1) singarayer(:,6)];
    c.source.Box3.hx = [singarayer(:,1) singarayer(:,5)];
    c.source.Box4.hx = [singarayer(:,1) singarayer(:,4)];
```

```
    c.source.Box5.hx = [singarayer(:,1) singarayer(:,3)];
    c.source.Box6.hx = [singarayer(:,1) singarayer(:,2)];

    yearStart = -850;
    yearEnd = 1800;
    %saveScenarioOutput = 'y';


elseif strcmp(scenario,'A12')
    fprintf('Houweling et al 2000.\n')
    c.source.BorealWetlands.hx = [-900  31; 2000 31];
    c.source.TropicalWetlands.hx = [-900 128; 2000 128];
    c.source.Rice.hx = [-900 10; 1500 10; 2000 10];
    c.source.Rice.scaling = 'PerCapita';
    sourceAllAnthroScaling = 'PerCapita';
    c.source.ARuminants.hx = [-900 5; 1500 5; 2000 5];
    c.source.ABiomassBurning.hx = [-900 10; 1500 10; 2000 10]; %
editited, should be 10.  checking C13
    c.source.Landfills.hx = [-900 5; 2000 5];
    c.source.Termites.hx = [-900 20; 2000 20];
    c.source.BiomassBurning.hx = [-900 5; 2000 5];
    c.source.Ocean.hx = [-900 15; 2000 15];
    c.source.Geologic.hx = [-900 3.5; 2000 3.5];
    c.source.WildAnimals.hx = [-900 15; 2000 15];
    sourceAnthroPerCapitaYear = 1500;
    yearStart = -850;
    yearEnd = 1800;
    %saveScenarioOutput = 'y';

elseif strcmp(scenario,'A13')
    fprintf('Houweling et al 2000 + budget updates.\n') % Looks pretty
good!!
    c.source.BorealWetlands.hx = [-900  13; 2000 13];
    c.source.TropicalWetlands.hx = [-900 121; 2000 121];
    c.source.Rice.hx = [-900 10; 1500 10; 2000 10];
    c.source.Rice.scaling = 'PerCapita';
    sourceAllAnthroScaling = 'PerCapita';
    c.source.ARuminants.hx = [-900 5; 1500 5; 2000 5];
    c.source.ABiomassBurning.hx = [-900 10; 1500 10; 2000 10]; %
editited, should be 10.  checking C13
    c.source.Landfills.hx = [-900 5; 2000 5];

    c.source.WildAnimals.hx = [-10000 15; 2000 15];
    c.source.Termites.hx = [-10000 20; 2000 20];
    c.source.Ocean.hx = [-10000 1; 2000 1]; % Rhee et al 2009, Bates et
al 1996
    c.source.Geologic.hx = [-10000 30; 2000 30];
    c.source.BiomassBurning.hx = [-10000 15; 2000 15];

    sourceAnthroPerCapitaYear = 1500;
    yearStart = -850;
```

```
    yearEnd = 1800;
    %saveScenarioOutput = 'y';


elseif strcmp(scenario,'A2')
    fprintf('Ruddiman 2007 w/ iso edits: ')
    % Climate feedbacks are incorporated into the natural emissions
(i.e.
    % wetlands)
    %
    % Ruddiman estimates that the rice anomaly at 1500 CE is 23-32 Tg
CH4/yr
    % and I think it must start at 0 Tg CH4/yr at 5000 BP.  If you
linearly
    % scale between these dates, you get 10.2-14.2 Tg CH4/yr at 3000 BP
    % (-1000 CE). (only use this estimate if you are linearly scaling
    % instead of PerCapita scaling).

    % Low Ruddiman rice estimate with constant natural sources.
    %c.source.Rice.hx =   [-1000  23; 1500 23; 2000 23];
    %c.source.BorealWetlands.hx =   [-900  25; -800 25; 1800 25];
    %c.source.TropicalWetlands.hx = [-900 127; -800 127; 1800 127];
    %fprintf('Low estimate with constant natural sources.\n')

    % Mid Ruddiman rice estimate with constant natural sources
    %c.source.Rice.hx =   [-1000  27.5; 1500 27.5; 2000 27.5];
    %c.source.BorealWetlands.hx =   [-900  8; 1800 8];
    %c.source.TropicalWetlands.hx = [-900 112; 1800 112];
    %fprintf('Mid estimate with constant natural sources.\n')

    % High Ruddiman rice estimate with constant natural sources
    c.source.BorealWetlands.hx =   [-900  7; 1800 7];
    c.source.TropicalWetlands.hx = [-900 109; 1800 109];
    c.source.Rice.hx =   [-1000  32; 2000 32];
    fprintf('High estimate with constant natural sources.\n')

    % Rice rice estimate to explain the entire anomaly with constant
natural sources
    %c.source.Rice.hx =   [-1000  40; 2000 40];
    %c.source.BorealWetlands.hx =   [-900  5; 1800 5];
    %c.source.TropicalWetlands.hx = [-900 104; 1800 104];
    %fprintf('Estimate where rice accounts for total increase with
constant natural sources.\n')

    %tt.BoxIPDFilter(dsearchn(tt.Year,1500))
    c.source.Rice.scaling = 'PerCapita';
    sourceAllAnthroScaling = 'PerCapita';
    sourceAnthroPerCapitaYear = 1500;
    c.source.ARuminants.hx = [-900 7; 1500 7; 2000 7];
    c.source.Landfills.hx = [-900 4; 2000 4];
```

```
    c.source.WildAnimals.hx = [-10000 15; 2000 15];
    c.source.Termites.hx = [-10000 20; 2000 20];
    c.source.Ocean.hx = [-10000 1; 2000 1]; % Rhee et al 2009, Bates et
al 1996
    c.source.Geologic.hx = [-10000 30; 2000 30];
    c.source.BiomassBurning.hx = [-10000 25; 2000 25];

    %c.d13cSolver = 'y';

    yearStart = -850;
    yearEnd = 1800;
    %saveScenarioOutput = 'y';

elseif strcmp(scenario,'Best')
    fprintf('Ruddiman 2007 w/ iso edits & Singarayer: ')
    % Climate feedbacks are incorporated into the natural emissions
(i.e.
    % wetlands)
    %
    % Ruddiman estimates that the rice anomaly at 1500 CE is 23-32 Tg
CH4/yr
    % and I think it must start at 0 Tg CH4/yr at 5000 BP.  If you
linearly
    % scale between these dates, you get 10.2-14.2 Tg CH4/yr at 3000 BP
    % (-1000 CE). (only use this estimate if you are linearly scaling
    % instead of PerCapita scaling).

    % Low Ruddiman rice estimate with constant natural sources.
    %c.source.Rice.hx =   [-1000  23; 2000 23];
    %c.source.BorealWetlands.hx =   [-900  9; 1800 9];
    %c.source.TropicalWetlands.hx = [-900 96; 1800 96];
    %fprintf('Low estimate with constant natural sources.\n')
    c.source.BorealWetlands.hx =   [-900  15; 1800 15];
    c.source.TropicalWetlands.hx = [-900 88; 1800 88];
    c.source.Rice.hx =   [-1000  13; 2000 13];
    fprintf('LEM edited Low estimate with constant natural sources.\n')

    % Mid Ruddiman rice estimate with constant natural sources
    %c.source.Rice.hx =   [-1000  27.5; 1500 27.5; 2000 27.5];
    %c.source.BorealWetlands.hx =   [-900  8; 1800 8];
    %c.source.TropicalWetlands.hx = [-900 93; 1800 93];
    %fprintf('Mid estimate with constant natural sources.\n')

    % High Ruddiman rice estimate with constant natural sources
    %c.source.Rice.hx =   [-1000  32; 1500 32; 2000 32];
    %c.source.BorealWetlands.hx =   [-900  22; -800 22; 1800 22];
    %c.source.TropicalWetlands.hx = [-900 124; -800 124; 1800 124];
    %fprintf('High estimate with constant natural sources.\n')

    %tt.BoxIPDFilter(dsearchn(tt.Year,1500))
    c.source.Rice.scaling = 'PerCapita';
```

```
    sourceAllAnthroScaling = 'PerCapita';
    sourceAnthroPerCapitaYear = 1500;
    c.source.ARuminants.hx = [-900 6; 2000 6];
    c.source.Landfills.hx = [-900 5; 2000 5];

    c.source.WildAnimals.hx = [-10000 15; 2000 15];
    c.source.Termites.hx = [-10000 20; 2000 20];
    c.source.Ocean.hx = [-10000 1; 2000 1]; % Rhee et al 2009, Bates et
al 1996
    c.source.Geologic.hx = [-10000 30; 2000 30];
    c.source.BiomassBurning.hx = [-10000 25; 2000 25];

    %c.d13cSolver = 'y';

    %singarayer = load('Data\Singarayer et al 2011-emissions.txt');
    singarayer = load('Data\Singarayer et al 2011-anomaly.txt');

    % Source specification by box (estimated from Singarayer figs):
    %c.source.Box3.hx = [-1000 0; 2000 11.2];
    %c.source.Box4.hx = [-1000 1.05; 2000 0];
    %c.source.Box5.hx = [-1000 0.35; 2000 0];

    c.source.Box1.hx = [singarayer(:,1) singarayer(:,7)];
    c.source.Box2.hx = [singarayer(:,1) singarayer(:,6)];
    c.source.Box3.hx = [singarayer(:,1) singarayer(:,5)*1.7];
    c.source.Box4.hx = [singarayer(:,1) singarayer(:,4)];
    c.source.Box5.hx = [singarayer(:,1) singarayer(:,3)];
    c.source.Box6.hx = [singarayer(:,1) singarayer(:,2)];


    yearStart = -850;
    yearEnd = 1800;
    combineWetlandOutput = 'y';
    %saveScenarioOutput = 'y';


elseif strcmp(scenario,'A21')
    fprintf('Ruddiman 2007 w/ (Original values): ')
    % Climate feedbacks are incorporated into the natural emissions
(i.e.
    % wetlands)
    %
    % Ruddiman estimates that the rice anomaly at 1500 CE is 23-32 Tg
CH4/yr
    % and I think it must start at 0 Tg CH4/yr at 5000 BP.  If you
linearly
    % scale between these dates, you get 10.2-14.2 Tg CH4/yr at 3000 BP
    % (-1000 CE). (only use this estimate if you are linearly scaling
    % instead of PerCapita scaling).
```

```
    % Low Ruddiman rice estimate with constant natural sources.
    %c.source.Rice.hx =   [-1000  23; 1500 23; 2000 23];
    %c.source.BorealWetlands.hx =   [-900  25; -800 25; 1800 25];
    %c.source.TropicalWetlands.hx = [-900 127; -800 127; 1800 127];
    %fprintf('Low estimate with constant natural sources.\n')

    % Mid Ruddiman rice estimate with constant natural sources
    c.source.Rice.hx =   [-1000  27.5; 1500 27.5; 2000 27.5];
    c.source.BorealWetlands.hx =   [-900  27; 1800 27];
    c.source.TropicalWetlands.hx = [-900 140; 1800 140];
    fprintf('Mid estimate with constant natural sources.\n')

    % High Ruddiman rice estimate with constant natural sources
    %c.source.Rice.hx =   [-1000  32; 1500 32; 2000 32];
    %c.source.BorealWetlands.hx =   [-900  22; -800 22; 1800 22];
    %c.source.TropicalWetlands.hx = [-900 124; -800 124; 1800 124];
    %fprintf('High estimate with constant natural sources.\n')

    %tt.BoxIPDFilter(dsearchn(tt.Year,1500))
%   These are the default values from Ruddiman.
    c.source.Rice.scaling = 'PerCapita';
    sourceAllAnthroScaling = 'PerCapita';
    sourceAnthroPerCapitaYear = 1500;
    c.source.ABiomassBurning.hx = [-1000 20; 2000 20];
    c.source.ARuminants.hx = [-900 7; 1500 7; 2000 7];
    c.source.Landfills.hx = [-900 4; 2000 4];
    c.source.BiomassBurning.hx = [-1000 5; 2000 5]; % Ruddiman = 5.
    c.source.Termites.hx = [-1000 20; 2000 20]; % Ruddiman 2001

    yearStart = -850;
    yearEnd = 1800;
    %saveScenarioOutput = 'y';



else
    disp('Using default scenario')
end

%%

% This will add in the LPIH base source scenario sources if they are
not defined above.
if exist('PIHBaseSources','var') && PIHBaseSources == 'y'
    if isfield(c.source, 'WildAnimals')==0; c.source.WildAnimals.hx =
[-10000 19; 2000 19]; end; % Harder et al 2007
    if isfield(c.source, 'Termites')==0; c.source.Termites.hx = [-10000
20.1; 2000 20.1]; end; % Harder et al 2007
    if isfield(c.source, 'Ocean')==0; c.source.Ocean.hx = [-10000 1;
2000 1]; end; % Rhee et al 2009, Bates et al 1996
```

```
    % if isfield(c.source, 'FreshWater')==0; c.source.FreshWater.hx =
[-10000 5.7; 2000 5.7]; end; Cannot find lat dist for this source
    if isfield(c.source, 'Geologic')==0; c.source.Geologic.hx = [-10000
30; 2000 30]; end; % Low estimate from Etiope et al 2008
    if isfield(c.source, 'BiomassBurning')==0;
c.source.BiomassBurning.hx = [-10000 20; 2000 20]; end; % Ferretti et
al 2005
    if isfield(c.source, 'BorealWetlands')==0;
c.source.BorealWetlands.hx = [-10000 45; 2000 45]; end; % Zhuang et
al., 2004, Table 5. 51.0 Tg CH4/yr modern, 47.8 Tg CH4/yr in 1900 CE.
    if isfield(c.source, 'TropicalWetlands')==0;
c.source.TropicalWetlands.hx = [-10000 125; 2000 125]; end;
end


if ~isfield(c,'transport'); c.transport = 'Season'; end;
if ~isfield(c,'RealLatSolver'); c.RealLatSolver = '0'; end;
if ~isfield(c,'LatSolver'); c.LatSolver = 'n'; end;
if ~isfield(c,'d13cSolver'); c.d13cSolver = 'n'; end;
if ~isfield(c,'solver'); c.solver.IPD = 'n'; end;
if ~isfield(c,'globalConc'); c.globalConc = 'n'; end;

% This allows you to turn off the seasonlity of all of the sources if
it is
% set to 'off'.  If it set to 'on' (or anything other than 'off') then
the
% seasonality is defined below for each source.
if ~exist('sourceAllSeasonality','var'); sourceAllSeasonality = 'off';
end;

% This allows you to set the sink to be either 'Constant' (currently
set
% at 8 years) or 'Feedback' which incorporates a 10% feedback of the
% concentration on the sink after Hopcroft et al 2011 (QSR).  The
default
% setting is 'Feedback'.

%c.sinkType = 'Constant'; % Uncomment this line if you want the sink to
be constant.
if ~isfield(c,'sinkType'); c.sinkType = 'Feedback'; end;


if ~isfield(c,'LatSolver'); c.LatSolver = 'n'; end;

% This lets the user know what parameters the model is using.
fprintf('Source Seasonality: %s.  Sink Type:
%s.\n',sourceAllSeasonality,c.sinkType)


% Can be set to 'PerCapita', 'Normalized', or 'Defined'.
```

```
% 'PerCapita' = emissions scaled to population, defined below (default
= 1500CE)
% 'Normalized' = Emissions are set in the scenario and are normalized
latitudinally.
% 'Default' = Use the default definitions below (usually PerCapita).
if ~exist('sourceAllAnthroScaling','var'); sourceAllAnthroScaling =
'PerCapita'; end;

% Population counts in each of the boxes from the HYDE database from
% 10,000BCE to 2000 CE
load('Data/HYDEpopulation.mat')
HYDEboxPop = fliplr(HYDEboxPop); % This is to properly orient the
boxes.  Box 1 = Antarctica, Box 6 = Greenland.
HYDEricePop = fliplr(HYDEricePop);

% logHYDE = 'y';
% if logHYDE == 'y'
%     HYDEboxPop = [HYDEboxPop(:,1) log(HYDEboxPop(:,2:6))];
%     HYDEricePop = [HYDEricePop(:,1:2) log(HYDEricePop(:,3:5))
HYDEricePop(:,6)];
% end



plt.fig99 = 'n';
if plt.fig99 == 'y'
    figure(99);clf;
    %plot(HYDEboxYear,HYDEboxPop(:,1),'.-
',HYDEboxYear,HYDEboxPop(:,2),'.-',HYDEboxYear,HYDEboxPop(:,3),'.-',...
    %    HYDEboxYear,HYDEboxPop(:,4),'.-
',HYDEboxYear,HYDEboxPop(:,5),'.-',HYDEboxYear,HYDEboxPop(:,6),'.-')
    %plot(HYDEboxYear,log(HYDEboxPop(:,3)),'.-')
    % percent of the total at each time step
    plot(HYDEboxYear,HYDEboxPop(:,1)./sum(HYDEboxPop,2),'.-
',HYDEboxYear,HYDEboxPop(:,2)./sum(HYDEboxPop,2),'.-
',HYDEboxYear,HYDEboxPop(:,3)./sum(HYDEboxPop,2),'.-',...
        HYDEboxYear,HYDEboxPop(:,4)./sum(HYDEboxPop,2),'.-
',HYDEboxYear,HYDEboxPop(:,5)./sum(HYDEboxPop,2),'.-
',HYDEboxYear,HYDEboxPop(:,6)./sum(HYDEboxPop,2),'.-')
    xlim([-800 1800])
    legend('B1','B2','B3','B4','B5','B6','Location','NorthWest')
    xlabel('Year C.E.')
    ylabel('Total Population')
end

plt.fig98 = 'n';
if plt.fig98 == 'y'
    figure(98);clf;
    plot(HYDEboxYear,HYDEricePop(:,1),'.-
',HYDEboxYear,HYDEricePop(:,2),'.-',HYDEboxYear,HYDEricePop(:,3),'.-
',...
```

```
        HYDEboxYear,HYDEricePop(:,4),'.-
',HYDEboxYear,HYDEricePop(:,5),'.-',HYDEboxYear,HYDEricePop(:,6),'.-')
    xlim([-800 1800])
    legend('B1','B2','B3','B4','B5','B6','Location','NorthWest')
    xlabel('Year C.E.')
    ylabel('Population in Rice Producing Areas')
end




if ~exist('sourceAnthroPerCapitaYear','var'); sourceAnthroPerCapitaYear
= 1500; end;
HYDEboxYearPerCapitaDefn =
dsearchn(HYDEboxYear,sourceAnthroPerCapitaYear); % Finds the value
closest to this year.
% Defines a scaling factor so that the source is per capita in the year
specified.
% So, it is 1 on the sourceAnthroPerCapitaYear and is scaled to
population changes after that.
c.stepPopPerCapitaScaler =
1/sum(HYDEboxPop(HYDEboxYearPerCapitaDefn,:));
c.stepRicePerCapitaScaler =
1/sum(HYDEricePop(HYDEboxYearPerCapitaDefn,:));


%% Source specific information.

c.sourceNames = fieldnames(c.source);
c.numSources = length(c.sourceNames);
c.sourceDist = [];
sourceIsoRatio = zeros(c.numSources,2);
c.maskSeason = [];
c.maskNoSeason = [];
c.sourceSeason = zeros(c.numSources*6,4);
sourcePlotNames{c.numSources,1} = [];
c.sourceRiceFlag = 0;
c.sourceAnthroFlag = [];

% This will use the annually avg source histories from a previous run.
% Note that the sources must match exactly.
if ~exist('usePrevScenarioSources','var'); usePrevScenarioSources =
'n'; end;
if strcmp(usePrevScenarioSources,'y')
    for i = 1:c.numSources
        if exist(['Scenario\Source-' c.sourceNames{i}
'.txt'],'file')==2
            c.source.(c.sourceNames{i}).hx = load(['Scenario\Source-'
c.sourceNames{i} '.txt']);
        else
```

```
            error('You must first run EBAMM to create the input
sources.')
        end
    end
end


for i = 1:c.numSources

    % Note: Total wetland sources are estimated to be between 80-230
Tg/yr. Not overly helpful, but its something.
    % Howeling 2000 estimates 130-194 Tg/yr for PIH.
    if strcmp(c.sourceNames{i},'BorealWetlands')
        c.source.BorealWetlands.name = 'Boreal Wetlands';
        %c.source.BorealWetlands.dist = [0 0.0018 0.0525 0.0575 0.6479
0.2403]; % BOSCAGE. Why is 10% of this source in the tropics??
        c.source.BorealWetlands.dist = [0 0 0 0 0.59 0.41]; % Zhuang et
al., 2004, Table 5. 51.0 Tg CH4/yr modern, 47.8 Tg CH4/yr in 1900 CE.
        c.source.BorealWetlands.iso = [-62 -380]; % dC13: Whiticar &
Schaefer 2007. dD: Whiticar & Schaefer 2007.
        c.source.BorealWetlands.seasonality = 'y';
        c.source.BorealWetlands.anthro = 'n';
        c.source.BorealWetlands.season = [...
            0.0000000e+000  0.0000000e+000  0.0000000e+000
0.0000000e+000
            6.1517145e-005  5.0558066e-005  5.7239299e-005 -2.9334404e-
005
            2.6493878e-003  4.1560309e-004 -5.8492219e-003 -7.9553386e-
004
            -1.7876002e-002 -2.1201428e-002  1.3767678e-003 -
2.1161591e-003
            -7.2108938e-001 -1.0564961e+000  1.8557603e-001
8.1791086e-002
            -3.1697171e-001 -3.9060413e-001  1.1169101e-001
2.7339620e-002];
    end

    if strcmp(c.sourceNames{i},'TropicalWetlands')
        c.source.TropicalWetlands.name = 'Tropical Wetlands';
        c.source.TropicalWetlands.dist = [0 0.0290 0.5019 0.3836 0.0820
0.0035]; % "Swamp" dist from BOSCAGE
        c.source.TropicalWetlands.iso = [-58.9 -360]; % d13C: Whiticar
& Schaefer 2007.  dD: Whiticar & Schaefer 2007.
        c.source.TropicalWetlands.seasonality = 'y';
        c.source.TropicalWetlands.anthro = 'n';
        c.source.TropicalWetlands.season = [...
            0.0000000e+000  0.0000000e+000  0.0000000e+000
0.0000000e+000
            3.1471755e-004  3.6164060e-004  5.7904531e-004  1.2914072e-
004
```

```
            -1.0693563e-003 -1.1285241e-003 -1.6888438e-003 -
1.6695957e-004
            -2.4436605e-003 -9.5885522e-003  3.5894072e-003
3.2205772e-003
            -1.5281658e-001 -4.8280462e-001 -3.5277294e-002 -
2.0856035e-002
            -2.1405476e-002 -4.4370930e-002  1.7031703e-002
1.6718498e-002];
    end

    if strcmp(c.sourceNames{i},'EASM')
        c.source.EASM.name = 'East Asian Monsoon';
        c.source.EASM.dist = [0 0 0 0.6 0.4 0]; % LEM
        c.source.EASM.iso = [-58.9 -360]; % d13C: Whiticar & Schaefer
2007.  dD: Whiticar & Schaefer 2007.
        c.source.EASM.seasonality = 'y';
        c.source.EASM.anthro = 'n';
        c.source.EASM.season = [...
            0.0000000e+000  0.0000000e+000  0.0000000e+000
0.0000000e+000
            3.1471755e-004  3.6164060e-004  5.7904531e-004  1.2914072e-
004
            -1.0693563e-003 -1.1285241e-003 -1.6888438e-003 -
1.6695957e-004
            -2.4436605e-003 -9.5885522e-003  3.5894072e-003
3.2205772e-003
            -1.5281658e-001 -4.8280462e-001 -3.5277294e-002 -
2.0856035e-002
            -2.1405476e-002 -4.4370930e-002  1.7031703e-002
1.6718498e-002]; % Seasonality is not correct.
    end

    if strcmp(c.sourceNames{i},'SASM')
        c.source.SASM.name = 'S. American Summer Monsoon';
        c.source.SASM.dist = [0 0.05 0.95 0 0 0]; % LEM
        c.source.SASM.iso = [-58.9 -360]; % d13C: Whiticar & Schaefer
2007.  dD: Whiticar & Schaefer 2007.
        c.source.SASM.seasonality = 'y';
        c.source.SASM.anthro = 'n';
        c.source.SASM.season = [...
            0.0000000e+000  0.0000000e+000  0.0000000e+000
0.0000000e+000
            3.1471755e-004  3.6164060e-004  5.7904531e-004  1.2914072e-
004
            -1.0693563e-003 -1.1285241e-003 -1.6888438e-003 -
1.6695957e-004
            -2.4436605e-003 -9.5885522e-003  3.5894072e-003
3.2205772e-003
            -1.5281658e-001 -4.8280462e-001 -3.5277294e-002 -
2.0856035e-002
            -2.1405476e-002 -4.4370930e-002  1.7031703e-002
1.6718498e-002]; % Seasonality is not correct
```

```
    end



    if strcmp(c.sourceNames{i},'WildAnimals')
        % This source should include all wild animals with methane
        % emissions except termites.
        c.source.WildAnimals.name = 'Wild Animals';
        c.source.WildAnimals.dist = [0 0.0494 0.1873 0.4113 0.3520 0];
% "Animal" dist from BOSCAGE.
        c.source.WildAnimals.iso = [-60.5 -330]; % Described as
Ruminants, but may be different...d13C: Whiticar & Schaefer 2007.  dD:
Whiticar & Schaefer 2007.
        c.source.WildAnimals.seasonality = 'n'; % This might be yes,
dependant on diet.
        c.source.WildAnimals.anthro = 'n';
    end

    if strcmp(c.sourceNames{i},'Termites')
        c.source.Termites.name = 'Termites';
        %c.source.Termites.dist = [0 0.20 0.30 0.30 0.20 0]; % Mitchell
estimated 2012-01-26. Need value and ref.  Houweling 2000 cites
Sanderson [ 1996] as a ref on Termite emissions.
        c.source.Termites.dist = [0 0.0230 0.4052 0.3713 0.2005 0]; %
Fung et al. 1991 (online data set, slightly different than the values
given in the paper)
        c.source.Termites.iso = [-61.5 -390]; % d13C: Whiticar and
Schaefer 2007. dD: Whiticar and Schaefer 2007.
        c.source.Termites.seasonality = 'n'; % This might be yes.
        c.source.Termites.anthro = 'n';
    end

    if strcmp(c.sourceNames{i},'BiomassBurning')
        % Note this is *Natural Biomass Burning*.
        c.source.BiomassBurning.name = 'Biomass Burning';
        c.source.BiomassBurning.dist = [0 0.0020 0.5595 0.4385 0 0]; %
BOSCAGE
        c.source.BiomassBurning.iso = [-25.6 -225]; % d13C: Whiticar &
Schaefer 2007 dD: Whiticar & Schaefer 2007 (PIH values)
        c.source.BiomassBurning.seasonality = 'y';
        c.source.BiomassBurning.anthro = 'n';
        c.source.BiomassBurning.season = [...
            0.0000000e+000  0.0000000e+000  0.0000000e+000
0.0000000e+000
            5.4473573e-003  9.1021875e-003  3.6043928e-003  1.9313382e-
003
            -2.5948164e+000 -8.3072635e-001  7.0500881e-001 -
8.5147033e-001
            8.8368868e-001  1.7004626e+000  5.7745412e-001  4.7057511e-
001
```

```
            0.0000000e+000  0.0000000e+000  0.0000000e+000
0.0000000e+000
            0.0000000e+000  0.0000000e+000  0.0000000e+000
0.0000000e+000];
    end

    if strcmp(c.sourceNames{i},'Ocean')
        c.source.Ocean.name = 'Ocean';
        %c.source.Ocean.dist = [0.0375  0.1273  0.1902  0.2182  0.2362
0.1906]; % CT-CH4 2010, (Lori Bruhwiler, 2012 Personal Communication)
        c.source.Ocean.dist = [0  0.21  0.47  0.32  0 0]; % Bates et al
1996
        c.source.Ocean.iso = [-58 -220]; % d13C: Whiticar & Schaefer
2007. dD: Whiticar & Schaefer 2007
        c.source.Ocean.seasonality = 'n';
        c.source.Ocean.anthro = 'n';
    end

    if strcmp(c.sourceNames{i},'FreshWater')
        c.source.FreshWater.name = 'Fresh Water';
        c.source.FreshWater.dist = [0 0.20 0.30 0.30 0.20 0]; % Need
value and ref.
        c.source.FreshWater.iso = [-53.8 -385]; % d13C: Whiticar &
Schaefer 2007. dD: Whiticar & Schaefer 2007.
        c.source.FreshWater.seasonality = 'n';
        c.source.FreshWater.anthro = 'n';
    end

    if strcmp(c.sourceNames{i},'MarineClathrates')
        c.source.MarineClathrates.name = 'Marine Clathrates';
        c.source.MarineClathrates.dist = [0 0 0 0 0 1]; % Fung et al
1991
        c.source.MarineClathrates.iso = [-62.5 -190]; % d13C: Whiticar
& Schaefer 2007. dD: Whiticar & Schaefer 2007.
        c.source.MarineClathrates.seasonality = 'n';
        c.source.MarineClathrates.anthro = 'n';
    end

    if strcmp(c.sourceNames{i},'Trees') % This is an speculative source
and it is not being used.
        c.source.Trees.name = 'Trees';
        c.source.Trees.dist = [0 0.20 0.30 0.30 0.20 0]; % Need value
and ref.
        c.source.Trees.iso = [-54 -300]; % d13C: Rice et al 2010. dD:
Need value and ref.
        c.source.Trees.seasonality = 'n'; % This is probably yes.
        c.source.Trees.anthro = 'n';
    end

    if strcmp(c.sourceNames{i},'Geologic')
        c.source.Geologic.name = 'Geologic';
```

```
        c.source.Geologic.dist = [0.000 0.004   0.049   0.074   0.622
0.251]; % Etiope 2012 Personal communication
        c.source.Geologic.iso = [-41.8 -200]; % d13C = Whiticar &
Schaefer 2007. dD = Whiticar & Schaefer 2007.
        c.source.Geologic.seasonality = 'n';
        c.source.Geologic.anthro = 'n';
    end

    % Anthropogenic sources.  All of these sources will be scaled to
population.
    if strcmp(c.sourceNames{i},'Rice')
        c.source.Rice.name = 'Rice';
        c.source.Rice.dist = [ 0 0.0018 0.1390 0.7750 0.0842 0]; %
BOSCAGE.
        c.source.Rice.iso = [-63 -320]; % d13C = Whiticar & Schaefer
2007. dD = Whiticar & Schaefer 2007.
        c.source.Rice.seasonality = 'n'; % This is obviously yes, but
the seasonal variability goes below 0 and messes with the stated source
strength, so I'm turning it off for now.
        c.source.Rice.anthro = 'n'; % This is set to 'n' because it is
scaled differently than the other anthropogenic sources.
        if isfield(c.source.Rice, 'scaling')==0; c.source.Rice.scaling
= 'PerCapita'; end; % Set this to 'PerCapita' (default) if you want
emissions scaled to population, 'Normalized' if you want it set to the
stated values in the scenario.
        c.source.Rice.season = [...
            0.0000000e+000  0.0000000e+000  0.0000000e+000
0.0000000e+000
            4.2627698e-003  1.0140951e-002  8.9084184e-004  2.1208445e-
003
            2.9993268e-001  2.0141328e-001  8.7953193e-002  4.5816198e-
002
            -2.1867322e+000 -1.7942316e+000  4.1577602e-001 -
3.3632247e-002
            -1.8266085e-001 -5.3713443e-001  9.2846468e-002
1.8170587e-001
            0.0000000e+000  0.0000000e+000  0.0000000e+000
0.0000000e+000  ];
    end



    if strcmp(c.sourceNames{i},'ARuminants')
        c.source.ARuminants.name = 'Anthropogenic Ruminants';
        c.source.ARuminants.dist = [0 0.0494 0.1873 0.4113 0.3520 0]; %
"Animal" dist from BOSCAGE.
        c.source.ARuminants.iso = [-60.5 -330]; % d13C: Whiticar &
Schaefer 2007. dD: Whiticar & Schaefer 2007
        c.source.ARuminants.seasonality = 'n'; % This might be yes.
        c.source.ARuminants.anthro = 'y';
        c.source.ARuminants.scaling = 'PerCapita'; % Set this to
'PerCapita' if you want emissions scaled to population, 'Normalized' if
you want it set to the stated values in the scenario.
```

```
    end

    if strcmp(c.sourceNames{i},'Landfills')
        c.source.Landfills.name = 'Landfills';
        c.source.Landfills.dist = [0 0.0025 0.0195 0.1635 0.8083
0.0062]; % BOSCAGE
        c.source.Landfills.iso = [-55 -310]; % d13C: Whiticar &
Schaefer 2007. dD: Whiticar & Schaefer 2007
        c.source.Landfills.seasonality = 'n';
        c.source.Landfills.anthro = 'y';
        c.source.Landfills.scaling = 'PerCapita'; % Set this to
'PerCapita' if you want emissions scaled to population, 'Normalized' if
you want it set to the stated values in the scenario.
    end


    if strcmp(c.sourceNames{i},'ABiomassBurning')
        c.source.ABiomassBurning.name = 'Anthropogenic Biomass
Burning';
        c.source.ABiomassBurning.dist = [0 0.0020 0.5595 0.4385 0 0]; %
BOSCAGE (same as natural BB).
        c.source.ABiomassBurning.iso = [-24.6 -225]; % d13C: Whiticar &
Schaefer 2007. dD: Whiticar & Schaefer 2007.
        c.source.ABiomassBurning.seasonality = 'y';
        c.source.ABiomassBurning.anthro = 'y';
        c.source.ABiomassBurning.scaling = 'PerCapita'; % Set this to
'PerCapita' if you want emissions scaled to population, 'Normalized' if
you want it set to the stated values in the scenario.
        c.source.ABiomassBurning.season = [...
            0.0000000e+000  0.0000000e+000  0.0000000e+000
0.0000000e+000
            5.4473573e-003  9.1021875e-003  3.6043928e-003  1.9313382e-
003
            -2.5948164e+000 -8.3072635e-001  7.0500881e-001 -
8.5147033e-001
            8.8368868e-001  1.7004626e+000  5.7745412e-001  4.7057511e-
001
            0.0000000e+000  0.0000000e+000  0.0000000e+000
0.0000000e+000
            0.0000000e+000  0.0000000e+000  0.0000000e+000
0.0000000e+000];
    end

    if strcmp(c.sourceNames{i},'Coal')
        c.source.Coal.name = 'Coal';
        c.source.Coal.dist = [0 0 0.0995 0.2593 0.6102 0.0310]; %
BOSCAGE
        c.source.Coal.iso = [-37.0 -140]; % d13C: Whiticar & Schaefer
2007. dD: Whiticar & Schaefer 2007.
        c.source.Coal.seasonality = 'n';
        c.source.Coal.anthro = 'y';
```

```
        c.source.Coal.scaling = 'PerCapita'; % Set this to 'PerCapita'
if you want emissions scaled to population, 'Normalized' if you want it
set to the stated values in the scenario.
    end

    if strcmp(c.sourceNames{i},'OilGas')
        c.source.OilGas.name = 'Oil & Gas';
        c.source.OilGas.dist = [0 0.0072 0.0822 0.4070 0.5036 0]; %
BOSCAGE
        c.source.OilGas.iso = [-35.2 -190]; % d13C = BOSCAGE. dD =
BOSCAGE.
        c.source.OilGas.seasonality = 'n';
        c.source.OilGas.anthro = 'y';
        c.source.OilGas.scaling = 'PerCapita'; % Set this to
'PerCapita' if you want emissions scaled to population, 'Normalized' if
you want it set to the stated values in the scenario.
    end

    if strcmp(c.sourceNames{i},'SiberianGas')
        c.source.SiberianGas.name = 'Siberian Gas';
        c.source.SiberianGas.dist = [0 0 0 0 0.5833 0.4167]; % BOSCAGE
        c.source.SiberianGas.iso = [-51 -205]; % d13C = BOSCAGE. dD =
BOSCAGE.
        c.source.SiberianGas.seasonality = 'n';
        c.source.SiberianGas.anthro = 'y';
        c.source.SiberianGas.scaling = 'PerCapita'; % Set this to
'PerCapita' if you want emissions scaled to population, 'Normalized' if
you want it set to the stated values in the scenario.
    end

    % These are sources that can be added to a box based on latitude.
    if strcmp(c.sourceNames{i},'Box1')
        c.source.Box1.name = 'Box 1';
        c.source.Box1.dist = [1 0 0 0 0 0];
        c.source.Box1.iso = [-58.9 -360]; % After tropical wetlands.
        c.source.Box1.seasonality = 'n';
        c.source.Box1.anthro = 'n';
    end

    if strcmp(c.sourceNames{i},'Box2')
        c.source.Box2.name = 'Box 2';
        c.source.Box2.dist = [0 1 0 0 0 0];
        c.source.Box2.iso = [-58.9 -360]; % After tropical wetlands.
        c.source.Box2.seasonality = 'n';
        c.source.Box2.anthro = 'n';
    end

    if strcmp(c.sourceNames{i},'Box3')
        c.source.Box3.name = 'Box 3';
        c.source.Box3.dist = [0 0 1 0 0 0];
        c.source.Box3.iso = [-58.9 -360]; % After tropical wetlands.
```

```
    c.source.Box3.seasonality = 'n';
    c.source.Box3.anthro = 'n';
end

if strcmp(c.sourceNames{i},'Box4')
    c.source.Box4.name = 'Box 4';
    c.source.Box4.dist = [0 0 0 1 0 0];
    c.source.Box4.iso = [-58.9 -360]; % After tropical wetlands.
    c.source.Box4.seasonality = 'n';
    c.source.Box4.anthro = 'n';
end

if strcmp(c.sourceNames{i},'Box5')
    c.source.Box5.name = 'Box 5';
    c.source.Box5.dist = [0 0 0 0 1 0];
    c.source.Box5.iso = [-62 -380]; % After boreal wetlands.
    c.source.Box5.seasonality = 'n';
    c.source.Box5.anthro = 'n';
end

if strcmp(c.sourceNames{i},'Box6')
    c.source.Box6.name = 'Box 6';
    c.source.Box6.dist = [0 0 0 0 0 1];
    c.source.Box6.iso = [-62 -380]; % After boreal wetlands.
    c.source.Box6.seasonality = 'n';
    c.source.Box6.anthro = 'n';
end


% Now some variables are set up that will be used later.
c.sourceDist(:,i) = c.source.(c.sourceNames{i}).dist';
sourceIsoRatio(i,:) = c.source.(c.sourceNames{i}).iso;
sourcePlotNames{i,:} = c.source.(c.sourceNames{i}).name;

% This is used in ebammODE45 to indicate which source is rice.
if strcmp(c.source.(c.sourceNames{i}).name,'Rice')
    c.sourceRiceFlag = i;
end

if strcmp(c.source.(c.sourceNames{i}).anthro,'y')
    c.sourceAnthroFlag = [c.sourceAnthroFlag; i];
        if strcmp(sourceAllAnthroScaling,'PerCapita')
            c.source.(c.sourceNames{i}).scaling = 'PerCapita';
        elseif strcmp(sourceAllAnthroScaling,'Normalized')
            c.source.(c.sourceNames{i}).scaling = 'Normalized';
        elseif strcmp(sourceAllAnthroScaling,'Default')
            return
        end
end

% Sets the source seasonality to 'n' if all of the seasonality is
```

```
    % turned off above.
    if strcmp(sourceAllSeasonality,'off');
        c.source.(c.sourceNames{i}).seasonality = 'n';
    end



    % This makes a mask that differentiates between sources with
seasonal
    % variability and those without.
    if c.source.(c.sourceNames{i}).seasonality == 'y'
        for j = 1:6
            if c.source.(c.sourceNames{i}).dist(1,j) ~= 0
                c.maskSeason = [c.maskSeason; j+(i-1)*6];
                c.sourceSeason(j+(i-1)*6,:) =
c.source.(c.sourceNames{i}).season(j,:);
            else
                c.maskNoSeason = [c.maskNoSeason; j+(i-1)*6];
            end
        end
    else
        c.maskNoSeason = [c.maskNoSeason; (1:6)'+(i-1)*6];
    end


end
```

File: ebammODE45.m

```
function [ dbdt ] = ebammODE45(t,b,c)
%boscageFun Summary of this function goes here
% t = model time.
% b = burden for each box
% More detail goes here.

global stepSource stepSink stepYear

% For testing, use these initial conditions:
%t = 1500;
%b = binit; % defined in the main program
% other constants (located in the c struct) need to be loaded also.



%% Methanequelle subsystem
% This prepares the sources for this time step.

% NOTE: Interp1 takes a lot of computing time to run each time it is
% called, so it is much faster to combine all of the time series you
intend
% to interpolate into one large array and only call interp1 once, then
% extract the interpolated values out again.  The disadvantage of this
is
% that the input data (population, etc) all have to be on the same x
(time)
% axis.  Use interp1 outside of the ode45 function to get all of the
time
% series on the same x (time) axis.
stepInterp = interp1q(c.InterpYear,c.Interp,t)';

stepSourceScalar = stepInterp(14:13+c.numSources,1);

% u has units of terramoles CH4.
u = zeros(6,c.numSources);

c.stepTotSourceStrength =
bsxfun(@times,[1;1;1;1;1;1],stepSourceScalar'); % repmat is slower than
bsxfun.

if ~isempty(c.maskSeason);
    s=[1;sin(2*pi*t);cos(2*pi*t);sin(4*pi*t);cos(4*pi*t)];
    u(c.maskSeason) =
[c.stepTotSourceStrength(c.maskSeason).*c.sourceDist(c.maskSeason)
c.sourceSeason(c.maskSeason,:)]*s;
end
if ~isempty(c.maskNoSeason);
```

```
    u(c.maskNoSeason) =
c.stepTotSourceStrength(c.maskNoSeason).*c.sourceDist(c.maskNoSeason);
end

if  c.sourceRiceFlag>0
    if
strcmp(c.source.(c.sourceNames{c.sourceRiceFlag}).scaling,'PerCapita')
        % Use this scaling factor to make emissions equal to the stated
value
        % at the year defined by sourceAnthroPerCapitaYear.  This is
essentially
        % a 'per capita' scaling.
        % Calculated by: 1/sum(HYDEricePop(HYDEboxYearPerCapitaDefn,:))
        stepRice = stepInterp(7:12)*c.stepRicePerCapitaScaler;
    else
        % Use this scaling if you would like the Rice emissions to
equal
        % the stated value all the time regardless of the total
population.
        % This allows the rice emissions to equal the stated value, but
        % distributed latitudinally according to population at each
        % latitude.
        stepRice =
stepInterp(7:12)/(stepInterp(7)+stepInterp(8)+stepInterp(9)+stepInterp(
10)+stepInterp(11)+stepInterp(12));
    end
    u(:,c.sourceRiceFlag) =
(u(1,c.sourceRiceFlag)+u(2,c.sourceRiceFlag)+...

u(3,c.sourceRiceFlag)+u(4,c.sourceRiceFlag)+u(5,c.sourceRiceFlag)+...
        u(6,c.sourceRiceFlag))*stepRice;
end

count = 0;
while count < length(c.sourceAnthroFlag)
    count = count+1;
    if
strcmp(c.source.(c.sourceNames{c.sourceAnthroFlag(count)}).scaling,'Per
Capita')
        % This scaling factor was chosen because it makes emissions be
equal to the
        % stated value in ebammSource with the variable
sourceAnthroPerCapitaYear.
        % i.e. this is per capita sources at e.g. 1500CE.
        % Calculated by 1/sum(HYDEboxPop(HYDEboxYearPerCapitaDefn,:))
        stepPop = stepInterp(1:6,1)*c.stepPopPerCapitaScaler;
    else
        % Normalized.  Use this to specify sources the scenarios and
        % have them equal to their specified value.  i.e. sources are
        % not scaled to total population, but they are still
distributed
```

```
        % latitudinally according to the latitudinal distribution of
population.
        stepPop =
stepInterp(1:6)/(stepInterp(1)+stepInterp(2)+stepInterp(3)+stepInterp(4
)+stepInterp(5)+stepInterp(6));
    end
    u(:,c.sourceAnthroFlag(count)) =
(u(1,c.sourceAnthroFlag(count))+...

u(2,c.sourceAnthroFlag(count))+u(3,c.sourceAnthroFlag(count))+...

u(4,c.sourceAnthroFlag(count))+u(5,c.sourceAnthroFlag(count))+...
        u(6,c.sourceAnthroFlag(count)))*stepPop;

end

%for i = 1:c.numSources
%    if strcmp(c.source.(c.sourceNames{i}).anthro,'y')
%        u(:,i) = u(:,i).*stepPopLatRatio;
%    end
%end

u(u<0) = 0; % If any source is below 0, set it to 0.

stepSource = reshape(u',1,c.numSources*6);

q12=u.*c.r12;
q13=u.*c.r13;
qD=u.*c.rD;
md=[sum(q12,2) sum(q13,2) sum(qD,2)];

% This is the source strength in this time step.
source = [md;0 0 0;0 0 0];%reshape(m,3,6); % 6 boxes, each with 12C,
13C, D source



%% Calculate the Sink

% y2 = x(1)+x(2)*sin(2*pi*x(3)*t+x(4));

% Box 3 = [   5.0910 1.7062 1.0000 1.8594];

%stepOH = (((0-1.4)/(1000-0))*(sum(sum(b))-1000)+0);
stepOH = stepInterp(13,1);

% The budget at this time step:
bStep = reshape(b,8,3);
bTrop = bStep(1:6,:);
bStrat = bStep(7:8,:);
```

```
sink = zeros(8,3);

%if t > 1500.5
%    i = 1; keyboard;
%end


if strcmp(c.sinkType,'Feedback')
    % This is the sink parameterization for the 10% feedback of the
    % concentration on the sink.  See Hopcroft et al 2011 (QSR).
    %   [bTrop-0.1*(bTrop-c.bStepTrop1500CE)  <- Alternate, but
equivalent.
    v = [0.9*bTrop+0.1*c.bStepTrop1500CE,
c.s_transTrop(:,1).*(1+c.s_transTrop(:,4)*t+c.s_transTrop(:,2).*cos(2*p
i*(t-c.s_transTrop(:,3)))+c.s_transTrop(:,5).*cos(2*pi*(2*t-
c.s_transTrop(:,6))))*stepOH, c.m_soil'];
    sink(1:6,:) =
[v(:,1).*(c.k12*v(:,4)+c.k_soil12*v(:,5)),v(:,2).*(c.k13*v(:,4)+c.k_soi
l13*v(:,5)),v(:,3).*(c.kD*v(:,4)+c.k_soilD*v(:,5))];

    v2 = [0.9*bStrat+0.1*c.bStepStrat1500CE,
c.s_transStrat(:,1).*(1+c.s_transStrat(:,4)*t+c.s_transStrat(:,2).*cos(
2*pi*(t-c.s_transStrat(:,3)))+c.s_transStrat(:,5).*cos(2*pi*(2*t-
c.s_transStrat(:,6))))*stepOH];
    sink(7:8,:) =
[c.k12*v2(:,1).*v2(:,4),c.k13st*v2(:,2).*v2(:,4),c.kDst*v2(:,3).*v2(:,4
)];
elseif strcmp(c.sinkType,'NoSeason')
    % This is the sink parameterization for the 10% feedback of the
    % concentration on the sink.  See Hopcroft et al 2011 (QSR).
    v = [0.9*bTrop+0.1*c.bStepTrop1500CE, c.s_transTrop(:,1)*stepOH,
c.m_soil'];
    sink(1:6,:) =
[v(:,1).*(c.k12*v(:,4)+c.k_soil12*v(:,5)),v(:,2).*(c.k13*v(:,4)+c.k_soi
l13*v(:,5)),v(:,3).*(c.kD*v(:,4)+c.k_soilD*v(:,5))];

    v2 = [0.9*bStrat+0.1*c.bStepStrat1500CE,
c.s_transStrat(:,1)*stepOH];
    sink(7:8,:) =
[c.k12*v2(:,1).*v2(:,4),c.k13st*v2(:,2).*v2(:,4),c.kDst*v2(:,3).*v2(:,4
)];
else
    % This is for a constant sink.
    v = [bTrop,
c.s_transTrop(:,1).*(1+c.s_transTrop(:,4)*t+c.s_transTrop(:,2).*cos(2*p
i*(t-c.s_transTrop(:,3)))+c.s_transTrop(:,5).*cos(2*pi*(2*t-
c.s_transTrop(:,6))))*stepOH, c.m_soil'];
    sink(1:6,:) =
[v(:,1).*(c.k12*v(:,4)+c.k_soil12*v(:,5)),v(:,2).*(c.k13*v(:,4)+c.k_soi
l13*v(:,5)),v(:,3).*(c.kD*v(:,4)+c.k_soilD*v(:,5))];
```

```
    v2 = [bStrat,
c.s_transStrat(:,1).*(1+c.s_transStrat(:,4)*t+c.s_transStrat(:,2).*cos(
2*pi*(t-c.s_transStrat(:,3)))+c.s_transStrat(:,5).*cos(2*pi*(2*t-
c.s_transStrat(:,6))))*stepOH];
    sink(7:8,:) =
[c.k12*v2(:,1).*v2(:,4),c.k13st*v2(:,2).*v2(:,4),c.kDst*v2(:,3).*v2(:,4
)];
end

sink(sink<0) = 1e-20; % If the sink is below 0, set it to 0.  This
happens in box 1 and 6 occasionally.

stepSink = reshape(sink',1,24);

%% Calculate the transport
if strcmp(c.transport,'NoSeason')
    % Box 1
    t12(1,1:3)=c.t_12(1)/c.boxMass(1)*bStep(1,:);
    t17(1,1:3)=c.t_17(1)/c.boxMass(1)*bStep(1,:);

    % Box 2
    t21(1,1:3)=c.t_12(1)/c.boxMass(2)*bStep(2,:);
    t23(1,1:3)=c.t_23(1)/c.boxMass(2)*bStep(2,:);
    t27(1,1:3)=c.t_27(1)/c.boxMass(2)*bStep(2,:);

    % Box 3
    t34(1,1:3)=c.t_34(1)/c.boxMass(3)*bStep(3,:);
    t32(1,1:3)=c.t_23(1)/c.boxMass(3)*bStep(3,:);
    t37(1,1:3)=c.t_37(1)/c.boxMass(3)*bStep(3,:);
    %t34 = t34*0.75;
    %The thesis says that interhemispheric transport should be reduced,
but in
    %the model that I got, the transport was not reduced.  I wonder
why?
    % 9-28-12 I can't find this in the thesis.

    % Box 4
    t43(1,1:3)=c.t_34(1)/c.boxMass(4)*bStep(4,:);
    t45(1,1:3)=c.t_45(1)/c.boxMass(4)*bStep(4,:);
    t48(1,1:3)=c.t_48(1)/c.boxMass(4)*bStep(4,:);
    %t43 = t43*0.75; % See note above for box 3.

    % Box 5
    t54(1,1:3)=c.t_45(1)/c.boxMass(5)*bStep(5,:);
    t56(1,1:3)=c.t_56(1)/c.boxMass(5)*bStep(5,:);
    t58(1,1:3)=c.t_58(1)/c.boxMass(5)*bStep(5,:);

    % Box 6
    t65(1,1:3)=c.t_56(1)/c.boxMass(6)*bStep(6,:);
```

```
    t68(1,1:3)=c.t_68(1)/c.boxMass(6)*bStep(6,:);

    % Box 7
    t71(1,1:3)=c.t_17(1)/c.boxMass(7)*bStep(7,:);
    t72(1,1:3)=c.t_27(1)/c.boxMass(7)*bStep(7,:);
    t73(1,1:3)=c.t_37(1)/c.boxMass(7)*bStep(7,:);
    t78(1,1:3)=c.t_78(1)/c.boxMass(7)*bStep(7,:);

    % Box 8
    t84(1,1:3)=c.t_48(1)/c.boxMass(8)*bStep(8,:);
    t85(1,1:3)=c.t_58(1)/c.boxMass(8)*bStep(8,:);
    t86(1,1:3)=c.t_68(1)/c.boxMass(8)*bStep(8,:);
    t87(1,1:3)=c.t_78(1)/c.boxMass(8)*bStep(8,:);

else % These transport terms have seasonal variations.
    % Box 1
    t12(1,1:3)=c.t_12(1)*(1+c.t_12(2)*cos(2*pi*(t-
c.t_12(3)))+c.t_12(4)*cos(4*pi*(t-c.t_12(5))))/c.boxMass(1)*bStep(1,:);
    t17(1,1:3)=c.t_17(1)*(1+c.t_17(2)*cos(2*pi*(t-
c.t_17(3)))+c.t_17(4)*cos(4*pi*(t-c.t_17(5))))/c.boxMass(1)*bStep(1,:);

    % Box 2
    t21(1,1:3)=c.t_12(1)*(1+c.t_12(2)*cos(2*pi*(t-
c.t_12(3)))+c.t_12(4)*cos(4*pi*(t-c.t_12(5))))/c.boxMass(2)*bStep(2,:);
    t23(1,1:3)=c.t_23(1)*(1+c.t_23(2)*cos(2*pi*(t-
c.t_23(3)))+c.t_23(4)*cos(4*pi*(t-c.t_23(5))))/c.boxMass(2)*bStep(2,:);
    t27(1,1:3)=c.t_27(1)*(1+c.t_27(2)*cos(2*pi*(t-
c.t_27(3)))+c.t_27(4)*cos(4*pi*(t-c.t_27(5))))/c.boxMass(2)*bStep(2,:);

    % Box 3
    t34(1,1:3)=c.t_34(1)*(1+c.t_34(2)*cos(2*pi*(t-
c.t_34(3)))+c.t_34(4)*cos(4*pi*(t-c.t_34(5))))/c.boxMass(3)*bStep(3,:);
    t32(1,1:3)=c.t_23(1)*(1+c.t_23(2)*cos(2*pi*(t-
c.t_23(3)))+c.t_23(4)*cos(4*pi*(t-c.t_23(5))))/c.boxMass(3)*bStep(3,:);
    t37(1,1:3)=c.t_37(1)*(1+c.t_37(2)*cos(2*pi*(t-
c.t_37(3)))+c.t_37(4)*cos(4*pi*(t-c.t_37(5))))/c.boxMass(3)*bStep(3,:);
    %t34 = t34*0.75;
    %The thesis says that interhemispheric transport should be reduced,
but in
    %the model that I got, the transport was not reduced.  I wonder
why?
    % 9-28-12 I can't find this in the thesis.

    % Box 4
    t43(1,1:3)=c.t_34(1)*(1+c.t_34(2)*cos(2*pi*(t-
c.t_34(3)))+c.t_34(4)*cos(4*pi*(t-c.t_34(5))))/c.boxMass(4)*bStep(4,:);
    t45(1,1:3)=c.t_45(1)*(1+c.t_45(2)*cos(2*pi*(t-
c.t_45(3)))+c.t_45(4)*cos(4*pi*(t-c.t_45(5))))/c.boxMass(4)*bStep(4,:);
    t48(1,1:3)=c.t_48(1)*(1+c.t_48(2)*cos(2*pi*(t-
c.t_48(3)))+c.t_48(4)*cos(4*pi*(t-c.t_48(5))))/c.boxMass(4)*bStep(4,:);
    %t43 = t43*0.75; % See note above for box 3.
```

```
    % Box 5
    t54(1,1:3)=c.t_45(1)*(1+c.t_45(2)*cos(2*pi*(t-
c.t_45(3)))+c.t_45(4)*cos(4*pi*(t-c.t_45(5))))/c.boxMass(5)*bStep(5,:);
    t56(1,1:3)=c.t_56(1)*(1+c.t_56(2)*cos(2*pi*(t-
c.t_56(3)))+c.t_56(4)*cos(4*pi*(t-c.t_56(5))))/c.boxMass(5)*bStep(5,:);
    t58(1,1:3)=c.t_58(1)*(1+c.t_58(2)*cos(2*pi*(t-
c.t_58(3)))+c.t_58(4)*cos(4*pi*(t-c.t_58(5))))/c.boxMass(5)*bStep(5,:);

    % Box 6
    t65(1,1:3)=c.t_56(1)*(1+c.t_56(2)*cos(2*pi*(t-
c.t_56(3)))+c.t_56(4)*cos(4*pi*(t-c.t_56(5))))/c.boxMass(6)*bStep(6,:);
    t68(1,1:3)=c.t_68(1)*(1+c.t_68(2)*cos(2*pi*(t-
c.t_68(3)))+c.t_68(4)*cos(4*pi*(t-c.t_68(5))))/c.boxMass(6)*bStep(6,:);

    % Box 7
    t71(1,1:3)=c.t_17(1)*(1+c.t_17(2)*cos(2*pi*(t-
c.t_17(3)))+c.t_17(4)*cos(4*pi*(t-c.t_17(5))))/c.boxMass(7)*bStep(7,:);
    t72(1,1:3)=c.t_27(1)*(1+c.t_27(2)*cos(2*pi*(t-
c.t_27(3)))+c.t_27(4)*cos(4*pi*(t-c.t_27(5))))/c.boxMass(7)*bStep(7,:);
    t73(1,1:3)=c.t_37(1)*(1+c.t_37(2)*cos(2*pi*(t-
c.t_37(3)))+c.t_37(4)*cos(4*pi*(t-c.t_37(5))))/c.boxMass(7)*bStep(7,:);
    t78(1,1:3)=c.t_78(1)*(1+c.t_78(2)*cos(2*pi*(t-
c.t_78(3)))+c.t_78(4)*cos(4*pi*(t-c.t_78(5))))/c.boxMass(7)*bStep(7,:);

    % Box 8
    t84(1,1:3)=c.t_48(1)*(1+c.t_48(2)*cos(2*pi*(t-
c.t_48(3)))+c.t_48(4)*cos(4*pi*(t-c.t_48(5))))/c.boxMass(8)*bStep(8,:);
    t85(1,1:3)=c.t_58(1)*(1+c.t_58(2)*cos(2*pi*(t-
c.t_58(3)))+c.t_58(4)*cos(4*pi*(t-c.t_58(5))))/c.boxMass(8)*bStep(8,:);
    t86(1,1:3)=c.t_68(1)*(1+c.t_68(2)*cos(2*pi*(t-
c.t_68(3)))+c.t_68(4)*cos(4*pi*(t-c.t_68(5))))/c.boxMass(8)*bStep(8,:);
    t87(1,1:3)=c.t_78(1)*(1+c.t_78(2)*cos(2*pi*(t-
c.t_78(3)))+c.t_78(4)*cos(4*pi*(t-c.t_78(5))))/c.boxMass(8)*bStep(8,:);


end


% Transport in and out of each box for this time step.
trans(1,:) = (t21+t71)-(t17+t12);
trans(2,:) = (t12+t32+t72)-(t21+t23+t27);
trans(3,:) = (t23+t43+t73)-(t32+t34+t37);
trans(4,:) = (t54+t34+t84)-(t45+t43+t48);
trans(5,:) = (t45+t65+t85)-(t54+t56+t58);
trans(6,:) = (t56+t86)-(t65+t68);
trans(7,:) = (t17+t27+t37+t87)-(t71+t72+t73+t78);
trans(8,:) = (t48+t58+t68+t78)-(t84+t85+t86+t87);
```

```
%% Latitudinal solver
if strcmp(c.RealLatSolver,'3-4')
%
%      l = sum(bStep,2)./sum(sink,2);
%     %l = 1./l;
%
%     % % This omega is if the transport does not have the bStep in it
%     % % already.
%     % omega = [l(1)+sum(t12(1)+t17(1)) sum(-t21(1)) 0 0 0 0
%     %          sum(-t12(1)) l(2)+sum(t21(1)+t23(1)+t27(1)) sum(-
t32(1)) 0 0 0
%     %          0 sum(-t23(1)) l(3)+sum(t32(1)+t34(1)+t37(1)) sum(-
t43(1)) 0 0
%     %          0 0 sum(-t34(1)) l(4)+sum(t43(1)+t45(1)+t48(1)) sum(-
t54(1)) 0
%     %          0 0 0 sum(-t45(1)) l(5)+sum(t54(1)+t56(1)+t58(1)) sum(-
t65(1))
%     %          0 0 0 0 sum(-t56(1)) l(6)+sum(t65(1)+t68(1))];
%     %
%     % % This omega is for use if the transport is in it.
%     % omega = [l(1)+(t12+t17)/bStep(1,:) -t21/bStep(2,:) 0 0 0 0
%     %          -t12/bStep(1,:) l(2)+(t21+t23+t27)/bStep(2,:) -
t32/bStep(3,:) 0 0 0
%     %          0 -t23/bStep(2,:) l(3)+(t32+t34+t37)/bStep(3,:) -
t43/bStep(4,:) 0 0
%     %          0 0 -t34/bStep(3,:) l(4)+(t43+t45+t48)/bStep(4,:) -
t54/bStep(5,:) 0
%     %          0 0 0 -t45/bStep(4,:) l(5)+(t54+t56+t58)/bStep(5,:) -
t65/bStep(6,:)
%     %          0 0 0 0 -t56/bStep(5,:) l(6)+(t65+t68)/bStep(6,:)];
%     %
%     % result = omega*sum(bStep(1:6,:),2);
%     % stratTrans =
[sum(t71);sum(t72);sum(t73);sum(t84);sum(t85);sum(t86)];
%     % % This compares the source and sink
%     % sum(source(1:6,:),2)-(result-stratTrans);
%
%     % This omega solves for emissions from boxes 3 & 4 as well as
finding
%     % the budget from boxes 2, 3, 4, and 5.  It uses the observed
budget
%     % from the ice cores for the budget in boxes 1 & 6.
    l = sum(sink,2)./sum(bStep,2);
    omega = [l(1)+(t12+t17)/bStep(1,:) -1 0 0 0 0
        -t12/bStep(1,:) 0 -1 0 0 0
        0 0 0 0 0 0
        0 0 0 0 0 0
        0 0 0 -1 0 -t65/bStep(6,:)
        0 0 0 0 -1 l(6)+(t65+t68)/bStep(6,:)];
```

```
    bObs = interp1q(c.burden(:,1),c.burden(:,2:3),t)';
    %bObs = [sum(bStep(1,:)); sum(bStep(6,:))];
    result = omega*[bObs(1)
        (source(1,1)+source(1,2)+source(1,3))
        (source(2,1)+source(2,2)+source(2,3))
        (source(5,1)+source(5,2)+source(5,3))
        (source(6,1)+source(6,2)+source(6,3))
        bObs(2)];

    b2p = result(1);
    b3p = result(2);
    s3p = result(3);
    s4p = result(4);
    b4p = result(5);
    b5p = result(6);

    b2 = (b2p-sum(t71))/(t21/bStep(2,:));
    b5 = (b5p-sum(t86))/(t56/bStep(5,:));
    b3 = (b3p-
sum(t72)+b2*(l(2)+(t21+t23+t27)/bStep(2,:)))/(t32/bStep(3,:));
    b4 = (b4p-
sum(t85)+b5*(l(5)+(t54+t56+t58)/bStep(5,:)))/(t45/bStep(4,:));

    s3 = s3p-sum(t73)-
b2*t23/bStep(2,:)+b3*(l(3)+(t32+t34+t37)/bStep(3,:))-b4*t43/bStep(4,:);
    s4 = s4p-sum(t84)-
b3*t34/bStep(3,:)+b4*(l(4)+(t43+t45+t48)/bStep(4,:))-b5*t54/bStep(5,:);

    u(3,3) = s3;
    u(4,4) = s4;


%     % This is the method using rref.  It is slower, but it works
fine.
%     %a = (0.34/(0.34+0.323));
%     %b = (0.22/(0.22+0.07));
%     bObs = interp1q(c.burden(:,1),c.burden(:,2:3),t)';
%
%
%     omega = [t21/bStep(2,:) 0 0 0 0 0
%         -(sink(2,:)+t21+t23+t27)/bStep(2,:) t32/bStep(3,:) 0 0 0 0
%         t23/bStep(2,:) -(sink(3,:)+t32+t34+t37)/bStep(3,:)
t43/bStep(4,:) 0 1 0
%         0 t34/bStep(3,:) -(sink(4,:)+t43+t45+t48)/bStep(4,:)
t54/bStep(5,:) 0 1
%         0 0 t45/bStep(4,:) -(sink(5,:)+t54+t56+t58)/bStep(5,:) 0 0
%         0 0 0 t56/bStep(5,:) 0 0];
%
%     v = [-sum(source(1,:))+bObs(1)*(sink(1,:)+t12+t17)/bStep(1,:)-
sum(t71)
%         -sum(source(2,:))-bObs(1)*t12/bStep(1,:)-sum(t72)
```

```
%         -sum(t73)
%         -sum(t84)
%         -sum(source(5,:))-bObs(2)*t65/bStep(6,:)-sum(t85)
%         -sum(source(6,:))+bObs(2)*(sink(6,:)+t65+t68)/bStep(6,:)-
sum(t86)];
%
%     result = rref([omega v]);
%
%    % This sets the sources in box 3-4 accordingly.
%    u(3,3) = result(5,end);
%    u(4,4) = result(6,end);

    %u(u<0) = 0; % If any source is below 0, set it to 0.

    stepSource = reshape(u',1,c.numSources*6);

    q12=u.*c.r12;
    q13=u.*c.r13;
    qD=u.*c.rD;
    md=[sum(q12,2) sum(q13,2) sum(qD,2)];

    % This is the source strength in this time step.
    source = [md;0 0 0;0 0 0];%reshape(m,3,6); % 6 boxes, each with
12C, 13C, D source

elseif strcmp(c.RealLatSolver,'3-5')
    l = sum(sink,2)./sum(bStep,2);
    omega = [l(1)+(t12+t17)/bStep(1,:) -1 0 0 0 0
        -t12/bStep(1,:) 0 -1 0 0 0
        0 0 0 0 0 0
        0 0 0 -1 0 0
        0 0 0 0 0 -t65/bStep(6,:)
        0 0 0 0 -1 l(6)+(t65+t68)/bStep(6,:)];
    bObs = interp1q(c.burden(:,1),c.burden(:,2:3),t)';
    %bObs = [sum(bStep(1,:)); sum(bStep(6,:))];
    result = omega*[bObs(1)
        (source(1,1)+source(1,2)+source(1,3))
        (source(2,1)+source(2,2)+source(2,3))
        (source(4,1)+source(4,2)+source(4,3))
        (source(6,1)+source(6,2)+source(6,3))
        bObs(2)];

    b2p = result(1);
    b3p = result(2);
    s3p = result(3);
    b4p = result(4);
    s5p = result(5);
    b5p = result(6);

    b2 = (b2p-sum(t71))/(t21/bStep(2,:));
    b5 = (b5p-sum(t86))/(t56/bStep(5,:));
```

```
    b3 = (b3p-
sum(t72)+b2*(l(2)+(t21+t23+t27)/bStep(2,:)))/(t32/bStep(3,:));
    b4 = (b4p-sum(t84)-b3*(t34/bStep(3,:))-b5*(t54/bStep(5,:)))/-
(l(4)+(t43+t45+t48)/bStep(4,:));
    %b4 = (b4p-
sum(t85)+b5*(l(5)+(t54+t56+t58)/bStep(5,:)))/(t45/bStep(4,:));

    s3 = s3p-sum(t73)-
b2*t23/bStep(2,:)+b3*(l(3)+(t32+t34+t37)/bStep(3,:))-b4*t43/bStep(4,:);
    s5 = s5p-sum(t85)-
b4*t45/bStep(4,:)+b5*(l(5)+(t54+t56+t58)/bStep(5,:));

    % This sets the sources in box 3 & 5 accordingly.
    u(3,3) = s3;
    u(5,5) = s5;

    %u(u<0) = 0; % If any source is below 0, set it to 0.

    stepSource = reshape(u',1,c.numSources*6);

    q12=u.*c.r12;
    q13=u.*c.r13;
    qD=u.*c.rD;
    md=[sum(q12,2) sum(q13,2) sum(qD,2)];

    % This is the source strength in this time step.
    source = [md;0 0 0;0 0 0];%reshape(m,3,6); % 6 boxes, each with
12C, 13C, D source

elseif strcmp(c.RealLatSolver,'34-5')
    omega = [(sink(1,:)+t12+t17)/bStep(1,:) -1 0 0 0 0
        -t12/bStep(1,:) 0 -1 0 0 0
        0 0 0 0 0 0
        0 0 0 0 0 0
        0 0 0 0 0 -t65/bStep(6,:)
        0 0 0 0 -1 (sink(6,:)+t65+t68)/bStep(6,:)];
    bObs = interp1q(c.burden(:,1),c.burden(:,2:3),t)';
    result = omega*[bObs(1)
        (source(1,1)+source(1,2)+source(1,3))
        (source(2,1)+source(2,2)+source(2,3))
        0
        (source(6,1)+source(6,2)+source(6,3))
        bObs(2)];

    b2p = result(1);
    b3p = result(2);
    st1p = result(3);
    st2p = result(4);
    s5p = result(5);
    b5p = result(6);
```

```
    x = (.34/(0.34+0.323));

    b2 = (b2p-sum(t71))/(t21/bStep(2,:));
    b5 = (b5p-sum(t86))/(t56/bStep(5,:));
    b3 = (b3p+b2*(sink(2,:)+t21+t23+t27)/bStep(2,:)-
sum(t72))/(t32/bStep(3,:));
    b4 = ((1-x)*x)*...
        (((st1p-
b2*t23/bStep(2,:)+b3*(sink(3,:)+t32+t34+t37)/bStep(3,:)-sum(t73))/x)-
...
        ((st2p-b3*t34/bStep(3,:)-b5*t54/bStep(5,:)-sum(t84))/(1-
x)))/...
        (x*(sink(4,:)+t43+t45+t48)/bStep(4,:)+(1-x)*t43/bStep(4,:));
    st = (st1p-b2*t23/bStep(2,:)+b3*(sink(3,:)+t32+t34+t37)/bStep(3,:)-
b4*t43/bStep(4,:)-sum(t73))/x;
    s3 = st*x;
    s4 = st*(1-x);
    s5 = s5p-b4*t45/bStep(4,:)+b5*(sink(5,:)+t54+t56+t58)/bStep(5,:)-
sum(t85);
    % This sets the sources in box 34-5 accordingly.
    u(3,3) = s3;
    u(4,4) = s4;
    u(5,5) = s5;


%     % Jimmy's method.
%     x = (.34/(0.34+0.323));
%     bObs = interp1q(c.burden(:,1),c.burden(:,2:3),t)';
%     b2 = (bObs(1)*(sink(1,:)+t12+t17)/bStep(1,:)-sum(source(1,:))-
sum(t71))/(t21/bStep(2,:));
%     b5 = (bObs(2)*(sink(6,:)+t65+t68)/bStep(6,:)-sum(source(6,:))-
sum(t86))/(t56/bStep(5,:));
%     b3 = (b2*(sink(2,:)+t21+t23+t27)/bStep(2,:)-sum(source(2,:))-
bObs(1)*t12/bStep(1,:)-sum(t72))/(t32/bStep(3,:));
%     s3 = (b3*(sink(3,:)+t32+t34+t37)/bStep(3,:)-b2*t23/bStep(2,:)-
sum(t73)-...
%         ((t43/bStep(4,:))*(-b3*t34/bStep(3,:)-b5*t54/bStep(5,:)-
sum(t84)))/...
%         ((-sink(4,:)-t43-t45-t48)/bStep(4,:)))/...
%         (1+(-t43/bStep(4,:)*(1-x))/(x*(-sink(4,:)-t43-t45-
t48)/bStep(4,:)));
%     s4 = (1-x)*s3/x;
%     b4 = (-s4-b3*t34/bStep(3,:)-b5*t54/bStep(5,:)-sum(t84))/((-
sink(4,:)-t43-t45-t48)/bStep(4,:));
%     s5 = b5*(sink(5,:)+t54+t56+t58)/bStep(5,:)-b4*t45/bStep(4,:)-
bObs(2)*t65/bStep(6,:)-sum(t85);
%
%     % This sets the sources in box 34-5 accordingly.
%     u(3,3) = s3;
%     u(4,4) = s4;
```

```
%     u(5,5) = s5;

%     % This is the method using rref.  It is slower, but it works
fine.
%     a = (0.34/(0.34+0.323));
%     %b = (0.22/(0.22+0.07));
%     bObs = interp1q(c.burden(:,1),c.burden(:,2:3),t)';
%
%
%     omega = [t21/bStep(2,:) 0 0 0 0 0 0
%         -(sink(2,:)+t21+t23+t27)/bStep(2,:) t32/bStep(3,:) 0 0 0 0 0
%         t23/bStep(2,:) -(sink(3,:)+t32+t34+t37)/bStep(3,:)
t43/bStep(4,:) 0 1 0 0
%         0 t34/bStep(3,:) -(sink(4,:)+t43+t45+t48)/bStep(4,:)
t54/bStep(5,:) 0 1 0
%         0 0 t45/bStep(4,:) -(sink(5,:)+t54+t56+t58)/bStep(5,:) 0 0 1
%         0 0 0 t56/bStep(5,:) 0 0 0
%         0 0 0 0 1-a -a 0];
%
%     v = [-sum(source(1,:))+bObs(1)*(sink(1,:)+t12+t17)/bStep(1,:)-
sum(t71)
%         -sum(source(2,:))-bObs(1)*t12/bStep(1,:)-sum(t72)
%         -sum(t73)
%         -sum(t84)
%         -bObs(2)*t65/bStep(6,:)-sum(t85)
%         -sum(source(6,:))+bObs(2)*(sink(6,:)+t65+t68)/bStep(6,:)-
sum(t86)
%         0];
%
%     result = rref([omega v]);
%
%     % This sets the sources in box 34-5 accordingly.
%     u(3,3) = result(5,end);
%     u(4,4) = result(6,end);
%     u(5,5) = result(7,end);

    %u(u<0) = 0; % If any source is below 0, set it to 0.

    stepSource = reshape(u',1,c.numSources*6);

    q12=u.*c.r12;
    q13=u.*c.r13;
    qD=u.*c.rD;
    md=[sum(q12,2) sum(q13,2) sum(qD,2)];

    % This is the source strength in this time step.
    source = [md;0 0 0;0 0 0];%reshape(m,3,6); % 6 boxes, each with
12C, 13C, D source

elseif strcmp(c.RealLatSolver,'34-6')
    % This is the method using rref.  It is slower, but it works fine.
```

```
    a = (0.34/(0.34+0.323));
    %b = (0.22/(0.22+0.07));
    bObs = interp1q(c.burden(:,1),c.burden(:,2:3),t)';


    omega = [t21/bStep(2,:) 0 0 0 0 0 0
        -(sink(2,:)+t21+t23+t27)/bStep(2,:) t32/bStep(3,:) 0 0 0 0 0
        t23/bStep(2,:) -(sink(3,:)+t32+t34+t37)/bStep(3,:)
t43/bStep(4,:) 0 1 0 0
        0 t34/bStep(3,:) -(sink(4,:)+t43+t45+t48)/bStep(4,:)
t54/bStep(5,:) 0 1 0
        0 0 t45/bStep(4,:) -(sink(5,:)+t54+t56+t58)/bStep(5,:) 0 0 0
        0 0 0 t56/bStep(5,:) 0 0 1
        0 0 0 0 1-a -a 0];

    v = [-sum(source(1,:))+bObs(1)*(sink(1,:)+t12+t17)/bStep(1,:)-
sum(t71)
        -sum(source(2,:))-bObs(1)*t12/bStep(1,:)-sum(t72)
        -sum(t73)
        -sum(t84)
        -sum(source(5,:))-bObs(2)*t65/bStep(6,:)-sum(t85)
        bObs(2)*(sink(6,:)+t65+t68)/bStep(6,:)-sum(t86)
        0];

    result = rref([omega v]);

    % This sets the sources in box 34-5 accordingly.
    u(3,3) = result(5,end);
    u(4,4) = result(6,end);
    u(6,6) = result(7,end);

    %u(u<0) = 0; % If any source is below 0, set it to 0.

    stepSource = reshape(u',1,c.numSources*6);

    q12=u.*c.r12;
    q13=u.*c.r13;
    qD=u.*c.rD;
    md=[sum(q12,2) sum(q13,2) sum(qD,2)];

    % This is the source strength in this time step.
    source = [md;0 0 0;0 0 0];%reshape(m,3,6); % 6 boxes, each with
12C, 13C, D source

elseif strcmp(c.RealLatSolver,'34-56')
    a = (0.34/(0.34+0.323));
    b = (0.22/(0.22+0.07));
    bObs = interp1q(c.burden(:,1),c.burden(:,2:3),t)';
```

```
    omega = [t21/bStep(2,:) 0 0 0 0 0 0 0
        -(sink(2,:)+t21+t23+t27)/bStep(2,:) t32/bStep(3,:) 0 0 0 0 0 0
        t23/bStep(2,:) -(sink(3,:)+t32+t34+t37)/bStep(3,:)
t43/bStep(4,:) 0 1 0 0 0
        0 t34/bStep(3,:) -(sink(4,:)+t43+t45+t48)/bStep(4,:)
t54/bStep(5,:) 0 1 0 0
        0 0 t45/bStep(4,:) -(sink(5,:)+t54+t56+t58)/bStep(5,:) 0 0 1 0
        0 0 0 t56/bStep(5,:) 0 0 0 1
        0 0 0 0 1-a -a 0 0
        0 0 0 0 0 0 1-b -b];

    v = [-sum(source(1,:))+bObs(1)*(sink(1,:)+t12+t17)/bStep(1,:)-
sum(t71)
        -sum(source(2,:))-bObs(1)*t12/bStep(1,:)-sum(t72)
        -sum(t73)
        -sum(t84)
        -bObs(2)*t65/bStep(6,:)-sum(t85)
        bObs(2)*(sink(6,:)+t65+t68)/bStep(6,:)-sum(t86)
        0
        0];


    result = rref([omega v]);

%     This is the explicit way of solving:
%     b2 = (bObs(1)*(sink(1,:)+t12+t17)/bStep(1,:)-sum(source(1,:))-
sum(t71))/(t21/bStep(2,:));
%     b3 = (b2*(sink(2,:)+t21+t23+t27)/bStep(2,:)-sum(source(2,:))-
bObs(1)*t12/bStep(1,:)-sum(t72))/(t32/bStep(3,:));
%     b4 = ((((1-b)*(bObs(2)*(sink(6,:)+t65+t68)/bStep(6,:)-
sum(t86))+b*(bObs(2)*t65/bStep(6,:)+sum(t85)))/(b*(sink(5,:)+t54+t56+t5
8)/bStep(5,:)+(1-b)*t56/bStep(5,:)))+...
%         ((a*(b3*(sink(3,:)+t32+t34+t37)/bStep(3,:)-b2*t23/bStep(2,:)-
sum(t73)))/((1-a)*t54/bStep(5,:)))+...
%         ((b3*t34/bStep(3,:)+sum(t84))/(t54/bStep(5,:))))/...
%         ((a*t43/bStep(4,:))/((1-a)*t54/bStep(5,:))+...
%         ((sink(4,:)+t43+t45+t48)/bStep(4,:))/(t54/bStep(5,:))-...
%         (b*t45/bStep(4,:))/(b*(sink(5,:)+t54+t56+t58)/bStep(5,:)+(1-
b)*t56/bStep(5,:)))
%     % Still need to solve for b5, s3, s4, s5, s6.

    %[sum(bStep,2) [bObs(1); b2; b3; b4; b5; bObs(2); 0;0]
sum(source,2)]

    % This sets the sources in box 34-5 accordingly.
    u(3,3) = result(5,end);
    u(4,4) = result(6,end);
    u(5,5) = result(7,end);
    u(6,6) = result(8,end);

    %u(u<0) = 0; % If any source is below 0, set it to 0.
```

```
    stepSource = reshape(u',1,c.numSources*6);

    q12=u.*c.r12;
    q13=u.*c.r13;
    qD=u.*c.rD;
    md=[sum(q12,2) sum(q13,2) sum(qD,2)];

    % This is the source strength in this time step.
    source = [md;0 0 0;0 0 0];%reshape(m,3,6); % 6 boxes, each with
12C, 13C, D source
end



%% Calculate dbdt (change in burden with time)

% For each integration step:
% Calc source (6 troposphere boxes)
% Calc sinks
% Calc transport in and out for each box
% Calc dbdt for all of the boxes.

source = reshape(source,24,1);
sink = reshape(sink,24,1);
trans = reshape(trans,24,1);

dbdt = source+trans-sink;

% Displays the current year the model is working on while it is running
so
% the user has an indication of how far along the model is in its
progress.
if floor(t)>stepYear
    fprintf(c.yearString,t) %#ok<PRTCAL>
    stepYear = stepYear+1;
end


end
```

File: saveData.m

```
function [ status ] = saveData(t,~,~)
%SAVEDATA Summary of this function goes here
%   This saves the data from boscageFun at the end of every time step.
%   Couple of things to note:
%   1.) This only saves data at the end of every time step.  ode45 also
has
%   a "refine" function which records data at intermediate time steps.
%   That is why when data is saved here I take the last value in the t
%   [t(end)] vector. This is a good deal because the refine function
lets
%   you get much more detailed integrated results with little extra
computing
%   cost...unfortunately the data saved here then has a lower
resolution.
%   If you want to plot things together, make a mask like has been
done.
%   2.) This IS more efficient than saving data from within the ode45
%   function because if ode45 makes a bad prediction (too large of a
time
%   step, etc) then it goes back, and tries again. If you are saving
data
%   within the ode45 function it records all these bad data points.  By
%   saving the data here, only the sucessful time steps are recorded.


global inputIndex inputSource inputSink stepSource stepSink

if size(t,1)>=1
%    inputPopLatRatio(inputIndex,:) = [t(end), stepPopLatRatio'];
%    inputRiceLatRatio(inputIndex,:) = [t(end), stepRiceLatRatio'];
    inputSource(inputIndex,:) = [t(end), stepSource];
    inputSink(inputIndex,:) = [t(end), stepSink];
    inputIndex = inputIndex+1;
end
status = 0;

end
```

File: ebammFigures.m

```
%% Code for determining the linear regression lines and text output.

p.linearSegments = 'y';
if p.linearSegments == 'y'

    p.year_Seg = [-800; 1400];
    p.IPD_Seg = dsearchn(IPD(:,1),p.year_Seg)';
    [p1 S1] =
polyfit(IPD(p.IPD_Seg(1):10:p.IPD_Seg(end),1),IPD(p.IPD_Seg(1):10:p.IPD
_Seg(end),2),1);
    [y1 delta] =
polyconf(p1,IPD(p.IPD_Seg(1):10:p.IPD_Seg(end),1),S1,'predopt','curve',
'simopt','on');
%     figure(80);clf;
%     hold on
%     plot(IPD(:,1),IPD(:,2))
%
plot(IPD(p.IPD_Seg(1):10:p.IPD_Seg(end),1),IPD(p.IPD_Seg(1):10:p.IPD_Se
g(end),2),'r.-')
%     plot(IPD(p.IPD_Seg(1):10:p.IPD_Seg(end),1),y1,'b-',...
%         IPD(p.IPD_Seg(1):10:p.IPD_Seg(end),1),y1+delta,'b--',...
%         IPD(p.IPD_Seg(1):10:p.IPD_Seg(end),1),y1-delta,'b--')
%     hold off


%     [p1 S1] =
polyfit(IPD(p.IPD_Seg(1):1:p.IPD_Seg(end),1),IPD(p.IPD_Seg(1):1:p.IPD_S
eg(end),2),1);
%     [y1 delta] =
polyconf(p1,IPD(p.IPD_Seg(1):1:p.IPD_Seg(end),1),S1,'predopt','curve','
simopt','on');
%     figure(81);clf;
%     hold on
%     plot(IPD(:,1),IPD(:,2))
%
plot(IPD(p.IPD_Seg(1):1:p.IPD_Seg(end),1),IPD(p.IPD_Seg(1):1:p.IPD_Seg(
end),2),'r.-')
%     plot(IPD(p.IPD_Seg(1):1:p.IPD_Seg(end),1),y1,'b-',...
%         IPD(p.IPD_Seg(1):1:p.IPD_Seg(end),1),y1+delta,'b--',...
%         IPD(p.IPD_Seg(1):1:p.IPD_Seg(end),1),y1-delta,'b--')
%     hold off
```

```
    %[b,bint,r,rint,stats] =
regress(IPD(1:10:end,2),[ones(size(IPD(1:10:end,1)))
polyval(p1,IPD(1:10:end,1))]);

    % This is using the annually interpolated data which I think is not
the
    % statistically correct way to do this because it implies that our
record
    % is a lot higher resolution than it actually is.
    %[b,bint,r,rint,stats] =
regress(IPD(1:end,2),[ones(size(IPD(1:end,1))) IPD(1:end,1)]);
    %fprintf('The IPD slope from %4.0f to %4.0f is %4.1f +/- %3.1f
(95%% confidence)\n',...
    %    IPD(1,1),IPD(end,1),b(2)*1000,1000*(bint(2,2)-bint(2,1))/2)

    % This is the correct way to do this, to subsample the records by
~10
    % years.  It is not correct to use the actual data points because
they
    % are not evenly weighted in time.  Using the subsampled data gives
    % each data point an equal time weight which is the correct way to
do
    % this.
    [p.ipdWholeLn,p.ipdWholeCI,~,~,~] =
regress(IPD(p.IPD_Seg(1):10:p.IPD_Seg(end),2),...
        [ones(size(IPD(p.IPD_Seg(1):10:p.IPD_Seg(end),1)))
IPD(p.IPD_Seg(1):10:p.IPD_Seg(end),1)]); % Whole record.
    fprintf('The IPD slope from %4.0f to %4.0f is %4.1f +/- %3.1f
ppb/ka (95%% confidence)\n',...

IPD(p.IPD_Seg(1),1),IPD(p.IPD_Seg(end),1),p.ipdWholeLn(2)*1000,1000*(p.
ipdWholeCI(2,2)-p.ipdWholeCI(2,1))/2)

    [p.ripdWholeLn,p.ripdWholeCI,~,~,~] =
regress(100*IPD(p.IPD_Seg(1):10:p.IPD_Seg(end),2)./((ts.gispInterp(p.IP
D_Seg(1):10:p.IPD_Seg(end),2)+...

ts.wdcInterp(p.IPD_Seg(1):10:p.IPD_Seg(end),2))/2),[ones(size(IPD(p.IPD
_Seg(1):10:p.IPD_Seg(end),1))) IPD(p.IPD_Seg(1):10:p.IPD_Seg(end),1)]);
% Whole record.
    fprintf('The rIPD slope from %4.0f to %4.0f is %4.1f +/- %3.1f
%%/ka (95%% confidence)\n',...

IPD(p.IPD_Seg(1),1),IPD(p.IPD_Seg(end),1),p.ripdWholeLn(2)*1000,1000*(p
.ripdWholeCI(2,2)-p.ripdWholeCI(2,1))/2)

    [p.wdcWholeLn,p.wdcWholeCI,~,~,~] =
regress(ts.wdcInterp(p.IPD_Seg(1):10:p.IPD_Seg(end),2),...
        [ones(size(IPD(p.IPD_Seg(1):10:p.IPD_Seg(end),1)))
ts.wdcInterp(p.IPD_Seg(1):10:p.IPD_Seg(end),1)]); % Whole record.
```

```
    [p.gispWholeLn,p.gispWholeCI,~,~,~] =
regress(ts.gispInterp(p.IPD_Seg(1):10:p.IPD_Seg(end),2),...
        [ones(size(IPD(p.IPD_Seg(1):10:p.IPD_Seg(end),1)))
ts.gispInterp(p.IPD_Seg(1):10:p.IPD_Seg(end),1)]); % Whole record.
    p.ipdWhole = p.ipdWholeLn(2)*p.year_Seg([1 2])+p.ipdWholeLn(1);
    p.wdcWhole = p.wdcWholeLn(2)*p.year_Seg([1 2])+p.wdcWholeLn(1);
    p.gispWhole = p.gispWholeLn(2)*p.year_Seg([1 2])+p.gispWholeLn(1);



    if size(p.year_Seg,1) == 4
        [p.ipdSeg1Ln,p.ipdSeg1CI,~,~,~] =
regress(IPD(p.IPD_Seg(1):10:p.IPD_Seg(2),2),...
            [ones(size(IPD(p.IPD_Seg(1):10:p.IPD_Seg(2),1)))
IPD(p.IPD_Seg(1):10:p.IPD_Seg(2),1)]); % -790 to 970 CE.
        fprintf('The IPD slope from %4.0f to %4.0f is %4.1f +/- %3.1f
ppb/ka (95%% confidence)\n',...

IPD(p.IPD_Seg(1),1),IPD(p.IPD_Seg(2),1),p.ipdSeg1Ln(2)*1000,1000*(p.ipd
Seg1CI(2,2)-p.ipdSeg1CI(2,1))/2)

        [p.ipdSeg2Ln,p.ipdSeg2CI,~,~,~] =
regress(IPD(p.IPD_Seg(3):10:p.IPD_Seg(4),2),...
            [ones(size(IPD(p.IPD_Seg(3):10:p.IPD_Seg(4),1)))
IPD(p.IPD_Seg(3):10:p.IPD_Seg(4),1)]); % -790 to 970 CE.
        fprintf('The IPD slope from %4.0f to %4.0f is %4.1f +/- %3.1f
ppb/ka (95%% confidence)\n',...

IPD(p.IPD_Seg(3),1),IPD(p.IPD_Seg(4),1),p.ipdSeg2Ln(2)*1000,1000*(p.ipd
Seg2CI(2,2)-p.ipdSeg2CI(2,1))/2)

        [p.wdcSeg1Ln,p.wdcSeg1CI,~,~,~] =
regress(ts.wdcInterp(p.IPD_Seg(1):10:p.IPD_Seg(2),2),...
            [ones(size(IPD(p.IPD_Seg(1):10:p.IPD_Seg(2),1)))
ts.wdcInterp(p.IPD_Seg(1):10:p.IPD_Seg(2),1)]); % Whole record.
        [p.wdcSeg2Ln,p.wdcSeg2CI,~,~,~] =
regress(ts.wdcInterp(p.IPD_Seg(3):10:p.IPD_Seg(4),2),...
            [ones(size(IPD(p.IPD_Seg(3):10:p.IPD_Seg(4),1)))
ts.wdcInterp(p.IPD_Seg(3):10:p.IPD_Seg(4),1)]); % Whole record.

        [p.gispSeg1Ln,p.gispSeg1CI,~,~,~] =
regress(ts.gispInterp(p.IPD_Seg(1):10:p.IPD_Seg(2),2),...
            [ones(size(IPD(p.IPD_Seg(1):10:p.IPD_Seg(2),1)))
ts.gispInterp(p.IPD_Seg(1):10:p.IPD_Seg(2),1)]); % Whole record.
        [p.gispSeg2Ln,p.gispSeg2CI,~,~,~] =
regress(ts.gispInterp(p.IPD_Seg(3):10:p.IPD_Seg(4),2),...
            [ones(size(IPD(p.IPD_Seg(3):10:p.IPD_Seg(4),1)))
ts.gispInterp(p.IPD_Seg(3):10:p.IPD_Seg(4),1)]); % Whole record.

        p.ipdSeg1 = p.ipdSeg1Ln(2)*p.year_Seg([1 2])+p.ipdSeg1Ln(1);
        p.ipdSeg2 = p.ipdSeg2Ln(2)*p.year_Seg([3 4])+p.ipdSeg2Ln(1);
```

```
        p.wdcSeg1 = p.wdcSeg1Ln(2)*p.year_Seg([1 2])+p.wdcSeg1Ln(1);
        p.wdcSeg2 = p.wdcSeg2Ln(2)*p.year_Seg([3 4])+p.wdcSeg2Ln(1);

        p.gispSeg1 = p.gispSeg1Ln(2)*p.year_Seg([1 2])+p.gispSeg1Ln(1);
        p.gispSeg2 = p.gispSeg2Ln(2)*p.year_Seg([3 4])+p.gispSeg2Ln(1);

    end
    %b(2)% is the slope
    %bint(2,:) % is the 95% confidence interval

    %xlswrite(['IPD slope analysis/IPD.csv'],IPD(1:10:end,:))
end




%% EBAMM Figure plotting

plt.fig1 = 'y';
if plt.fig1 == 'y'
    figure(1);clf;%figure(fc);fc=fc+1;
    title(['Scenario: ',scenario])
    hold on
    ax1 = gca;
    grid on
    set(ax1,'Position',get(ax1,'Position')+[0 0 0 -0.35]);
    plot(ts.ch4Atm(:,1),ts.ch4Atm(:,2),'-','Color',[.5 .5 .5]);
    plot(ts.gisp(:,1),ts.gisp(:,2),'.-','Color',[0 1 0],'LineWidth',1);
    %plot(ts.gispLow(:,1),ts.gispLow(:,2),'.-','Color',[0 .5
0],'LineWidth',1);
    %plot(ts.gispLowSpline(:,1),ts.gispLowSpline(:,2),'-','Color',[0 .4
0],'LineWidth',2);
    %plot(ch4WDC05A(:,1),ch4WDC05A(:,2),'.-','Color',[0 0 .9]);
    %plot(ch4WDC06A(:,1),ch4WDC06A(:,2),'.-','Color',[.5 0 .5]);
    plot(ts.wdc(:,1),ts.wdc(:,2),'.-','Color',[.5 0 .5],'LineWidth',1);
    plot(IPD(:,1),ts.gispLowpass,'-','Color',[.3 .8 .3],'LineWidth',2)
    plot(IPD(:,1),ts.wdcLowpass,'Color',[.6 .3 .6],'LineWidth',2)
    %plot(ts.wdcLowSpline(:,1),ts.wdcLowSpline(:,2),'-','Color',[.5 .2
.5],'LineWidth',2);
    % for i = 1:length(WDCdepthAge) % Plots the chron tie points.
    %     tempGISP =
interp1(ts.gisp(:,1),ts.gisp(:,2),WDCdepthAge(i,2));
    %     tempWDC = interp1(ts.wdc(:,1),ts.wdc(:,2),WDCdepthAge(i,2));
    %     plot([WDCdepthAge(i,2) WDCdepthAge(i,2)],[tempWDC
tempGISP],'k.-');
    % end
    if p.linearSegments == 'y'
        if size(p.year_Seg,1) == 2
```

```
            plot(p.year_Seg(1:2),p.wdcWhole,'-','Color',[.3 0
.3],'LineWidth',3)
            plot(p.year_Seg(1:2),p.gispWhole,'-','Color',[0 .5
0],'LineWidth',3)
        end
        if size(p.year_Seg,1) == 4
            plot(p.year_Seg(1:2),p.wdcSeg1,'-','Color',[.3 0
.3],'LineWidth',3)
            plot(p.year_Seg(1:2),p.gispSeg1,'-','Color',[0 .5
0],'LineWidth',3)
            plot(p.year_Seg(3:4),p.wdcSeg2,'-','Color',[.3 0
.3],'LineWidth',3)
            plot(p.year_Seg(3:4),p.gispSeg2,'-','Color',[0 .5
0],'LineWidth',3)
        end
    end
    plot(tt.Year,tt.BoxCH4Filter(:,1),'-','Color',[.5 1
1],'LineWidth',3)
    plot(tt.Year,tt.BoxCH4Filter(:,6),'-','Color',[1 .6
.6],'LineWidth',3); % Ice core CH4
    plot(tt.Mean(:,1),tt.BoxCH4concMean(:,1),'-','Color',[0 0 .8])
    plot(tt.Mean(:,1),tt.BoxCH4concMean(:,6),'-','Color',[.6 0 0]); %
Mean annual CH4
    %plot(tt.Year,tt.BoxCH4conc(:,1),'k-',...
    %    tt.Year,tt.BoxCH4conc(:,6),'m-')
    xlabel('Year C.E.');ylabel('CH_4 (ppb)');
    %legend('Box 1','Box 6','Box 1 Ice','Box 6
Ice','LD+ATM','GISP2D','WDC','Chron pts','Location','NorthWest')

    axis([yearStart+50 yearEnd 580 800])
    %ylim([590 710])
    hold off
    % Add 50 years here because the ice core smoothing filter causes
some funny
    % values at the beginning of the record.
    %xlim([yearStart+50 yearEnd])
    %axis([yearStart+50 yearEnd 580 800])
    ax1p = get(ax1,'Position');
    ax2 = axes('Position',[ax1p(1) ax1p(4)+0.1 ax1p(3) 0.35]
,...%get(ax1,'Position')+[0 0.5 0 -0.5],...
        'XAxisLocation','top',...
        'YAxisLocation','right');
    hold on
    %figure(11)
    %plot(IPDsmooth(:,1),IPDsmooth(:,2),'LineWidth',2)
    %plot(IPDsmooth(:,1),IPDsmooth(:,2)+IPDsmooth(:,3),'b-',...
    %    IPDsmooth(:,1),IPDsmooth(:,2)-IPDsmooth(:,3),'b-')
    %plot(IPD(:,1),ts.ipdLowpass,'b-','LineWidth',2)
    plot(IPD(:,1),IPD(:,2),'r-')

%plot(ts.wdc(:,1),interp1(IPD(:,1),IPD(:,2),ts.wdc(:,1)),'.','Color',[.
5 0 .5])
```

```
%plot(ts.gisp(:,1),interp1(IPD(:,1),IPD(:,2),ts.gisp(:,1)),'.','Color',
[0 1 0])
    plot(tt.Year,tt.BoxIPDFilter,'k-','LineWidth',3)
    plot(tt.Mean,tt.BoxCH4concMean(:,6)-tt.BoxCH4concMean(:,1),'g-')
    %plot(IPDLowSpline(:,1),IPDLowSpline(:,2),'g-','LineWidth',4)

    if p.linearSegments == 'y'
        hold on
        if size(p.year_Seg,1) == 2
            plot(p.year_Seg(1:2),p.ipdWhole,'-','Color',[0 1
1],'LineWidth',3)
        end
        if size(p.year_Seg,1) == 4
            plot(p.year_Seg(1:2),p.ipdSeg1,'-','Color',[0 1
1],'LineWidth',3)
            plot(p.year_Seg(3:4),p.ipdSeg2,'-','Color',[0 1
1],'LineWidth',3)
        end
        hold off
    end
    axis([yearStart+50 yearEnd 30 60])
    %xlim([yearStart+50 yearEnd])
    grid on
    ylabel('IPD (Cn-Cs, ppb)')
    hold off
end

plt.fig11 = 'n';
if plt.fig11 == 'y'
    figure(11);clf;hold on
    % These are for plotting the IPD as a % instead of Cn-Cs

plot(IPD(:,1),100*IPD(:,2)./((ts.gispInterp(:,2)+ts.wdcInterp(:,2))/2),
'r-')

plot(IPD(:,1),100*ts.ipdLowpass./((ts.gispLowpass+ts.wdcLowpass)/2),'b-
','LineWidth',2)

plot(tt.Year,100*tt.BoxIPDFilter./((tt.BoxCH4Filter(:,1)+tt.BoxCH4Filte
r(:,6))./2),'k-','LineWidth',3)
    xlim([yearStart+50 yearEnd])
    xlabel('Year C.E.');ylabel('rIPD');
    %mean(100*IPD(:,2)./((ts.gispInterp+ts.wdcInterp)/2))
    %std(100*IPD(:,2)./((ts.gispInterp+ts.wdcInterp)/2))
    grid on
    hold off
end

plt.fig2 = 'n';
if plt.fig2 == 'y'
    figure(2);clf;%figure(fc);fc=fc+1;
```

```
    % plot(mT,boxdC13(:,1),'k-',...
    %     mT,boxdC13(:,2),'m-',...
    %     mT,boxdC13(:,3),'c-',...
    %     mT,boxdC13(:,4),'r-',...
    %     mT,boxdC13(:,5),'y-',...
    %     mT,boxdC13(:,6),'g-',...
    %     mT,boxdC13(:,7),'r-',...
    %     mT,boxdC13(:,8),'b-');
    %axis([1820 2000 -70 -30])
    hold on
    plot(ts.d13cLD(:,1),ts.d13cLD(:,2),'.-','Color',[.9 .5 .5]);
    %plot(ts.d13cWDC05A(:,1),ts.d13cWDC05A(:,2),'.-','Color',[0 0 .9]);

errorbar(ts.d13cWDC05A(:,1),ts.d13cWDC05A(:,2),(ones(length(ts.d13cWDC0
5A),1)*0.2),'.-','Color',[0.4 0.4 1]);

errorbar(ts.d13cGISP(:,1),ts.d13cGISP(:,2),(ones(length(ts.d13cGISP),1)
*0.3),'.-','Color',[.5 .9 .5]);

errorbar(ts.d13cNEEM(:,1),ts.d13cNEEM(:,2),(ones(length(ts.d13cNEEM),1)
*0.12),'k.-');
    plot(tt.Mean(:,1),tt.BoxdC13Mean(:,1),'c-',...
        tt.Mean(:,1),tt.BoxdC13Mean(:,6),'r-','LineWidth',1);
    plot(tt.Year,tt.BoxdC13Filter(:,1),'c.-',...
        tt.Year,tt.BoxdC13Filter(:,6),'r.-','LineWidth',2);
%    plot(tt.Mean,tt.BoxdC13FilterMean(:,1),'k.-',...
%        tt.Mean,tt.BoxdC13FilterMean(:,6),'g.-','LineWidth',2);
    legend('LD','WDC05A','GISP','NEEM','Box 1','Box 6','Box 1 Ice','Box
6 Ice','Location','SouthWest')
    grid on
    hold off
    ylabel('\delta^{13}C')
    xlabel('Year C.E.')
    xlim([yearStart+50 yearEnd])
end

plt.fig3 = 'n';
offset = 0;%-8
if plt.fig3 == 'y'
    figure(3);clf;hold on; % dD plot
    ylabel('\deltaD')
    xlabel('Year C.E.')
    % plot(mT,boxdD(:,1),'k-',...
    %     mT,boxdD(:,2),'m-',...
    %     mT,boxdD(:,3),'c-',...
    %     mT,boxdD(:,4),'r-',...
    %     mT,boxdD(:,5),'y-',...
    %     mT,boxdD(:,6),'g-',...
    %     mT,boxdD(:,7),'r-',...
    %     mT,boxdD(:,8),'b-');
```

```
errorbar(ts.dDWDC05A(:,1),ts.dDWDC05A(:,2),ones(length(ts.dDWDC05A(:,1)
),1)*3,'.-','Color',[0 0 0.9])

errorbar(ts.dDGISP(:,1),ts.dDGISP(:,2),ones(length(ts.dDGISP),1)*3,'.-
','Color',[.5 .9 .5])
    plot(tt.Mean(:,1),tt.BoxdDMean(:,1)+offset,'c-',...
        tt.Mean(:,1),tt.BoxdDMean(:,6)+offset,'r-','LineWidth',1);
    plot(tt.Year,tt.BoxdDFilter(:,1)+offset,'c-',...
        tt.Year,tt.BoxdDFilter(:,6)+offset,'r-','LineWidth',3);
    legend('WDC05A','GISP2','Box 1','Box 6','Box 1 Ice','Box 6
Ice','Location','SouthWest')
    grid on
    hold off
    xlim([yearStart+50 yearEnd])
end

plt.fig4 = 'n';
if plt.fig4 == 'y'
    figure(4);clf;
    plot(inputSink(:,1),inputSinkSum(:,1)*16.04,'k-',...
        inputSink(:,1),inputSinkSum(:,2)*16.04,'m-',...
        inputSink(:,1),inputSinkSum(:,3)*16.04,'c-',...
        inputSink(:,1),inputSinkSum(:,4)*16.04,'r-',...
        inputSink(:,1),inputSinkSum(:,5)*16.04,'y-',...
        inputSink(:,1),inputSinkSum(:,6)*16.04,'g-',...
        inputSink(:,1),inputSinkSum(:,7)*16.04,'r.-',...
        inputSink(:,1),inputSinkSum(:,8)*16.04,'b.-');
    xlim([yearStart yearEnd])
    title('Sink for the 8 boxes.')
    xlabel('Years C.E.')
    ylabel('Tg of CH_4 yr^{-1}')

legend('B1','B2','B3','B4','B5','B6','B7','B8','Location','NorthWest')
end

plt.fig41 = 'n';
if plt.fig41 == 'y'
    figure(41);clf;
    plot(tt.Mean,tt.SinkMean(:,1)*16.04,'k-',...
        tt.Mean,tt.SinkMean(:,2)*16.04,'m-',...
        tt.Mean,tt.SinkMean(:,3)*16.04,'c-',...
        tt.Mean,tt.SinkMean(:,4)*16.04,'r-',...
        tt.Mean,tt.SinkMean(:,5)*16.04,'y-',...
        tt.Mean,tt.SinkMean(:,6)*16.04,'g-',...
        tt.Mean,tt.SinkMean(:,7)*16.04,'r.-',...
        tt.Mean,tt.SinkMean(:,8)*16.04,'b.-');
    xlim([yearStart yearEnd])
    title('Annual mean sink for the 8 boxes.')
    xlabel('Years C.E.')
    ylabel('Tg of CH_4 yr^{-1}')
```

```
legend('B1','B2','B3','B4','B5','B6','B7','B8','Location','NorthWest')
end

plt.fig42 = 'n';
if plt.fig42 == 'y'
    figure(42)
    plot(tt.Mean,sum(tt.SinkMean,2)*16.04,'k-');
    xlim([yearStart yearEnd])
    title('Annual global sink.')
    xlabel('Years C.E.')
    ylabel('Tg of CH_4 yr^{-1}')
end

plt.fig5 = 'n';
if plt.fig5 == 'y'
    figure(5);clf;hold on;
    title('Source input from the individual sources.')
    for i = 1:c.numSources

plot(inputSource(:,1),inputSourceSum(:,i)*16.04,'Color',[i/c.numSources
1-i/c.numSources 1-i/c.numSources])
    end
    hold off
    legend(sourcePlotNames)
    xlim([yearStart+50 yearEnd])
    xlabel('Years C.E.')
    ylabel('Tg of CH_4 yr^{-1}')
end

plt.fig51 = 'n';
if plt.fig51 == 'y'
    figure(51);clf;hold on;
    title('Mean annual source input from the individual sources.')
    plt.lineOption = {'-','--'};
    plt.lineOptionIndex =
repmat(1:size(plt.lineOption,2),1,ceil(c.numSources/size(plt.lineOption
,2)));
    for i = 1:c.numSources

plot(tt.Mean,tt.SourceMean(:,i)*16.04,plt.lineOption{plt.lineOptionInde
x(i)},'Color',[i/c.numSources 1-i/c.numSources 1-
i/c.numSources],'LineWidth',3);
    end
    hold off
    grid on
    %legend(sourcePlotNames,'Location','NorthWest','FontSize',6)
    xlim([yearStart+50 yearEnd])
    xlabel('Years C.E.')
    ylabel('Tg of CH_4 yr^{-1}')
```

```
%     bb = strcmp(c.sourceNames,'BiomassBurning');
%     bbSource = [tt.Mean tt.SourceMean(:,bb)*16.04];
%     save('Scenario\BiomassBurningSource.txt','bbSource','-ascii')

end

plt.fig52 = 'n';
if plt.fig52 == 'y'
    figure(52)
    %tt.MidIndex = round(length(tt.SourceMean)/2);
    tt.MidIndex = 50; % beginning of model run
    %tt.MidIndex = length(tt.SourceMean)-1; % End of the model run
    title(['Latitudinal distribution of sources in year
',num2str(tt.Mean(tt.MidIndex))])

    bar(-
75:30:75,reshape(tt.InputSourceMean(tt.MidIndex,:)*16.04,c.numSources,6
)','stacked')
    legend(sourcePlotNames,'Location','NorthWest')
    %bar(-75:30:75,tt.SourceLatMean(tt.MidIndex,:)*16.04)
    %plot(-75:30:75,tt.SourceLatMean(tt.MidIndex,:),'*')
    ylabel('Tg of CH_4 yr^{-1}')
    xlabel('Latitude')

end

plt.fig53 = 'n';
if plt.fig53 == 'y'
    figure(53);clf;
    tt.MidIndex = length(tt.SourceMean)-1; % End of the model run
    %modernSource = tt.SourceLatMean(tt.MidIndex,:)*16.04;
    %save('ModelOutput/modernSource.mat','modernSource')
    load('ModelOutput/modernSource.mat')

    %PIHSource = tt.SourceLatMean(tt.MidIndex,:)*16.04;
    %save('ModelOutput/PIHSource.mat','PIHSource')
    %load('ModelOutput/PIHSource.mat')

    bar(-
75:30:75,([modernSource;tt.SourceLatMean(tt.MidIndex,:)*16.04])')
    legend('2009 Source Distribution',[num2str(tt.Mean(tt.MidIndex)),'
Source Distribution'],'Location','NorthWest')

end


plt.fig54 = 'n';
if plt.fig54 == 'y'
    figure(54);clf;
    plot(tt.Mean,tt.SourceLatMean*16.04)
```

```
    legend('Box1','Box 2','Box 3','Box 4','Box 5','Box 6')
    xlabel('Years C.E.')
    ylabel('Tg of CH_4 yr^{-1}')
    title('Latitudinal Distribution of Sources With Time')

    p.year = [-800; 1400];
    p.yearInd = dsearchn(tt.Mean,p.year)';
    [p.b3.p p.b3.s] =
polyfit(tt.Mean(p.yearInd(1):1:p.yearInd(end),1),tt.SourceLatMean(p.yea
rInd(1):1:p.yearInd(end),3)*16.04,1);
    [p.b4.p p.b4.s] =
polyfit(tt.Mean(p.yearInd(1):1:p.yearInd(end),1),tt.SourceLatMean(p.yea
rInd(1):1:p.yearInd(end),4)*16.04,1);
    [p.b5.p p.b5.s] =
polyfit(tt.Mean(p.yearInd(1):1:p.yearInd(end),1),tt.SourceLatMean(p.yea
rInd(1):1:p.yearInd(end),5)*16.04,1);
    [p.b6.p p.b6.s] =
polyfit(tt.Mean(p.yearInd(1):1:p.yearInd(end),1),tt.SourceLatMean(p.yea
rInd(1):1:p.yearInd(end),6)*16.04,1);
    [p.b3.y p.b3.delta] =
polyconf(p.b3.p,tt.Mean(p.yearInd(1):1:p.yearInd(end),1),p.b3.s,'predop
t','observation','simopt','off','alpha',0.32);
    [p.b4.y p.b4.delta] =
polyconf(p.b4.p,tt.Mean(p.yearInd(1):1:p.yearInd(end),1),p.b4.s,'predop
t','observation','simopt','off','alpha',0.32);
    [p.b5.y p.b5.delta] =
polyconf(p.b5.p,tt.Mean(p.yearInd(1):1:p.yearInd(end),1),p.b5.s,'predop
t','observation','simopt','off','alpha',0.32);
    [p.b6.y p.b6.delta] =
polyconf(p.b6.p,tt.Mean(p.yearInd(1):1:p.yearInd(end),1),p.b6.s,'predop
t','observation','simopt','off','alpha',0.32);

    hold on
    plot(tt.Mean(p.yearInd(1):1:p.yearInd(end),1),p.b3.y,'r-')
    plot(tt.Mean(p.yearInd(1):1:p.yearInd(end),1),p.b3.y+p.b3.delta,'r-
-')
    plot(tt.Mean(p.yearInd(1):1:p.yearInd(end),1),p.b3.y-p.b3.delta,'r-
-')
    plot(tt.Mean(p.yearInd(1):1:p.yearInd(end),1),p.b4.y,'g-')
    plot(tt.Mean(p.yearInd(1):1:p.yearInd(end),1),p.b4.y+p.b4.delta,'g-
-')
    plot(tt.Mean(p.yearInd(1):1:p.yearInd(end),1),p.b4.y-p.b4.delta,'g-
-')
    plot(tt.Mean(p.yearInd(1):1:p.yearInd(end),1),p.b5.y,'b-')
    plot(tt.Mean(p.yearInd(1):1:p.yearInd(end),1),p.b5.y+p.b5.delta,'b-
-')
    plot(tt.Mean(p.yearInd(1):1:p.yearInd(end),1),p.b5.y-p.b5.delta,'b-
-')
    plot(tt.Mean(p.yearInd(1):1:p.yearInd(end),1),p.b6.y,'c-')
    plot(tt.Mean(p.yearInd(1):1:p.yearInd(end),1),p.b6.y+p.b6.delta,'c-
-')
```

```
    plot(tt.Mean(p.yearInd(1):1:p.yearInd(end),1),p.b6.y-p.b6.delta,'c-
-')
    hold off

    fprintf('Box 6 change (%4.0f to %4.0f CE): %4.0f +/- %1.0f Tg
CH4/yr.\n',p.year(1),p.year(2),p.b6.y(end)-p.b6.y(1),2*p.b6.delta(1))
    fprintf('Box 5 change (%4.0f to %4.0f CE): %4.0f +/- %1.0f Tg
CH4/yr.\n',p.year(1),p.year(2),p.b5.y(end)-p.b5.y(1),2*p.b5.delta(1))
    fprintf('Box 4 change (%4.0f to %4.0f CE): %4.0f +/- %1.0f Tg
CH4/yr.\n',p.year(1),p.year(2),p.b4.y(end)-p.b4.y(1),2*p.b4.delta(1))
    fprintf('Box 3 change (%4.0f to %4.0f CE): %4.0f +/- %1.0f Tg
CH4/yr.\n',p.year(1),p.year(2),p.b3.y(end)-p.b3.y(1),2*p.b3.delta(1))

end

plt.fig55 = 'n';
if plt.fig55 == 'y'
    figure(55);clf;
    %tt.MidIndex = round(length(tt.SourceMean)/2); % Middle of the
model run
    %tt.MidIndex = length(tt.SourceMean)-1; % End of the model run
    tt.MidIndex = 50; % 50 years afte the start of the model run, after
it has reached equilibrium.

    plot(-75:30:75,tt.BoxCH4concMean(tt.MidIndex,1:6));
    %xlabel('Latitude')
    %ylabel('CH_4 (ppb)')

    %ylim([min(floor(tt.BoxCH4concMean(tt.MidIndex,1:6)/100)*100)
max(ceil(tt.BoxCH4concMean(tt.MidIndex,1:6)/100)*100)])
    %ylim([1700 2000])
    %plot(sin(-
75/90*pi/2:30/90*pi/2:75/90*pi/2),tt.BoxCH4concMean(tt.MidIndex,1:6),'.
-'); % Sin of Latitude
    %xlabel('Latitude')
    %xlabel('Sin of Latitude')

    title(['Latitudinal distribution of CH_4 in year
',num2str(tt.Mean(tt.MidIndex))])

    if strcmp(scenario,'N21')
        hold on
        load('Data/NOAA CCG/CH4_IPG_2009.1.mat');
        plot(ch4_ipg_20091(:,1),ch4_ipg_20091(:,2),'b*')
        fprintf('Modern measured IPD is %4.1f - %4.1f = %4.1f ppb
(%4.1f %%).  Modeled IPD is %4.1f\n',...
            nanmean(ch4_ipg_20091(end-7:end,2)),...
            nanmean(ch4_ipg_20091(1:4,2)),...
            nanmean(ch4_ipg_20091(end-7:end,2))-
nanmean(ch4_ipg_20091(1:4,2)),...
```

```
            (nanmean(ch4_ipg_20091(end-7:end,2))-
nanmean(ch4_ipg_20091(1:4,2)))/mean([nanmean(ch4_ipg_20091(end-
7:end,2));nanmean(ch4_ipg_20091(1:4,2))]),...
            tt.BoxCH4concMean(tt.MidIndex,6)-
tt.BoxCH4concMean(tt.MidIndex,1));
            % The data is averaged over all data pts greater than 60
            % degrees latitude.
        plot(ch4_ipg_20091([1:4,end-7:end],1),ch4_ipg_20091([1:4,end-
7:end],2),'r*')
        hold off
    end
end

plt.fig56 = 'n';
if plt.fig56 == 'y'
    figure(56);clf;
    %tt.MidIndex = round(length(tt.SourceMean)/2); % Middle of the
model run
    %tt.MidIndex = length(tt.SourceMean)-1; % End of the model run
    tt.MidIndex = 50; % 50 years afte the start of the model run, after
it has reached equilibrium.
    hold on
    plot(-75:30:75,tt.BoxCH4concMean(tt.MidIndex,1:6)-
tt.BoxCH4concMean(tt.MidIndex,1),'b.-'); % Compare this to Fig 8 in
[Kaplan et al., 2006]
    plot(-75:30:75,[0 1 10 20 30 34],'r.-'); % Compare this to Fig 8 in
[Kaplan et al., 2006]
    ylabel('CH_4-CH_4[min] (ppb)')
    xlabel('Latitude')
    legend(['EBAMM ' num2str(tt.Mean(tt.MidIndex)) ' C.E.'],'Kaplan et
al., 2006','Location','NorthWest')
    hold off
end


plt.fig57 = 'n'; % Total Annual Mean CH4 Source Emissions.
if plt.fig57 == 'y'
    figure(57);clf;
    plot(tt.Mean,sum(tt.SourceMean,2)*16.04,'k.-')
    title('Total Annual Mean CH_4 Source Emissions')
    xlim([yearStart+50 yearEnd])
    xlabel('Years C.E.')
    ylabel('Tg of CH_4 yr^{-1}')

    p.year = [-800; 1400];
    p.yearInd = dsearchn(tt.Mean,p.year)';
    [p.bMean.p p.bMean.s] =
polyfit(tt.Mean(p.yearInd(1):1:p.yearInd(end),1),sum(tt.SourceLatMean(p
.yearInd(1):1:p.yearInd(end),:),2)*16.04,1);
```

```
    [p.bMean.y p.bMean.delta] =
polyconf(p.bMean.p,tt.Mean(p.yearInd(1):1:p.yearInd(end),1),p.bMean.s,'
predopt','observation','simopt','off','alpha',0.32);

    hold on
    plot(tt.Mean(p.yearInd(1):1:p.yearInd(end),1),p.bMean.y,'r-')

plot(tt.Mean(p.yearInd(1):1:p.yearInd(end),1),p.bMean.y+p.bMean.delta,'
r--')
    plot(tt.Mean(p.yearInd(1):1:p.yearInd(end),1),p.bMean.y-
p.bMean.delta,'r--')
    hold off

    fprintf('Total change (%4.0f to %4.0f CE): %4.0f +/- %1.0f Tg
CH4/yr.\n',p.year(1),p.year(2),p.bMean.y(end)-p.bMean.y(1),
2*p.bMean.delta(1))


end


plt.fig58 = 'n'; % Total CH4 Source Emissions.
if plt.fig58 == 'y'
    figure(58);clf;
    plot(tt.Year,sum(tt.Source,2)*16.04,'k.-')
    title('Total CH_4 Source Emissions')
    xlim([yearStart+50 yearEnd])
    xlabel('Years C.E.')
    ylabel('Tg of CH_4 yr^{-1}')
end

% figure(6);clf;
% plot(inputSource(:,1),totalSource*16.04)
% title('Global CH_4 emissions')
% xlabel('Years C.E.')
% ylabel('Tg of CH_4 yr^{-1}')

%figure(7);clf;
%plot(mT,totalBurden*16.04)
%title('Total burden of methane (Tg CH4)')

plt.fig8 = 'n';
if plt.fig8 == 'y'
    figure(8);clf;
    hold on
    plot(inputSource(:,1),lifetime)
    plot(tt.Mean,tt.LifetimeMean,'r-','LineWidth',3)
    title('Atmospheric lifetime of methane (years)')
    xlim([yearStart+50 yearEnd])
    hold off
```

```
end

plt.fig81 = 'n';
if plt.fig81 == 'y'
    figure(81);clf;
    hold on
    plot(inputSource(:,1),lifetimeBox,'.-')
    %plot(tt.Mean,tt.LifetimeMean,'r-','LineWidth',3)
    title('Atmospheric lifetime of methane in each box (years)')
    xlim([yearStart+50 yearEnd])

    hold off
end


plt.fig9 = 'n';
if plt.fig9 == 'y'
    sourceSig = zeros(c.numSources,2);
    sourceSig(:,1:2) = [(1000*(c.r13(1,:)./c.r12(1,:)/r13st-1))'
(1000*(c.rD(1,:)./c.r12(1,:)/rDst-1))'];
    midIndex = dsearchn(tt.Mean,1400);
    meanSourceIso =
[sum(tt.SourceMean(midIndex,:)'.*sourceSig(:,1))/sum(tt.SourceMean(midI
ndex,:)) ...

sum(tt.SourceMean(midIndex,:)'.*sourceSig(:,2))/sum(tt.SourceMean(midIn
dex,:))];
    %meanSinkIso =
sum(tt.SinkMean(midIndex,:)'.*c.boxMass)/sum(tt.SinkMean(midIndex,:));
    meanAtmIso =
[sum(tt.BoxdC13Mean(midIndex,:)'.*c.boxMass)/sum(c.boxMass) ...
        sum(tt.BoxdDMean(midIndex,:)'.*c.boxMass)/sum(c.boxMass)];

    figure(9);clf;
    hold on
    plot(sourceSig(:,1),sourceSig(:,2),'k.')
    text(sourceSig(:,1)-0.7,sourceSig(:,2),sourcePlotNames(:,1))

plot(meanSourceIso(:,1),meanSourceIso(:,2),'r*',meanAtmIso(:,1),meanAtm
Iso(:,2),'b*')
    text([meanSourceIso(:,1) meanAtmIso(:,1)]-0.7,[meanSourceIso(:,2)
meanAtmIso(:,2)],{'Source' 'Atm'})
    text(-30,-350,['e_{^{13}C} = ' num2str(meanSourceIso(1,1)-
meanAtmIso(1,1),'%3.1f')])
    text(-30,-320,['e_D = ' num2str(meanSourceIso(1,2)-
meanAtmIso(1,2),'%5.1f')])
    set(gca,'XDir','reverse','YDir','reverse');
    hold off
    xlabel('\delta^{13}CH_4')
    ylabel('\deltaD(CH_4)')
    %axis([-80 -20 -400 -100])
```

```
end

% figure(fc);clf;
% "Flying carpet" diagram of concentration
% surf(mT,([-75 -45 -15 15 45 75]),boxCH4conc(:,1:6)','LineStyle',':')
% xlabel('Year C.E.')
% ylabel('Latitude')
% zlabel('CH_4 (ppb)')

plt.fig97 = 'n';
if plt.fig97 == 'y'
    figure(97);clf;
    clf;hold on
    for i=1:c.numSources
        plot(-75:30:75,c.sourceDist(:,i)*16.04,'o-
','Color',[i/c.numSources 1-i/c.numSources 1-
i/c.numSources],'LineWidth',3);
    end
    legend(sourcePlotNames)
    xlim([-90 90]);title('Latitudinal Source Distribution');ylabel('Tg
of CH_4 yr^{-1}');xlabel('Latitude')
    hold off
end

% Output the data in the "Scenario" folder.
if ~exist('saveScenarioOutput','var'); saveScenarioOutput = 'n'; end;%
Export data into the Scenario folder.
if saveScenarioOutput == 'y'

xlswrite('Scenario/dc13WDC05A.xls',[ts.d13cWDC05A(:,1),ts.d13cWDC05A(:,
2),ones(length(ts.d13cWDC05A),1)*0.2])

xlswrite('Scenario/dDWDC05A.xls',[ts.dDWDC05A(:,1),ts.dDWDC05A(:,2),one
s(length(ts.dDWDC05A),1)*3])
    xlswrite('Scenario/d13cLD.xls',[ts.d13cLD(:,1),ts.d13cLD(:,2)])
    xlswrite(['Scenario/S' scenario '-records.xls'],[...
        [{'Year'};num2cell(tt.Mean(51:end))],...
        [{'B1 CH4'},{'B6 CH4'},{'B1 dC13'},{'B6 dC13'},{'B1 dD'},{'B6
dD'},{'IPD'};...
        num2cell([tt.BoxCH4FilterMean(51:end,1),...
        tt.BoxCH4FilterMean(51:end,6),...
        tt.BoxdC13FilterMean(51:end,1),...
        tt.BoxdC13FilterMean(51:end,6),...
        tt.BoxdDFilterMean(51:end,1)+offset,...
        tt.BoxdDFilterMean(51:end,6)+offset,...
        tt.BoxIPDFilterMean(51:end)])]])

    if ~exist('combineWetlandOutput','var');
        combineWetlandOutput = 'n';
    end
```

```
    if strcmp(combineWetlandOutput,'y')
        wetlandIndex = sum([strcmp(c.sourceNames,'Box1'),...
            strcmp(c.sourceNames,'Box2'),...
            strcmp(c.sourceNames,'Box3'),...
            strcmp(c.sourceNames,'Box4'),...
            strcmp(c.sourceNames,'Box5'),...
            strcmp(c.sourceNames,'Box6'),...
            strcmp(c.sourceNames,'TropicalWetlands'),...
            strcmp(c.sourceNames,'BorealWetlands')],2);
        xlswrite(['Scenario/S' scenario '-sources.xls'],...
            [[{'Year'};num2cell(tt.Mean)], ...
            [['Wetlands' sourcePlotNames(~wetlandIndex)']; ...

[num2cell(sum(reshape(tt.SourceMean(logical(repmat(wetlandIndex',size(t
t.Mean,1),1)))*16.04,size(tt.Mean,1),sum(wetlandIndex)),2)),...

reshape(num2cell(tt.SourceMean(logical(repmat(~wetlandIndex',size(tt.Me
an,1),1)))*16.04),size(tt.Mean,1),sum(~wetlandIndex))]]]);
    else
        xlswrite(['Scenario/S' scenario '-sources.xls'],...
            [[{'Year'};num2cell(tt.Mean)],[sourcePlotNames';
num2cell(tt.SourceMean*16.04)]])
    end

end

if ~exist('saveScenarioSources','var'); saveScenarioSources = 'n';
end;% Export data into the Scenario folder.
if saveScenarioSources == 'y'
    for i = 1:size(c.sourceNames,1)
        foo = [tt.Mean,tt.SourceMean(:,i)*16.04];
        %file = ['Scenario\' c.sourceNames{i} '.txt'];
        save(['Scenario\Source-' c.sourceNames{i} '.txt'],'foo','-
ascii');
    end

end
% Summary statistics:
plt.summary = 'y';
if plt.summary == 'y'
    startIndex = dsearchn(tt.Mean,-800);
    %endIndex = length(tt.Mean);
    endIndex = dsearchn(tt.Mean,1400);

    summary.SourceIncrease = (sum(tt.SourceMean(endIndex,:),2)-
sum(tt.SourceMean(startIndex,:),2))*16.04;
    summary.Box1 = (tt.SourceLatMean(endIndex,1)-
tt.SourceLatMean(startIndex,1))*16.04;
    summary.Box2 = (tt.SourceLatMean(endIndex,2)-
tt.SourceLatMean(startIndex,2))*16.04;
```

```
    summary.Box3 = (tt.SourceLatMean(endIndex,3)-
tt.SourceLatMean(startIndex,3))*16.04;
    summary.Box4 = (tt.SourceLatMean(endIndex,4)-
tt.SourceLatMean(startIndex,4))*16.04;
    summary.Box5 = (tt.SourceLatMean(endIndex,5)-
tt.SourceLatMean(startIndex,5))*16.04;
    summary.Box6 = (tt.SourceLatMean(endIndex,6)-
tt.SourceLatMean(startIndex,6))*16.04;

    summary.SourceIncreasePercent =
((sum(tt.SourceMean(endIndex,:),2)/sum(tt.SourceMean(startIndex,:),2))-
1)*100;
    summary.Box1Percent =
((tt.SourceLatMean(endIndex,1)/tt.SourceLatMean(startIndex,1))-1)*100;
    summary.Box2Percent =
((tt.SourceLatMean(endIndex,2)/tt.SourceLatMean(startIndex,2))-1)*100;
    summary.Box3Percent =
((tt.SourceLatMean(endIndex,3)/tt.SourceLatMean(startIndex,3))-1)*100;
    summary.Box4Percent =
((tt.SourceLatMean(endIndex,4)/tt.SourceLatMean(startIndex,4))-1)*100;
    summary.Box5Percent =
((tt.SourceLatMean(endIndex,5)/tt.SourceLatMean(startIndex,5))-1)*100;
    summary.Box6Percent =
((tt.SourceLatMean(endIndex,6)/tt.SourceLatMean(startIndex,6))-1)*100;

    summary.Box1CH4 = tt.BoxCH4concMean(endIndex,1)-
tt.BoxCH4concMean(startIndex,1);
    summary.Box6CH4 = tt.BoxCH4concMean(endIndex,6)-
tt.BoxCH4concMean(startIndex,6);
    summary.TropCH4 = tt.TropCH4concMean(endIndex,1)-
tt.TropCH4concMean(startIndex,1);

    summary.Box1CH4Percent = 100*(tt.BoxCH4concMean(endIndex,1)-
tt.BoxCH4concMean(startIndex,1))/mean(tt.BoxCH4concMean(startIndex:endI
ndex,1));
    summary.Box6CH4Percent = 100*(tt.BoxCH4concMean(endIndex,6)-
tt.BoxCH4concMean(startIndex,6))/mean(tt.BoxCH4concMean(startIndex:endI
ndex,6));
    summary.TropCH4Percent = 100*(tt.TropCH4concMean(endIndex,1)-
tt.TropCH4concMean(startIndex,1))/mean(tt.TropCH4concMean(startIndex:en
dIndex,1));

    summary.IPDpoly =
polyfit(tt.Year(dsearchn(tt.Year,yearStart+startIndex):endIndex),tt.Box
IPDFilter(dsearchn(tt.Year,yearStart+startIndex):endIndex),1);
    %plot(-800:1:1800,polyval(summary.IPDpoly,-800:1:1800))
    summary.IPDslope = summary.IPDpoly(1,1)*1000;

    summary.ln1 =
polyval(polyfit(tt.Mean(startIndex:endIndex,1),tt.SourceLatMean(startIn
dex:endIndex,1)*16.04,1),[tt.Mean(startIndex) tt.Mean(endIndex)]);
```

```
    summary.ln2 =
polyval(polyfit(tt.Mean(startIndex:endIndex,1),tt.SourceLatMean(startIn
dex:endIndex,2)*16.04,1),[tt.Mean(startIndex) tt.Mean(endIndex)]);
    summary.ln3 =
polyval(polyfit(tt.Mean(startIndex:endIndex,1),tt.SourceLatMean(startIn
dex:endIndex,3)*16.04,1),[tt.Mean(startIndex) tt.Mean(endIndex)]);
    summary.ln4 =
polyval(polyfit(tt.Mean(startIndex:endIndex,1),tt.SourceLatMean(startIn
dex:endIndex,4)*16.04,1),[tt.Mean(startIndex) tt.Mean(endIndex)]);
    summary.ln5 =
polyval(polyfit(tt.Mean(startIndex:endIndex,1),tt.SourceLatMean(startIn
dex:endIndex,5)*16.04,1),[tt.Mean(startIndex) tt.Mean(endIndex)]);
    summary.ln6 =
polyval(polyfit(tt.Mean(startIndex:endIndex,1),tt.SourceLatMean(startIn
dex:endIndex,6)*16.04,1),[tt.Mean(startIndex) tt.Mean(endIndex)]);
    summary.lnSum =
polyval(polyfit(tt.Mean(startIndex:endIndex,1),sum(tt.SourceMean(startI
ndex:endIndex,:),2)*16.04,1),[tt.Mean(startIndex) tt.Mean(endIndex)]);

%polyval(polyfit(tt.Mean(startIndex:endIndex,1),sum(tt.SourceMean(start
Index:endIndex,:),2)*16.04,1),[tt.Mean(startIndex) tt.Mean(endIndex)])

    summary.ln1CH4 =
polyval(polyfit(tt.Mean(startIndex:endIndex,1),tt.BoxCH4concMean(startI
ndex:endIndex,1),1),[tt.Mean(startIndex) tt.Mean(endIndex)]);
    summary.ln6CH4 =
polyval(polyfit(tt.Mean(startIndex:endIndex,1),tt.BoxCH4concMean(startI
ndex:endIndex,6),1),[tt.Mean(startIndex) tt.Mean(endIndex)]);
    summary.lnTropCH4 =
polyval(polyfit(tt.Mean(startIndex:endIndex,1),tt.TropCH4concMean(start
Index:endIndex,1),1),[tt.Mean(startIndex) tt.Mean(endIndex)]);

    summary.ln1CH4Percent = 100*(summary.ln1CH4(2)-
summary.ln1CH4(1))/mean(tt.BoxCH4concMean(startIndex:endIndex,1));
    summary.ln6CH4Percent = 100*(summary.ln6CH4(2)-
summary.ln6CH4(1))/mean(tt.BoxCH4concMean(startIndex:endIndex,6));
    summary.lnTropCH4Percent = 100*(summary.lnTropCH4(2)-
summary.lnTropCH4(1))/mean(tt.TropCH4concMean(startIndex:endIndex,1));

    %fprintf('Total Increase: %5.0f Tg/yr
(%4.1f%%)\n',summary.SourceIncrease,summary.SourceIncreasePercent);
    %fprintf('Box 3 Increase: %5.0f Tg/yr
(%4.1f%%)\n',summary.Box3,summary.Box3Percent);
    %fprintf('Box 4 Increase: %5.0f Tg/yr
(%4.1f%%)\n',summary.Box4,summary.Box4Percent);
    %fprintf('Box 5 Increase: %5.0f Tg/yr
(%4.1f%%)\n',summary.Box5,summary.Box5Percent);
    %fprintf('Box 6 Increase: %5.0f Tg/yr
(%4.1f%%)\n',summary.Box6,summary.Box6Percent);
    %fprintf('Box 1 CH4     : %5.0f ppb
(%4.1f%%)\n',summary.Box1CH4,summary.Box1CH4Percent);
```

```
    %fprintf('Box 6 CH4     : %5.0f ppb
(%4.1f%%)\n',summary.Box6CH4,summary.Box6CH4Percent);
    %fprintf('IPD slope     : %5.0f ppb/ka\n',summary.IPDslope);

    % Uses the actual numbers from the model
    fprintf('Year: %4.0f to %4.0f    |  1  |  2  |  3  |  4  |  5  |  6
| Total |\n',tt.Mean(startIndex),tt.Mean(endIndex))
    fprintf('---------------------Scenario source changes:------------
---------\n')
    fprintf('Source Change (Tg/yr)
|%5.0f|%5.0f|%5.0f|%5.0f|%5.0f|%5.0f| %5.0f
|\n',summary.Box1,summary.Box2,summary.Box3,summary.Box4,summary.Box5,s
ummary.Box6,summary.SourceIncrease)
    fprintf('Source %% Change
|%5.0f|%5.0f|%5.0f|%5.0f|%5.0f|%5.0f| %5.0f
|\n',summary.Box1Percent,summary.Box2Percent,summary.Box3Percent,summar
y.Box4Percent,summary.Box5Percent,summary.Box6Percent,summary.SourceInc
reasePercent)
    fprintf('CH4 Change (ppb)      |%5.0f|     |     |     |
|%5.0f| %5.0f |\n',summary.Box1CH4,summary.Box6CH4,summary.TropCH4)
    fprintf('CH4 %% Change          |%5.0f|     |     |     |
|%5.0f| %5.0f
|\n',summary.Box1CH4Percent,summary.Box6CH4Percent,summary.TropCH4Perce
nt)
    %fprintf('IPD slope: %5.0f ppb/ka\n',summary.IPDslope);

    % Reports the linear regression of emission changes.
    %fprintf('Year: %4.0f to %4.0f    |  1  |  2  |  3  |  4  |  5  |
6  | Total |\n',tt.Mean(startIndex),tt.Mean(endIndex))
    fprintf('---------------Linear regression of source changes:-------
---------\n')
    fprintf('Source Change (Tg/yr)
|%5.0f|%5.0f|%5.0f|%5.0f|%5.0f|%5.0f| %5.0f |\n',summary.ln1(2)-
summary.ln1(1),summary.ln2(2)-summary.ln2(1),summary.ln3(2)-
summary.ln3(1),summary.ln4(2)-summary.ln4(1),summary.ln5(2)-
summary.ln5(1),summary.ln6(2)-summary.ln6(1),summary.lnSum(2)-
summary.lnSum(1))
    %fprintf('Source %% Change
|%5.0f|%5.0f|%5.0f|%5.0f|%5.0f|%5.0f| %5.0f
|\n',summary.Box1Percent,summary.Box2Percent,summary.Box3Percent,summar
y.Box4Percent,summary.Box5Percent,summary.Box6Percent,summary.SourceInc
reasePercent)
    fprintf('CH4 Change (ppb)      |%5.0f|     |     |     |
|%5.0f| %5.0f |\n',summary.ln1CH4(2)-
summary.ln1CH4(1),summary.ln6CH4(2)-
summary.ln6CH4(1),summary.lnTropCH4(2)-summary.lnTropCH4(1))
    fprintf('CH4 %% Change          |%5.0f|     |     |     |
|%5.0f| %5.0f
|\n',summary.ln1CH4Percent,summary.ln6CH4Percent,summary.lnTropCH4Perce
nt)
    fprintf('IPD slope: %5.0f ppb/ka\n',summary.IPDslope);
end
```